Mechanisms and applications of the transduction of heat into sound by arrays of thin metallic films

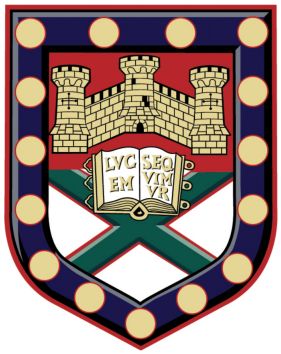

David Tatnell

A thesis submitted for the degree of
Doctor of Philosophy in Physics

in the

EPSRC Centre for Doctoral Training in Metamaterials
College of Engineering, Mathematics and Physical Sciences
University of Exeter

April, 2022

Declaration

Submitted by David Tatnell to the University of Exeter as a thesis for the degree of Doctor of Philosophy in Physics in April 2022.

I acknowledge financial support from the Engineering and Physical Sciences Research Council (EPSRC) of the United Kingdom, via the EPSRC Centre for Doctoral Training in Metamaterials (Grant No. EP/L015331/1) and the QinetiQ Prosperity Partnership (EP/R004781/1).

David Tatnell

April, 2022

Abstract

The work presented in this thesis concerns the generation of sound via heat; namely, the thermoacoustic effect. This heat is typically provided by electric heating in thin film devices, resulting in non-resonant, broadband sound generation. The aim of this work is to develop a deeper understanding of the mechanisms behind this process, as well as identify potential applications. This is achieved via analytical and numerical simulations, and experimental measurements.

A novel analytical model is derived for describing the sound generated by thermoacoustic sources. This is validated by simulation, as well as electrical, thermal and acoustic measurements of a variety of sources.

Multiple sources are also considered, in the context of acoustic phased arrays. It is found that thermoacoustic sources can successfully reproduce typical phased array behaviour, such as beam forming and steering. It is shown that the unique characteristics of this transduction method make thermoacoustic sources highly favourable for this application. In particular, the sources are non-reciprocal, eliminating issues with element cross-talk. The thermal profile is spatially dependent on the local current flow, which offers the ability to define thermal sources by confining the current to specific regions in the film, such that a full phased array can be produced using a single film. Electrical coupling between elements, due to the nonlinearity of the source, results in an additional sound source that is highly sensitive to the configuration of the array. It is shown how this coupling can be used to infer properties of the array elements themselves by measuring the generated sound.

A new method of thermoacoustic generation via thermoelectric effects is also explored. Measurements using thermocouple devices show that this results in linear sound generation, at the source fundamental frequency, due to the reversible nature of the effect. This reversibility also presents opportunities to further optimise sound output via dynamic control of the device temperature.

Acknowledgements

Well, here we are; after a whirlwind four-ish years, the book is written and it is finally done. While this work represents a measurable degree of progress, it is the experiences that I have shared with others along the way that I feel have truly shaped the final outcome. I owe so much to those who have joined me in this journey, and I hope to acknowledge them here.

Firstly, a huge thanks has to go to my supervisors, David Horsell and Alastair Hibbins. Your patient and supportive approach has been invaluable during my development as a researcher. I have always felt that I had free rein to explore the research to the full extent, with our discussions creating many more exciting directions for investigation. Your ability to keep the big picture in mind also helped me to find my way back to the path when I strayed too far down the rabbit hole. I feel very fortunate to have had you as my supervisors, and for that I am incredibly grateful.

I would also like to thank my collaborators: Mark Heath, Steve Hepplestone, Simon Horsley and Chris Lawrence. Working with you these past few years has been a pleasure, and the many discussions have challenged me and helped me to develop in many ways. This is also true for the acoustics research group: Ben, Beth, Cameron, Dan, David, Emily, Greg, Ian, Jake, Joseph, Nicholas, Roy, Sam, Tim and Will. Thanks for all the (not always trivial) questions and suggestions that have kept me on my toes for the past few years. Also, thank you to the CDT admin team – Anja, Deb and Kelyn – for keeping everything running in the background, as well as the rest of the CDT students for cultivating a friendly and inclusive environment that has been a joy to be a part of.

Outside of the CDT, the very first person I'd like to thank is Sarah. Without your encouragement (and that very long car trip) at the start, I doubt the past few years would have happened. Of course, then I have to thank my family who, on top of occasionally making sure I still exist, have never failed to support me in whatever I choose to do, as well as at least pretend to understand what it is I am doing. Simon and Peter – thanks for being my cell buddies throughout these past few years and seemingly endless lockdowns. Your camaraderie helped me feel at home no matter how loud the bird screeches were. Also, to Jess, Ed, Iago, Emily, Katie and Dirac (and his magnificent whiteboard-erasing thumpers.) Thanks for providing a steady source of distractions with all the pub trips, BBQs, wild swimming adventures and more. To my fellow plastic-pullers: Jake, Patrick and Shane. Thanks for joining me in making sure I was only climbing walls in a literal sense, rather than figurative.

Finally, Alice and Horatio. You may have joined towards the end of my time here, but your energy (and constant affirmations that you were, in fact, real) helped me cross that final hurdle. I'm looking forward to the next adventure!

Contents

List of Figures

List of Symbols

A	area	m^2
$B_{s,T}$	isentropic, isothermal bulk modulus	Pa
$c_{p,\mathcal{V}}$	isobaric, isochoric specific heat capacity	$\mathrm{J\ K^{-1}\ kg^{-1}}$
C	heat capacity	$\mathrm{J\ K^{-1}}$
d	thickness, separation	m
D	directivity factor	
e	thermal effusivity	$\mathrm{J\ m^{-2}\ K^{-1}\ s^{-\frac{1}{2}}}$
$\boldsymbol{E}$	electric field	$\mathrm{V\ m^{-1}}$
f	frequency	Hz
G	electrical conductance	S
I	electric current	A
$\boldsymbol{j}_e$	electric current density	$\mathrm{A\ m^{-2}}$
$\boldsymbol{j}_q$	heat flux	$\mathrm{W\ m^{-2}}$
k	wavenumber	$\mathrm{m^{-1}}$
L	length	m
p	pressure	Pa
P	power	W
Q	heat energy density	$\mathrm{J\ m^{-3}}$
r, θ, ϕ	spherical coordinates	m, rad, rad
R	electrical resistance	Ω
s	entropy per unit mass	$\mathrm{J\ K^{-1}\ kg^{-1}}$
S	Seebeck coefficient	$\mathrm{V\ K^{-1}}$
t	time	s
T	temperature	K
$\boldsymbol{u}$	velocity	$\mathrm{m\ s^{-1}}$
U	internal energy	J
v_s	isentropic speed of sound	$\mathrm{m\ s^{-1}}$
V	electric potential	V
x, y, z	Cartesian coordinates	m
α	thermal pressure coefficient	Pa K

β	thermal expansion coefficient	K^{-1}
γ	ratio of specific heats	
δ	thermal diffusion length	m
η	efficiency	
κ	thermal conductivity	W m^{-1} K^{-1}
μ	fluid viscosity	kg m^{-1} s^{-1}
Π	Peltier coefficient	V
ρ	density	kg m^{-3}
σ	electrical conductivity	S m^{-1}
φ	electrical phase	rad
ψ	acoustic phase	rad
ω	angular frequency	rad s^{-1}
$\mathcal{E}$	thermal energy ratio	
$\mathcal{G}$	Green function	
$\mathcal{I}$	acoustic intensity	W m^{-2}
$\mathcal{L}_{T,v}$	thermoviscous charateristic lengths	m
$\mathcal{T}$	Thomson coefficient	V K^{-1}
$\mathcal{V}$	volume	m^3

Chapter 1

Introduction

Sound is a vibration that is characterised by small fluctuations in fluid pressure. These pressure fluctuations can be described in terms of the first law of thermodynamics,

$$\mathrm{d}U = T\mathrm{d}s - p\mathrm{d}\mathcal{V}\,,$$

where U is the internal energy, T is the temperature, s is entropy, p is the pressure and $\mathcal{V}$ is volume. The study of sound, acoustics, is traditionally associated with the latter part of this equation, where sound is produced as a result of volume work being performed on the fluid. Thermoacoustics, on the other hand, explores the close relationship between a fluid's pressure and temperature.

Thermoacoustics explains a number of interesting phenomena, such as: thunder [1], the sounds made by bombardier beetles [2], the hydrogen 'pop' test, and the operation of the traditional Japanese Kibitsunokama [3]. The work in this thesis focuses on a specific branch of thermoacoustics; namely, the generation of sound purely by electric heating [4]. This is most commonly achieved via resistive (Joule) heating of a thin conductor due to a time-varying electric current. A basic overview of the process is illustrated in Fig. 1.1. Fluid molecules impinging on the heated conductor gain kinetic energy, resulting in a pressure gradient near the surface. For an oscillating heat source, this results in the generation of sound waves. The Joule heat generated is independent of the direction of the electric current, so the air can only be heated, not cooled. This results in sound generation at the second harmonic of the source. The main advantage of this method of sound generation is that it requires no moving parts, and is therefore non-resonant. Paired with the simple electrical control, this allows for an incredibly versatile sound source to be realised.

An overview of the historical development of Joule-based thermoacoustics will now be given. This chapter then concludes by outlining the intended role of this thesis in the development of the field.

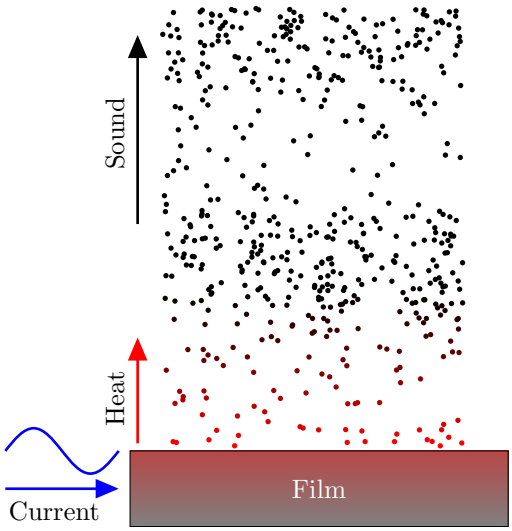

FIGURE 1.1: Thermoacoustic generation due to Joule heating in a thin conductive film (not to scale). An alternating current periodically transfers heat to the nearby air, resulting in pressure changes that propagate as sound.

1.1 Historical Perspective

The first mention of Joule-based thermoacoustics came from Preece in 1880 [5], who investigated suspended metal wires, attached at one end to a diaphragm. They noticed that, upon application of alternating current to the wire, sound was produced at the diaphragm. This they attributed to the rapid thermal expansion and contraction of the wire due to Joule heating. Later, De Lange [6] proposed the approach of using the heat itself to produce the sound, as opposed to moving a diaphragm. They presented measurements of the sound produced by a suspended platinum wire, which they referred to as a 'thermophone'. Insufficient data was obtained to produce any significant theory of their operation, however.

The first detailed description of the thermophone came from Arnold and Crandall in 1917 [4]. They measured the sound output from a 700 nm platinum strip, as shown in Fig. 1.2, driven by alternating currents of frequency up to around 3 kHz. They also provided an in-depth mathematical treatment of the phenomenon. This assumed that the heat dissipated by the film causes expansion and contraction in a small thermal boundary layer of air at the film's surface. The expanding boundary layer was then assumed to behave as a piston, which drives the acoustic behaviour in the surrounding air. From these assumptions, they derived a relationship for the generated acoustic pressure, p,

$$p(P, f, r) \propto \frac{P\sqrt{f}}{r},$$

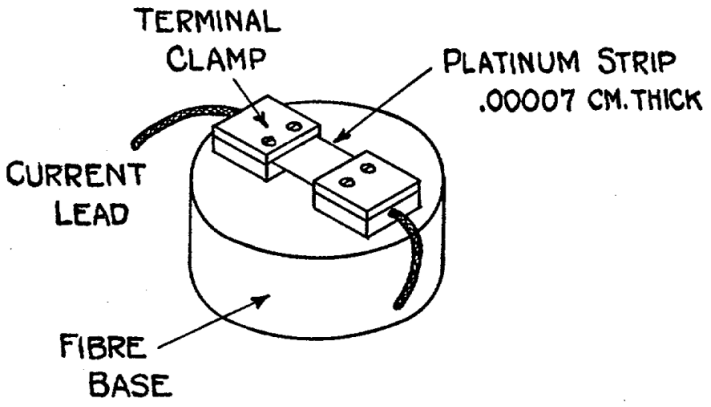

FIGURE 1.2: Arnold and Crandall's early thermophone. A 700 nm platinum strip was suspended between two electrical terminals. Passing an alternating current through the strip generated sound due to Joule heating. Image taken from [4].

where P is the supplied AC power, f is the driving frequency and r is the measurement distance. The proportionality arises from a combination of the thermal parameters of the system. In general, they found that the efficiency of the sound transduction was poor compared to standard mechanical transducers; however, they noted some advantageous characteristics of thermophones. Primarily, thermophones are remarkably easy to fabricate, requiring only a conductive film. The lack of moving parts also leads to a broadband, non-resonant source. In addition to this, the Joule heating mechanism is thermodynamically irreversible. As such, thermophones are non-reciprocal, *i.e.*, they are not able to act as receivers. They concluded that these characteristics, along with the predictable frequency response of the devices, made thermophones ideal as precision sources for use in calibration.

Due to the poor efficiency, thermophones were largely disregarded until 1999, where advances in fabrication allowed Shinoda *et al.* [7] to demonstrate an aluminium thin film thermophone on a porous silicon substrate. The field has seen continued development ever since. The majority of thermophone research to-date has been to address the issue of efficiency, mostly through exploration of different materials for devices. There are three main aspects when considering the efficiency of thermophones: the background temperature, the distribution of the generated heat across the device and air, and the generation of sound in air due to heat.

When a thermophone is driven, a large portion of the heat generated results in simply increasing the average temperature of the device and the surrounding air. A thermophone can be considered as a heat engine, operating between a hot reservoir (the alternating heat source) and a cold reservoir (the surrounding air) to produce

mechanical work in the form of sound. As such, the efficiency of transduction is limited by the Carnot efficiency,

$$\eta_{\text{Carnot}} = 1 - \frac{T_{\text{cold}}}{T_{\text{hot}}}\,, \tag{1.1}$$

where T_{hot} and T_{cold} are the reservoir temperatures. Clearly then, the increased background temperature due to wasted heat serves only to further limit the efficiency of transduction. As such, it was found to be necessary to reduce the background temperature with appropriate heat-sinking [8–10].

The aspect with the greatest scope for optimisation is the choice of materials for the active film and substrate. Arnold and Crandall mentioned that, to produce a significant amount of sound, it was required that the heating element be very thin and have a low heat capacity, such that its thermal inertia was low. A high thermal inertia results in smaller differences between the film temperature and the surroundings, as well as limiting the frequency at which the device can be driven. As thermophones developed into devices involving thin films on rigid substrates, the limitations of the thermal inertia became very clear. This was highlighted by a model presented by Daschewski *et al.* [11], where the film, substrate, and nearby air layer are treated as parallel thermal capacitances, through which the Joule heat is distributed. This is illustrated in Fig. 1.3. By assuming that the heat transferred to the air and substrate layers is distributed only within the thermal boundary layer, it can be shown that the proportion of heat transferred to the air is given by

$$Q_{\text{air}} = \frac{e_{\text{air}}}{e_{\text{air}} + e_{\text{substrate}} + e^*_{\text{film}}} Q_{\text{total}}\,, \tag{1.2}$$

where e is the thermal effusivity, and e^*_{film} is a similar quantity for the film. The salient point this model evinces is that, for typical material properties, the vast majority of the heat is transferred to the substrate, as opposed to the air. As such, the substrate material is a severely limiting factor in a thermophone's efficiency. La Torraca *et al.* [12] further showed that this also has an effect on the spectral response of the thermophone, with a lower proportion of heat being transferred to the air as the frequency is increased, as seen in Fig. 1.4.

To reduce the amount of heat going to the substrate, as well as to demonstrate the application potential of thermophones, many different substrate materials have been investigated. Some of which are shown in Fig. 1.5. These include (but are not limited to) silicon [7], quartz-glass [13], polymers [14, 15], and paper [16]. The best way to avoid the substrate issue, however, is to simply avoid using a substrate. Because of

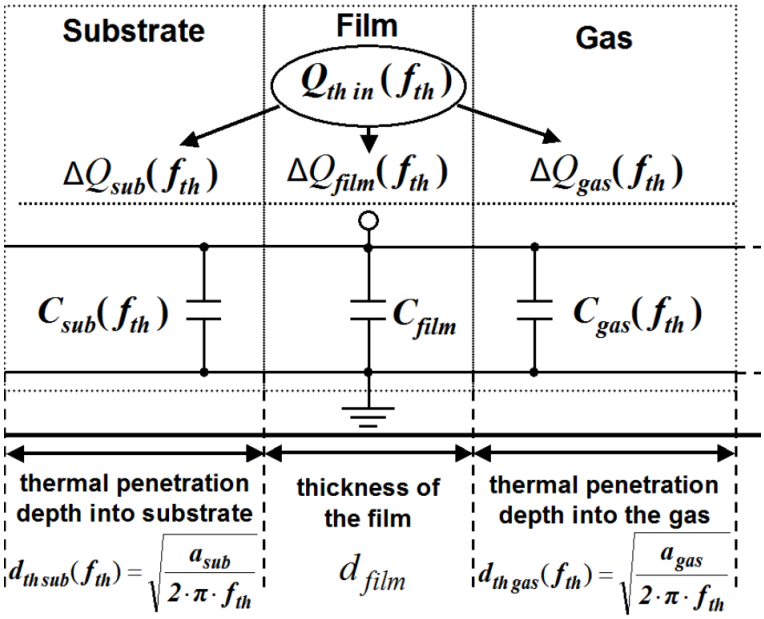

FIGURE 1.3: Thermophone heat distribution model from Daschewski *et al.* The dissipated Joule heat is spread throughout the active film, substrate, and gas layers. The proportion of heat transferred to each layer can be determined by modelling the layers as parallel thermal capacitances. Image taken from [11].

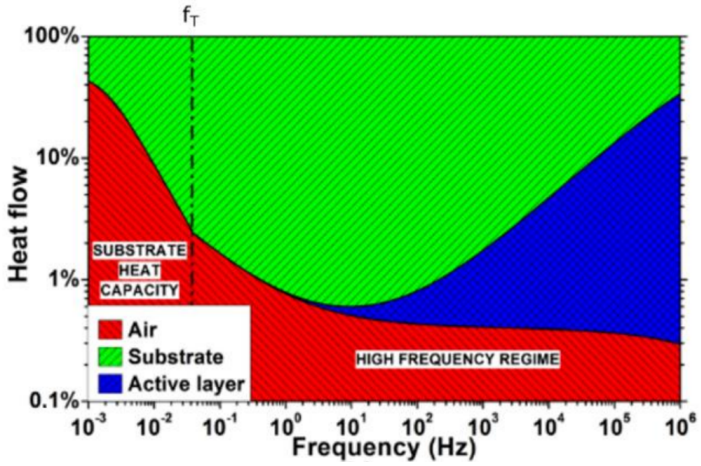

FIGURE 1.4: Proportion of the heat transferred to each layer as a function of frequency, using the model from Daschewski *et al.* As the frequency increases, the thermal inertia of the active film becomes more significant, with a greater proportion of the generated heat being localised to the film. Image taken from [12].

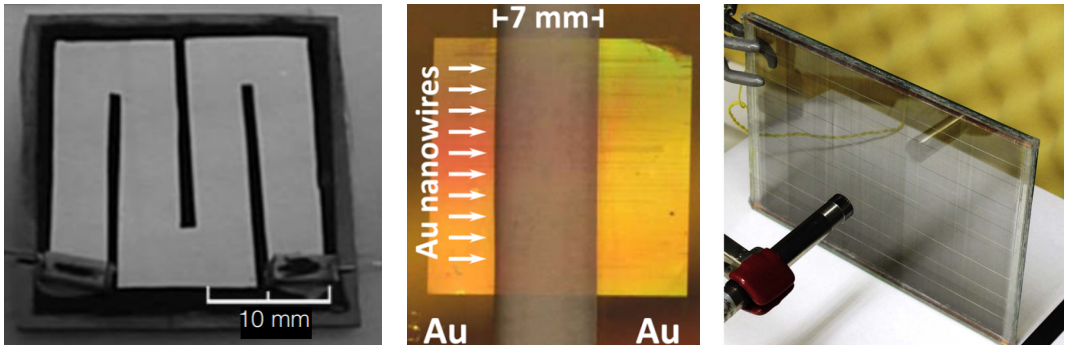

FIGURE 1.5: Various thermophone designs. **Left:** A serpentine aluminium film on porous silicon substrate [7]. **Middle:** Gold nanowires suspended over a substrate [19]. **Right:** Freestanding, layered carbon nanotube sheets [45].

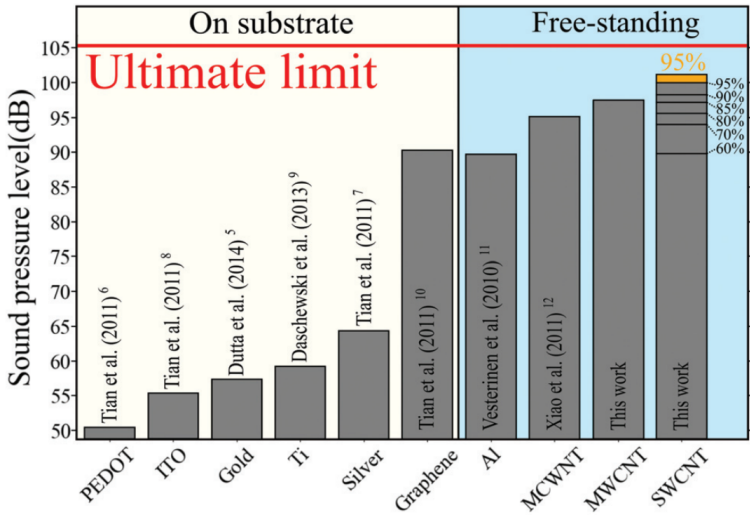

FIGURE 1.6: Reported sound pressures for different thermophone film materials, measured at 100 kHz and normalised to a distance of 3 cm and power of 1 W. Image taken from [46].

this, research has predominantly shifted into using suspended films and nanowires [12, 17–21]. The active film materials have also been investigated, involving many functionally-relevant materials, such as aluminium [7], titanium [22], gold [23], silver [24], ITO [25], organic materials [26] and nanoparticles [27]. A comparison of the sound pressures achieved from different film materials is shown in Fig. 1.6. Particular attention has been paid to carbon-based materials, such as graphene [28–30] and carbon nanotubes (CNTs) [31–39]. These materials boast some of the lowest heat capacities, whilst being able to withstand very high current densities. They can also be readily incorporated into flexible devices [36, 37, 40] and made porous, further increasing surface area [41–43]. Measurements by Bouman, Barnard and Asgarisabet [44] place the efficiency of CNT-based thermophones in the range $(4.3 - 319) \times 10^{-6}\%$ for an input power of 72 W and frequency range 100-10000 Hz.

Even assuming all of the generated heat is transferred to the air, there is one final issue: the weak coupling between temperature and pressure in the air. Vesterinen *et al.* [47] showed that the maximum possible efficiency for a baffled planar heat source of area A (in the high-frequency limit and assuming zero viscosity) is

$$\eta_{\max} = \frac{P v_s}{2 A \rho_0 c_p^2 T_0^2} , \tag{1.3}$$

where P is the driving power, v_s is the adiabatic speed of sound in the medium, ρ_0 is the medium density, c_p is the medium isobaric heat capacity and T_0 is the ambient temperature. The efficiency limit as a function of frequency is illustrated in Fig. 1.7. This is an unavoidable limit, since it depends only on the properties of the medium itself. Because of this, thermophones have been measured in a variety of different media [13, 48, 49]. A natural candidate for this is water, due to its range of applications. Water, however, presents additional issues with its electrical conductivity and heat capacity. Despite this, CNTs have been shown to be surprisingly effectively underwater [10]. This is owed to their hydrophobicity, where, upon submersion, the individual nanotubes would be encased in a small layer of air, which would act as the transduction medium, rather than the water itself. Suspended CNTs are, however, very fragile and easily damaged by water flows. Underwater solutions therefore typically involve a thermophone encased within a resonant cavity, filled with an inert gas, where acoustic energy is coupled to the water via the cavity walls [50–53]. This does remove the broadband nature of the source, although, since the source itself is non-resonant, the cavity dimensions can be tuned for a specific spectral response. The resonant nature of the cavity also affords opportunities to improve efficiency via applying pulses, rather than continuous driving of the thermophone [45].

The work by Arnold and Crandall highlighted some unique characteristics of Joule-based thermoacoustics. One of these is second harmonic generation: since the Joule power is quadratic with respect to the applied voltage, the sound pressure generated is the square of the driving signal. When the driving signal consists of a single frequency component, this results in sound pressure being generated at the second harmonic of the source, as well as producing a substantial DC component. This second harmonic generation is not immediately an issue, since the driving frequency can simply be halved. The main concern in this case is the DC component, which is ultimately wasted to the surroundings as excess heat, increasing the device temperature and reducing efficiency. For higher powers it can also lead to degradation of the film layer. The nonlinearity becomes more of a problem when considering signals with multiple frequency components, where it leads to harmonic distortion

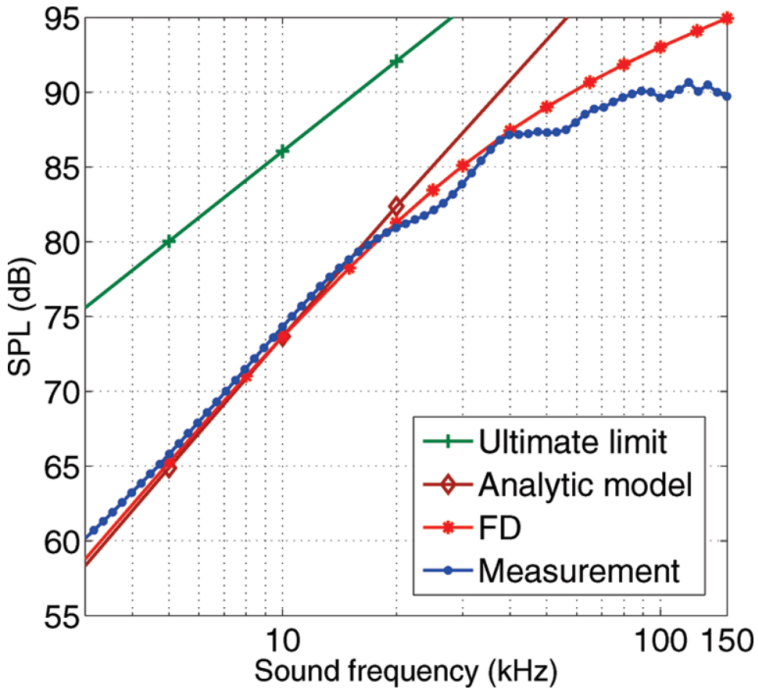

FIGURE 1.7: Ultimate limit of thermophone efficiency predicted by Vesterinen *et al.*, compared to analytical and finite difference models, as well as measurement of a typical device. Image taken from [47].

in the form of sum and difference heterodynes. The effects of the source nonlinearity can be negated by applying a sufficiently large DC bias; however, this also leads to greater DC heat dissipation as a consequence. There has been a substantial amount of work to avoid this issue [54–56]. Most efforts to this effect have involved preconditioning of the driving signal to minimise unwanted harmonics. Notably, Sugimoto and Nakajima [57] proposed the use of a 'square-root' circuit to cancel out the squaring effect of the Joule heat. This is simulated in Fig. 1.8. This method does still require the use of a DC bias, since the input signal to the square root circuit must be entirely positive. However, the resulting sound contains significantly reduced second harmonic distortion, as opposed to a simple DC bias of the same magnitude. This approach was further developed by La Torraca *et al.* [58], who developed a computer algorithm to dynamically adjust the DC bias, in real-time, to minimise both the harmonic distortion and the DC bias. This approach achieved a reported 0.48 % total harmonic distortion, as well as reductions in average film temperature up to 85%. The actual reduction was highly dependent on the driving signal, since broadband signals required greater use of the DC bias, compared to simpler signals. Despite the efforts to avoid the additional distortion, it has also been demonstrated that it can be useful in certain applications. For example, Heath

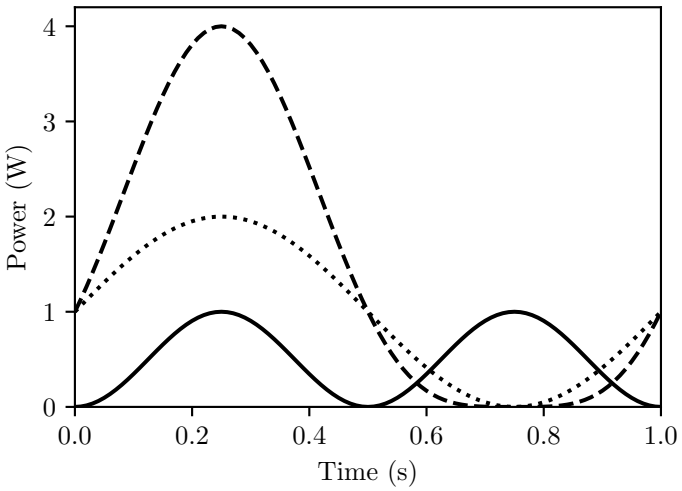

FIGURE 1.8: Simulated power dissipation in a 1 Ω resistor due to a sinusoidal voltage of amplitude 1 V and frequency 1 Hz. For the DC biased cases, the amplitude of the bias is 1 V. In the unbiased case (solid line), the power dissipation (and therefore sound generation) occurs at the second harmonic of the source since the voltage oscillates between positive and negative values. Applying a DC bias (dashed line), such that the voltage is always positive, causes the power dissipation to occur at the first harmonic, with a small second harmonic distortion that decreases with the magnitude of the bias. Feeding the biased signal through a square-root circuit before driving the resistor removes this second harmonic distortion (dotted line).

and Horsell [59] showed that nonlinear conduction in graphene led to an additional third harmonic distortion, and were able to use sound measurements at the third harmonic to measure the degree of nonlinearity.

Another unique characteristic of thermoacoustics is that the Joule heating mechanism is thermodynamically irreversible. As such, thermophones only act as sources, not receivers. Despite this, there have been some efforts to use thermophones as a microphone [60]. This is mostly based upon the principle of hot-wire anemometry, which exploits the temperature dependence of resistance. While this does, in principle, work, the observed signal is low and is difficult to separate from electromagnetic interference effects.

Thermophones are currently not suitable for music reproduction. This is on account of the nonlinearity of the source, which leads to distortion in the sound. They have been shown to be advantageous in other acoustic applications, however. Perhaps the most prominent is in non-destructive evaluation (NDE) [22, 61, 62]. Since thermophones are non-resonant, they have an incredibly well-defined pulse response, free of the post-excitation ringing effects that their mechanical counterparts experience, as demonstrated in Fig. 1.9. Because of this, thermophones could achieve

much greater precision and signal-to-noise ratio with time-of-flight measurements. Such attributes have also proven useful for various sensing and measurement applications [63–65]. The potential of the thermophone is further enhanced by the ability to make flexible sources that can conform to the shape of the sample. This has found other applications in areas such as active noise cancelling, where thermophones can be deposited on vibrating surfaces to reduce mechanical noise [66–68]. Flexibility of thermophones is also attractive for consumer applications. Coupled with the favourable optical properties of materials such as graphene and the ease at which devices can be miniaturised, this makes them ideally suited to screen-based and wearable technologies [69, 70]. A few thermophone applications are outlined in Fig. 1.10.

Since Arnold and Crandall's original theory on thermophones, many alternative descriptions have been published [11, 47, 71–74]. The most complete descriptions come from previous considerations of sound attenuation due to thermal and viscous effects [75]. Here the acoustic wave equation is coupled to the thermal diffusion equation via a temperature- and pressure-dependent fluid density, assuming small, linear changes over a large background field. The main conclusion from these models, in contrast to that of Arnold and Crandall, is that the pressure radiated from a point-like thermophone is

$$p(P, f, r) \propto \frac{Pf}{r},$$

where P is the AC Joule power, f is the driving frequency and r is the measurement distance. The proportionality arises from the fluid material properties.

1.2 This Work

The works discussed in the previous section leave some important questions unanswered: how do individual thermoacoustic sources behave when in proximity to each other? Can the sound generated by a thermophone be used to infer properties of the source itself? Are there alternative methods to Joule heating, and do they behave differently? This thesis aims to address these questions. The following is an outline of the content that can be found in the subsequent chapters.

Chapter 2 focuses on the essential background physics for describing thermoacoustic generation. This includes both the Joule heating mechanism and the resulting thermoacoustic waves. This will be referred to throughout this thesis. Chapter 3 describes the experimental and computational methods used throughout this work, including device fabrication, acoustic and thermal measurements, and numerical

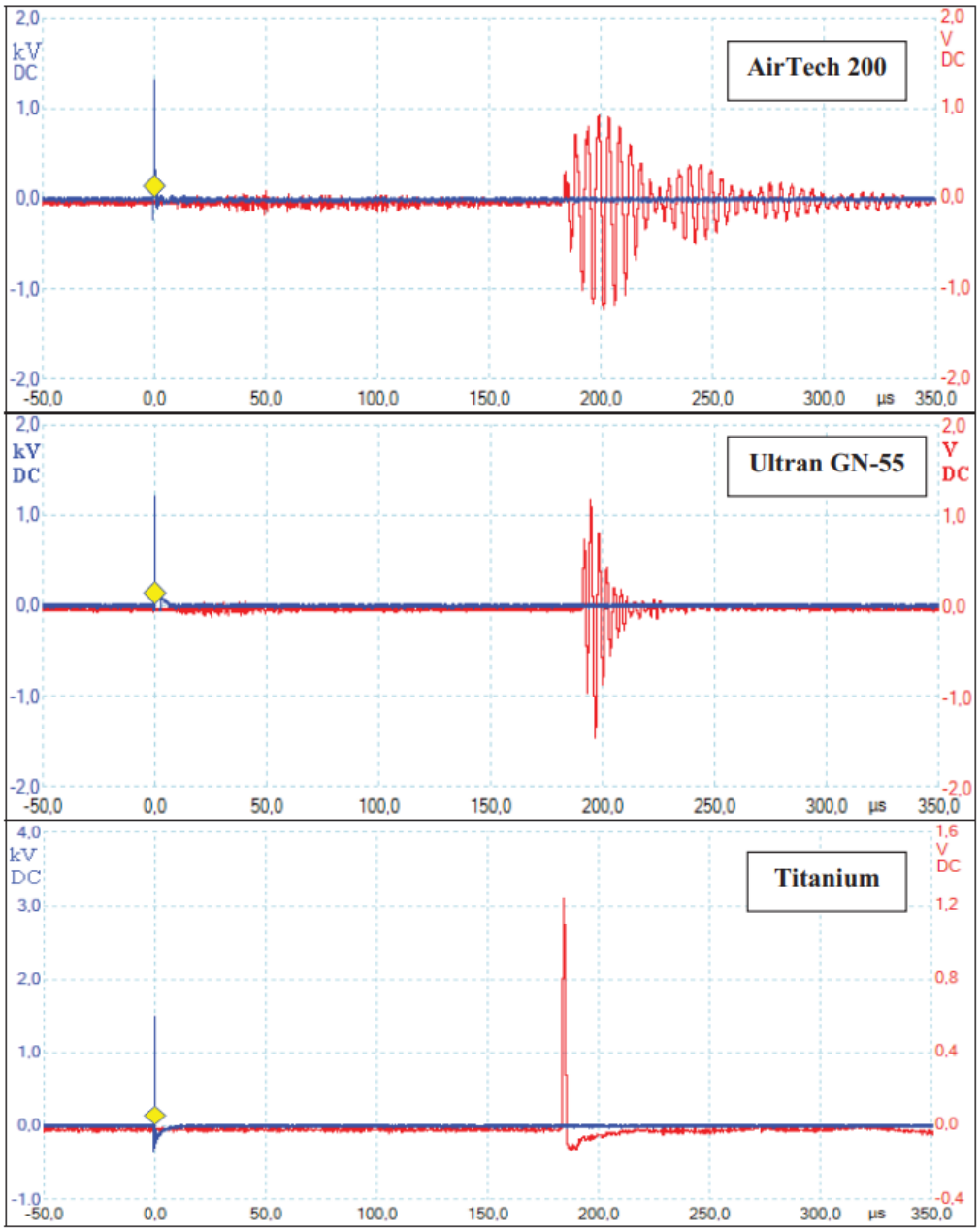

FIGURE 1.9: Response of a titanium thermophone (bottom) excited with a 500 ns pulse, compared to two commercial mechanical transducers. Shown is the measured sound at a distance of 6 cm as a function of time (red), compared to the electrical signal (blue). Image taken from [22].

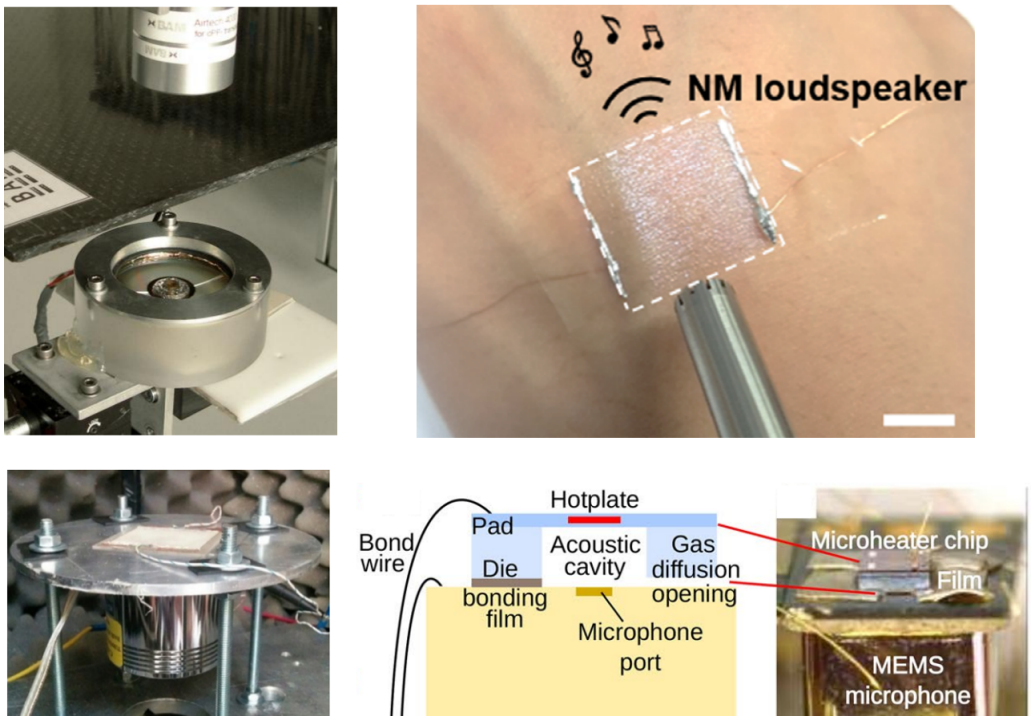

FIGURE 1.10: Various applications of thermophones. **Top left:** Non-destructive evaluation [61]. **Top right:** A skin-attachable thermophone consisting of a mesh of silver nanowires [70]. **Bottom left:** Active noise cancellation using a thermophone deposited on a vibrating surface [67]. **Bottom right:** A thermophone-based gas sensor [65].

modelling. Chapter 4 marks the beginning of the experimental work in this thesis. Here, a new model for predicting the sound output from thermoacoustic devices will be presented, which will subsequently be verified with experimental measurements. This chapter also serves to demonstrate the methods presented in the previous chapter. Chapter 5 expands on this work by considering the collective behaviour of groups of thermophones driven simultaneously, in the context of ultrasonic phased arrays. Chapter 6 explores how the unique behaviour of thermophone arrays can be used to make acoustic measurements of electrical properties. Finally, in Chapter 7, the suitability of the thermoelectric effect, as an alternative to Joule heating, will be discussed. In Chapters 8 and 9, some future directions for further investigation will be suggested, and the work presented in this thesis will be summarised.

Chapter 2

Background Theory

The aim of this chapter is to introduce the fundamental concepts necessary for describing the operation of thermoacoustic devices. The concepts presented in this chapter are not the work of the author; however, they form the mathematical basis that will be built upon throughout this thesis.

The chapter begins with a description of the Joule heating mechanism, and how it leads to second harmonic generation for thermoacoustics. The thermal modelling of devices is then discussed, including the distribution of the dissipated heat between the air and the device itself. A set of equations describing coupled temperature and pressure waves in air is then derived. Finally, some standard acoustic definitions are given, which will be used for characterising devices.

2.1 Joule Heating

Thermoacoustic sound generation can be achieved using any oscillating heat source. The focus of the present work, however, is sound generation via electric Joule heating [76], since this offers a convenient way to control the sound output with high precision. In this section, the principles behind Joule heating will be described, as well as the unique characteristics this method affords for thermoacoustic generation.

Ohm's Law states that the electric current density, $\boldsymbol{j}_\mathrm{e}$, is related to the electric field, $\boldsymbol{E}$, by

$$\boldsymbol{j}_\mathrm{e} = \sigma \boldsymbol{E}\,, \tag{2.1}$$

where σ is the electrical conductivity. The Joule heat dissipated per unit volume is then

$$Q_\mathrm{Joule} = \boldsymbol{E} \cdot \boldsymbol{j}_\mathrm{e} = \boldsymbol{E}^2 \sigma = \frac{\boldsymbol{j}_\mathrm{e}^2}{\sigma}\,. \tag{2.2}$$

The work in this thesis will primarily use the lumped form of Ohm's law,

$$I = \frac{V}{R}\,, \tag{2.3}$$

where I is the total electric current, V is the applied potential difference and R is the total resistance. The total Joule heat is then given by the electric power,

$$P = VI = \frac{V^2}{R} = I^2 R\,. \tag{2.4}$$

Using Joule heating for thermoacoustic generation has two main consequences. The first is that, since Joule heat is a result of inelastic scattering of electrons, it is thermodynamically irreversible. Therefore, Joule-based thermophones can only act as sources of sound, not receivers. The second is that the generated heat is nonlinear with respect to the driving voltage, hence the sound generation occurs at the second harmonic of the driving signal. The physical reasoning for this is that the Joule heat generated is not dependent on the direction of the electric current. The consequences of this for thermoacoustic generation will now be shown.

Consider a time-varying voltage, consisting of a single frequency component, ω,

$$V\left(t\right) = V_0 \sin\left(\omega t\right)\,,$$

where V_0 is the voltage amplitude. The power dissipated across a resistive load, R, in this case is

$$\begin{aligned} P\left(t\right) &= \frac{V_0^2}{R} \sin^2\left(\omega t\right) \\ &= \frac{V_0^2}{2R}\left[1 - \cos\left(2\omega t\right)\right]\,. \end{aligned}$$

The power therefore has two components: a DC part, which contributes to the steady-state heating of the surroundings and is ultimately wasted, and an AC part that generates the sound. This AC part occurs at twice the frequency of the source, hence Joule heating leads to sound generation at the second harmonic. For signals consisting of multiple frequency components, this results in additional harmonic distortion. For example,

$$V\left(t\right) = V_\mathrm{A} \sin\left(\omega_\mathrm{A} t\right) + V_\mathrm{B} \sin\left(\omega_\mathrm{B} t\right)\,,$$

leads to

$$\begin{aligned} P(t) &= \frac{1}{R}\left[V_{\mathrm{A}}\sin(\omega_{\mathrm{A}}t) + V_{\mathrm{B}}\sin(\omega_{\mathrm{B}}t)\right]^2 \\ &= \frac{1}{R}\left[V_{\mathrm{A}}^2\sin^2(\omega_{\mathrm{A}}t) + V_{\mathrm{B}}^2\sin(\omega_{\mathrm{B}}t) + 2V_{\mathrm{A}}V_{\mathrm{B}}\sin(\omega_{\mathrm{A}}t)\sin(\omega_{\mathrm{B}}t)\right] \\ &= \frac{V_{\mathrm{A}}^2 + V_{\mathrm{B}}^2}{2R} - \frac{V_{\mathrm{A}}^2}{2R}\cos(2\omega_{\mathrm{A}}t) \\ &- \frac{V_{\mathrm{B}}^2}{2R}\cos(2\omega_{\mathrm{B}}t) - \frac{V_{\mathrm{A}}V_{\mathrm{B}}}{R}\cos(\omega_{\mathrm{A+B}}t) + \frac{V_{\mathrm{A}}V_{\mathrm{B}}}{R}\cos(\omega_{\mathrm{A-B}}t)\ , \end{aligned}$$

where $\omega_{\mathrm{A\pm B}} \equiv \omega_{\mathrm{A}} \pm \omega_{\mathrm{B}}$. In addition to the DC and second harmonic components, there is additional harmonic distortion in the form of sum and difference heterodynes. This is illustrated in Fig. 2.1.

The effects of second harmonic generation and heterodyning can be negated by applying a DC bias. For example,

$$V(t) = V_0 + V_{\mathrm{A}}\sin(\omega_{\mathrm{A}}t) + V_{\mathrm{B}}\sin(\omega_{\mathrm{B}}t)\ ,$$

such that

$$\begin{aligned} P(t) &= \frac{2V_0^2 + V_{\mathrm{A}}^2 + V_{\mathrm{B}}^2}{2R} + \frac{2V_0V_{\mathrm{A}}}{R}\sin(\omega_{\mathrm{A}}t) + \frac{2V_0V_{\mathrm{B}}}{R}\sin(\omega_{\mathrm{B}}t) \\ &- \frac{V_{\mathrm{A}}^2}{2R}\cos(2\omega_{\mathrm{A}}t) - \frac{V_{\mathrm{B}}^2}{2R}\cos(2\omega_{\mathrm{B}}t) \\ &- \frac{V_{\mathrm{A}}V_{\mathrm{B}}}{R}\cos(\omega_{\mathrm{A+B}}) + \frac{V_{\mathrm{A}}V_{\mathrm{B}}}{R}\cos(\omega_{\mathrm{A-B}})\ . \end{aligned}$$

The power now has components at the first harmonic of the source frequency that scale linearly with the bias. For large V_0, these terms become dominant and nonlinear effects can be ignored. In general, for a signal consisting of n components of varying amplitude, V_i, frequency, ω_i, and phase, φ_i, as well as DC bias, V_0,

$$V(t) = V_0 + \sum_{i=1}^{n} V_i\sin(\omega_i t + \varphi_i)\ ,$$

$$\begin{aligned} P(t) &= \frac{V_0^2}{R} + \frac{1}{2R}\sum_{i=1}^{n} V_i^2 + \frac{2V_0}{R}\sum_{i=1}^{n} V_i\sin(\omega_i t + \varphi_i) - \frac{1}{2R}\sum_{i=1}^{n} V_i^2\cos(2\omega_i t + 2\varphi_i) \\ &+ \frac{1}{R}\sum_{\substack{i=1 \\ i\neq j}}^{n}\sum_{j=1}^{n} V_iV_j\left[\cos(\omega_{i-j}t + \varphi_{i-j}) - \cos(\omega_{i+j}t + \varphi_{i-j})\right]\ . \end{aligned} \tag{2.5}$$

This was pointed out in the original paper by Arnold and Crandall [4], although

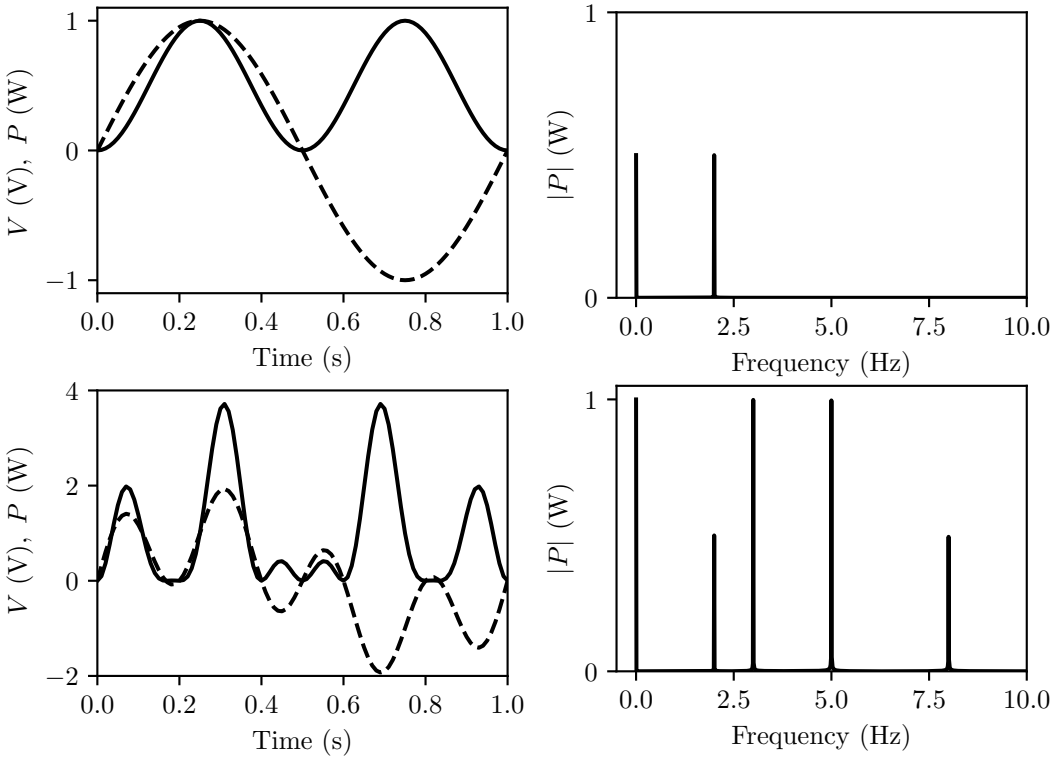

FIGURE 2.1: Simulated second harmonic generation due to Joule heating. **Top row**: Time dependence (left) and frequency spectrum (right) for an applied sinusoidal voltage at 1 Hz. Voltage is represented by the dashed line, and power by the solid line. **Bottom row:** Applied frequencies of 1 and 4 Hz. The resistance in both cases is set to 1 Ω.

they only considered the frequencies involved, not the phases. The phase terms have been added by the present author as they will be useful in Chapter 5 when dealing with phased arrays.

The framework presented in this section will be sufficient for describing the electrical nature of thermophones explored in this thesis. The next section will discuss the thermal behaviour of devices.

2.2 Thermal Description

The previous section described the generation of Joule heat by devices. This section concerns the transfer of the generated heat to the air for sound generation. First, the thermal diffusion equation will be introduced. This will then be applied to the case of a thermoacoustic device.

The heat energy flux, $\boldsymbol{j}_q$, associated with a small temperature gradient, ∇T, is given by

$$\boldsymbol{j}_q = -\kappa \nabla T \,, \tag{2.6}$$

where κ is the thermal conductivity of the medium [77]. The conservation of heat energy is described by the continuity equation,

$$\frac{\partial Q}{\partial t} + \nabla \cdot \boldsymbol{j}_q = 0\,,$$

where Q is the heat energy density. The heat energy density can be related to the temperature via the specific heat capacity

$$c_{p,\mathcal{V}} = \frac{1}{\rho_0}\left(\frac{\partial Q}{\partial T}\right)_{p,\mathcal{V}}\,, \tag{2.7}$$

where ρ_0 is the density of the medium, and the subscripts $c_{p,\mathcal{V}}$ refer to the isobaric and isochoric heat capacities, respectively. Use of the isobaric heat capacity and (2.6) allows for the continuity equation to be expressed purely in terms of the temperature,

$$\rho_0 c_p \frac{\partial T}{\partial t} + \nabla \cdot (-\kappa \nabla T) = 0\,,$$

which, for constant κ, results in

$$\kappa \nabla^2 T - \rho_0 c_p \frac{\partial T}{\partial t} = 0\,. \tag{2.8}$$

This is the thermal diffusion equation. In the previous section it was mentioned that Joule heating results in both DC and AC components in the dissipated heat. It will therefore be useful to consider time-harmonic solutions to the thermal diffusion equation. In this case, the temperature field can be written in terms of a DC field, where $\frac{\partial T}{\partial t} = 0$,

$$\kappa \nabla^2 T = 0\,, \tag{2.9}$$

and a number of AC components,

$$\kappa \nabla^2 T + \mathrm{i}\omega \rho_0 c_p T = 0\,, \tag{2.10}$$

where ω is the angular frequency. In 1D, the AC components consist of plane wave solutions,

$$T(x) = A\mathrm{e}^{\mathrm{i}kx}\,, \tag{2.11}$$

where A is a constant and substitution reveals that the wavevector has both real and imaginary components,

$$k = \pm\,(1+\mathrm{i})\sqrt{\frac{\rho_0 c_p \omega}{2\kappa}}\,.$$

The thermal waves are therefore evanescent, with a decay length given by

$$\delta = \sqrt{\frac{2\kappa}{\rho_0 c_p \omega}} \,. \tag{2.12}$$

The thermal diffusion equation can also be expressed in terms of entropy, s, via the first law,

$$\kappa \nabla^2 T - \rho_0 T_0 \frac{\partial s}{\partial t} = 0 \,, \tag{2.13}$$

with the specific heat capacity,

$$c_{p,\mathcal{V}} = T_0 \left(\frac{\partial s}{\partial T} \right)_{p,\mathcal{V}} \,. \tag{2.14}$$

Only a portion of the Joule heat dissipated by the film is transferred to the air for thermoacoustic generation. As mentioned in Section 1.1, Daschewski *et al.* [11] proposed a model for calculating this, which will now be outlined here.

The basis of the model is an electrical analogue circuit, where different materials in the system are represented by thermal capacitances, as shown in Fig. 2.2. In this case, the Joule heat is split up into each of the elements,

$$Q_{\text{Joule}} = Q_{\text{film}} + Q_{\text{substrate}} + Q_{\text{air}} \,.$$

The heat transferred to a particular element can be determined by the relative heat capacities,

$$Q_{\text{x}} = \frac{C_{\text{x}}}{C_{\text{film}} + C_{\text{substrate}} + C_{\text{air}}} Q_{\text{Joule}} \,,$$

where C_{x} is the heat capacity of the desired element. For a film of thickness d_{film} and surface area A, the heat capacity is

$$C_{\text{film}} = A d_{\text{film}} \rho_{\text{film}} c_{p,\text{film}} \,,$$

where it is assumed that the film thickness is smaller than the thermal diffusion length. For the air and substrate 'layers', the layer thickness is given by the thermal diffusion length, such that, for the air layer,

$$\begin{aligned} C_{\text{air}} &= A \delta_{\text{air}} \rho_{\text{air}} c_{p,\text{air}} \\ &= A \sqrt{\frac{2\kappa_{\text{air}}}{\rho_{\text{air}} c_{p,\text{air}} \omega}} \rho_{\text{air}} c_{p,\text{air}} \\ &= A \frac{e_{\text{air}}}{\sqrt{\pi f}} \,, \end{aligned}$$

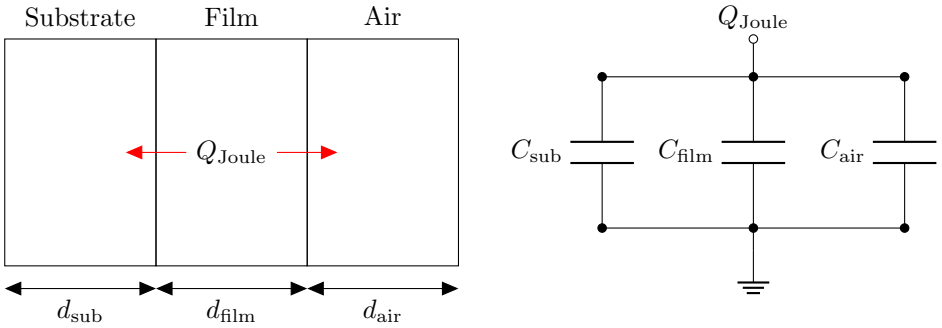

FIGURE 2.2: Thermal distribution model. **Left:** Physical representation. The thermal system consists of three layers: substrate, film and air. The thickness of the film layer is simply the film thickness. The thickness of the substrate and air layers are the thermal diffusion lengths in each of the materials. A total heat input, Q_{Joule} will be distributed throughout this system according to the layer thermal properties. **Right:** Circuit analogue for the system, representing each of the layers as a thermal capacitance.

where $e = \sqrt{\kappa \rho c_p}$ is the thermal effusivity, essentially a measure of thermal 'inertia'. Similarly, for the substrate layer,

$$C_{\text{substrate}} = A \frac{e_{\text{substrate}}}{\sqrt{\pi f}} \, .$$

Substitution then yields

$$\begin{aligned} Q_{\text{air}} &= \frac{e_{\text{air}}}{e_{\text{air}} + e_{\text{substrate}} + d_{\text{film}} \rho_{\text{film}} c_{p,\text{film}} \sqrt{\pi f}} Q_{\text{Joule}} \\ &= \mathcal{E} Q_{\text{Joule}} \, , \end{aligned} \tag{2.15}$$

which is the portion of the Joule heat that is transferred to the air. The final aspect of modelling thermophones is the generation of sound from the heat transferred to the air. This will be described in the following section.

2.3 Acoustic Wave Propagation

In the previous section, the total heat transferred to the air by a thermoacoustic device was determined. In this section, it will be shown how the transferred heat results in the generation of an acoustic wave. This will be achieved by first introducing the conservation equations for fluid mass and momentum. It will then be demonstrated how these can be combined to obtain the classical wave equation for acoustics. Finally, by inclusion of the thermal diffusion equation, a set of equations for describing thermoacoustic waves will be derived. The derivations in this section are based upon the comprehensive works of Kinsler and Frey [78], and Morse and

Ingard [75].

The following derivations consider a fixed element in space, of volume $\mathcal{V}$, through which fluid flow may occur. The acoustic behaviour is assumed to be a small perturbation from equilibrium, such that the acoustic variables can be described by first-order Taylor expansion:

- Pressure: $p' = p_0 + p\,,$
- Temperature: $T' = T_0 + T\,,$
- Density: $\rho' = \rho_0 + \rho\,,$
- Entropy (per unit mass): $s' = s_0 + s\,,$
- Fluid velocity: $\boldsymbol{u}\,,$

where the modifiers a' and a_0 refer to the instantaneous and background values, respectively. The background velocity is assumed to be zero. Since only small changes are considered, it is assumed that the fluid material parameters are constant. In reality, this is not the case, since the parameters are temperature-dependent. As such, the framework presented here is only suitable for describing acoustic behaviour in the linear limit. Nonlinear effects lie beyond the scope of the present work.

To model the acoustic behaviour of fluids, relationships are required that describe the conservation of certain quantities. This conservation is enforced by the continuity equation, which allows for the local conservation of a quantity within some volume by relating its density to the flux across the bounding surface. The first conserved quantity of interest is the fluid mass, in which case the mass flux across a closed surface, $\mathcal{S}$, is

$$\oint_{\mathcal{S}} \rho' \boldsymbol{u} \cdot \mathrm{d}\boldsymbol{\mathcal{S}}\,.$$

To conserve mass, this flux must equal the rate of change of the mass density within the enclosed volume,

$$\oint_{\mathcal{S}} \rho' \boldsymbol{u} \cdot \mathrm{d}\boldsymbol{\mathcal{S}} = \frac{\partial}{\partial t} \int_{\mathcal{V}} \rho' \,\mathrm{d}\mathcal{V}\,.$$

The divergence theorem allows for the surface integral to be replaced with a volume integral,

$$\int_{\mathcal{V}} \nabla \cdot (\rho' \boldsymbol{u}) \,\mathrm{d}\mathcal{V} = -\int_{\mathcal{V}} \frac{\partial \rho'}{\partial t} \,\mathrm{d}\mathcal{V}\,,$$

such that

$$\frac{\partial \rho'}{\partial t} + \nabla \cdot (\rho' \boldsymbol{u}) = 0\,. \tag{2.16}$$

The second conserved quantity is the fluid momentum, which is described by the Navier-Stokes equation,

$$\rho' \left[\frac{\partial \boldsymbol{u}}{\partial t} + (\boldsymbol{u} \cdot \nabla)\, \boldsymbol{u} \right] = -\nabla p + \left(\mu_\mathrm{b} + \frac{4}{3}\mu \right) \nabla (\nabla \cdot \boldsymbol{u}) - \mu \nabla \times \nabla \times \boldsymbol{u}\,, \tag{2.17}$$

where μ is the fluid viscosity and μ_b is the bulk viscosity (for completeness, a derivation of this equation is included in Appendix A.) The current discussion only considers acoustics in the linear limit, in which case the two equations simplify to

$$\frac{\partial \rho}{\partial t} + \rho_0 \nabla \cdot \boldsymbol{u} = 0\,, \tag{2.18}$$

$$\rho_0 \frac{\partial \boldsymbol{u}}{\partial t} = -\nabla p + \left(\mu_\mathrm{b} + \frac{4}{3}\mu \right) \nabla (\nabla \cdot \boldsymbol{u}) - \mu \nabla \times \nabla \times \boldsymbol{u}\,. \tag{2.19}$$

It will now be demonstrated how these conservation equations can be combined to describe standard non-thermal acoustics. After this, the discussion will be extended to include thermal and viscous effects.

2.3.1 Acoustic Wave Equation

The continuity equations previously derived will now be used to construct a wave equation for describing the propagation of sound in fluids. To begin with, this will be performed under the assumptions of zero viscosity and adiabatic conditions, *i.e.*, neglecting thermal conduction. As mentioned previously, changes in the system variables will only be considered to first order.

Under the above assumptions, the equation of state for the fluid takes the form

$$p'(\rho') = f(\rho')\,,$$

where f is an arbitrary function. Taking the first-order Taylor expansion of this and subtracting the background values,

$$p(\rho) \approx \left(\frac{\partial p}{\partial \rho} \right)_s \rho\,. \tag{2.20}$$

The adiabatic (isentropic) bulk modulus is defined as

$$B_s \equiv \mathcal{V} \left(\frac{\partial \mathcal{V}}{\partial p} \right)_s = \rho_0 \left(\frac{\partial p}{\partial \rho} \right)_s\,, \tag{2.21}$$

and is a measure of the resistance of the fluid to compression. Substituting this, the equation of state then becomes

$$\rho = \frac{\rho_0}{B_s} p \,. \tag{2.22}$$

A relationship describing the acoustic behaviour of the fluid can now be obtained by applying the appropriate continuity equation. Taking the linearised Navier-Stokes equation, (2.19), and neglecting the viscosity terms,

$$\rho_0 \frac{\partial \boldsymbol{u}}{\partial t} = -\nabla p \,, \tag{2.23}$$

which is known as the Euler equation. Taking the divergence of this,

$$\rho_0 \nabla \cdot \frac{\partial \boldsymbol{u}}{\partial t} = -\nabla^2 p \,,$$

and comparing to the time derivative of the linear mass continuity equation, (2.18),

$$\frac{\partial^2 \rho}{\partial t^2} + \rho_0 \nabla \cdot \frac{\partial \boldsymbol{u}}{\partial t} = 0 \,,$$

allows for the velocity to be eliminated,

$$\frac{\partial^2 \rho}{\partial t^2} - \nabla^2 p = 0 \,.$$

Substituting the equation of state then results in

$$\nabla^2 p - \frac{\rho_0}{B_s} \frac{\partial^2 p}{\partial t^2} = 0 \,. \tag{2.24}$$

In 1D, this has plane wave solutions,

$$p(x,t) = A \mathrm{e}^{\mathrm{i}(kx - \omega t)} \,,$$

where A is a constant, k is the wavenumber and ω is the angular frequency. Substitution of this solution into (2.24) yields

$$\frac{B_s}{\rho_0} = \frac{\omega^2}{k^2} = v_s^2 \,,$$

where v_s is the phase velocity of the wave. The acoustic wave equation is therefore

$$\nabla^2 p - \frac{1}{v_s^2} \frac{\partial^2 p}{\partial t^2} = 0 \,, \tag{2.25}$$

where v_s is the (adiabatic) speed of sound in the medium. For time-harmonic solutions, this becomes the Helmholtz equation

$$\nabla^2 p + k^2 p = 0\,. \tag{2.26}$$

The acoustic wave equation is sufficient for modelling many acoustic phenomena; however, for thermoacoustics a more general approach is required. This is achieved by relaxing the adiabatic assumption, which will now be demonstrated.

2.3.2 The Thermoacoustic Equations

The acoustic wave equation will now be extended to include the effects of viscous dissipation and thermal conduction. This will be achieved by coupling the Navier-Stokes and thermal diffusion equations via the fluid density, which is allowed to depend on both pressure and temperature. The resulting equations are typically used to describe the attenuation of sound due to thermal and viscous losses; however, they will also be useful for modelling thermoacoustics.

Relaxing the requirement of adiabatic conditions, such that heat flow is present, the equation of state for the fluid becomes, to first order,

$$\rho\,(p,T) = \left(\frac{\partial \rho}{\partial p}\right)_T p + \left(\frac{\partial \rho}{\partial T}\right)_p T\,. \tag{2.27}$$

Considering the isothermal bulk modulus,

$$B_T \equiv \rho_0 \left(\frac{\partial p}{\partial \rho}\right)_T\,, \tag{2.28}$$

and thermal expansion coefficient,

$$\beta \equiv -\frac{1}{\rho_0}\left(\frac{\partial \rho}{\partial T}\right)_p\,, \tag{2.29}$$

the equation of state can be written as

$$\rho(p,T) = \frac{\rho_0}{B_T} p - \rho_0 \beta T\,.$$

This can be further simplified with the thermal pressure coefficient,

$$\alpha \equiv \left(\frac{\partial p}{\partial T}\right)_V = B_T \beta\,, \tag{2.30}$$

resulting in

$$\rho(p,T) = \frac{\rho_0}{B_T}\left(p - \alpha T\right) .$$

This can be related to the adiabatic case via the ratio of specific heats,

$$\gamma \equiv \frac{c_p}{c_v} = \frac{B_s}{B_T} , \tag{2.31}$$

to obtain

$$\begin{aligned}\rho(p,T) &= \frac{\gamma\rho_0}{B_s}\left(p - \alpha T\right) \\ &= \frac{\gamma}{v_s^2}\left(p - \alpha T\right) ,\end{aligned} \tag{2.32}$$

It is also important to consider the change in entropy, since this is associated with an irreversible loss of energy to the surrounding fluid. This also depends on the pressure and temperature. To first order,

$$s(p,T) = \left(\frac{\partial s}{\partial p}\right)_T p + \left(\frac{\partial s}{\partial T}\right)_p T . \tag{2.33}$$

Note that viscous dissipation also contributes to the entropy production; however, this is not included here as it is a second-order effect. Substituting the heat capacity, (2.14), as well as the Maxwell relation,

$$\left(\frac{\partial s}{\partial p}\right)_T = -\left(\frac{\partial V}{\partial T}\right)_p = \frac{\beta}{\rho_0} ,$$

yields

$$s(p,T) = \frac{c_p}{T_0}\left(T - \frac{\beta T_0}{\rho_0 c_p} p\right) .$$

This can be further simplified using the thermodynamic relation

$$\gamma - 1 = \frac{B_s \beta^2 T_0}{\rho_0 c_p} ,$$

as well as α, to obtain

$$s(p,T) = \frac{c_p}{T_0}\left(T - \frac{\gamma - 1}{\alpha\gamma} p\right) . \tag{2.34}$$

The continuity equations for fluid momentum and heat can now be used to derive wave equations for this system. To begin with, the linearised Navier-Stokes equation, (2.19), will be considered. The velocity here can be separated into a longitudinal component, $\boldsymbol{u}_\parallel$, for which $\nabla \times \boldsymbol{u}_\parallel = 0$, and a transverse component, $\boldsymbol{u}_\perp$, where

$\nabla \cdot \boldsymbol{u}_\perp = 0$. Since $\nabla \times \nabla \boldsymbol{A} = 0$, this allows the Navier-Stokes equation to be split into two equations,

$$\rho_0 \frac{\partial \boldsymbol{u}_\parallel}{\partial t} = -\nabla p + \left(\mu_\mathrm{b} + \frac{4}{3}\mu\right) \nabla^2 \boldsymbol{u}_\parallel \,, \tag{2.35}$$

$$\rho_0 \frac{\partial \boldsymbol{u}_\perp}{\partial t} = -\mu \nabla \times \nabla \times \boldsymbol{u}_\perp \,, \tag{2.36}$$

which can be solved for separately. The first equation relates the longitudinal velocity component to the pressure, providing a description of the sound waves. The second equation only involves the transverse velocity component. This is unrelated to the sound waves, and is only important for satisfying the boundary conditions of the problem. Taking the divergence of the longitudinal part and comparing to the time derivative of the mass continuity equation, (2.18),

$$\rho_0 \nabla \cdot \frac{\partial \boldsymbol{u}_\parallel}{\partial t} = -\nabla^2 p + \left(\mu_\mathrm{b} + \frac{4}{3}\mu\right) \nabla \cdot \left(\nabla^2 \boldsymbol{u}_\parallel\right) \,,$$

$$\rho_0 \nabla \cdot \frac{\partial \boldsymbol{u}_\parallel}{\partial t} = -\frac{\partial^2 \rho}{\partial t^2} \,,$$

allows for $\frac{\partial \boldsymbol{u}_\parallel}{\partial t}$ to be eliminated,

$$-\frac{\partial^2 \rho}{\partial t^2} = -\nabla^2 p + \left(\mu_\mathrm{b} + \frac{4}{3}\mu\right) \nabla^2 \left(\nabla \cdot \boldsymbol{u}_\parallel\right) \,,$$

where $\nabla \cdot \left(\nabla^2 \boldsymbol{u}_\parallel\right) = \nabla^2 \left(\nabla \cdot \boldsymbol{u}_\parallel\right)$. Applying (2.18) again,

$$\frac{\partial^2 \rho}{\partial t^2} = \nabla^2 p + \frac{1}{\rho_0} \left(\mu_\mathrm{b} + \frac{4}{3}\mu\right) \nabla^2 \frac{\partial \rho}{\partial t}.$$

Substituting the density equation of state, (2.32), yields

$$\frac{\gamma}{v_s^2} \frac{\partial^2}{\partial t^2} \left(p - \alpha T\right) = \nabla^2 p + \frac{\mu_\mathrm{b} + \frac{4}{3}\mu}{\rho_0} \frac{\gamma}{v_s^2} \frac{\partial}{\partial t} \nabla^2 \left(p - \alpha T\right) \,,$$

which can be recast as

$$\nabla^2 p = \frac{\gamma}{v_s^2} \left(\frac{\partial^2}{\partial t^2} - \mathcal{L}_v v_s \frac{\partial}{\partial t} \nabla^2\right) \left(p - \alpha T\right) \,, \tag{2.37}$$

where $\mathcal{L}_v$ is the characteristic length of viscous diffusion,

$$\mathcal{L}_v \equiv \frac{\mu_\mathrm{b} + \frac{4}{3}\mu}{\rho_0 v_s} \,. \tag{2.38}$$

Equation (2.37) relates the pressure and temperature in the sound wave. To fully characterise this interaction, the thermal diffusion equation, (2.13), must also be considered. Applying this to the entropy production, (2.34),

$$\kappa\nabla^2 T - \rho_0 T_0 \frac{c_p}{T_0}\frac{\partial}{\partial t}\left(T - \frac{\gamma-1}{\alpha\gamma}p\right),$$

which simplifies to

$$\nabla^2 T = \frac{1}{\mathcal{L}_T v_s}\frac{\partial}{\partial t}\left(T - \frac{\gamma-1}{\alpha\gamma}p\right), \tag{2.39}$$

where $\mathcal{L}_T$ is the characteristic length of thermal diffusion,

$$\mathcal{L}_T \equiv \frac{\kappa}{\rho_0 c_p v_s}. \tag{2.40}$$

It will also be useful to relate the pressure and temperature to the longitudinal velocity. This can be achieved by combining the mass continuity equation, (2.18), with the longitudinal velocity, (2.35),

$$\rho_0\frac{\partial \boldsymbol{u}_\parallel}{\partial t} = -\nabla\left(p + \mathcal{L}_v v_s \frac{\partial \rho}{\partial t}\right). \tag{2.41}$$

Substituting the density equation of state, (2.32),

$$\rho_0\frac{\partial \boldsymbol{u}_\parallel}{\partial t} = -\nabla\left[p + \frac{\gamma\mathcal{L}_v}{v_s}\frac{\partial}{\partial t}\left(p - \alpha T\right)\right]. \tag{2.42}$$

The thermoacoustic equations are therefore

$$\nabla^2 p = \frac{\gamma}{v_s^2}\left(\frac{\partial^2}{\partial t^2} - \mathcal{L}_v v_s \frac{\partial}{\partial t}\nabla^2\right)\left(p - \alpha T\right), \tag{2.43}$$

$$\nabla^2 T = \frac{1}{\mathcal{L}_T v_s}\frac{\partial}{\partial t}\left(T - \frac{\gamma-1}{\alpha\gamma}p\right), \tag{2.44}$$

$$\rho_0\frac{\partial \boldsymbol{u}_\parallel}{\partial t} = -\nabla\left[p + \frac{\gamma\mathcal{L}_v}{v_s}\frac{\partial}{\partial t}\left(p - \alpha T\right)\right], \tag{2.45}$$

$$\rho_0\frac{\partial \boldsymbol{u}_\perp}{\partial t} = -\mu\nabla\times\nabla\times\boldsymbol{u}_\perp, \tag{2.46}$$

To determine the acoustic field, equations (2.43) and (2.44) must be solved simultaneously. Equations (2.45) and (2.46) are used when defining boundary conditions. Equations (2.43) and (2.44) essentially form a modified version of the standard wave equation, (2.25). This can be seen by setting $\mathcal{L}_{v,T} = 0$, such that (2.44) becomes $T = \frac{\gamma-1}{\alpha\gamma}p$, which can then be substituted into (2.43) to recover the wave equation.

Some insight into the thermoacoustic equations can be gained by considering plane wave solutions in the homogeneous case. To solve the equations, it is convenient to combine equations (2.43) and (2.44) in matrix form,

$$\begin{bmatrix} A_{11} & A_{12} \\ A_{21} & A_{22} \end{bmatrix} \begin{bmatrix} x_1 \\ x_2 \end{bmatrix} = \begin{bmatrix} 0 \\ 0 \end{bmatrix}, \tag{2.47}$$

such that

$$\begin{bmatrix} \left(1 + \frac{\gamma\mathcal{L}_v}{v_s}\frac{\partial}{\partial t}\right)\nabla^2 - \frac{\gamma}{v_s^2}\frac{\partial^2}{\partial t^2} & -\frac{\alpha\gamma\mathcal{L}_v}{v_s}\frac{\partial}{\partial t}\nabla^2 + \frac{\alpha\gamma}{v_s^2}\frac{\partial^2}{\partial t^2} \\ \frac{\gamma-1}{\alpha\gamma\mathcal{L}_T v_s}\frac{\partial}{\partial t} & \nabla^2 - \frac{1}{\mathcal{L}_T v_s}\frac{\partial}{\partial t} \end{bmatrix} \begin{bmatrix} p \\ T \end{bmatrix} = \begin{bmatrix} 0 \\ 0 \end{bmatrix}. \tag{2.48}$$

In the present case, it will be useful to have an equation in one variable. Equation (2.47) can be recast to obtain

$$\det(A) \begin{bmatrix} x_1 \\ x_2 \end{bmatrix} = \begin{bmatrix} 0 \\ 0 \end{bmatrix}.$$

Equation (2.48) can therefore be recast to obtain a single equation for the temperature field,

$$\left[\mathcal{L}_T\left(v_s + \gamma\mathcal{L}_v\frac{\partial}{\partial t}\right)\right]\nabla^4 T - \left[\frac{\partial}{\partial t} + \frac{1}{v_s}\left(\mathcal{L}_v + \gamma\mathcal{L}_T\right)\frac{\partial^2}{\partial t^2}\right]\nabla^2 T + \frac{1}{v_s^2}\frac{\partial^3 T}{\partial t^3} = 0\,.$$

Or, in time-harmonic form,

$$\left[\mathcal{L}_T\left(\mathrm{i}\frac{v_s}{\omega} + \gamma\mathcal{L}_v\right)\right]\nabla^4 T + \left[\mathrm{i}\frac{\omega}{v_s}\left(\mathcal{L}_v + \gamma\mathcal{L}_T\right) - 1\right]\nabla^2 T - \frac{\omega^2}{v_s^2}T = 0\,. \tag{2.49}$$

It can be seen that, for $\mathcal{L}_{v,T} = 0$, the Helmholtz equation, (2.26), is recovered. The system can now be solved to determine the temperature field. For plane waves, $\nabla^4 \to k^4$, $\nabla^2 \to -k^2$, such that

$$k_\pm^2 = \frac{\mathrm{i}\frac{\omega}{v_s}\left(\mathcal{L}_v + \gamma\mathcal{L}_T\right) - 1 \pm \sqrt{\left[\mathrm{i}\frac{\omega}{v_s}\left(\mathcal{L}_v + \gamma\mathcal{L}_T\right) - 1\right]^2 + 4\frac{\omega^2}{v_s^2}\mathcal{L}_T\left(\mathrm{i}\frac{v_s}{\omega} + \gamma\mathcal{L}_v\right)}}{2\mathcal{L}_T\left(\mathrm{i}\frac{v_s}{\omega} + \gamma\mathcal{L}_v\right)}, \tag{2.50}$$

where $k = \pm\sqrt{k_\pm^2}$. The temperature field therefore consists of four wave components,

$$T(x) = C_1\mathrm{e}^{\mathrm{i}k_+ x} + C_2\mathrm{e}^{-\mathrm{i}k_+ x} + C_3\mathrm{e}^{\mathrm{i}k_- x} + C_4\mathrm{e}^{-\mathrm{i}k_- x}\,,$$

which correspond to two different modes. The k_+ mode is a propagating wave with a small imaginary component (which can be seen by plotting (2.50)). This is the

sound wave, where the small imaginary component results in attenuation of the sound over large distances due to viscous and thermal dissipation. The k_- mode is an evanescent wave, which is only significant in the vicinity of sources or boundaries.

Once the temperature field has been calculated, the pressure field can be determined by recasting (2.44), in time-harmonic form,

$$p = \frac{\alpha\gamma}{\gamma - 1}\left(1 - \mathrm{i}\frac{v_s}{\omega}\mathcal{L}_T\nabla^2\right)T\,. \tag{2.51}$$

If required, the temperature can also be substituted into (2.45) to obtain the longitudinal velocity,

$$\boldsymbol{u}_{\parallel} = \frac{1}{\rho_0 v_s}\frac{\alpha\gamma}{\gamma - 1}\left[\frac{v_s}{\omega}\mathcal{L}_T\left(\mathrm{i}\gamma\mathcal{L}_v - \frac{v_s}{\omega}\right)\nabla^2 - \left(\mathrm{i}\frac{v_s}{\omega} + \mathcal{L}_v\right)\right]\nabla T\,. \tag{2.52}$$

To determine the sound generated by a thermoacoustic device, the thermoacoustic equations can be coupled directly to the thermal diffusion equation [74]. However, this approach quickly becomes complex even for simple cases. The work presented in Chapter 4 aims to simplify this by combining the concepts in the present chapter with a new point source solution to the thermoacoustic equations.

The remainder of this chapter is reserved for outlining some useful acoustic definitions.

2.4 Acoustic Definitions

In this section, some standard acoustics definitions will be given, which will be useful for the work in subsequent chapters. The discussions here are based on work by Kinsler and Frey [78].

2.4.1 Acoustic Sources

When modelling acoustic systems, a useful result is the field due to a point-like source. When the dimensions of an acoustic source are small relative to the wavelength, their field will approximate that of a point source.

For the standard acoustic wave equation, the field due to a point source can be obtained by considering a small sphere, of radius r_0, pulsating with radial velocity u_0. Considering the wave equation in spherical coordinates and assuming angular symmetry,

$$\nabla^2 = \frac{\partial^2}{\partial r^2} + \frac{2}{r}\frac{\partial}{\partial r}\,,$$

such that

$$\frac{\partial^2 p}{\partial r^2} + \frac{2}{r}\frac{\partial p}{\partial r} = \frac{1}{c^2}\frac{\partial^2 p}{\partial t^2}\,. \tag{2.53}$$

The general solution to this can be found by considering a wave equation where rp is instead the dependent variable,

$$r\frac{\partial^2 p}{\partial r^2} + 2\frac{\partial p}{\partial r} = \frac{r}{c^2}\frac{\partial^2 p}{\partial t^2}\,,$$

which is simply (2.53) multiplied by r. The general solution therefore consists of plane wave solutions, divided by r,

$$p(r,t) = \frac{C_1}{r}\mathrm{e}^{\mathrm{i}(kr-\omega t)} + \frac{C_2}{r}\mathrm{e}^{-\mathrm{i}(kr-\omega t)}\,,$$

where $C_{1,2}$ are constants found by applying the boundary conditions. In the case of the pulsating sphere, the acoustic field is expected to only consist of outgoing waves, such that $C_2 = 0$. The boundary condition for determining C_1 is

$$u(r_0,t) = u_0\mathrm{e}^{-\mathrm{i}\omega t}\,.$$

To solve the boundary problem, consider the Euler equation, in time-harmonic form,

$$\begin{aligned}\mathrm{i}\omega\rho_0 u &= \nabla p \\ &= \frac{\mathrm{i}kr-1}{r^2}p\,.\end{aligned}$$

Applying the boundary condition,

$$C_1 = \frac{\mathrm{i}\omega\rho_0 r_0^2 u_0}{\mathrm{i}kr_0 - 1}\mathrm{e}^{-\mathrm{i}kr_0}\,.$$

The point source solution can then be obtained by considering the case where $kr_0 \ll 1$,

$$p(r) = -\frac{\mathrm{i}\rho_0\omega Q}{4\pi r}\mathrm{e}^{\mathrm{i}kr}\,, \tag{2.54}$$

where $Q = 4\pi r_0^2 u_0$ is the source strength, a measure of the rate of change of volume.

In reality, any acoustic source will have finite dimensions. If these dimensions are much smaller than the acoustic wavelength involved, then the point source approximation can be used for the sound field. In the case where the point source approximation is not valid, the source can be modelled as a collection of point sources. Consider a rectangular planar source in the xy-plane, centred at the origin. By convolution of the point source function with the rectangular source, the acoustic

pressure at a point $\boldsymbol{r}$ is given by

$$p(\boldsymbol{r}) = -\frac{\mathrm{i}\rho_0\omega}{4\pi}\frac{Q}{A}\int_{-L_y/2}^{L_y/2}\int_{-L_x/2}^{L_x/2}\frac{1}{|\boldsymbol{r}-\boldsymbol{r}'|}\mathrm{e}^{\mathrm{i}k|\boldsymbol{r}-\boldsymbol{r}'|}\,\mathrm{d}x'\mathrm{d}y'\,,$$

where $L_{x,y}$ are the source dimensions and $A = L_xL_y$ is the source surface area. Primed coordinates refer to the locations of the point sources. In the far-field ($|\boldsymbol{r}| \gg |\boldsymbol{r}'|$), the following approximation can be made,

$$\begin{aligned}|\boldsymbol{r}-\boldsymbol{r}'| &\approx \boldsymbol{r} - \boldsymbol{r}'\cdot\hat{\boldsymbol{r}}\\ &= r - x\sin\theta\cos\phi - y\sin\theta\sin\phi\,,\end{aligned}$$

such that

$$p(r,\theta,\phi) \approx -\frac{\mathrm{i}\rho_0\omega}{4\pi}\frac{Q}{r}\frac{\mathrm{e}^{\mathrm{i}kr}}{A}\int_{-L_y/2}^{L_y/2}\int_{-L_x/2}^{L_x/2}\mathrm{e}^{\mathrm{i}kx'\sin\theta\cos\phi/2}\mathrm{e}^{\mathrm{i}ky'\sin\theta\sin\phi/2}\,\mathrm{d}x'\mathrm{d}y'\,. \tag{2.55}$$

Evaluation of this integral yields the far-field pressure approximation for a rectangular planar source,

$$p(r,\theta,\phi) = -\frac{\mathrm{i}\rho_0\omega Q}{4\pi r}D(\theta,\phi)\,,$$

where

$$D(\theta,\phi) \equiv \operatorname{sinc}\left(\frac{kL_x}{2}\sin\theta\cos\phi\right)\operatorname{sinc}\left(\frac{kL_y}{2}\sin\theta\sin\phi\right)\,, \tag{2.56}$$

is the far-field directivity factor and $\operatorname{sinc} x \equiv \frac{\sin x}{x}$. For small kL_x and kL_y, the directivity factor becomes unity, such that the point source result is recovered. Inspection of (2.55) leads to an important and well-known conclusion: the far-field directivity of a planar source is given by its Fourier transform. This will be particularly useful later, where it will be shown that this can be applied in reverse to 'reconstruct' the shape of a source (Section 3.3).

2.4.2 Efficiency

To quantify the efficiency of acoustic sources, a quantity describing the rate of acoustic energy flow will be needed. In time-harmonic form, per unit area, this is given by the acoustic intensity

$$\boldsymbol{\mathcal{I}} = p\boldsymbol{u}\,. \tag{2.57}$$

This can be recast purely in terms of the pressure by considering Euler's equation. For a plane wave, $p = \rho_0 v_s u$, such that

$$\mathcal{I} = \frac{p^2}{\rho_0 v_s}\,. \tag{2.58}$$

The total acoustic power can then be found by integrating the intensity over a surface, $\mathcal{S}$, that encloses the source,

$$P_{\text{acoustic}} = \oint_{\mathcal{S}} \boldsymbol{\mathcal{I}} \cdot \mathrm{d}\boldsymbol{\mathcal{S}} \,. \tag{2.59}$$

It is important to note that this assumes that the sound is propagating perpendicularly to the surface, and that the velocity and pressure have a constant phase relationship. Practically, this requires measuring the pressure at a large distance away from the source.

Once the acoustic power is known, the efficiency of an acoustic source is then

$$\eta = \frac{P_{\text{acoustic}}}{P_{\text{in}}} \,, \tag{2.60}$$

where P_{in} is the driving power supplied to the source.

For a point source, the integral in (2.59) is simple. Taking $\mathcal{S}$ as an enclosing sphere, the integral leads to a factor of $4\pi r^2$, such that the acoustic power is

$$P_{\text{acoustic}} = \frac{\rho_0 \omega^2 Q^2}{4\pi v_s} \,. \tag{2.61}$$

For finite sources, the integral often has no closed-form solution and must be evaluated numerically.

2.5 Summary

In this chapter, methods for modelling thermoacoustic devices were discussed, and some useful acoustic definitions given.

To begin with, the Joule heating mechanism was described, including the effects of second harmonic generation. It was then demonstrated how the dissipated heat is transferred to the air. A set of equations for describing the coupling between temperature and pressure waves in fluids were then derived. These methods will be combined in Chapter 4 to obtain a description of the sound generated by a thermoacoustic device. Finally, the concepts of source geometry and efficiency were discussed.

In the next chapter, the experimental and computational methods used throughout the rest of this thesis will be described.

Chapter 3

Experimental Methods

3.1 Introduction

In this chapter, the experimental and computational methods used in this work will be outlined.

The chapter begins by describing the procedure for device fabrication. The experimental techniques used for characterising the acoustic and thermal behaviour of thermophones are then explained. The chapter ends with a discussion of the numerical methods used for simulating thermoacoustic behaviour in cases where analytical methods are not sufficient.

3.2 Device Fabrication

Thermoacoustic generation requires the Joule heat source to have a low thermal mass, which is typically achieved with thin films ('thin' in this context refers to the film thickness being smaller than the thermal diffusion length, such that the temperature gradient across the film's thickness is negligible.) In this work, thin film devices were fabricated using electron beam (e-beam) lithography, the process of which will be outlined here.

An overview for the process of e-beam lithography is shown in Fig. 3.1. First, the substrate is coated with a layer of photoresist. This layer is then patterned via e-beam. After patterning, the exposed regions are removed via chemical etchants, or bombardment by reactive ions. The conductive layer is then deposited and finally the remainder of the photoresist removed.

The fabrication process for the typical device will now be described. First, the substrate was cleaned using ultrasonication in acetone, then in isopropanol, each for 20 minutes. The substrate was then dried using N_2 gas. Next, the photoresist (950K

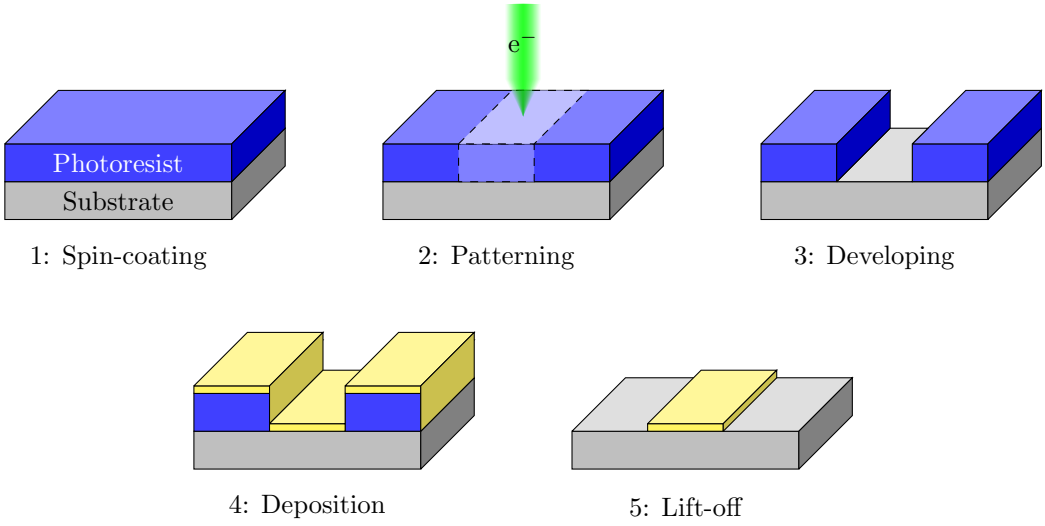

FIGURE 3.1: Outline of device lithography process for a single film. The substrate is coated with a photoresist, which is subsequently patterned and developed to leave voids where film deposition is desired. The film is then deposited and the excess removed.

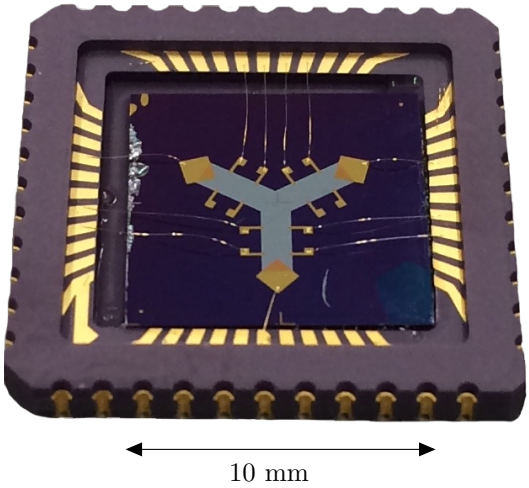

FIGURE 3.2: Example device used in this work. This particular device consists of a zinc film, with gold contact pads, on an Si/SiO_2 substrate, packaged in a ceramic chip carrier. Electrical contact is achieved between the contact pads and the package pins via gold wires.

polymethyl methacrylate) was deposited on the substrate via spin-coating at 4000 RPM to produce an even layer with defined thickness, which was baked at 170 °C for 10 minutes. This was then patterned with a NanoBeam nB4 e-beam system and developed for 30 s in isopropanol and methyl isobutyl ketone solution with a ratio 3:1, stopping with isopropanol. The conductive layers were deposited using either sputter deposition (Moorfield nanoPVD S10A), at 30 W RF power using argon gas at 5×10^{-1} mbar, or thermal evaporation (HHV Auto306), with a base pressure of 2×10^{-6} mbar and rate $1\,\text{Å}\,\text{s}^{-1}$. Lift-off of the debris from deposition was achieved via further ultrasonication in acetone and isopropanol. This process was repeated for each conductive layer of the device. Finally, the device was mounted in a 44-pin ceramic chip carrier using superglue, with electrical contact made between the device and chip carrier via 25 µm gold wires, attached using a K&S 4700 wedge bonder. An example of a completed device is shown in Fig. 3.2.

3.3 Acoustic Measurements

An overview of a typical experimental setup used in this work is shown in Fig. 3.3. The driving signal for devices was provided by a Rigol DG4102 waveform generator. The driving signals were then amplified by Rigol PA1011 or Falco WMA-300 power amplifiers, depending on the electrical resistance of the devices. The devices were mounted in a Newmark Systems 2-axis rotary gimbal, which rotated the devices relative to a microphone at a fixed distance, allowing for the far-field directivity to be mapped. Sound measurements were taken with an Earthworks M50 calibrated condenser microphone, paired with an Earthworks ZDT 1022 pre-amplifier. The calibrated frequency response and noise characteristics of the microphone are shown in Fig. 3.4. The microphone signal was measured with a Signal Recovery 7265 lock-in amplifier, typically locked to the second harmonic of the source signal due to the second harmonic nature of the Joule heating (for an explanation of the lock-in process, see Appendix D.) The setup was controlled, and data acquisition performed, by computer, using an in-house interface written in Python.

The far-field directivity of devices was measured by rotating the device relative to the microphone, which remained at a fixed distance, r. The device was considered to lie in the xy-plane, with the z-axis pointing along the device normal, resulting in the following coordinate system,

$$\begin{aligned} x &= r\cos(\theta)\sin(\phi)\,, & y &= r\sin(\theta)\,, & z &= r\cos(\theta)\cos(\phi)\,, \\ r &= \sqrt{x^2+y^2+z^2}\,, & \theta &= r\arcsin\left(\frac{y}{r}\right)\,, & \phi &= \arctan\left(\frac{x}{z}\right)\,, \end{aligned} \tag{3.1}$$

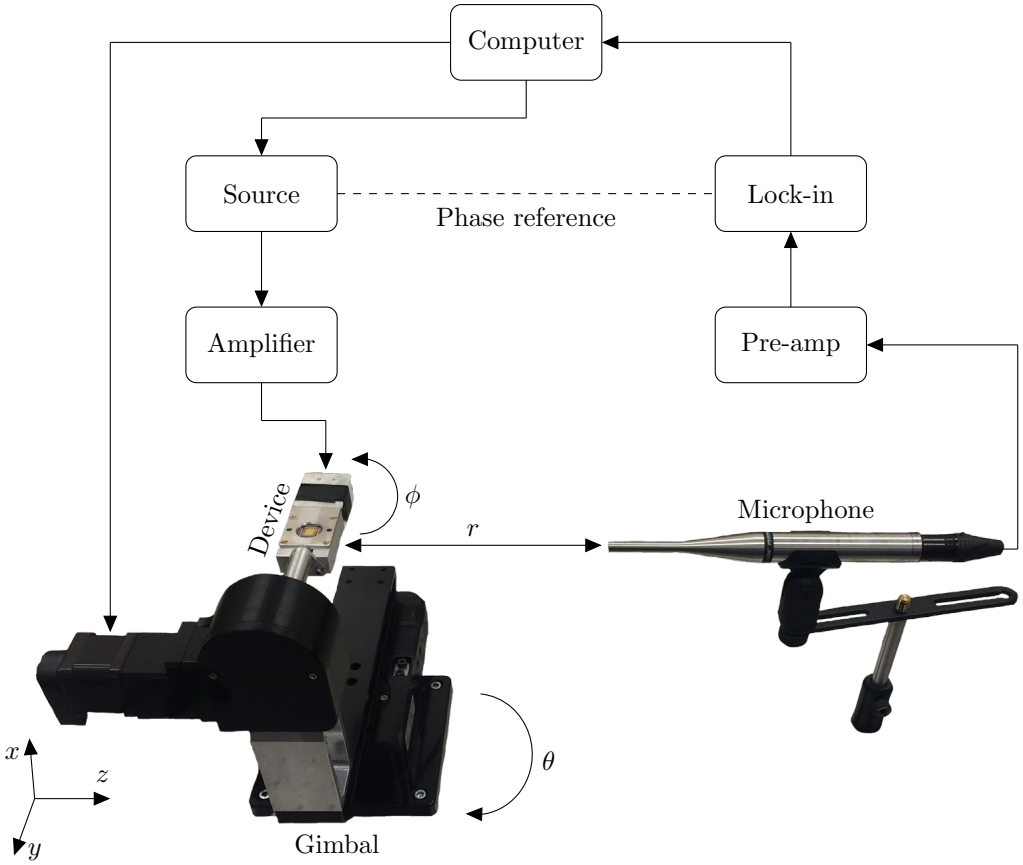

FIGURE 3.3: Typical experimental setup used for acoustic measurements. Devices are mounted in a 2-axis rotary gimbal, which is able to map the sound field by rotating the device relative to a fixed microphone. The acoustic pressure is measured using a lock-in amplifier, phase locked to the second harmonic of the voltage source.

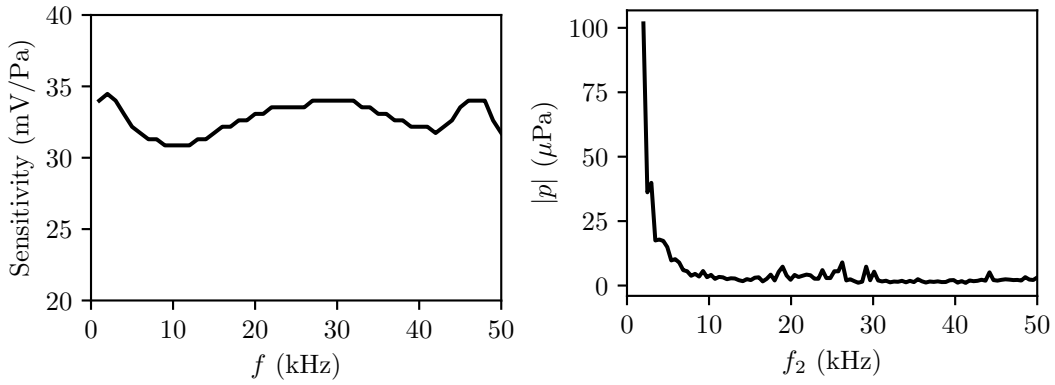

FIGURE 3.4: Frequency characteristics of the Earthworks M50 condenser microphone used in this work. **Left:** Sensitivity calibration data, provided by Earthworks upon purchase. **Right:** Typical noise floor measurement.

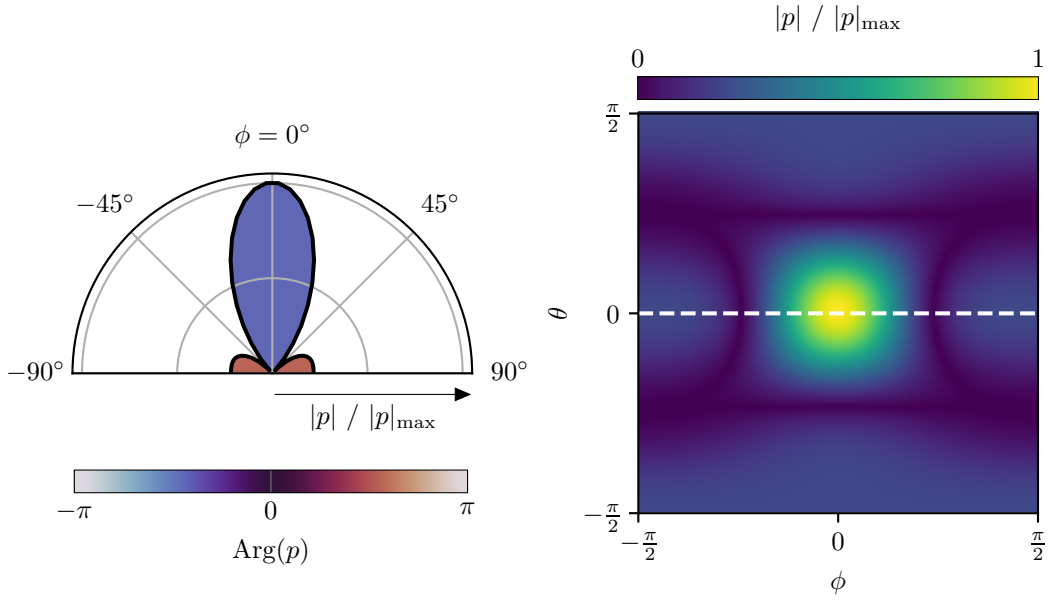

FIGURE 3.5: Examples of 1 and 2-axis far-field acoustic directivity scans, simulated using (2.56) for a 1×1 cm planar source driven at 50 kHz. **Left:** 1-axis scan over ϕ, for $\theta = 0$. The radial extent represents the normalised sound pressure magnitude, and the colour represents the sound pressure phase. **Right:** 2-axis scan over both θ and ϕ. Shown is the sound pressure magnitude only – phase will typically be shown in a separate figure. The white dashed line indicates the data seen in the 1-axis scan.

where $-\frac{\pi}{2} \leq \theta \leq \frac{\pi}{2}$ and $-\frac{\pi}{2} \leq \phi \leq \frac{\pi}{2}$. Performing a raster scan over θ and ϕ therefore allowed for the directivity to be mapped over a hemisphere in front of the device. Both 1-axis (over ϕ) and 2-axis (θ and ϕ) scans were used in this work, modelled examples of which are shown in Fig. 3.5. For the 2-axis scan, the result is a Mercator-like projection [79] of the sound field. It is worth noting that this leads to some visual distortion around the poles ($\theta = \left\{-\frac{\pi}{2}, \frac{\pi}{2}\right\}$), which is due to repeated measurements of the same point in space. For far-field integration measurements (for instance, when measuring acoustic power), this distortion is accounted for by weighting the far-field map by $|\cos(\theta)|$.

A useful tool for characterising acoustic sources is the ability to estimate the sound field at the source, and therefore the geometry of the source itself. As mentioned in Section 2.4.1, the far-field directivity of a finite acoustic source is the Fourier transform of the source geometry. This can be applied in reverse: by measuring the far-field directivity of a source and performing an inverse Fourier transform, the acoustic pressure near the source can be estimated. This method is commonly known as acoustic holography [80]. The process for the acoustic reconstruction is outlined in Fig. 3.6. First, the far-field directivity must be recast in terms of wavevector components. This is achieved by converting to Cartesian coordinates, then applying

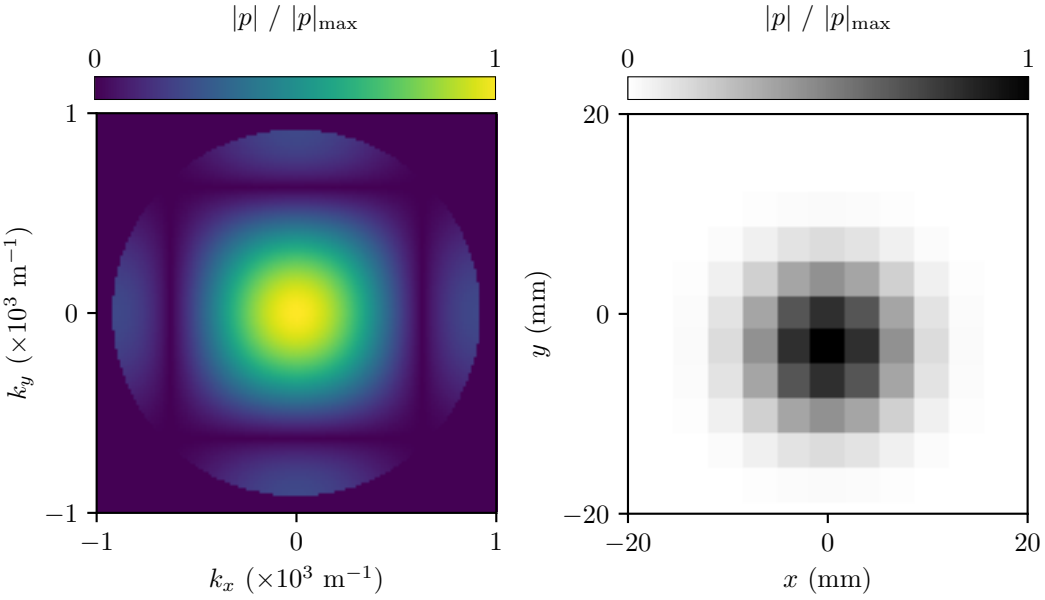

FIGURE 3.6: Acoustic reconstruction of a 1×1 cm planar source driven at 50 kHz, using the far-field directivity data from Fig. 3.5. **Left:** k-space representation of far-field sound. **Right:** Reconstructed image of the source.

the transformation

$$k_x = k\frac{y}{\sqrt{x^2+y^2+z^2}},$$
$$k_y = k\frac{x}{\sqrt{x^2+y^2+z^2}},$$

where k is the acoustic wavenumber. An inverse Fourier transform can then be applied to obtain an image of the source. Since this is a diffraction-based method, the resolution of the resulting image is limited by the acoustic wavelength.

3.4 Thermal Measurements

A key aspect of characterising thermoacoustic devices is measuring their thermal response. This was achieved via imaging with a thermal camera (FLIR A655sc). The process for thermal measurement will now be outlined.

Measuring the thermoacoustic behaviour of devices requires separating the oscillating temperature field, which is responsible for the sound generation, from the DC background temperature. This was achieved by taking regular thermal images over a fixed period of time and converting to frequency domain via Fourier transform, returning both the magnitude and phase of the oscillations. Typically, devices were

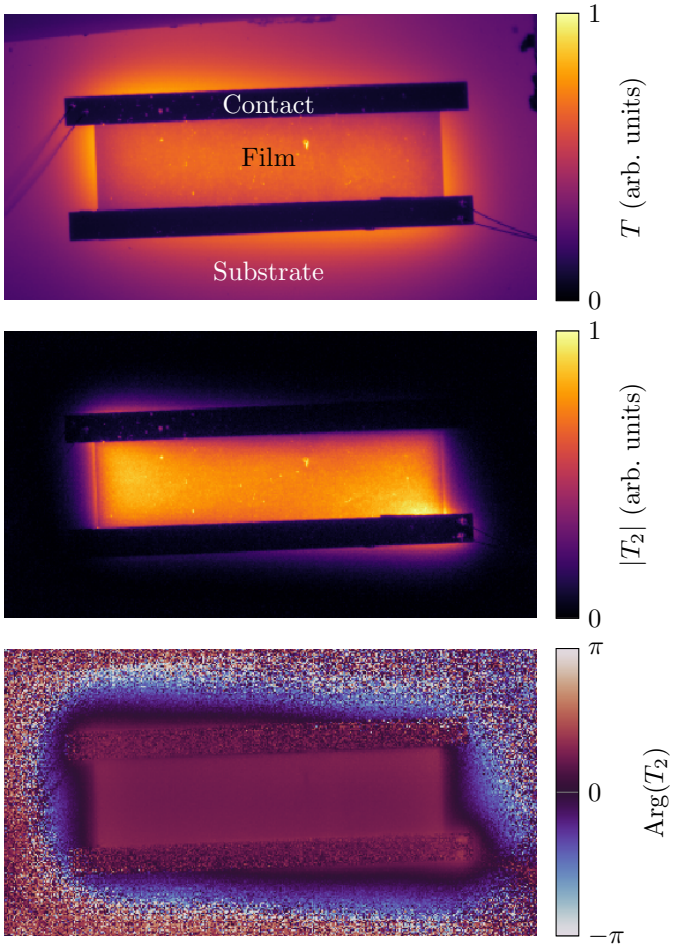

FIGURE 3.7: Thermal reconstruction of a device. The device in this case is an indium tin oxide thin film on a fused quartz substrate, with gold contacts. **Top:** Single frame from the recorded image sequence. **Middle:** Magnitude of the temperature field at the second harmonic. **Bottom:** Thermal phase at the second harmonic.

driven with a frequency of 1 Hz and recorded over a period of 10 s at 50 frames-per-second. An example frame from a measurement is shown in Fig. 3.7, along with the resulting magnitude and phase of the temperature at the second harmonic. The harmonic number with these measurements will be indicated by the subscript, *e.g.*, T_2 for the second harmonic. It is important to note here that the gold contacts in this reconstruction appear to be 'cold'. This is not the case; rather, it is due to the low thermal emissivity of the gold films compared to the ITO film and substrate material. This can usually be discerned by measuring the temperature of the device at ambient conditions, when it is known that all regions of the device are at the same temperature.

3.5 Finite Element Analysis

This work contains a number of physical problems where, due to complexity, solution by analytical methods is not feasible. In such cases, modelling was performed using the Finite Element Method (FEM) [81], which is a numerical technique for solving Partial Differential Equations (PDEs) via discretisation. There are many software implementations of this method. For this work, COMSOL Multiphysics® was used due to the ease with which different systems of PDEs can be coupled together. The remainder of this section is dedicated to outlining the method itself, as well as some typical modelling considerations.

The basic principle behind FEM is the approximation of continuous fields by series of discrete elements, referred to as the mesh. Consider a 1D PDE with dependent variable ν. This can be approximated with a linear combination of basis functions, Ψ_i, such that

$$\nu_n \approx \sum_i c_i \Psi_i \,,$$

where c_i are scaling constants. The basis functions are chosen such that

$$\Psi_i = \begin{cases} 1, & i = n \\ 0, & i \neq n \,. \end{cases}$$

This is illustrated in Fig. 3.8. For time-dependent simulations, the temporal behaviour of the system is discretised using finite differences,

$$\frac{\partial \nu_i}{\partial t} \approx \frac{\nu_i(t + \delta t) - \nu_i(t)}{\delta t}$$

where δt is the time step. Once the problem has been sufficiently discretised, it can be recast as a series of linear algebraic equations, which can then be solved by numerical methods to obtain an approximation of the true solution. The example in Fig. 3.8 uses basis functions that provide linear interpolation of the solution between points. This approximation becomes worse as the curvature increases. The error between the approximation and the true solution can be reduced by increasing the density of points, with the approximation approaching the true solution in the limit of infinite mesh density, although this comes at additional computational cost. Typically, basis functions that provide quadratic interpolation are used to reduce the error further. One of the key advantages of FEM is that the mesh elements do not need to be equally spaced. As such, the mesh density can be increased in regions where the solution is expected to exhibit greater curvature, although this requires prior knowledge of the behaviour of the system. In cases where there is no prior

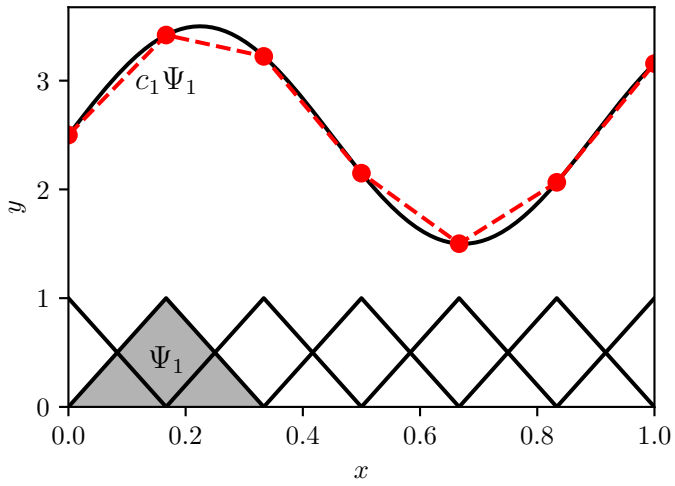

FIGURE 3.8: Finite-element discretisation of the function $y = 2.5 + \sin(7x)$ (black line) using a linear combination of basis functions, Ψ_i. The value of y at each point is approximated by $c_i\Psi_i$ (red circles), with linear interpolation present between points (red dashed line).

knowledge, a mesh refinement study can be performed, where multiple iterations are performed with increasing mesh density until sufficient convergence is obtained.

Attention will now be turned to some modelling considerations made when simulating thermoacoustics using FEM. The modelling of devices consists of three distinct elements: an electrical model to calculate the dissipated Joule heat in the thin film, a thermal model to determine the proportion of heat transfer to the substrate and the air, and an acoustic model to obtain the resulting sound field. It is possible to two-way couple all of these elements for the most general case; however, this comes at the cost of increased computational cost and in certain situations a one-way coupling is more favourable. For example, if the temperature dependence of the electrical conductivity is to be ignored, then the electrical model can be solved separately and the resulting Joule heat added as an arbitrary source in the thermal model. This approach is particularly useful when performing simulations where the one-way coupled element is not affected by the parameters being studied, avoiding the need to recalculate a solution unnecessarily. This work used a mix of 1 and 2-way coupling, depending on the specific case. Also, in some cases, only a single aspect of the problem was considered to reduce complexity. For instance, in modelling diffraction-related phenomena, the electrical and thermal aspects of the model were often neglected, and instead approximated with an arbitrary acoustic source. The approach used for each aspect of the FEM models will now be discussed.

Electrical modelling was performed using the 'Electric Currents' interface in COMSOL®, which solves a continuity equation based upon Ohm's law. The modelling of thin films using FEM poses an immediate issue, since the large aspect ratio between the planar dimensions of the films and their thickness results in highly anisotropic mesh elements, making convergence difficult. This is resolved by using the 'Layered Shells' feature, which treats the thin films as 2D boundaries in the 3D model, with an internal dimension for the thickness profile that has its own separate mesh.

Thermal modelling was performed using the 'Heat Transfer in Solids' interface, which solves the thermal diffusion equation. Typically only the time-varying component of the temperature field is of interest, since it is this that produces the sound, and the background field can be largely ignored. There are two different approaches for isolating this component. The first method is to simulate the device in time domain and isolate the desired component via Fourier transform. This method is not ideal, since it often requires solving over a sufficiently large time period that the thermal transients are negligible. A more efficient approach is to solve for the average steady state temperature, using RMS values for the dissipated Joule heat, then solve for the time-varying component via a small harmonic perturbation of the steady state solution. This was the preferred method for this work, and was achieved using the 'Thermal Perturbation, Frequency Domain' study type. The thermal modelling required some special meshing considerations since there was a large disparity between the device feature size and the thermal diffusion length. To account for this, the regions close to the film were meshed using a boundary layer mesh, which consisted of highly anisotropic mesh elements. Here, the in-plane element size was dictated by the device feature size, and the element thickness by the thermal diffusion length.

Acoustic modelling was performed using the 'Thermoviscous Acoustics' interface, which solves the full thermoacoustic equations. In Section 2.3.2 it was seen that the solutions to these equations consist of two distinct modes: a thermal mode, and an acoustic mode. In air, these modes occur over vastly different length scales, which is an issue for FEM as it requires a large mesh density. To avoid this issue, the thermoacoustic equations were typically only solved in a small region close to the device (around 2 or 3 times the thermal diffusion length). This region was meshed with a boundary layer mesh, as with the thermal model. Outside of this region, the acoustic pressure was coupled to the 'Pressure Acoustics' interface, which solves the acoustic Helmholtz equation, applying an additional isothermal boundary condition to terminate the thermal mode. To solve for the sound field, the Boundary Element Method (BEM) [82] was used, rather than FEM. The difference here is that BEM

recasts the PDE in the form of an integral equation that exists on the boundary of the domain of interest. The solution within the domain is then related to the solution on the boundary via an integral. This is advantageous in the sense that it only requires discretisation and solution of the fields on the radiating surface of an acoustic source, rather than in the volume of air the sound is being radiated into. Once the solution on the boundary has been found, the field at any point in space outside of this boundary can easily be found. For open radiation problems, where the air domain is essentially infinite in extent, this has obvious advantages, since it does not require discretisation of large, open regions of space. The FEM approach to this problem is to use perfectly matched layers, which is an absorbing layer that mimics an infinite void by coordinate stretching; however, this is often still more computationally intensive than BEM and requires careful tuning of the layer properties. COMSOL® has native support for BEM, with the ability to perform hybrid FEM-BEM modelling.

3.6 Summary

This chapter has detailed the main experimental and computational techniques that will be seen in the chapters to follow. e-beam lithography is used to fabricate the devices seen in Chapters 4, 5 and 6. The acoustic setup is used in all experimental chapters to capture the acoustic behaviour of devices. Chapters 4 and 5 utilise the acoustic reconstruction technique to map out the origins of the sound generated by individual thermophones, as well as thermophone arrays. The thermal reconstruction method is used in Chapters 4, 5 and 7 to characterise the device thermal behaviour. Finite Element Analysis is used in Chapter 4 to verify the predictions of analytical modelling, as well as quantify the effects of scattering in the acoustic setup, Chapter 5 for modelling localised heating within devices, and Chapter 7 for predicting the output characteristics of thermocouple devices.

The next chapter involves all of the methods listed above, and explores the basic characteristics of thermoacoustic devices, as well as presenting an analytical model for predicting the generated sound.

Chapter 4

Thermoacoustic Sources

4.1 Introduction

The purpose of this chapter is to characterise some of the basic properties of thermophones, as well as testing the experimental methods discussed in Chapter 3. These characteristics will be compared to models based upon the framework derived in Chapter 2.

The chapter begins with a new derivation of the acoustic fields expected from a thermoacoustic point source. This will then be extended to include the factors of the device-to-air heat transfer and finite source dimensions to produce a model to predict the sound output from real thermophones. This model will then be compared to experimental measurements.

4.2 A Point-Like Source of Heat

As seen in Section 2.4.1, the point source solution to the wave equation is useful as it can be used to model sources of arbitrary shape. It was also mentioned that there is no published point source solution to the thermoacoustic equations derived in 2.3.2. The aim of this section is to derive such a solution and produce an expression for predicting the sound generated from a thermophone.

4.2.1 Derivation

Consider a point-like heat source injecting heat into the fluid at a rate Q, per unit volume. Taking (2.48) in time harmonic form, the source term can be added to the

right-hand side,

$$\begin{bmatrix} \left(1 - \mathrm{i}\frac{\omega}{v_s}\gamma\mathcal{L}_v\right)\nabla^2 + \frac{\omega^2}{v_s^2}\gamma & \mathrm{i}\frac{\omega}{v_s}\alpha\gamma\mathcal{L}_v\nabla^2 - \frac{\omega^2}{v_s^2}\alpha\gamma \\ -\mathrm{i}\frac{\omega}{v_s}\frac{\gamma-1}{\alpha\gamma\mathcal{L}_T} & \nabla^2 + \mathrm{i}\frac{\omega}{v_s}\frac{1}{\mathcal{L}_T} \end{bmatrix} \begin{bmatrix} p \\ T \end{bmatrix} = \begin{bmatrix} 0 \\ -\frac{Q}{\kappa}\delta^3\left(\boldsymbol{x} - \boldsymbol{x}_0\right) \end{bmatrix}, \quad (4.1)$$

where δ^3 is the 3D delta function,

$$\delta^3(\boldsymbol{x} - \boldsymbol{x}_0) = \delta(x - x_0)\delta(y - y_0)\delta(z - z_0) = \begin{cases} 1, & \boldsymbol{x} = \boldsymbol{x}_0 \\ 0, & \text{otherwise} \end{cases}.$$

This can be solved by considering the Green function, $\mathcal{G}$, of the system, which satisfies

$$\begin{bmatrix} \left(1 - \mathrm{i}\frac{\omega}{v_s}\gamma\mathcal{L}_v\right)\nabla^2 + \frac{\omega^2}{v_s^2}\gamma & \mathrm{i}\frac{\omega}{v_s}\alpha\gamma\mathcal{L}_v\nabla^2 - \frac{\omega^2}{v_s^2}\alpha\gamma \\ -\mathrm{i}\frac{\omega}{v_s}\frac{\gamma-1}{\alpha\gamma\mathcal{L}_T} & \nabla^2 + \mathrm{i}\frac{\omega}{v_s}\frac{1}{\mathcal{L}_T} \end{bmatrix} \begin{bmatrix} \mathcal{G}_p \\ \mathcal{G}_T \end{bmatrix} = \begin{bmatrix} \delta^3\left(\boldsymbol{x} - \boldsymbol{x}_0\right) \\ \delta^3\left(\boldsymbol{x} - \boldsymbol{x}_0\right) \end{bmatrix}.$$

To find the Green function, first take the Fourier transform,

$$\int \frac{\mathrm{d}^3\boldsymbol{k}}{(2\pi)^3}\mathrm{e}^{\mathrm{i}\boldsymbol{k}\cdot(\boldsymbol{x}-\boldsymbol{x}_0)} \begin{bmatrix} -\left(1 - \mathrm{i}\frac{\omega}{v_s}\gamma\mathcal{L}_v\right)\boldsymbol{k}^2 + \frac{\omega^2}{v_s^2}\gamma & -\mathrm{i}\frac{\omega}{v_s}\alpha\gamma\mathcal{L}_v\boldsymbol{k}^2 - \frac{\omega^2}{v_s^2}\alpha\gamma \\ -\mathrm{i}\frac{\omega}{v_s}\frac{\gamma-1}{\alpha\gamma\mathcal{L}_T} & -\boldsymbol{k}^2 + \mathrm{i}\frac{\omega}{v_s}\frac{1}{\mathcal{L}_T} \end{bmatrix} \begin{bmatrix} \tilde{\mathcal{G}}_p \\ \tilde{\mathcal{G}}_T \end{bmatrix} = \int \frac{\mathrm{d}^3\boldsymbol{k}}{(2\pi)^3}\mathrm{e}^{\mathrm{i}\boldsymbol{k}\cdot(\boldsymbol{x}-\boldsymbol{x}_0)} \begin{bmatrix} 1 \\ 1 \end{bmatrix},$$

which can be recast as

$$\begin{bmatrix} \mathcal{G}_p \\ \mathcal{G}_T \end{bmatrix} = \int \frac{\mathrm{d}^3\boldsymbol{k}}{(2\pi)^3}\mathrm{e}^{\mathrm{i}\boldsymbol{k}\cdot(\boldsymbol{x}-\boldsymbol{x}_0)} \begin{bmatrix} -\left(1 - \mathrm{i}\frac{\omega}{v_s}\gamma\mathcal{L}_v\right)\boldsymbol{k}^2 + \frac{\omega^2}{v_s^2}\gamma & -\mathrm{i}\frac{\omega}{v_s}\alpha\gamma\mathcal{L}_v\boldsymbol{k}^2 - \frac{\omega^2}{v_s^2}\alpha\gamma \\ -\mathrm{i}\frac{\omega}{v_s}\frac{\gamma-1}{\alpha\gamma\mathcal{L}_T} & -\boldsymbol{k}^2 + \mathrm{i}\frac{\omega}{v_s}\frac{1}{\mathcal{L}_T} \end{bmatrix}^{-1}. \quad (4.2)$$

The matrix inverse is given by

$$\begin{bmatrix} A_{11} & A_{12} \\ A_{21} & A_{22} \end{bmatrix}^{-1} = \frac{1}{A_{11}A_{22} - A_{21}A_{12}} \begin{bmatrix} A_{22} & -A_{12} \\ -A_{21} & A_{11} \end{bmatrix},$$

which becomes singular when the denominator is zero. Considering the denominator for (4.2) yields

$$\left[\mathcal{L}_T\left(\mathrm{i}\frac{v_s}{\omega} + \gamma\mathcal{L}_v\right)\right]\boldsymbol{k}^4 - \left[\mathrm{i}\frac{\omega}{v_s}\left(\mathcal{L}_v + \gamma\mathcal{L}_T\right) - 1\right]\boldsymbol{k}^2 - \frac{\omega^2}{v_s^2} = 0, \quad (4.3)$$

which is the dispersion relation seen in Section 2.3.2. Equation (4.2) is therefore singular when the dispersion relation is satisfied, leading to poles in the complex

plane. These occur at

$$\boldsymbol{k}_{\pm}^2 = \frac{\mathrm{i}\frac{\omega}{v_s}\left(\mathcal{L}_v + \gamma\mathcal{L}_T\right) - 1 \pm \sqrt{\left[\mathrm{i}\frac{\omega}{v_s}\left(\mathcal{L}_v + \gamma\mathcal{L}_T\right) - 1\right]^2 + 4\frac{\omega^2}{v_s^2}\mathcal{L}_T\left(\mathrm{i}\frac{v_s}{\omega} + \gamma\mathcal{L}_v\right)}}{2\mathcal{L}_T\left(\mathrm{i}\frac{v_s}{\omega} + \gamma\mathcal{L}_v\right)}\,, \quad (4.4)$$

where $\boldsymbol{k} = \pm\sqrt{\boldsymbol{k}_{\pm}^2}$. Substitution of (4.4) allows for (4.3) to be recast as

$$\left(\boldsymbol{k} + \boldsymbol{k}_+\right)\left(\boldsymbol{k} - \boldsymbol{k}_+\right)\left(\boldsymbol{k} + \boldsymbol{k}_-\right)\left(\boldsymbol{k} - \boldsymbol{k}_-\right) = 0\,,$$

from which it is apparent that (4.2) has four poles, illustrated in Fig. 4.1. As with the plane wave solutions, the poles $\pm\boldsymbol{k}_+$ correspond to the sound wave, which has a small imaginary component due to viscous and thermal dissipation. The poles $\pm\boldsymbol{k}_-$ correspond to the thermal boundary layer. The sign $\pm\boldsymbol{k}$ describes the direction of the waves, with $+\boldsymbol{k}_\pm$ corresponding to waves generated from the source travelling out to infinity, and the reverse for $-\boldsymbol{k}_\pm$.

The integral in (4.2) can be solved via contour integration in the complex plane. Let $f(z)$ be a function of a complex variable z that has a pole at z_0. Next, take a contour, $\mathcal{C}$, in the complex plane that encloses the pole. Cauchy's residue theorem then states that, in the limit of the contour radius approaching zero,

$$f(z_0) = \frac{1}{2\pi\mathrm{i}}\oint_{\mathcal{C}} \frac{f(z)}{z - z_0}\,\mathrm{d}z\,. \quad (4.5)$$

Looking at Fig. 4.1, poles occur in both the positive and negative half-spaces of the complex plane. Since the current discussion pertains to a source, contour integrals will only be performed around the poles in the positive half-space, *i.e.*, $\boldsymbol{k} - \boldsymbol{k}_\pm = 0$. Two contour integrals must be performed, around each of the poles $\boldsymbol{k}_\pm$.

To perform the contour integrals, (4.2) must first be put in a more appropriate form. Performing the matrix inverse yields

$$\begin{bmatrix}\mathcal{G}_p\\ \mathcal{G}_T\end{bmatrix} = \frac{1}{(2\pi)^3}\int \frac{M(\boldsymbol{k})\mathrm{e}^{\mathrm{i}\boldsymbol{k}\cdot(\boldsymbol{x}-\boldsymbol{x}_0)}}{\left(\boldsymbol{k} + \boldsymbol{k}_+\right)\left(\boldsymbol{k} - \boldsymbol{k}_+\right)\left(\boldsymbol{k} + \boldsymbol{k}_-\right)\left(\boldsymbol{k} - \boldsymbol{k}_-\right)}\,\mathrm{d}^3\boldsymbol{k}\,,$$

where, for brevity,

$$M(\boldsymbol{k}) \equiv \begin{bmatrix} -\boldsymbol{k}^2 + \mathrm{i}\frac{\omega}{v_s}\frac{1}{\mathcal{L}_T} & \mathrm{i}\frac{\omega}{v_s}\alpha\gamma\mathcal{L}_v\boldsymbol{k}^2 + \frac{\omega^2}{v_s^2}\alpha\gamma \\ \mathrm{i}\frac{\omega}{v_s}\frac{\gamma-1}{\alpha\gamma\mathcal{L}_T} & -\left(1 - \mathrm{i}\frac{\omega}{v_s}\gamma\mathcal{L}_v\right)\boldsymbol{k}^2 + \frac{\omega^2}{v_s^2}\gamma \end{bmatrix}\,.$$

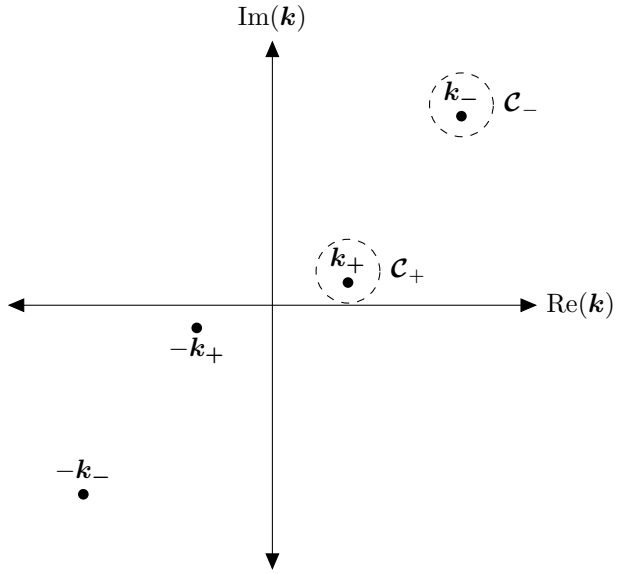

FIGURE 4.1: Poles in the complex $\boldsymbol{k}$-plane for the Green function of the thermoacoustic equations. The poles in the upper half-plane correspond to a point source, with $\boldsymbol{k}_\pm$ being the propagation and thermal boundary modes, respectively. The poles in the lower half-plane correspond to a point sink, and are not of interest. To solve for the Green function, contour integrals, $\boldsymbol{\mathcal{C}}_\pm$, must be performed around the $\boldsymbol{k}_\pm$ poles, indicated by dashed lines.

recasting the integral in spherical coordinates in $\boldsymbol{k}$, where $\boldsymbol{x}-\boldsymbol{x}_0$ lies on the $\theta_k = 0$ axis, $\boldsymbol{x}-\boldsymbol{x}_0 = \cos\theta_k\,|\boldsymbol{x}-\boldsymbol{x}_0|$,

$$\begin{bmatrix}\mathcal{G}_p\\ \mathcal{G}_T\end{bmatrix} = \frac{1}{(2\pi)^3}\int_0^\infty \mathrm{d}k \int_0^\pi \mathrm{d}\theta_k \int_0^{2\pi} \frac{k^2 \sin\theta_k M(k) \mathrm{e}^{\mathrm{i}k\cos\theta_k|\boldsymbol{x}-\boldsymbol{x}_0|}}{(k+k_+)\,(k-k_+)\,(k+k_-)\,(k-k_-)}\,\mathrm{d}\phi_k\,.$$

The integral in ϕ_k simply leads to additional factor of 2π. For θ_k, make the substitution $u = \cos\theta_k$, so $\mathrm{d}\theta_k = \frac{-1}{\sin\theta_k}\,\mathrm{d}u$,

$$\begin{aligned}\begin{bmatrix}\mathcal{G}_p\\ \mathcal{G}_T\end{bmatrix} &= \frac{1}{(2\pi)^2}\int_0^\infty \mathrm{d}k \int_1^{-1} \frac{-k^2 M(k)\mathrm{e}^{\mathrm{i}k|\boldsymbol{x}-\boldsymbol{x}_0|u}}{(k+k_+)\,(k-k_+)\,(k+k_-)\,(k-k_-)}\,\mathrm{d}u\,,\\ &= \frac{1}{(2\pi)^2}\frac{1}{\mathrm{i}\,|\boldsymbol{x}-\boldsymbol{x}_0|}\int_{-\infty}^\infty \frac{k M(k)\mathrm{e}^{\mathrm{i}k|\boldsymbol{x}-\boldsymbol{x}_0|}}{(k+k_+)\,(k-k_+)\,(k+k_-)\,(k-k_-)}\,\mathrm{d}k\,.\end{aligned}$$

The denominator can now be recast to separate the integral into two contours around k_+ and k_-,

$$\begin{aligned}\frac{1}{(k+k_+)(k-k_+)(k+k_-)(k-k_-)} &= \frac{1}{k_+^2-k_-^2}\left[\frac{1}{k^2-k_-^2}-\frac{1}{k^2-k_+^2}\right]\\ &= \frac{1}{k_+^2-k_-^2}\left[\frac{1}{(k+k_+)(k-k_+)}\right.\\ &\quad\left.-\frac{1}{(k+k_-)(k-k_-)}\right],\end{aligned}$$

$$\begin{aligned}\begin{bmatrix}\mathcal{G}_p\\ \mathcal{G}_T\end{bmatrix} = \frac{1}{2\pi\left|\boldsymbol{x}-\boldsymbol{x}_0\right|}\frac{1}{k_+^2-k_-^2}\frac{1}{2\pi\mathrm{i}}&\left[\oint_{\mathcal{C}_+}\frac{kM(k)\mathrm{e}^{\mathrm{i}k|\boldsymbol{x}-\boldsymbol{x}_0|}}{(k+k_+)(k-k_+)}\,\mathrm{d}k\right.\\ &\left.-\oint_{\mathcal{C}_-}\frac{kM(k)\mathrm{e}^{\mathrm{i}k|\boldsymbol{x}-\boldsymbol{x}_0|}}{(k+k_-)(k-k_-)}\,\mathrm{d}k\right].\end{aligned}$$

Comparing the first contour integral to (4.5), since $k-k_\pm=0$,

$$f(k)=\frac{M(k)k\mathrm{e}^{\mathrm{i}k|\boldsymbol{x}-\boldsymbol{x}_0|}}{(k+k_+)},$$

resulting in

$$f(k_+)=\frac{M(k_+)\mathrm{e}^{\mathrm{i}k_+|\boldsymbol{x}-\boldsymbol{x}_0|}}{2}.$$

Similarly, for the other integral,

$$f(k_-)=\frac{M(k_-)\mathrm{e}^{\mathrm{i}k_-|\boldsymbol{x}-\boldsymbol{x}_0|}}{2}.$$

Substitution of these results then yields the Green function,

$$\begin{bmatrix}\mathcal{G}_p\\ \mathcal{G}_T\end{bmatrix} = \frac{1}{4\pi\left|\boldsymbol{x}-\boldsymbol{x}_0\right|}\frac{1}{k_+^2-k_-^2}\left[M(k_+)\mathrm{e}^{\mathrm{i}k_+|\boldsymbol{x}-\boldsymbol{x}_0|}-M(k_-)\mathrm{e}^{\mathrm{i}k_-|\boldsymbol{x}-\boldsymbol{x}_0|}\right]. \tag{4.6}$$

Returning to (4.1) and including the heat source, Q,

$$\begin{aligned}M(k) &= \begin{bmatrix}-k^2+\mathrm{i}\frac{\omega}{v_s}\frac{1}{\mathcal{L}_T} & \mathrm{i}\frac{\omega}{v_s}\alpha\gamma\mathcal{L}_v k^2+\frac{\omega^2}{v_s^2}\alpha\gamma\\ \mathrm{i}\frac{\omega}{v_s}\frac{\gamma-1}{\alpha\gamma\mathcal{L}_T} & -\left(1-\mathrm{i}\frac{\omega}{v_s}\gamma\mathcal{L}_v\right)k^2+\frac{\omega^2}{v_s^2}\gamma\end{bmatrix}\begin{bmatrix}0\\ -\frac{Q}{\kappa}\end{bmatrix}\\ &= \frac{Q}{\kappa}\begin{bmatrix}-\mathrm{i}\frac{\omega}{v_s}\alpha\gamma\mathcal{L}_v k^2-\frac{\omega^2}{v_s^2}\alpha\gamma\\ \left(1-\mathrm{i}\frac{\omega}{v_s}\gamma\mathcal{L}_v\right)k^2-\frac{\omega^2}{v_s^2}\gamma\end{bmatrix},\end{aligned}$$

which results in the following for the temperature and pressure fields,

$$\begin{bmatrix} p \\ T \end{bmatrix} = \frac{P}{4\pi\kappa\left|\boldsymbol{x}-\boldsymbol{x}_0\right|}\frac{1}{k_+^2-k_-^2}\left(\begin{bmatrix} -\mathrm{i}\frac{\omega}{v_s}\alpha\gamma\mathcal{L}_v k_+^2 - \frac{\omega^2}{v_s^2}\alpha\gamma \\ \left(1-\mathrm{i}\frac{\omega}{v_s}\gamma\mathcal{L}_v\right)k_+^2 - \frac{\omega^2}{v_s^2}\gamma \end{bmatrix}\mathrm{e}^{\mathrm{i}k_+\left|\boldsymbol{x}-\boldsymbol{x}_0\right|}\right.$$
$$\left. - \begin{bmatrix} -\mathrm{i}\frac{\omega}{v_s}\alpha\gamma\mathcal{L}_v k_-^2 - \frac{\omega^2}{v_s^2}\alpha\gamma \\ \left(1-\mathrm{i}\frac{\omega}{v_s}\gamma\mathcal{L}_v\right)k_-^2 - \frac{\omega^2}{v_s^2}\gamma \end{bmatrix}\mathrm{e}^{\mathrm{i}k_-\left|\boldsymbol{x}-\boldsymbol{x}_0\right|}\right). \tag{4.7}$$

This is the solution for the acoustic field due to a thermoacoustic point source. Note that the heat source density, Q (units $\frac{\mathrm{W}}{\mathrm{m}^3}$), is replaced with the source power, P (units W), since the integral of the delta function is normalised to unity.

Equation (4.7) is somewhat cumbersome and does not permit much in the way of physical intuition. A significantly simplified relation can be obtained by considering that sound propagation in air is mostly adiabatic. As such, $\mathcal{L}_{v,T}$ are small and the k_- mode can be neglected,

$$p\left(P,\omega,\boldsymbol{x}\right) \approx \frac{-P}{4\pi\kappa\left|\boldsymbol{x}-\boldsymbol{x}_0\right|}\frac{1}{k_+^2-k_-^2}\frac{\omega^2}{v_s^2}\alpha\gamma\mathrm{e}^{\mathrm{i}k_+\left|\boldsymbol{x}-\boldsymbol{x}_0\right|}.$$

Considering (4.4),

$$\frac{1}{k_+^2-k_-^2} \approx \mathrm{i}\frac{v_s}{\omega}\mathcal{L}_T,$$

such that

$$p\left(P,\omega,\boldsymbol{x}\right) = \frac{-\mathrm{i}\omega P}{4\pi\left|\boldsymbol{x}-\boldsymbol{x}_0\right|}\frac{\alpha\gamma\mathcal{L}_T}{\kappa v_s}\mathrm{e}^{\mathrm{i}k_+\left|\boldsymbol{x}-\boldsymbol{x}_0\right|}.$$

This can then be recast in terms of readily available material parameters,

$$p\left(P,f,r\right) = -\frac{\mathrm{i}}{2}\frac{Pf}{r}\frac{\beta}{c_p}\mathrm{e}^{\mathrm{i}k_s r}, \tag{4.8}$$

where r is the distance from the source and k_s is the adiabatic wavenumber,

$$k_s = \frac{\omega}{v_s}. \tag{4.9}$$

It can therefore be seen that the sound generated by a thermoacoustic source is linear with the source power and frequency, in agreement with models proposed by other groups [11, 47]. The ratio $\frac{\beta}{c_p}$ is simply the conversion factor between the dissipated heat and the corresponding density change in air,

$$\frac{\beta}{c_p} = \left(\frac{\partial\rho}{\partial Q}\right)_p.$$

The remainder of this section will be used to explore some of the properties of thermoacoustic point sources, as well as modifying the model for a full thermoacoustic device.

4.2.2 Properties

To verify the validity of (4.8), the dependence of the acoustic pressure on each of the variables was modelled, compared to both (4.7) and an FEM model based upon the same equations (COMSOL Multiphysics®, Thermoviscous Acoustics module). For the FEM model, the point source was modelled as a sphere of radius 1 µm, which radiates heat into the surrounding air via a heat flux boundary condition on its surface. The heat flux was normalised by the sphere's surface area to inject a total power P into the air. Material parameters used in these models can be found in Appendix E.

The spatial dependence of the acoustic fields for each of the models is shown in Fig. 4.2. As can be seen, (4.7) agrees with the FEM model in all regions, including the thermal boundary layer. There is a slight offset in the magnitudes, which is attributed to the finite size of the 'point' source in the FEM model. The simplified solution, (4.8), does not include the effects of the boundary layer, so the temperature and pressure fields within this region are not accurate. Outside of this region, however, there is excellent agreement between all three models, showing a $1/r$ dependence of the acoustic pressure on the measurement distance. The dependence of the pressure on the source power and driving frequency are shown in Fig. 4.3. The power and frequency dependence are linear, as expected, showing agreement between all models. The exception to this is (4.7), where the frequency dependence becomes sub-linear for $f > 10^5\,\mathrm{Hz}$. This is not a unique feature of thermoacoustic generation; rather, it is simply the attenuation of sound over distance due to thermal and viscous losses. The agreement seen between the models in each of these cases suggests that (4.8) is a valid approximation for the acoustic pressure due to a point heat source.

The simplified point source expression allows for the theoretical maximum efficiency of a thermoacoustic source to be determined. This assumes that all heat produced by the source is transferred to the air. From (2.59), the acoustic power radiated by a point heat source is

$$P_{\mathrm{acoustic}}(P, f) = \frac{\pi\beta^2}{\rho_0 v_s c_p^2} P^2 f^2 \,,$$

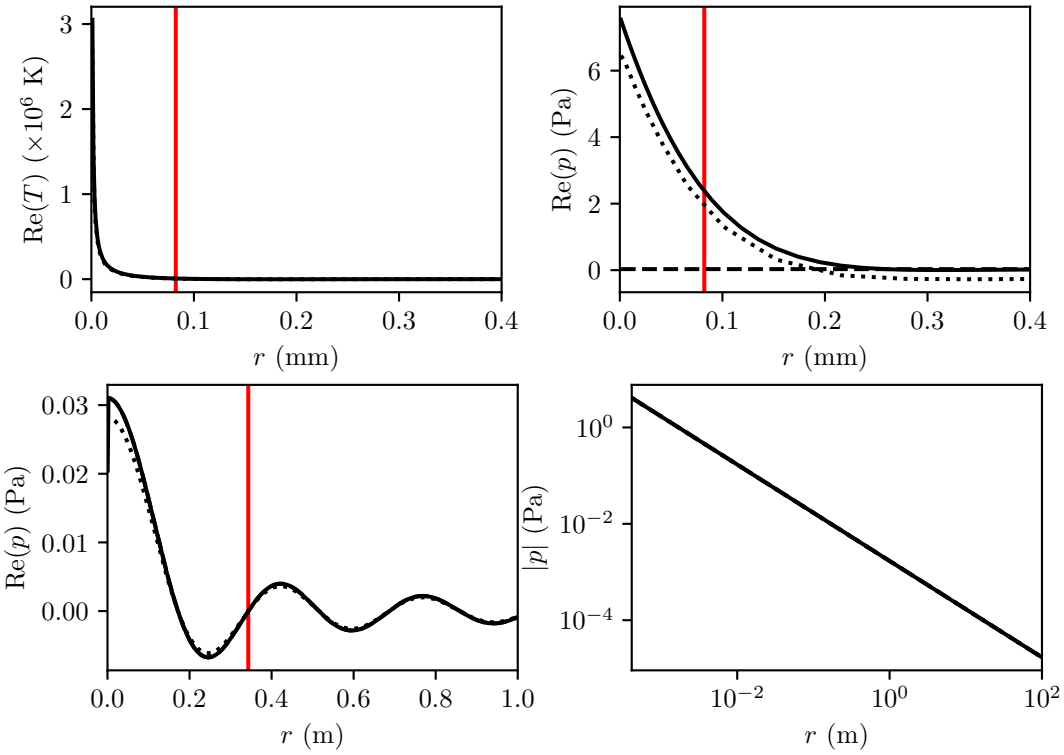

FIGURE 4.2: Acoustic fields due to a thermoacoustic point source, comparing (4.7) (solid line) and (4.8) (dashed line) to the FEM model (dotted line). $P = 1\,\mathrm{W}$, $f = 1\,\mathrm{kHz}$. **Top row:** Temperature and pressure fields close to the source. Red lines indicate the thermal diffusion length. **Bottom row:** Acoustic pressure outside of the boundary layer. Red line indicates the acoustic wavelength.

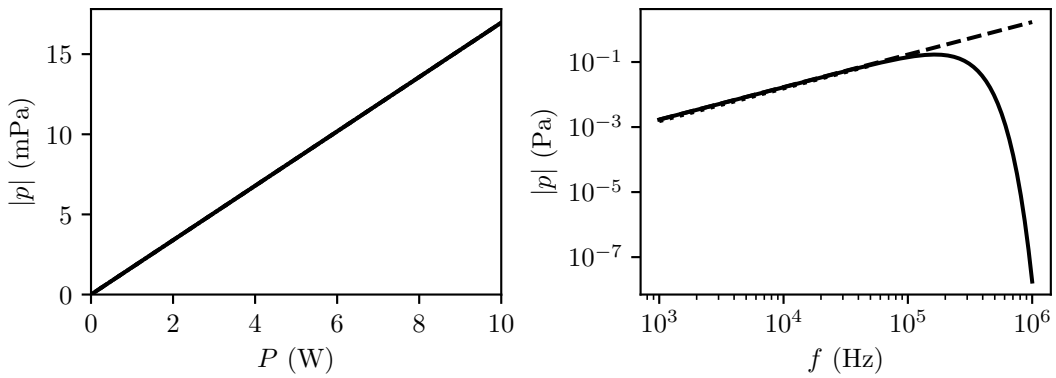

FIGURE 4.3: Power and frequency dependence of a thermoacoustic point source, comparing (4.7) (solid line) and (4.8) (dashed line) to the FEM model (dotted line). **Left:** Power dependence. $f = 1\,\mathrm{kHz}$, $r = 1\,\mathrm{m}$. **Right:** Frequency dependence. $P = 1\,\mathrm{W}$, $r = 1\,\mathrm{m}$.

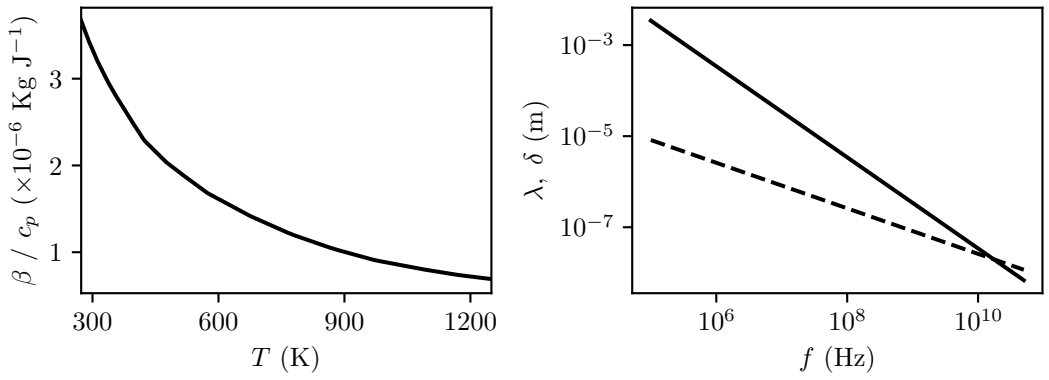

FIGURE 4.4: Limiting factors in the maximum efficiency of a thermoacoustic point source. **Left:** Temperature dependence of $\frac{\beta}{c_p}$ for air at atmospheric pressure. Data from [83]. **Right:** Comparison of acoustic wavelength (solid line) and thermal diffusion length (dashed line) as a function of frequency.

so, from (2.60),

$$\eta_{\max} = \frac{\pi \beta^2}{\rho_0 v_s c_p^2} P f^2 \,. \tag{4.10}$$

This may initially appear alarming, since the efficiency monotonically increases with both the source power and frequency; however, the oscillating heat source has a background DC temperature field associated with it, which also increases with the source power. This DC field will affect the thermal parameters of the air around the source, which are temperature dependent (as shown in Fig. 4.4), in turn limiting the efficiency. The issue with the source frequency is resolved by considering that, as the acoustic frequency increases, the thermal diffusion length increases relative to the acoustic wavelength (demonstrated in Fig. 4.4). This results in greater losses due to thermal conduction as the sound waves transition between adiabatic ($\delta \ll \lambda$) and isothermal ($\delta \gg \lambda$) behaviour. In air, this transition occurs at frequencies far beyond that which are typically used in acoustic applications, so the adiabatic assumption is suitable. The theoretical maximum efficiency of a thermoacoustic point source is shown as a function of frequency in Fig. 4.5. In reality, thermophones are unlikely to achieve such efficiency, since there is the additional issue of the heat transfer efficiency between the active film and the surrounding medium. This will be explored in the following section.

4.2.3 Real Thermophones

In reality, thermophones have finite dimensions, and not all of the Joule heat is transferred to the air. The point source solution will now be modified to enable comparison to practical devices. The first modification required is a factor describing the ratio of input Joule power and the heat energy transferred to the air. This is

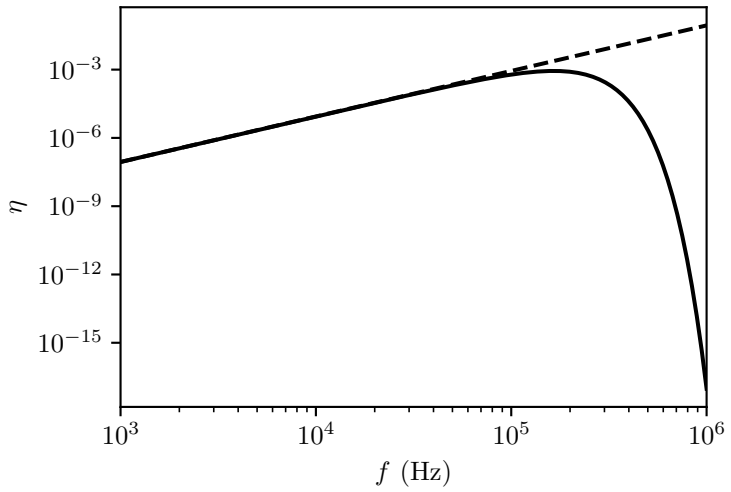

FIGURE 4.5: Theoretical maximum efficiency of a thermoacoustic point source as a function of frequency. $P = 1\,\mathrm{W}$, $r = 1\,\mathrm{m}$. Shown is a comparison between the efficiency from (4.7) (solid line) and (4.8) (dashed line).

provided by the ratio of the thermal effusivities, as discussed in Section 2.2. Also, the heat energy is transferred from the film into a half-space of air. As such, the pressure is doubled compared to radiating into full space. Finally, the directivity of the source, due to its finite dimensions must be included. This is provided by the directivity factor derived in Section 2.4.1. Making these modifications to (4.8) yields

$$p(P, f, r, \theta, \phi) = -\mathrm{i}\frac{Pf}{r}\frac{\beta}{c_p}\mathcal{E}(f)D(f, \theta, \phi)\mathrm{e}^{\mathrm{i}k_s r}\,, \tag{4.11}$$

where P is the power dissipated at the frequency f. This model will now be compared to experimental thermophone measurements. The thermal properties used with this model are given in Appendix E.

4.3 Experimental Measurements

To test the model in the previous section, the device shown in Fig. 4.6 was fabricated. This consisted of a 25×13 mm ITO film, of thickness 100 nm, on a microscope slide. Electrical contact was achieved via 5/100 nm Cr/Au pads on either end of the ITO film, which were contacted with copper tape. To begin with, the electrical and thermal properties of the device were characterised. The device was connected to a DC power supply and a voltage sweep was performed. At each step, the device was allowed to reach thermal equilibrium, at which point the current was measured, and a thermal image taken using the setup given in Section 3.4. Figure 4.7 shows the I-V characteristics, as well as the average film temperature as a function of electric

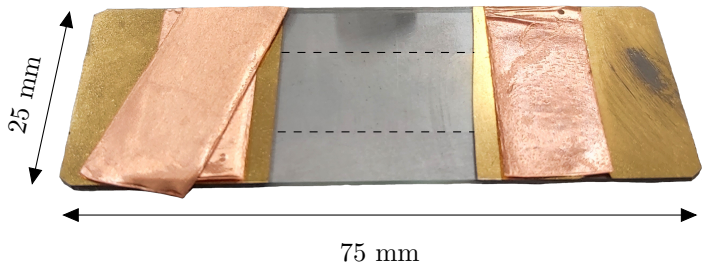

FIGURE 4.6: A rectangular thermophone on a microscope slide. The thermophone was a 100 nm thick ITO thin film, with planar dimensions 25 × 13 mm and thickness 100 nm (outlined with dashed lines). Electrical contact was made via copper tape to Cr/Au (5/100 nm) pads on either end.

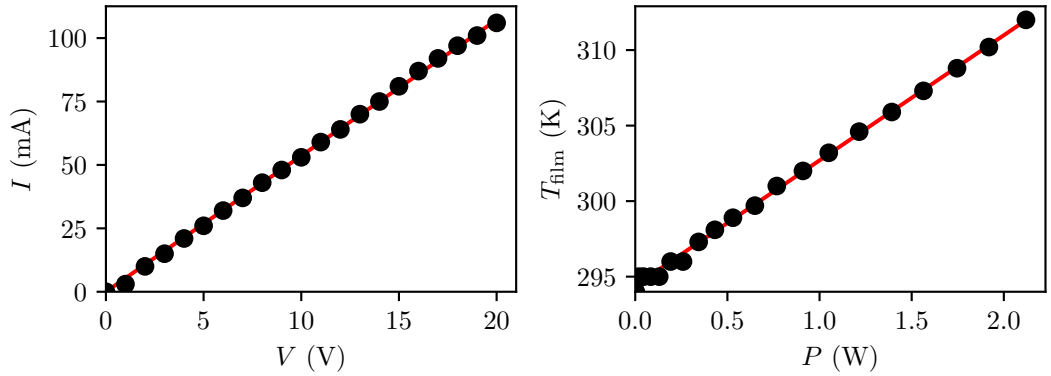

FIGURE 4.7: DC electrical and thermal measurements for the 25 × 13 mm ITO thermophone. **Left:** I-V characteristic curve. Measurements are represented by black circles, with dashed red line indicating a linear fit. The linear fit gives a resistance of $186.6 \pm 0.4\,\Omega$. **Right:** Average film temperature as a function of power (black circles), with linear fit (dashed red line).

power, for DC driving. Within the voltage range tested, the device showed Ohmic behaviour, with a linear fit returning a resistance of $186.6 \pm 0.4\,\Omega$. The average film temperature was also linear with the electric power. Next, the thermal behaviour of the device was investigated when driven with AC. The device was driven with $f_1 = 1\,\text{Hz}$ and $P_2 = 360\,\text{mW}$, and the average film temperature was measured as a function of time. The results of these measurements are shown in Fig. 4.8. The transient response of the device clearly shows a small oscillation in the temperature on top of a larger DC background temperature, as expected from the effects of second harmonic generation discussed in Section 2.1. To verify the second harmonic nature of the heating, the spectral response of the heating, once the device had reached equilibrium, was also measured. As can be seen, this consists of a large dc component, as well as a second harmonic component at 2 Hz.

After characterising the thermal response of the device, the acoustic properties were investigated. The device was placed on a bench top and acoustic measurements were

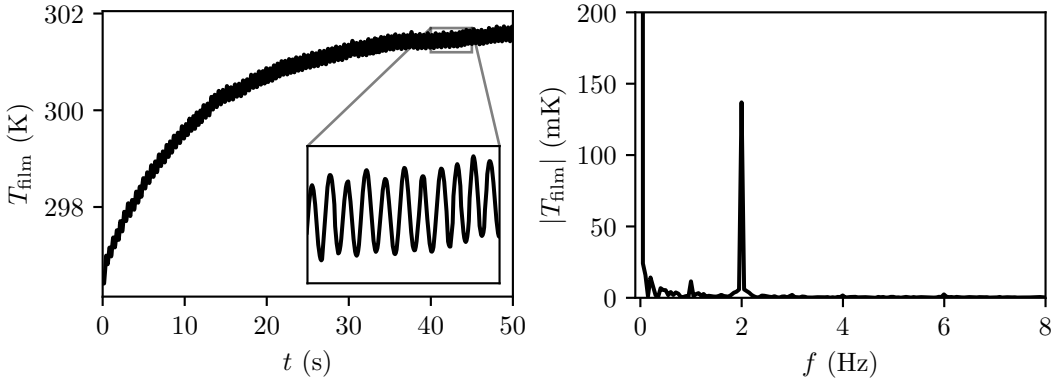

FIGURE 4.8: Time dependence of the average film temperature of the 25 × 13 mm ITO thermophone, when driven with AC. $f_1 = 1\,\text{Hz}$, $P_2 = 360\,\text{mW}$. **Left:** Transient response. The AC source was switched on at $t = 0\,\text{s}$. **Right:** Spectral response, once the device had reached thermal equilibrium.

performed normal to the device at a distance of 30 cm, varying the driving power and frequency. The results of these measurements are shown in Fig. 4.9, compared to (4.11). Good agreement is seen between the experiment and model, with the sound pressure depending linearly on both the power and frequency. There is some suppression to the sound at frequencies above 25 kHz. This feature was unique to this particular device, and resolving this feature lies beyond the current scope of this work. The far-field directivity of the source was also measured by mounting the device in the rotary gimbal, as discussed in Section 3.3. This is compared to the directivity from (4.11) in Fig. 4.10. There is agreement with respect to the width of the main lobe, although the sound level is not adequate to resolve the side lobes. This far-field map can be used to perform an acoustic reconstruction of the source, as discussed in Section 3.3. The result of this is compared to the second harmonic thermal response of the device in Fig. 4.11. The thermal reconstruction shows that the heat is dissipated reasonably evenly throughout the film, resulting in an acoustic source of the same dimensions as the film. This is reflected in the acoustic reconstruction, which shows a source of similar dimensions. To further verify the far-field characteristics of thermophones, a similar device, shown in Fig. 4.12, was fabricated. This device was identical to that in Fig. 4.6, except the ITO film had dimensions 37 × 7 mm. The far-field directivity of this device is shown as a function of frequency in Fig. 4.13, compared to (4.11). As can be seen, there is very good agreement between the experiment and model, including the number of diffracted side lobes as the frequency is increased. The horizontal banding seen is a result of small variations in the rotation speed of the gimbal during measurement. Integration of these far-field maps, taking into account the coordinate stretching factor encountered in Section 3.3, allows for the efficiency to be determined. This is shown in Fig. 4.14, compared to (4.10) and the expected efficiency from (4.11).

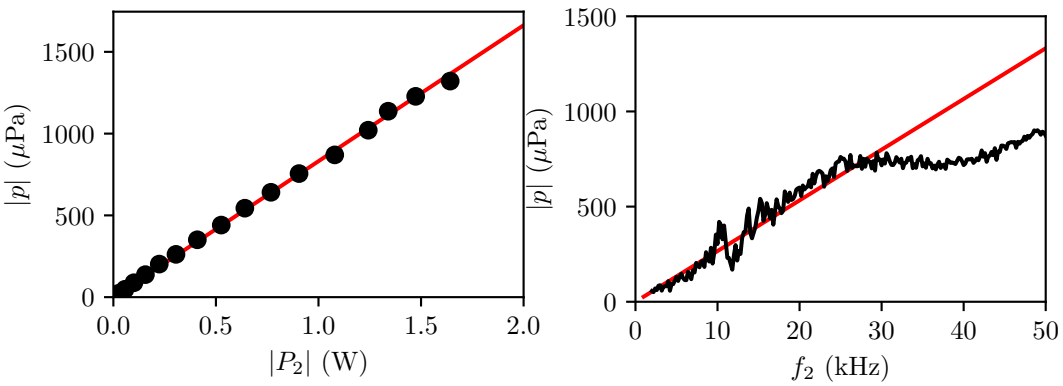

FIGURE 4.9: Experimental power and frequency dependence of the 25×13 mm ITO thermophone (black dots), compared to (4.11) (red lines). **Left:** Power dependence for $f_2 = 20$ kHz. **Right:** Frequency dependence for $P_2 = 0.64$ W. Material parameters used for the model are given in Appendix E.

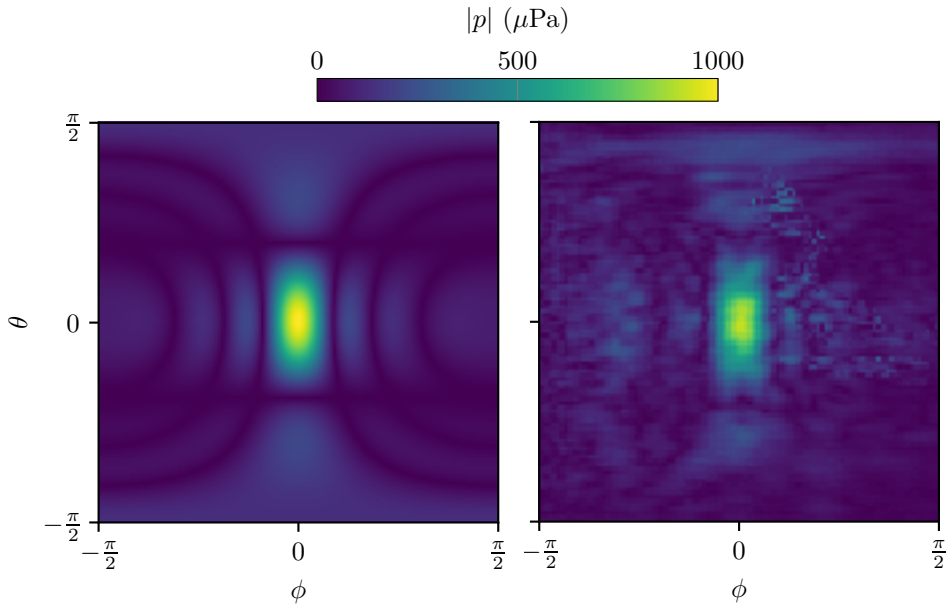

FIGURE 4.10: Far-field directivity of the 25×13 mm ITO thermophone for $f_2 = 50$ kHz and $P_2 = 0.5$ W. **Left:** Modelled directivity from (4.11). **Right:** Experimental measurement.

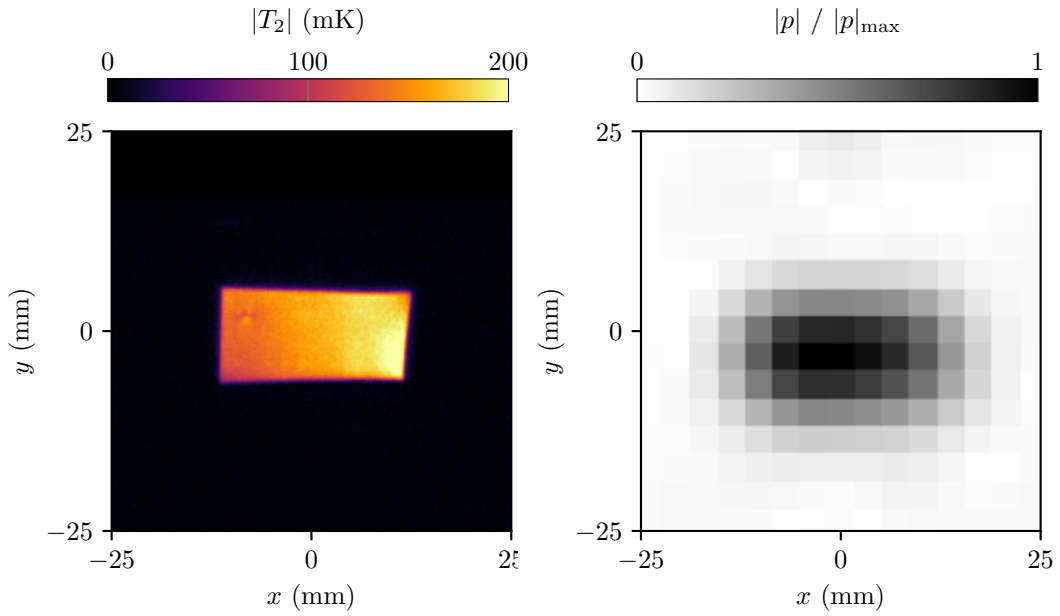

FIGURE 4.11: Thermal and acoustic reconstructions of the 25 × 13 mm ITO thermophone. **Left:** Thermal reconstruction, showing the magnitude of the temperature field at the second harmonic, where $f_2 = 2\,\text{Hz}$. **Right:** Acoustic reconstruction for $f_2 = 50\,\text{kHz}$.

For the latter, the far-field integration was performed numerically. The results show an efficiency of order 10^{-10} within the measured frequency range, far below the maximum efficiency achievable with such a device ($\sim 10^{-6}$). This is due to the effect of the substrate on the distribution of the generated Joule heat. The acoustic reconstruction of this device is shown in Fig. 4.15. Again, the reconstruction clearly shows an acoustic source of the expected dimensions.

Smaller gold and ITO-based devices were also measured. These are shown in

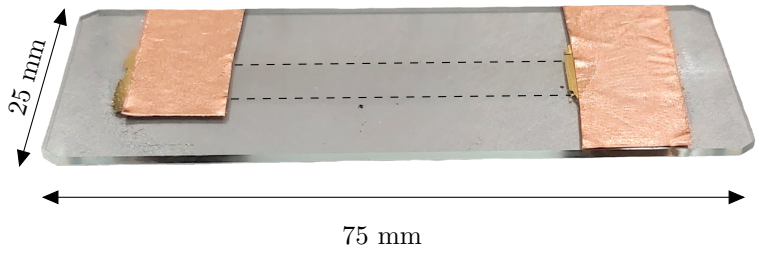

FIGURE 4.12: Rectangular thermophone on a microscope slide. The thermophone was a 100 nm thick ITO thin film, with planar dimensions 37 × 7 mm and thickness 100 nm (outlined with dashed lines). Electrical contact was made via copper tape to Cr/Au (5/100 nm) pads on either end.

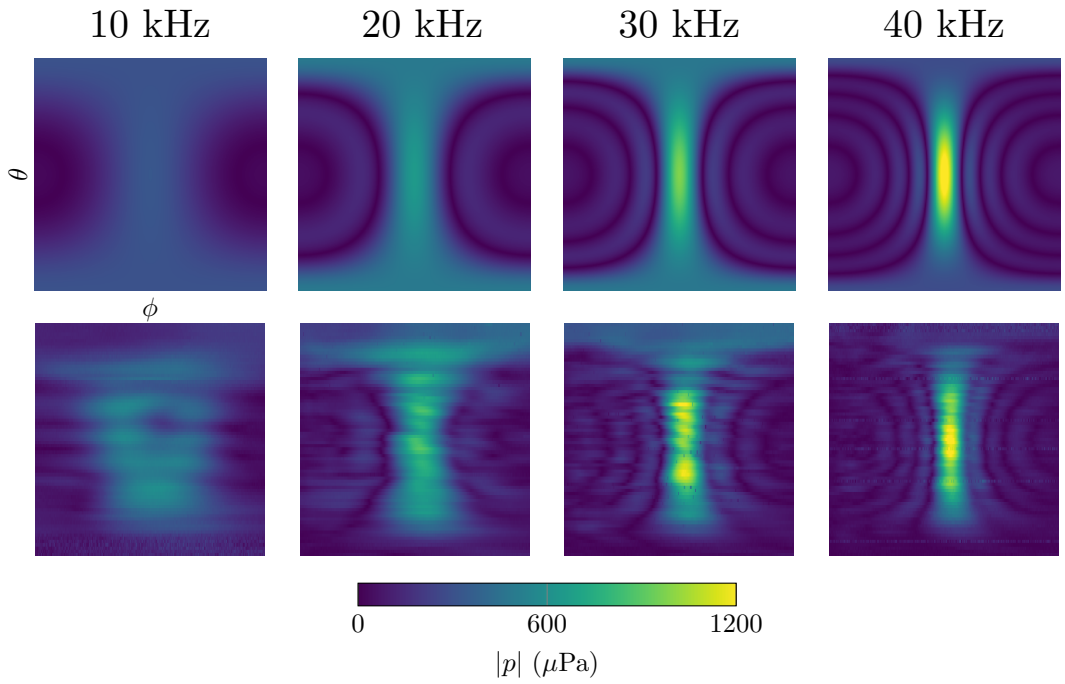

FIGURE 4.13: Far-field directivity of the 37×7 mm thermophone as a function of frequency. $P_2 = 0.5$ W. **Top row:** Far-field directivity predicted from (4.11). **Bottom row:** Experimentally measured far-field directivity.

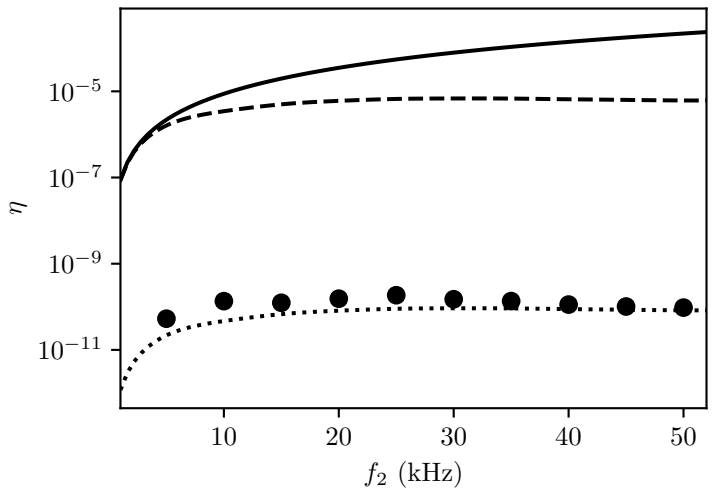

FIGURE 4.14: Measured efficiency of the 37×7 mm ITO device as a function of frequency (black points) for $P_2 = 0.5$ W and $r = 30$ cm. Compared to the theoretical maximum efficiency of a point source (solid line), as well as the finite source case for both $\mathcal{E} = 1$ (dashed line) and using device material parameters for $\mathcal{E}$ (dotted line).

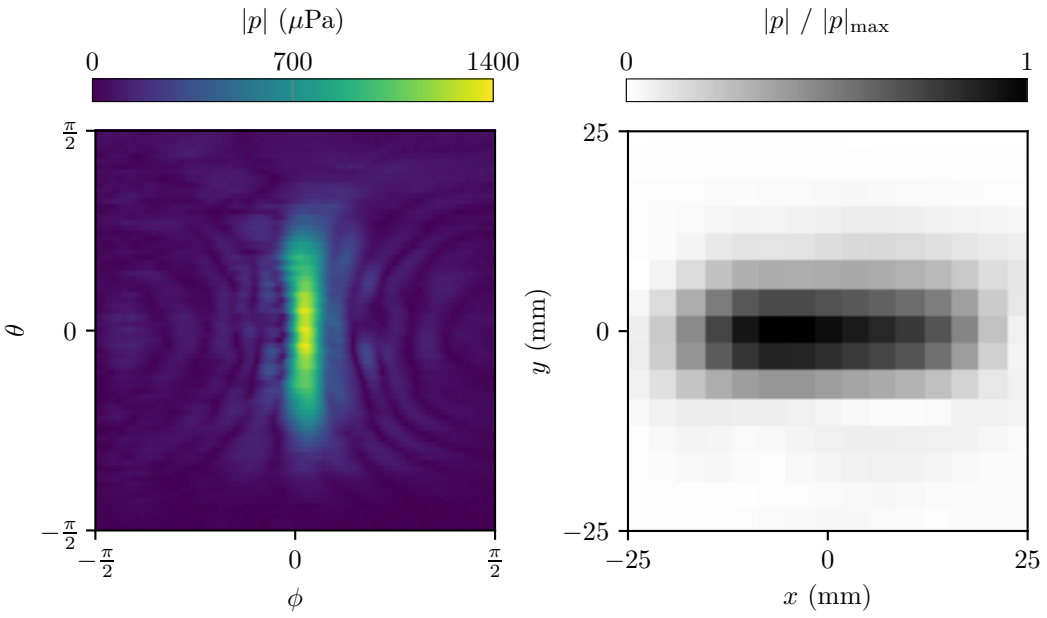

FIGURE 4.15: Acoustic reconstruction of the 37×7 mm thermophone, for $P_2 = 0.5$ W, $f_2 = 50$ kHz. **Left:** Measured far-field directivity. **Right:** Acoustic reconstruction.

Fig. 4.16, along with the mounting used for these devices with the rotary gimbal. To test the effectiveness of the thermal and acoustic reconstruction methods with these devices, they were performed on the inner track of the Π-shaped device. This is shown in Fig. 4.17. As can be seen, both methods are successful in resolving the geometry of the device. It should be noted, however, that the acoustic reconstruction was performed for $f_2 = 300$ kHz. At this frequency, no calibration data exists for the microphone used, however the signal-to-noise ratio was still sufficient to perform the measurement. As such, only relative values for the sound pressure can be obtained at this frequency.

The frequency response of these devices was also measured and compared to (4.8), shown in Fig. 4.18. This response, while loosely agreeing with the point source model, does show some additional features; notably, a sharp dip around 34 kHz. In air, this frequency corresponds to a wavelength of around 1 cm, which is similar to the dimensions of the mounting ring. Looking at the acoustic reconstruction of the Π-shaped device in Fig. 4.18, it can be seen that there is finite amplitude in the region where the ring is located, indicating scattering of the generated sound off the mounting ring. To quantify the effect of the mounting on the sound output, a FEM model of the device including the mounting was performed. The results of this modelling are shown in Fig. 4.19. As can be seen, the presence of the mounting leads to additional features in the frequency response, due to diffraction and scattering,

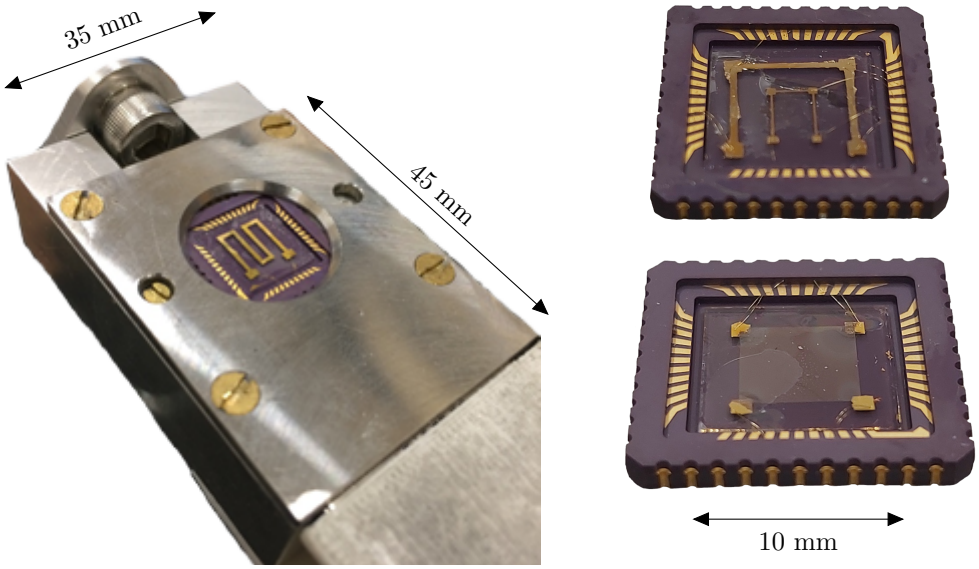

FIGURE 4.16: Smaller thermophone devices, deposited on 10×10 mm fused quartz substrates. **Left:** Serpentine Cr/Au device (thickness 5/50 nm), shown in the rotary gimbal mounting. **Upper right:** Π-shaped Cr/Au device (thickness 5/50 nm). **Bottom right:** 6×6 mm square ITO device (80 nm), with Cr/Au contact pads (5/100 nm).

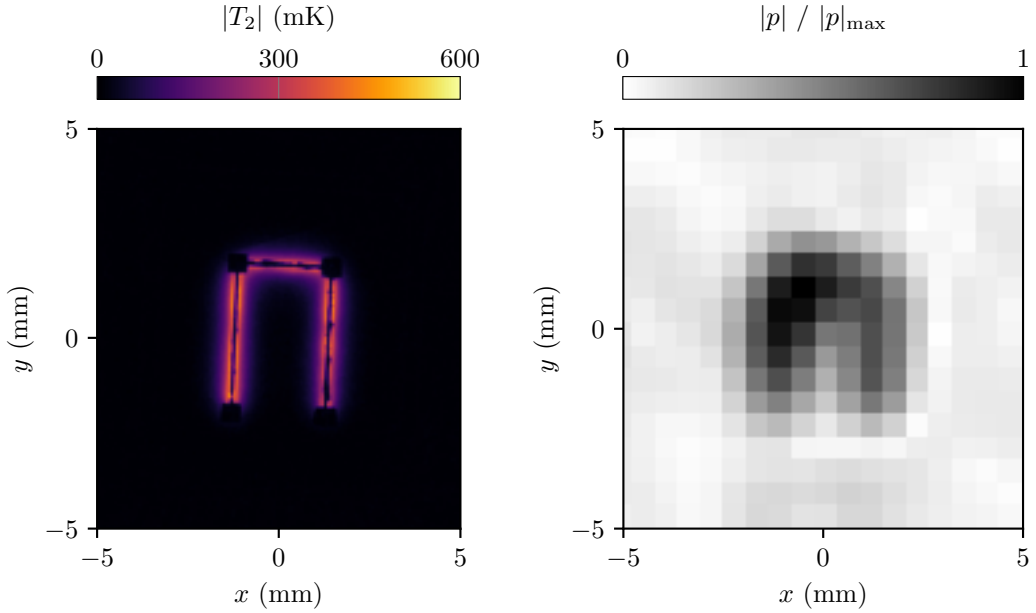

FIGURE 4.17: Thermal and acoustic reconstructions of the Π-shaped device. **Left:** Thermal reconstruction, $P_2 = 13$ mW, $f_2 = 2$ Hz. **Right:** Acoustic reconstruction at $f_2 = 300$ kHz.

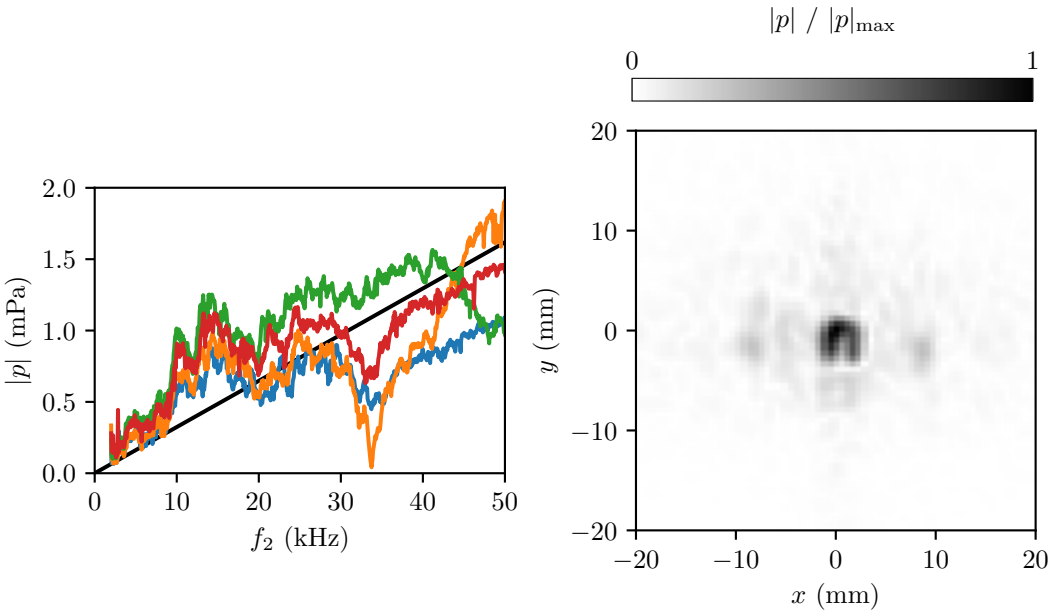

FIGURE 4.18: Acoustic measurements of the devices shown in Fig. 4.16. **Left:** Head-on acoustic pressure as a function of frequency, for $P_2 = 1\,\mathrm{W}$, $r = 20\,\mathrm{cm}$. Shown are the serpentine gold device (blue), inner and outer tracks of the Π-shaped device (orange/green), and the square ITO device (red). The black line is the expected sound generation from (4.11), for $D = 1$ and assuming the film effective effusivity is small relative to the air and substrate. **Right:** Acoustic reconstruction of Π-shaped device, from Fig. 4.17, zoomed out to show the effect of scattering due to the mounting ring.

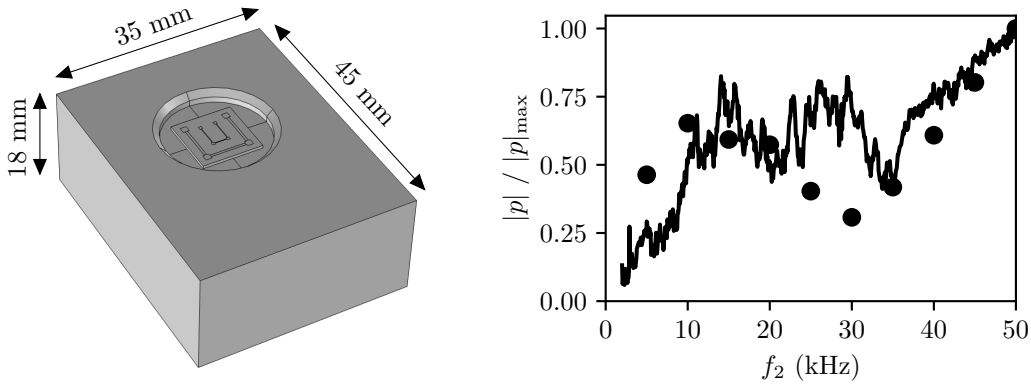

FIGURE 4.19: FEM model of the Π-shaped device, including the device mounting. **Left:** Model schematic. **Right:** Comparison of model (black circles) and experimental (black line) frequency responses when using the inner track of the device.

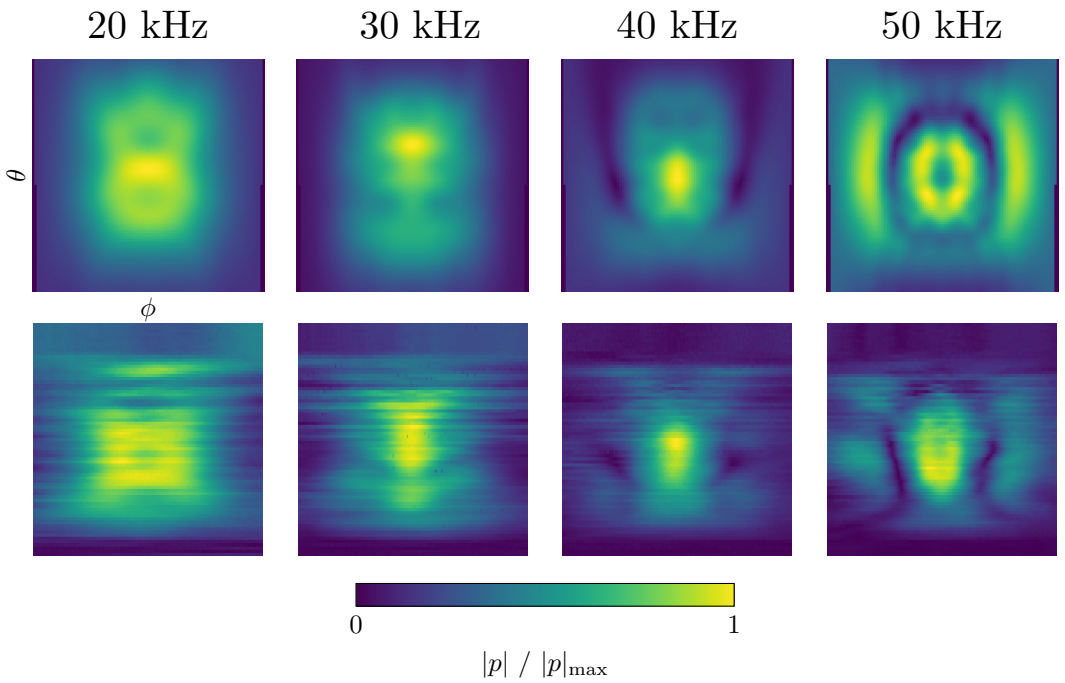

FIGURE 4.20: Far-field directivity of the Πshaped device when driving the inner track, compared to the FEM model of the device including the mounting. **Top row:** FEM model. **Bottom row:** Experimental measurements.

including a dip around 30 kHz. The far-field directivity was also modelled, shown in Fig. 4.20, compared to experimental results. Again, the mounting leads to additional features in the directivity, which are also replicated in the experimental results. For both of these data sets the modelled response is not expected to exactly match the experimental results since only part of the mounting was modelled. Despite this, the modelling gives a clear indicator that the additional features seen in Fig. 4.18 are simply experimental artefacts.

4.4 Conclusions

In this chapter, the characteristics of thermoacoustic devices were explored, and experimental methods were tested.

A new expression was derived to describe the sound generated by a thermoacoustic point source. This was then generalised to enable the modelling of real thermoacoustic devices.

Some simple thermoacoustic devices were then fabricated and characterised with electrical, thermal and acoustic measurements. It was found that the model was able to successfully describe the behaviours seen experimentally. Included in these measurements were the thermal and acoustic reconstruction methods discussed in

Chapter 3. These were shown to be effective methods for characterising thermophones. Finally, the effect of the device mounting for far-field acoustic measurements was measured. It was found that this mounting has a significant impact on the sound generation, due to diffraction and scattering. This impact can be minimised by reducing the acoustic frequency.

In the next chapter, the interactions of multiple thermoacoustic sources in a single device will be explored, in the context of thermoacoustic phased arrays.

Chapter 5

Thermoacoustic Phased Arrays

5.1 Introduction

In the previous chapter, only single thermoacoustic sources were considered. This chapter extends the discussion to multiple sources, by exploring the concept of thermoacoustic phased arrays.

The chapter begins with a brief overview of acoustic phased arrays, including their characteristics, applications and limitations. It then describes how thermoacoustic array elements may be able to overcome some of the limitations associated with traditional array transducers. The potential for thermoacoustic phased arrays will then be explored using the experimental methods developed in the previous chapter, characterising arrays thermally, electrically and acoustically, marking the first study of its type. It will be seen that the unique characteristics of the Joule heating mechanism result in some promising opportunities for phased array design.

The work in this chapter contributed to the publication in [84]. The work presented here is that of the author, with the exceptions of the analytical model presented in Section 5.4 (Simon Horsley, University of Exeter) and the device fabrication (Mark Heath, University of Exeter).

5.2 Acoustic Phased Arrays

Acoustic phased arrays are collections of individually addressable acoustic transmitters and receivers [85]. The precise control of individual elements allows for generation of complex wavefronts that are not attainable by singular transducers. Some examples of phased acoustic array geometries are shown in Fig. 5.1. The simplest array type is perhaps the linear array. This allows for beam manipulation in two dimensions; for example, focusing a beam and then steering it by some angle

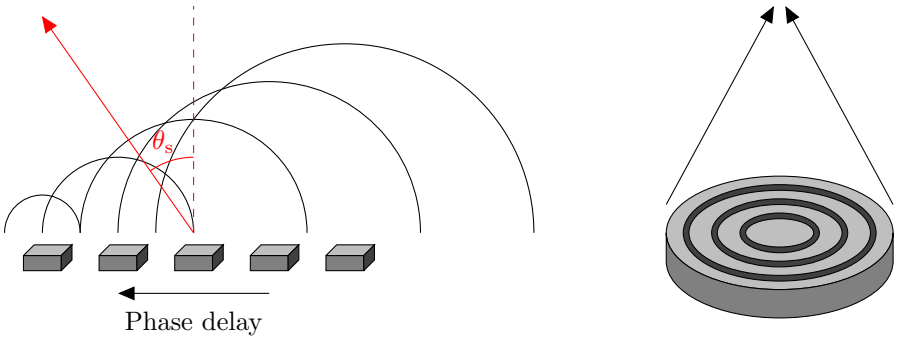

FIGURE 5.1: Examples of beam forming with acoustic phased arrays. **Left:** Beam steering in a linear array due to a phase delay across the sources. **Right:** Beam focusing using sources arranged in annular rings.

relative to the device normal. This steering is achieved by applying a progressive phase delay across the sources. Assuming the elements behave as point sources, the steering angle in the far field, θ_s, is given by

$$\theta_s = \arcsin\left(\frac{\Delta\psi}{kd}\right), \tag{5.1}$$

where $\Delta\psi$ is the acoustic phase difference between adjacent array elements, k is the acoustic wavenumber and d is the element separation [78]. The concept of beam steering can be extended to 2D planar arrays, allowing for multi-axis steering. Phase delays can also be applied in a circular fashion, which results in beams that rotate in phase as they propagate, *i.e.*, they carry orbital angular momentum (OAM) [86]. Another example is arrays of annular rings, which can produce highly-focused beams.

The ability to shape and control beams of sound has many practical applications, some of which are highlighted in Fig. 5.2. They are particularly useful in non-destructive evaluation and medical imaging, where beam steering allows for samples to be acoustically 'scanned' for features of interest [87]. More recently, they have been used in acoustic levitation [88], where objects can be trapped within sound beams and manipulated, allowing for technology such as 3D displays. Other uses involve haptic feedback [89], wireless power [90] and information transfer via highly-directive and/or OAM beams [91].

The ideal phased array would have an infinite number of elements placed infinitesimally close together with infinite bandwidth [85], allowing for very fine control over the beam characteristics. While this is obviously not an achievable goal, array performance can still be improved by increasing the number of elements involved.

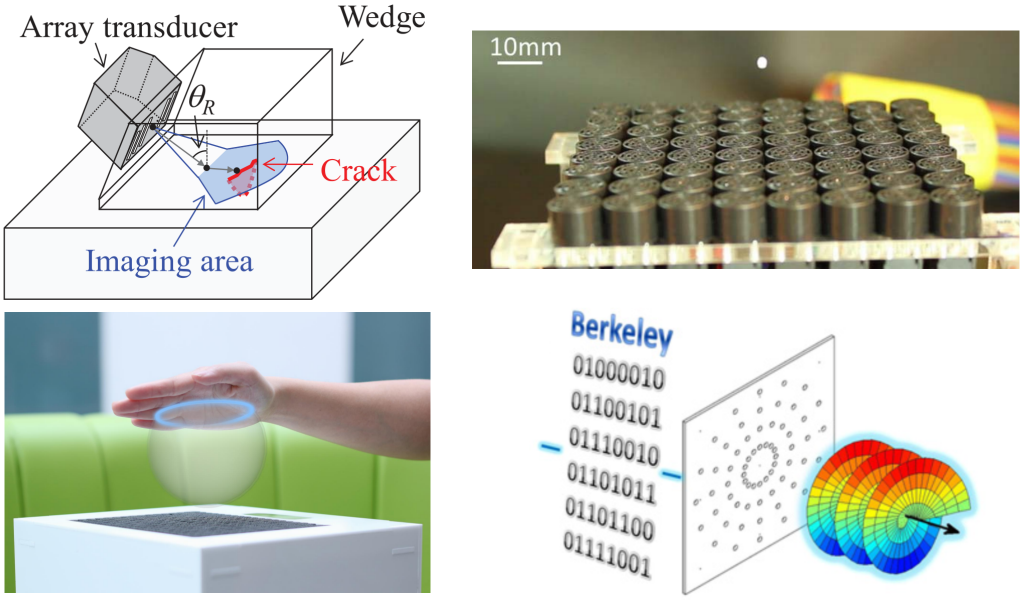

FIGURE 5.2: Applications of acoustic phased arrays. **Top left:** Non-destructive evaluation [92]. Beam steering and time-of-flight measurements can be used to acoustically scan samples for defects. **Top right:** Acoustic levitation [93]. Arrays can be used to form beams that can trap and manipulate objects in the air. **Bottom right:** Haptic feedback [94]. Arrays can simulate the sensation of touch mid-air. **Bottom right:** Communication using OAM beams [91]. Information can be encoded in the angular momentum states of the propagating sound.

There are, however, a number of practical limitations associated with increasing the number of array elements. As the number of elements increases, so does the number of electrical connections required to individually source each element. This presents issues with fabrication, where the contacts take up more physical space, as well as with the computing power associated with controlling the array and processing the data. This is particularly relevant in applications such as medical imaging, where image processing typically occurs in real-time [87]. Common approaches to mitigate these effects involve sharing common ground rails between elements and using multiplexing to reduce computational load. The number of elements is also limited by the properties of the elements themselves, since increasing the spatial density of the elements in an array inherently requires decreasing the element dimensions. For mechanical transducers this can present a significant challenge as miniaturising devices based upon moving parts quickly becomes expensive and/or unfeasible. There can also be losses in efficiency due to the resonant nature of such devices. Another issue with phased arrays is cross-talk (coupling) between the array elements [95]. Mechanical transducers are reciprocal, *i.e.*, they can both emit and receive sound. Because of this, the sound emitted by one element of the array can affect the sound emission from nearby elements, and vice-versa. This predominantly occurs via elastic waves in the backing material for the arrays, but can also be a result of using common ground rails or poor shielding. Cross-talk between elements typically results in distortion in the array directivity, as well as poor impulse response.

Some of the transducer types found in acoustic phased arrays are illustrated in Fig. 5.3. Most commonly found are arrays based upon piezoceramics, where arrays are formed by sawing slabs of material into individual elements [96]. The nature of this fabrication method tends to result in considerable cross-talk, due to mechanical coupling through the backing material. Miniaturisation of elements is also severely limited by the size and precision of saw required. More recently, advances have been made with micromachined ultrasonic transducers (MUTs), of which there are two main types: piezoelectric [97] and capacitive [98]. Here, elements are formed by layering of materials on the backing to create suspended membranes. This method of fabrication affords much greater scope for miniaturisation, with the ability to define array elements lithographically; however, they are still susceptible to mechanical cross-talk and resonance.

Thermoacoustic phased arrays would offer a number of unique benefits compared to their mechanical counterparts. Primarily, the transduction mechanism – Joule heating – is thermodynamically irreversible. Because of this, cross-talk between elements is expected to be much less of an issue. In addition to this, the lack of

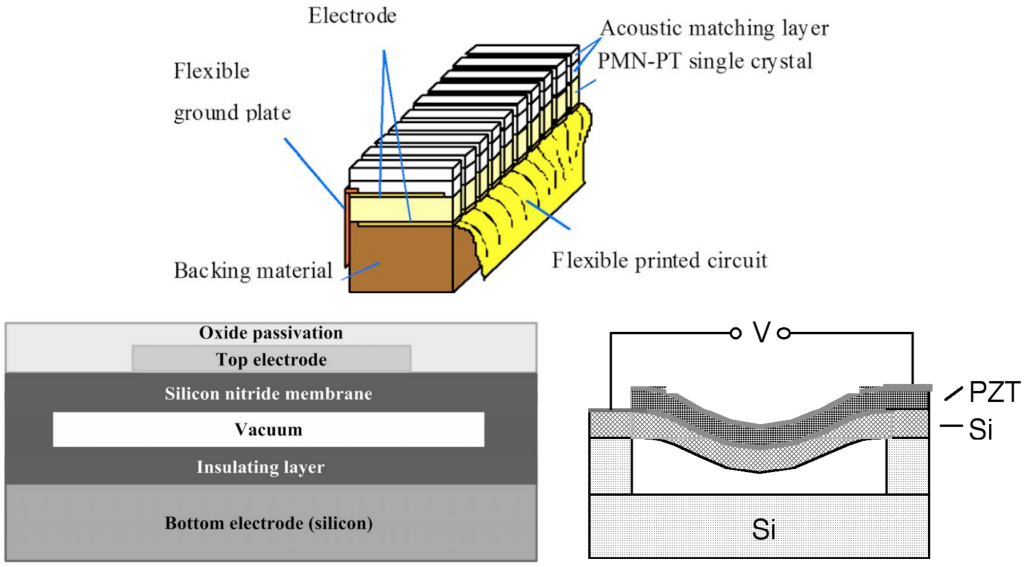

FIGURE 5.3: Examples of mechanical array transducers. **Top:** Typical piezoelectric array [96]. The piezoelectric material is mounted on a backing layer, and array elements are then defined by sawing the material. **Bottom left:** Capacitive micromachined ultrasonic transducer (CMUT) [98]. **Bottom right:** Piezoelectric micromachined ultrasonic transducer (PMUT) [97].

moving parts, coupled with the simple fabrication methods, makes miniaturisation of such arrays trivial. It is surprising, then, that thermoacoustic phased arrays have not been explored prior to this work. Thermoacoustic sources do, however, come with their own limitations. Firstly, the non-reciprocal nature of the transduction is a double-edged sword: the cross-talk is eliminated, but this comes at the cost only being able to use thermoacoustic sources as transmitters in phased arrays, not receivers. Ultimately, though, this could be compensated for by using thermoacoustic sources in tandem with mechanical receivers. Perhaps the main limiting factor is the poor conversion efficiency of thermoacoustic devices. This is somewhat mitigated by the fact that thermoacoustic sources are broadband, with their efficiency increasing at higher frequencies (a fact seen in Chapter 4). Therefore, while their efficiency may be limiting in audio applications, the increased efficiency at ultrasonic frequencies may make them an attractive candidate for phased arrays.

The remainder of this chapter is dedicated to answering some of the questions surrounding thermoacoustic phased arrays, and experimentally demonstrating their unique characteristics.

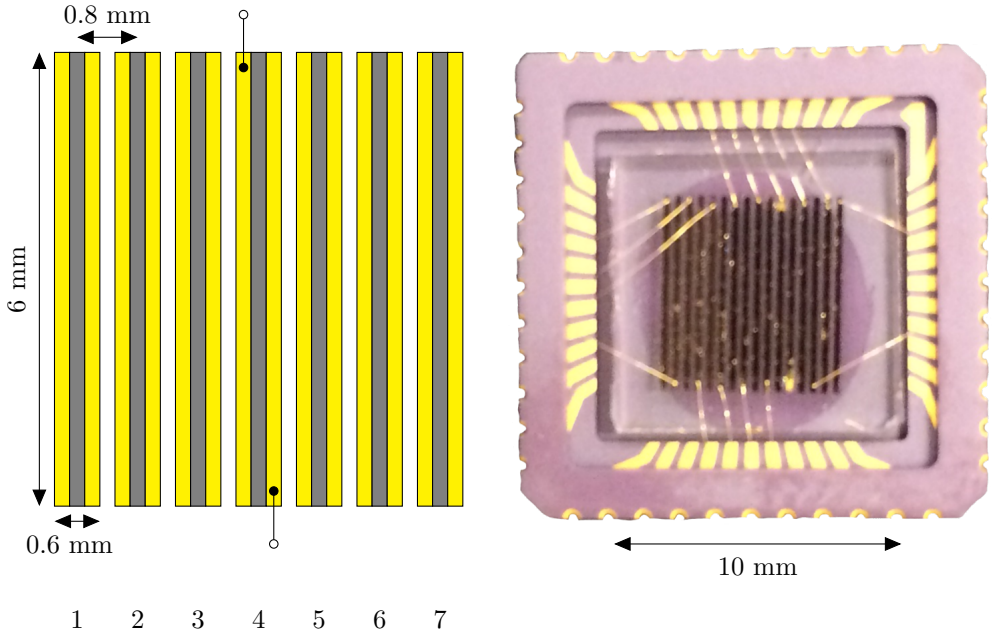

FIGURE 5.4: A 7-element linear thermoacoustic phased array. **Left:** Device schematic. The array elements were formed by 50 nm ITO films (grey), with 5/100 nm Cr/Au contacts (yellow), on a fused quartz substrate. The locations of the 25 µm diameter wire bonds are shown for the central element only. **Right:** Device photograph.

5.3 Thermoacoustic Phased Arrays

The first geometry explored for a thermoacoustic phased array was a linear array, shown in Fig. 5.4. This consisted of seven 0.6×6.0 mm ITO elements, with thickness 50 nm and pitch 0.8 mm, on a fused quartz substrate. Electrical contact was made via 25 µm diameter gold wires to 0.2×6.0 mm Cr/Au bilayer films (5/100 nm) deposited on the faces of the ITO films, such that the exposed ITO films formed elements of dimensions 0.2×6.0 mm.

To begin with, only two of the elements were used. Elements 3 and 5 were individually addressed by phase-locked sources, set to dissipate 1 W per element. Thermal and acoustic measurements were then performed, varying the driving phase of the sources, φ. Values of φ are presented as a comma-separated list within braces, based upon the numbering of the sources. For example, driving two elements with a phase difference of π, $\varphi = \{0, \pi\}$. Measurements were taken for $\varphi = \{0, 0\}$ and $\varphi = \{0, \frac{\pi}{2}\}$, which, from the discussion in Section 2.1, should result in monopolar and dipolar sound fields, respectively. The thermal measurements involved thermal reconstructions, as described in Section 3.4, with the device driven with $f_2 = 2$ Hz. The acoustic measurements involved a 1-axis far-field scan, as described in Section 3.3, performed along the primary axis of the array, with $f_2 = 50$ kHz and $r = 20$ cm.

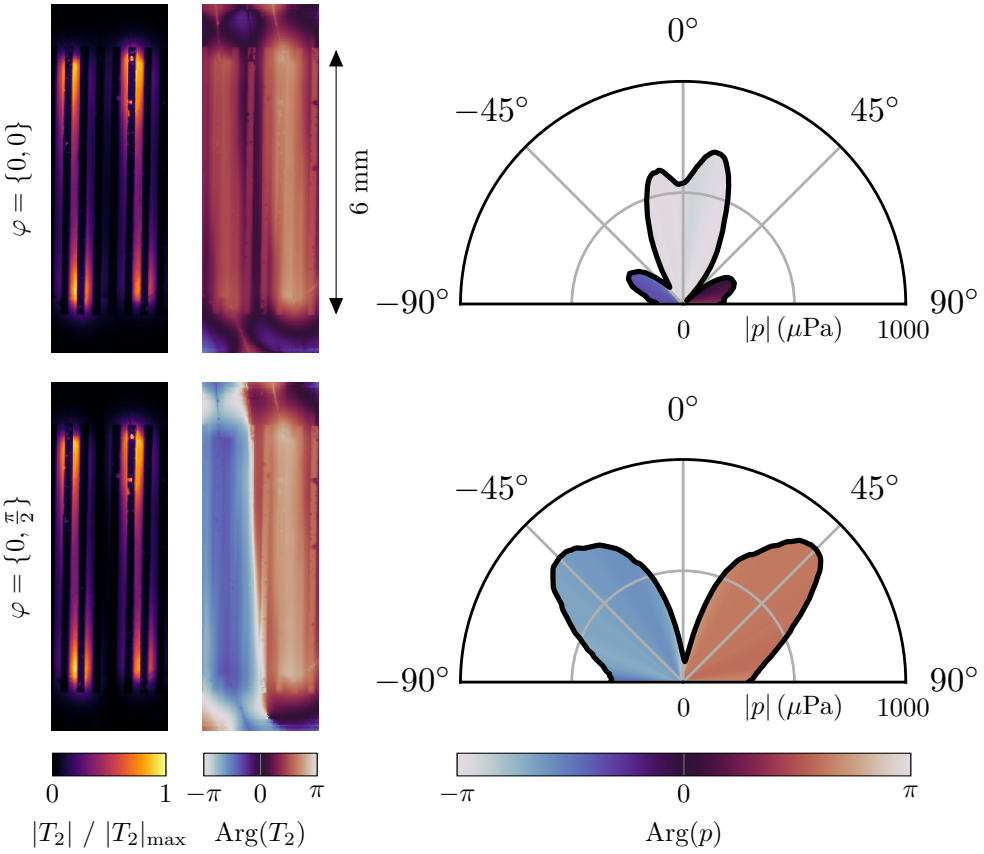

FIGURE 5.5: 2-element thermal and acoustic measurements of the linear array. Shown are the thermal reconstruction ($f_2 = 2\,\text{Hz}$) and far-field sound ($f_2 = 50\,\text{kHz}$) for source phase differences of $\varphi = \{0, 0\}$ (top row) and $\varphi = \{0, \frac{\pi}{2}\}$ (bottom row).

The results of these measurements are shown in Fig. 5.5. The thermal measurements show the elements behaving as independent thermal sources, with the heat dissipation localised to each element. For $\varphi = \{0, 0\}$, the heat dissipation from both elements is in phase. For $\varphi = \{0, \frac{\pi}{2}\}$ the sources are of opposite phase, as expected from the second-harmonic generation. The behaviour seen in the thermal reconstructions is clearly reproduced in the acoustic far-field measurements, with monopolar and dipolar sound fields being observed for $\varphi = \{0, 0\}$ and $\varphi = \{0, \frac{\pi}{2}\}$, respectively. The monopolar case shows a dip in the centre of the main lobe—this is a diffraction-related artefact from the sample mount, as discussed in Chapter 4.

The array was then connected with all 7 elements individually sourced. Each element was driven to dissipate 1 W per element at $f_2 = 16\,\text{kHz}$, with a progressive phase shift of $\Delta\varphi = \pm\frac{\pi}{12}$ per element along the array. 1-axis far-field scans were then performed, with $r = 20\,\text{cm}$. The results of the measurements are shown in Fig. 5.6. It should be noted that the choice of frequency in this case makes the wavelength

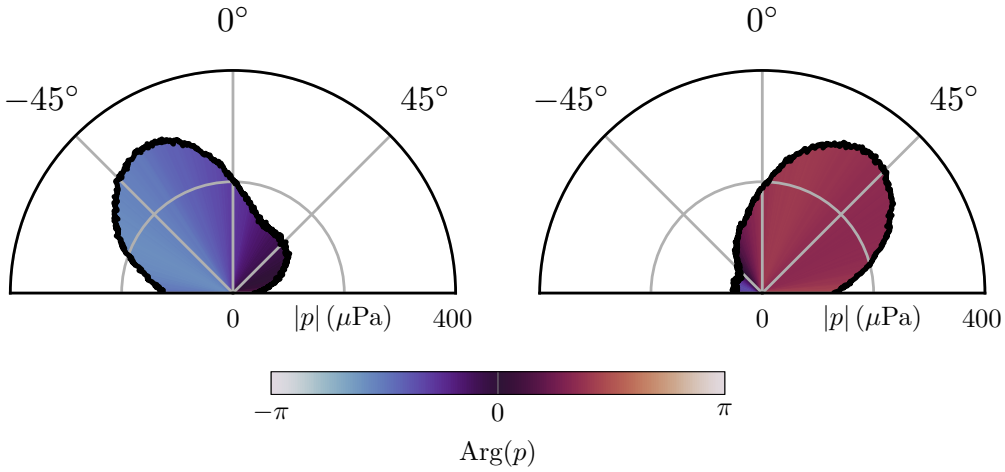

FIGURE 5.6: Beam steering with the 7-element linear array. Shown are far-field sound measurements ($f_2 = 16\,\text{kHz}$) for progressive phase shifts of $\Delta\varphi = -\frac{\pi}{12}$ (left) and $\Delta\varphi = \frac{\pi}{12}$ (right) per element.

greater than the device dimensions. It would therefore normally be expected that the resulting sound would not exhibit any beaming effects. However, as discussed in Chapter 4, the device mount has a noticeable impact on the far-field directivity characteristics. To verify this, the device mount FEM model was used to simulate the sound generation from the mounted array. The simulated data is shown in Fig. 5.7. As can be seen, the mounting results in some focusing of the sound, which can be steered by application of a phase delay. This behaviour is replicated in the experimental data, demonstrating the ability of the array to produce a beam steering effect.

Two-dimensional arrays were also explored. For this purpose, the device shown in Fig. 5.8 was fabricated. This consisted of a graphene monolayer film on an Si/SiO_2 substrate, etched into $1 \times 1\,\text{mm}$ elements with pitch 1.5 mm. Electrical contact was made via $0.25 \times 1.00\,\text{mm}$ Au films (50 nm) deposited on the sides of the elements, such that the exposed graphene films formed elements of dimensions $0.5 \times 1.0\,\text{mm}$. Thermal and acoustic measurements were performed, driving each of the elements at 1 W and varying the phase differences. Thermal measurements were the same as with the linear array. The acoustic measurements involved 2-axis far-field scans, as described in Section 3.3, with $f_2 = 24\,\text{kHz}$ and $r = 20\,\text{cm}$. Five different driving phase patterns were investigated, the results of which are shown in Fig. 5.9. The first set of measurements involved driving all elements in phase to produce a monopolar sound field ($\varphi = \{0, 0, 0, 0\}$, following the element ordering in Fig. 5.8). For the second and third sets, the elements were driven as pairs out of phase to produce dipolar ($\varphi = \{0, \frac{\pi}{2}, 0, \frac{\pi}{2}\}$) and quadrupolar ($\varphi = \{0, \frac{\pi}{2}, \frac{\pi}{2}, 0\}$) sound fields. Finally, the fourth and fifth sets involved driving each element with unique phase, applied

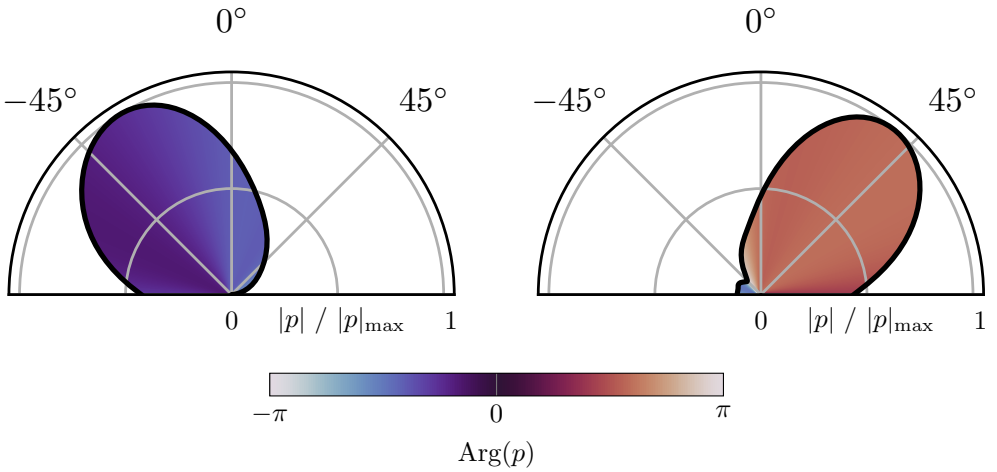

FIGURE 5.7: FEM simulation of beam steering with the 7-element linear array, including the sample mount. Shown are far-field sound measurements ($f_2 = 16\,\text{kHz}$) for progressive phase shifts of $\Delta\varphi = -\frac{\pi}{12}$ (left) and $\Delta\varphi = \frac{\pi}{12}$ (right) per element.

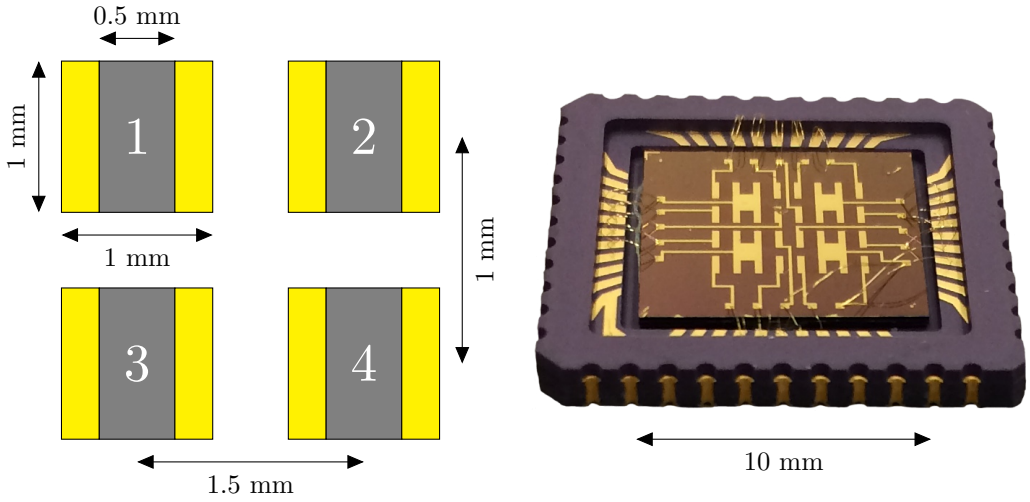

FIGURE 5.8: Device schematic for a 2D planar array. The elements were formed by a graphene monolayer (grey) on an Si/SiO_2 substrate, with 50 nm gold contacts (yellow). **Left:** Device schematic. **Right:** Device photograph. Note that the device shown is a 4×4 array; however, only the central four elements were used in this study.

both clockwise ($\varphi = \{0, \frac{\pi}{4}, \frac{3\pi}{4}, \frac{\pi}{2}\}$) and anti-clockwise ($\varphi = \{0, \frac{3\pi}{4}, \frac{\pi}{4}, \frac{\pi}{2}\}$) around the array to produce an OAM beam. For these measurements, multiple far-field scans were performed with with increasing distance, spanning one acoustic wavelength, to observe the phase rotation of the beam. In each case, the applied phase differences produced the expected sound field, where, as the wave propagates, the phase of the sound rotates in a vortex around a point of zero magnitude at the centre.

The measurements in this section demonstrate that thermoacoustic phased arrays are capable of reproducing standard array behaviour. Attention will now be turned to some unique characteristics they possess due to the nature of the Joule heating mechanism.

5.4 Current Crowding

The thermal measurements of the devices in the previous section show some features that have important consequences for thermoacoustic sound generation via Joule heating. For example, consider a single element of the linear array, where the active film is sandwiched between two contact films, shown in Fig. 5.10. The heat dissipation in this case is clearly not homogeneous; rather, it is focused towards the ends of the film and around the bonding points. This behaviour is elucidated in the simulation in Fig. 5.11. Here electrical and thermal contact is assumed perfect, hence it is not a result of contact resistance between film layers. Instead, it is important to consider the electrical current density, with respect to the local conductivity and geometry. The combined effect of these two factors is commonly referred to as ‘current crowding‘ [99].

The effect of the local conductivity is two-fold. Firstly, the conductivity determines the spatial current density. In the case of the sandwiched contacts, this results in a large current density within the contact material (which has a greater conductivity than the central film), then a greater density towards the ends of the central film as the current seeks to minimise energy. Secondly, the dissipated power is linearly related to the conductivity, such that, for the same current density, the central film will dissipate more power than the contact material. The combination of these effects results in the majority of the power dissipation occurring towards the ends of the central film, where the current density is maximised and the conductivity is minimised. With the experimental thermal data in Fig. 5.10, it is important to note that the effect of the conductivity on the power dissipation is exaggerated by

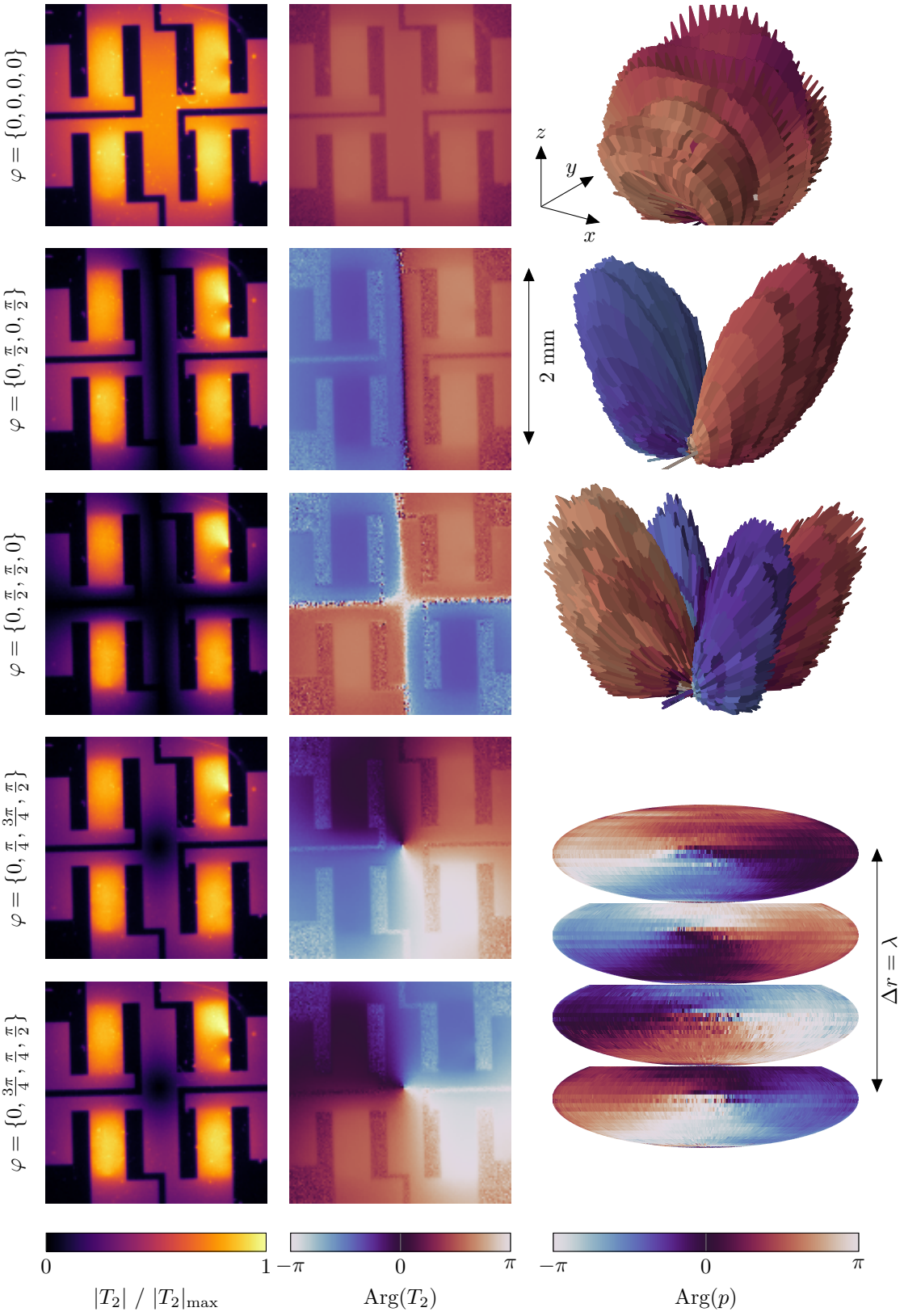

FIGURE 5.9: Thermal and acoustic measurements for the 2×2 array. Shown are the thermal reconstruction ($f_2 = 2\,\mathrm{Hz}$) and 3D far-field sound ($f_2 = 24\,\mathrm{kHz}$) for different applied phase patterns. For the OAM phase patterns, far-field data is shown as stacked orthographic phase plots as a function of measurement distance. This is shown for $\varphi = \{0, \frac{3\pi}{4}, \frac{\pi}{4}, \frac{\pi}{2}\}$ only.

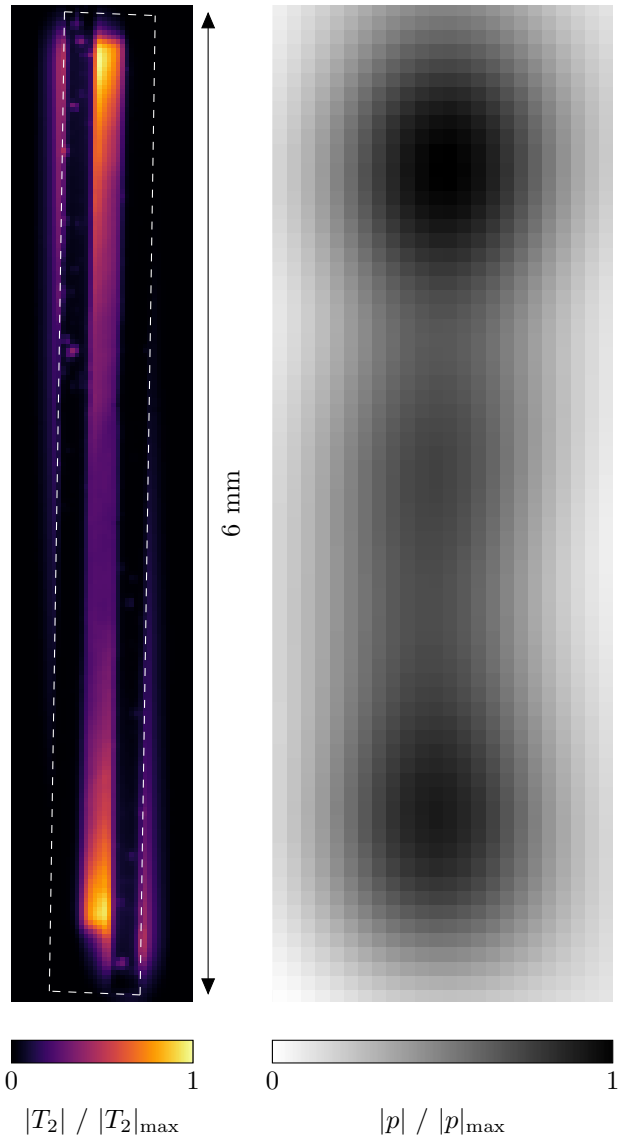

FIGURE 5.10: Inhomogenous heat dissipation in sandwich contact geometry. Shown are the thermal ($f_2 = 2\,\mathrm{Hz}$) and acoustic ($f_2 = 300\,\mathrm{kHz}$) reconstructions of a single element of the linear array. The white dashed line in the thermal reconstruction highlights the outline of the element.

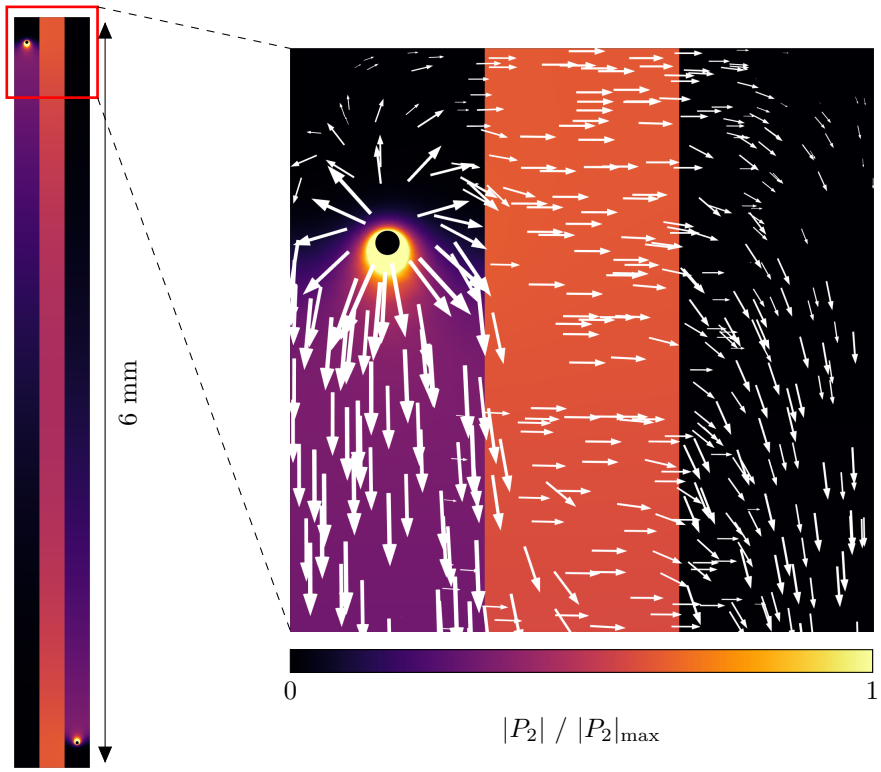

FIGURE 5.11: FEM model of sandwich contact geometry. Model geometry is identical to that in Fig. 5.4, with circular 25 µm diameter terminals in the top-left and bottom-right corners to represent the wire bonds. Only the electrical nature of the device was simulated. The electrical current density and dissipated power are shown at the instant in time corresponding to maximum magnitude. The white arrows represent the electrical current density, with the arrow size normalised by the log of the magnitude. The colour map represents the dissipated power. Note that the colour limits have been adjusted to better visualise heat dissipation throughout the device. This leads to colour saturation around the wire bond.

the measurement technique due to the poor thermal emissivity of the contact material; however, it is apparent from the temperature distribution in the surrounding substrate material that substantial heat is also being generated in the contacts.

The geometrical aspect of current crowding can be explored with a simple model of the junction between one of the wire bonds and the contact film. Consider the system shown in Fig. 5.12. Here a wire, located along the z-axis, of length d_1, radius r_1 and conductivity σ_1 joins a thin film in the xy-plane of thickness d_2, radius r_2, and conductivity σ_2. The free end of the wire is held at potential V and the outer edge of the thin film is held at 0 V, such that a total current I is driven down the wire and out towards the edge of the film. Finite element modelling of this system, shown in Fig. 5.12 for the case where $\sigma_1 = \sigma_2$, shows that the power dissipation is maximised around the base of the wire where it joins the film. This increased power dissipation is a result of the higher current density in this region and the discontinuity in current direction at the inside edge. For a perfect right angle corner, the current density on the inside edge is singular. This is not seen in the numerical simulation due to the finite resolution of the mesh elements. Instead, a finite value is obtained, which continually increases as the mesh resolution is increased. Attempts to solve the system analytically, by replacing the corner with a small arc and using conformal mapping, are also unsuccessful in finding the current density distribution [100]. Obviously, a perfect right angle is not a realistic representation of the experimental case. Outside of the singular region, there will be further current crowding around the base of the junction due to the cylindrical geometry and the divergence of the current away from this point. This permits some additional insight. Referring back to Fig. 5.12, the current density in the wire, excluding the immediate vicinity of the junction, will be

$$\boldsymbol{j}_1 = -\frac{I}{\pi r_1^2}\hat{\boldsymbol{z}}\,.$$

Since the current diverges from the junction, the current density in the thin film will be radially dependent. If $d_2 \ll r_1$, such that the current is uniform across the thickness of the film, the current density is then

$$\boldsymbol{j}_2(r) = \frac{I}{2\pi d_2 r}\hat{\boldsymbol{r}}\,,$$

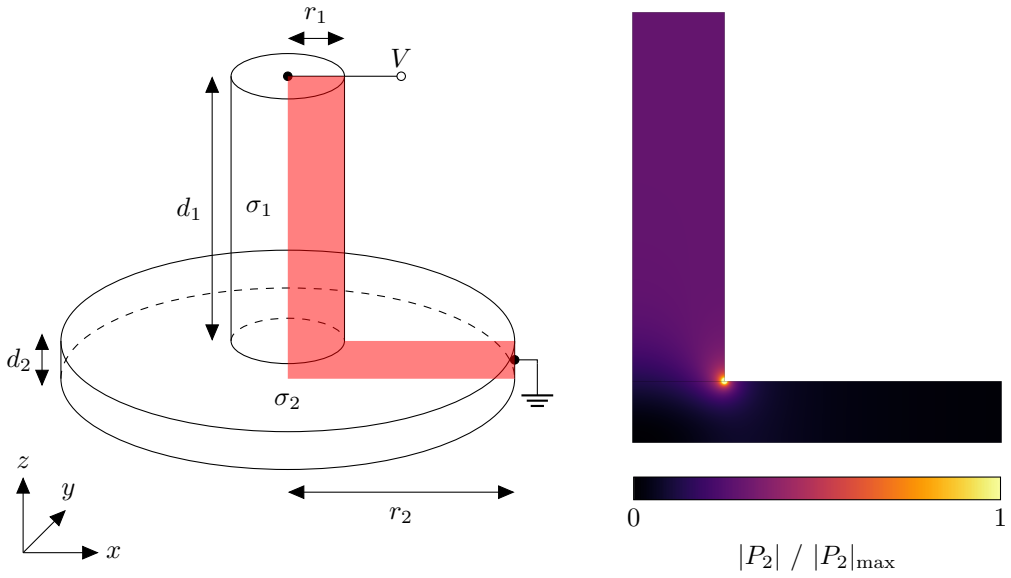

FIGURE 5.12: Current crowding in a wire bond. **Left:** Model schematic and parameters. Red region highlights the simulated region shown. **Right:** FEM simulation of the heat dissipation in the highlighted region. $r_1 = 7.5$ mm, $r_2 = 30$ mm, $d_1 = 35$ mm, $d_2 = 5$ mm. Note that the colour limits have been adjusted to better visualise heat dissipation throughout the device. This leads to colour saturation around the crowding region.

which, again, is valid up until the vicinity of the junction. Comparing the power dissipation in both the wire and the film,

$$P_1 = \frac{j_1^2}{\sigma_1} = \frac{I^2}{\left(\pi r_1^2\right)^2 \sigma_1},$$
$$P_2 = \frac{I^2}{\left(2\pi d_2 r\right)^2 \sigma_2},$$

hence, for $r = r_1$,

$$\frac{P_2}{P_1} \approx \frac{1}{4}\frac{\sigma_1}{\sigma_2}\left(\frac{r_1}{d_2}\right)^2. \tag{5.2}$$

In the experimental case ($r_1 = 12.5$ µm, $d_2 = 50$ nm, $\sigma_1 \approx \sigma_2$), this leads to a factor difference of $\sim 10^4$. For the linear array measurements in Fig. 5.5 and Fig. 5.6, the effects of current crowding on the generated sound field are largely irrelevant since, in this case, the acoustic wavelength is much larger than the device geometry. This is not always the case. Consider the square device from Chapter 4, shown in Fig. 5.13. Thermal measurements and simulations of this device, shown in Fig. 5.14, highlight the potential issue with using such a contact geometry for a thermophone. As can be seen, due to the divergence of the current density away from the corner contacts, the heat dissipation is primarily localised in the corners of the film. As such, this contact arrangement is unsuitable if a square source is intended. To avoid

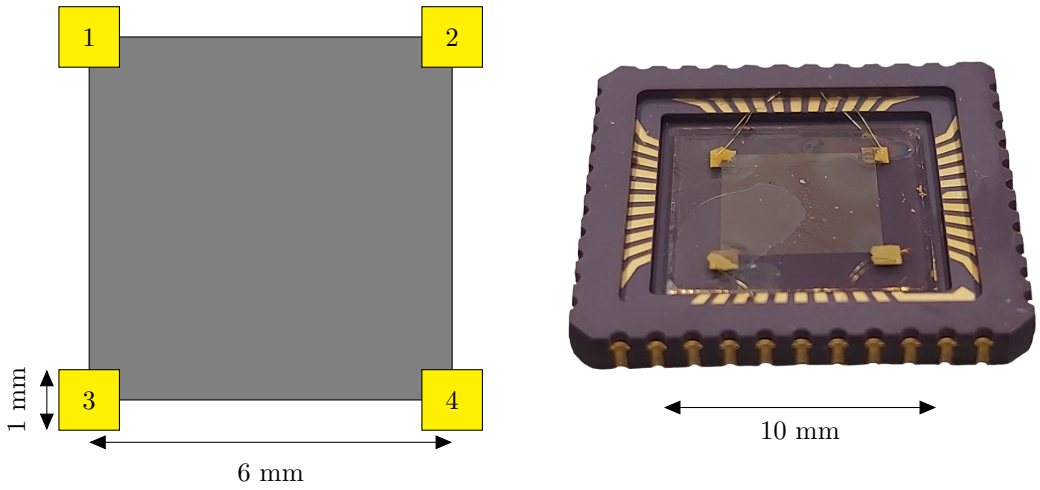

FIGURE 5.13: Square device. An 80 nm-thick ITO film (grey) with 5/100 nm Cr/Au contacts (yellow). **Left:** Device schematic. **Right:** Device photograph.

this, contacts must run along the entire length of the edges, such that the current density throughout the film is uniform. This is demonstrated by the FEM model in Fig. 5.15. If this is not possible, the effects of current crowding can also be mitigated by tapering or rounding sharp edges in the film geometry.

Current crowding may be considered a limitation in electronic applications, with many works aiming to mitigate its effects [99]. However, for thermophones it presents a unique opportunity to greatly simplify device design, particularly for arrays of sources. Consider again the square device. The heat dissipation occurs in the corners, with little elsewhere. Acoustically, then, this device behaves as four sub-wavelength, point-like sources, from which there is the possibility to create a phased array using a single film. To demonstrate this, contacts 1 and 4 were individually driven with equal magnitudes and a phase difference of $\frac{\pi}{2}$. Contacts 2 and 3 were connected to ground. Thermal ($f_2 = 2\,\text{kHz}$) and acoustic ($f_2 = 300\,\text{kHz}$) reconstructions were then performed, as well as a 2-axis far-field scan ($f_2 = 24\,\text{kHz}$). The results of these measurements are shown in Fig. 5.16. The thermal reconstruction clearly shows localised heating around the contacts, with the heat dissipated at the two source contacts being of opposite phase. There is also heat dissipation at the ground contacts, although the magnitude is lower due to there being two grounding points for each source. It is also interesting to note that the heat dissipation at the ground points occurs at a phase unique to the two sources, leading to phase vortices in the bulk of the film. The reason for this will be addressed in detail in Section 5.5. In this case, however, these additional features will have negligible impact on the sound field, since the magnitude of the heating in these regions is low. This behaviour is also seen in the acoustic reconstruction and far-field map, which,

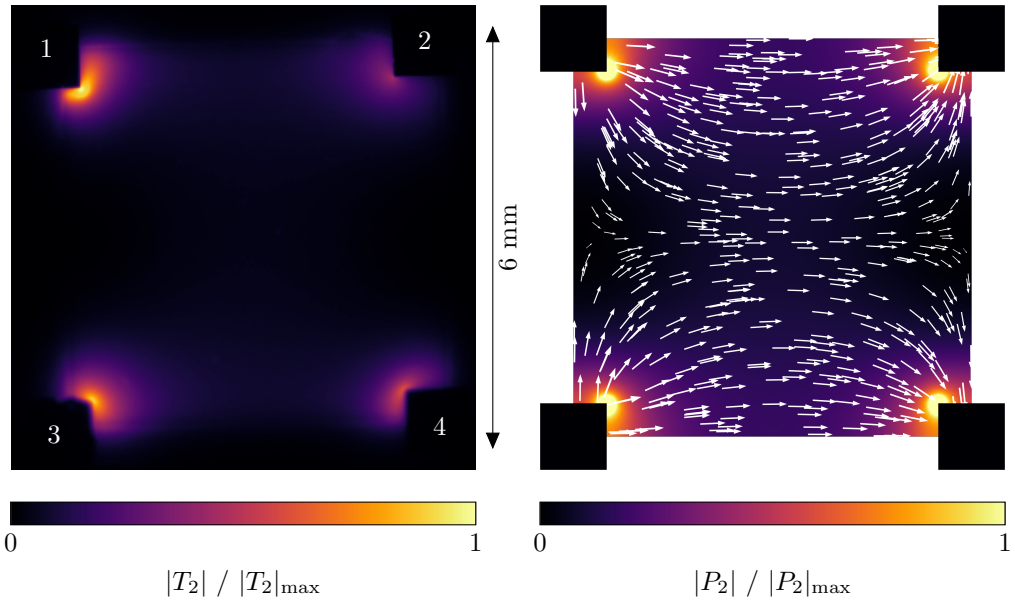

FIGURE 5.14: Current crowding in the square device. Contacts 1 and 3 were connected to the same source, with contacts 2 and 4 connected to ground. **Left:** Thermal reconstruction ($f_2 = 1\,\text{Hz}$). **Right:** FEM simulation of power dissipation and current density arrow plot, with arrow size normalised to the log of the magnitude. Note that the colour limits have been adjusted to better visualise heat dissipation throughout the device. This leads to colour saturation around the crowding regions.

ignoring the finer features, show that the resulting sound field is largely dipolar.

Up to this point, all of the experimental demonstrations of current crowding have involved devices consisting of multiple materials. To demonstrate that current crowding can be purely a geometrical effect, a device consisting of a single gold film with gold wire bonds attached was fabricated, shown in Fig. 5.17. The edges of the gold film were connected to ground via many wire bonds, to minimise crowding in these regions. Seven wire bonds were then placed in the centre, with roughly equal pitch, and then individually sourced. From (5.2), it is expected that the majority of the heat dissipation occurs around the base of the central wire bonds, such that they form a linear array of point sources. To verify this point source behaviour, thermal ($f_2 = 2\,\text{Hz}$) and acoustic ($f_2 = 300\,\text{kHz}$) reconstructions were performed whilst driving bonds 3 and 5 as a dipole, shown in Fig. 5.18. In both measurements it is clearly seen that the heating is localised around the bonding points, resulting in the junctions behaving as acoustic point sources. To demonstrate the capability of this device as a phased array, all seven elements were then connected and driven with progressive phase shift of $\Delta\varphi = \pm\frac{\pi}{12}$ and 1-axis far-field scans, with $f_2 = 16\,\text{kHz}$ and $r = 20\,\text{cm}$, were performed, as with the linear array. The results of these measurements are shown in Fig. 5.19. In both cases, the driving conditions reproduce

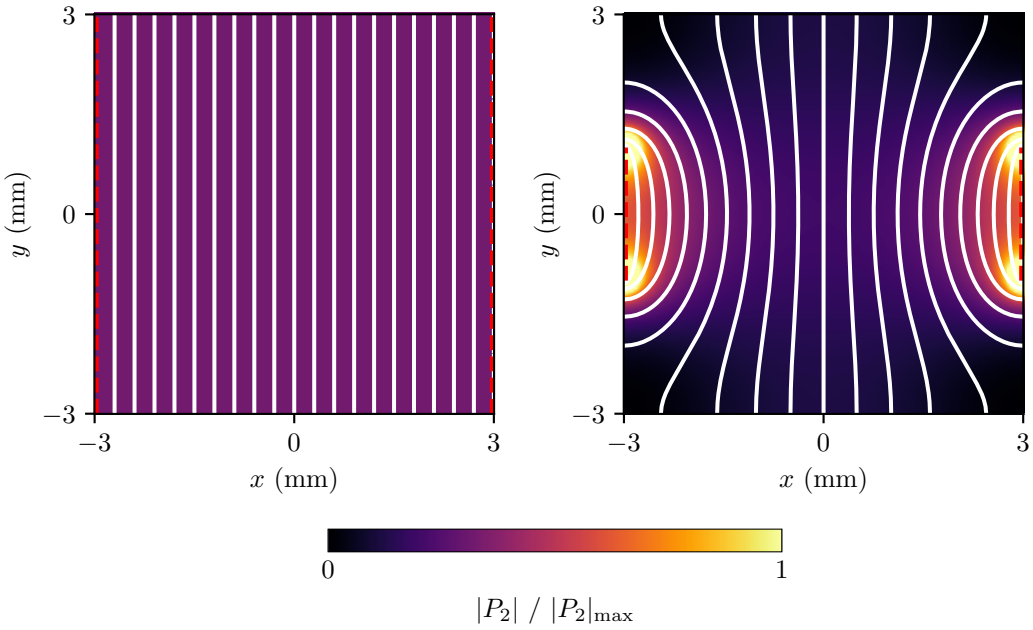

FIGURE 5.15: FEM electrical simulation of crowding in a square film due to contact positions. Shown are colour plots of the dissipated power, with white isopotential lines. Red dashed lines indicate the locations of the contacts. **Left:** Electrical contacts run along the entirety of both edges, leading to homogeneous power dissipation throughout the film. **Right:** Contacts only run partially along each edge, leading to current crowding at the ends of the contacts. Note that the colour limits have been adjusted to better visualise heat dissipation throughout the device. This leads to colour saturation around the crowding regions.

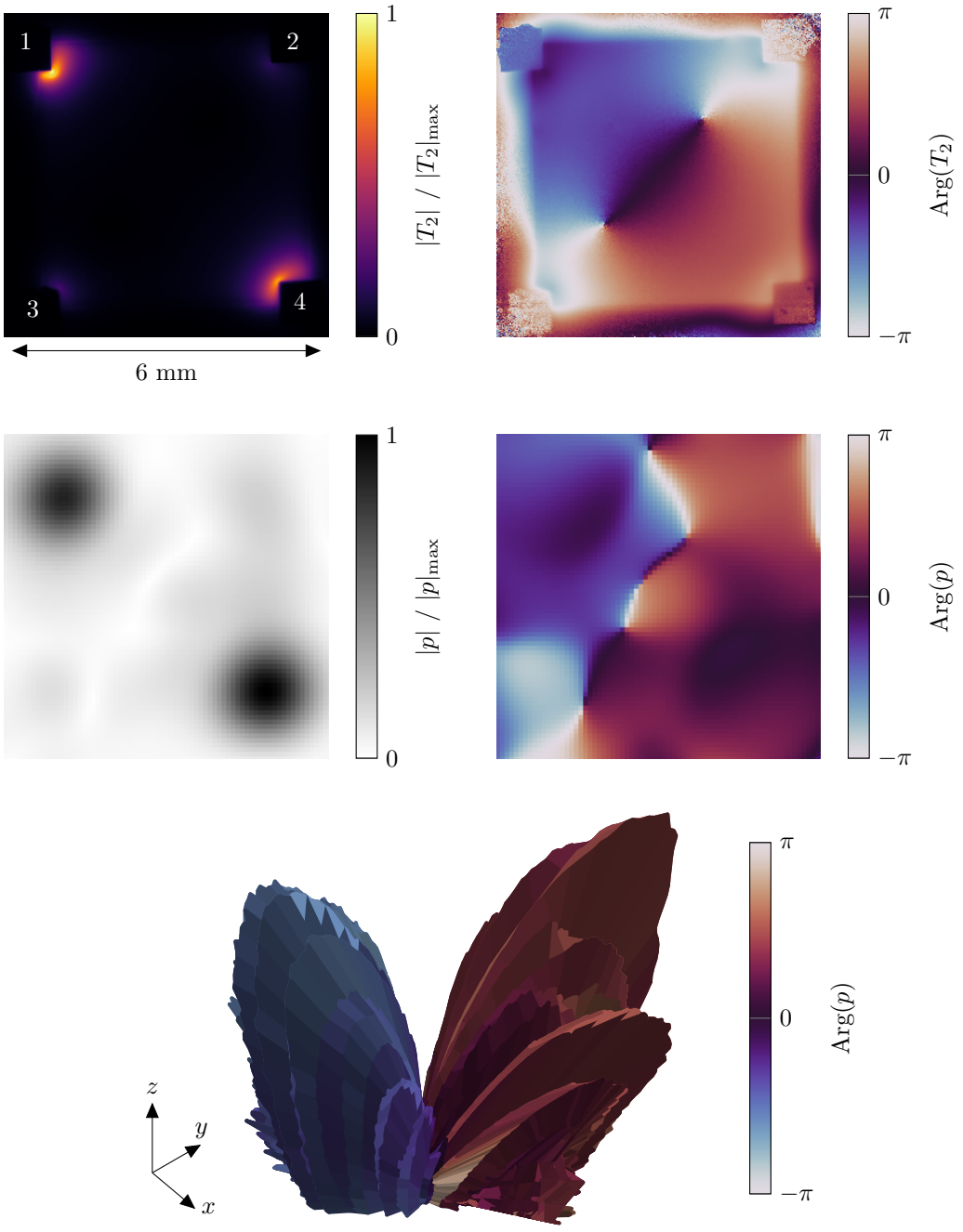

FIGURE 5.16: Dipolar sound from current crowding in the square device. Contacts 1 and 4 were driven with equal magnitude and phase difference of $\frac{\pi}{2}$. Contacts 2 and 3 were grounded. **Top row:** Thermal reconstruction ($f_2 = 2\,\text{Hz}$). Blue and red rectangles indicate the locations of the source contacts, driven with equal magnitude and $\frac{\pi}{2}$ phase difference. **Middle row:**, Acoustic reconstruction ($f_2 = 300\,\text{kHz}$). **Bottom row:**, Acoustic far-field ($f_2 = 24\,\text{kHz}$).

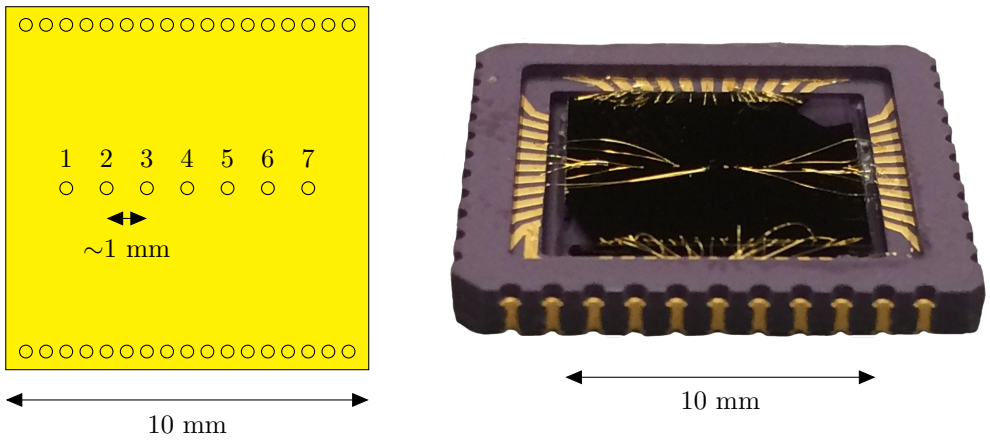

FIGURE 5.17: A linear phased array based upon current crowding in wire bonds. A 50 nm thick gold film with electrical contact made via 25 µm diameter gold wires. The central wire bonds form the elements of the linear array and are driven by individual sources. The bonds on the outer edges are all connected to the ground point. **Left:** Device schematic. Gold wires are indicated by circles. The density of the wires at the edges is much greater than shown. **Right:** Device photograph.

similar behaviour to that seen with the linear array of individual elements.

5.5 Electrical Coupling

A common problem with arrays is electrical connectivity. Since each element needs to be individually addressable, as the number of elements grows, so does the number of connections required. One way to mitigate this is by allowing elements to share a common connection, typically a ground rail. With traditional phased arrays, the inclusion of common ground rails can lead to additional distortion of the sound field due to electrical signals travelling between elements [95]. With a thermoacoustic phased array, the sound output depends on the square of the input signal, so the inclusion of a common ground rail may lead to further effects not seen in traditional devices.

To investigate this concept with thermoacoustic phased arrays, the device in Fig. 5.20 was fabricated. This consisted of 16 0.3×6.0 mm graphene monolayer elements, with 100 nm sandwiched gold contacts, on an Si/SiO_2 substrate. This array was split into two halves, with elements 1-8 and 9-16 sharing common ground rails. The effect of a common ground rail was tested by creating monopole and dipole pairs using elements that were either electrically isolated from each other or electrically coupled by a common ground. For the uncoupled case, elements 4 and 9 were used.

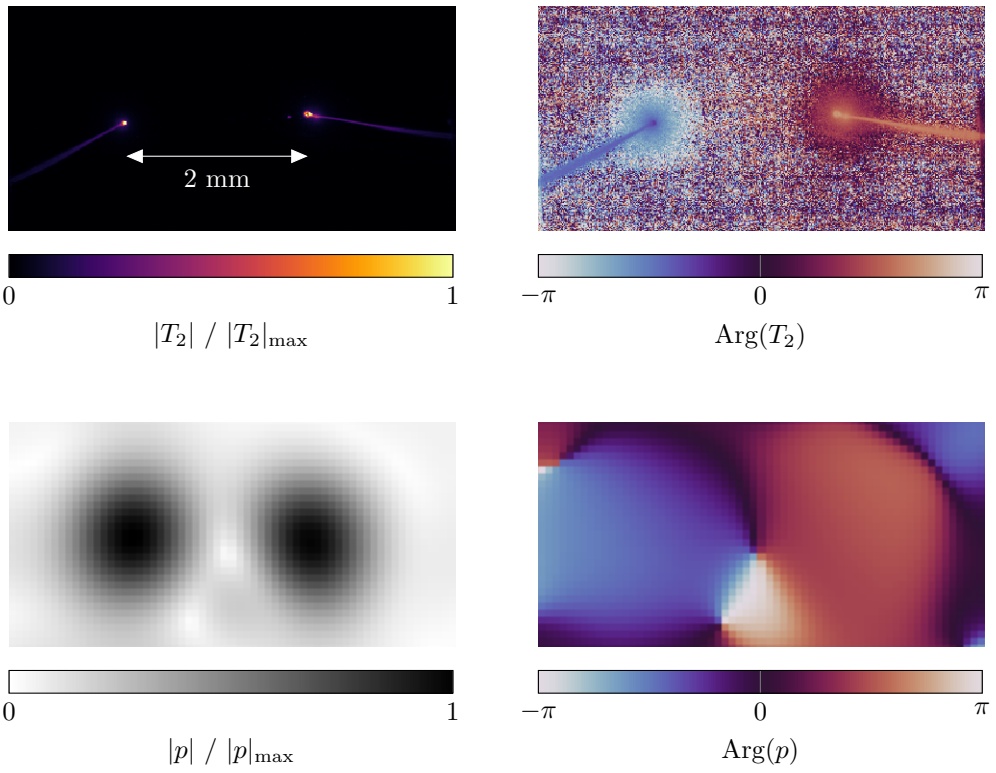

FIGURE 5.18: Thermal (top row, $f_2 = 2\,\text{kHz}$) and acoustic (bottom row, $f_2 = 300\,\text{kHz}$) reconstructions of the linear wire bond array, driving two elements with $\varphi = \{0, \frac{\pi}{2}\}$.

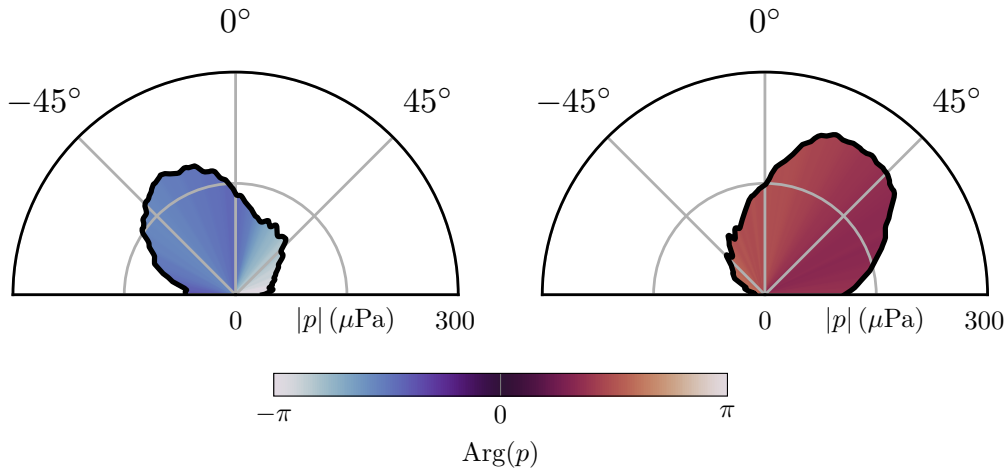

FIGURE 5.19: Beam steering using the linear wire bond array. Each source wire was driven with the same magnitude ($f_2 = 16\,\text{kHz}$), with a $\pm\frac{\pi}{12}$ progressive phase delay across the elements, *c.f.*, Fig. 5.6.)

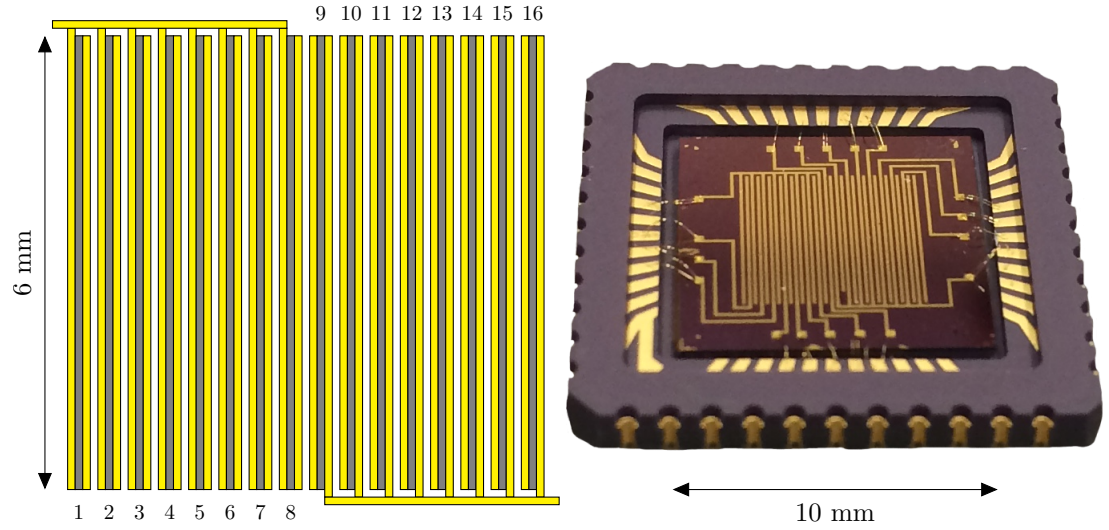

FIGURE 5.20: A 16-element linear array with common ground rails. The elements (0.3×6.0 mm) were formed by a graphene monolayer (grey) on an Si/SiO_2 substrate, with 50 nm gold contacts (yellow). Elements 1-8 and 9-16 share common ground rails. **Left:** Device schematic. **Right:** Device photograph.

For the coupled case, elements 4 and 8 were used. In each case, thermal reconstructions ($f_2 = 2$ Hz) and 1-axis far-field sound measurements ($f_2 = 50$ kHz) were performed for both $\varphi = \{0, 0\}$ and $\varphi = \{0, \frac{\pi}{2}\}$, with 1 W power dissipation per element. The results of these measurements are shown in Fig. 5.21. In the uncoupled case, the device behaves as expected, with the two elements acting as individual sources capable of reproducing the desired monopolar and dipolar sound fields. The sound fields show some asymmetry; however, it is clear from the thermal data that this is due to the contribution of the ground rails to the sound field, resulting in asymmetric source shapes. The coupled elements do not show the same behaviour. This is particularly apparent for the $\varphi = \{0, \frac{\pi}{2}\}$ case, where the vortex in the thermal phase data indicates the presence of a source with a third phase component, which, in this case, is located at the common ground rail. The appearance of a third phase component was also seen previously with the square device, Fig. 5.16, when attempting to produce a dipole, where the heat dissipation at the ground contacts had a unique phase to the two source contacts.

The behaviour of the coupled case can be explained with a simple circuit model. Consider the circuit shown in Fig. 5.22. The circuit consists of three electrically conductive branches of conductance $G_{1,2,3}$. The thermoacoustic array elements are represented by conductances G_1 and G_2, and the ground rail by G_3. The choice to use conductances ($G = \frac{1}{R}$) here, rather than resistances, is purely for mathematical convenience. The two array elements are driven by separate voltage sources, V_1 and V_2, with G_3 connected to ground and held at 0 V. The Joule power dissipated in

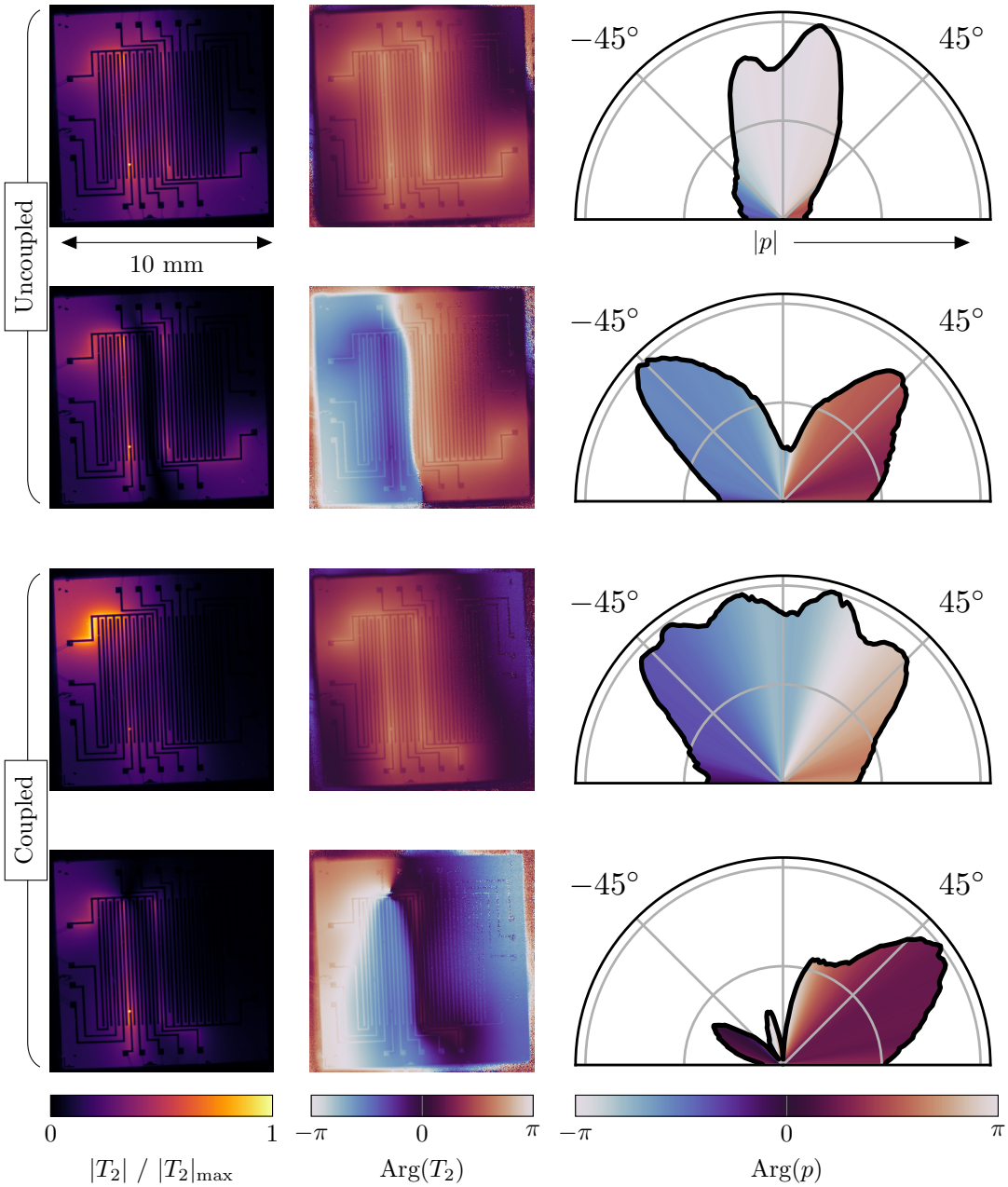

FIGURE 5.21: Electrical coupling in thermoacoustic phased arrays. Thermal reconstructions ($f_2 = 2\,\text{Hz}$) and far-field sound measurements ($f_2 = 50\,\text{kHz}$) of the 16-element linear array. Shown are measurements for driving elements 4 and 9 (uncoupled) with $\varphi = \{0, 0\}$ (top row) and $\varphi = \{0, \frac{\pi}{2}\}$ (bottom row). The same measurements are then shown for elements 4 and 8 (coupled).

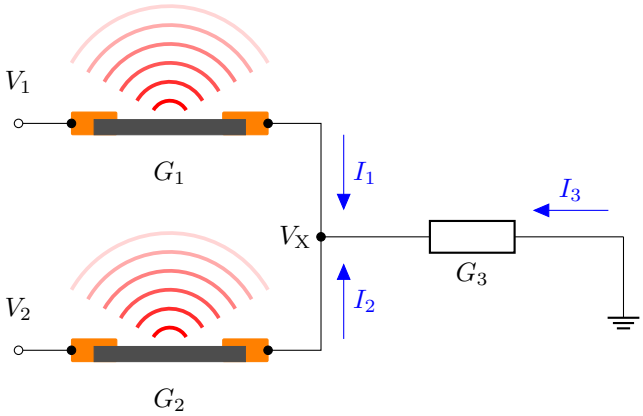

FIGURE 5.22: Circuit model for a two-element thermophone array with a common ground rail. The two array elements are represented by conductances $G_{1,2}$, and the common ground by conductance G_3. The array elements are driven by two alternating sources, and the common ground branch is terminated at 0 V.

each of the branches must then be determined, as this is what will produce the resulting sound field.

From Kirchhoff's junction rule,

$$I_1 + I_2 + I_3 = 0\,. \tag{5.3}$$

From Ohm's law, the currents in the branches are

$$\begin{aligned} I_1 &= G_1\,(V_1 - V_\mathrm{X})\ , \\ I_2 &= G_2\,(V_2 - V_\mathrm{X})\ , \\ I_3 &= G_3\,(V_3 - V_\mathrm{X}) \\ &= -G_3 V_\mathrm{X}\,, \end{aligned} \tag{5.4}$$

where $V_3 = 0$ and V_X is the voltage at the junction of the branches. V_X can then be eliminated by combining (5.3) and (5.4),

$$V_\mathrm{X} = \frac{G_1 V_1 + G_2 V_2}{\Sigma}\,,$$

where $\Sigma \equiv G_1 + G_2 + G_3$. The currents can now be recast in terms of measurable experimental parameters,

$$\begin{aligned} I_1 &= \left(G_1 - \frac{G_1^2}{\Sigma}\right) V_1 - \frac{G_1 G_2}{\Sigma} V_2 \,, \\ I_2 &= \left(G_2 - \frac{G_2^2}{\Sigma}\right) V_2 - \frac{G_1 G_2}{\Sigma} V_1 \,, \\ I_3 &= -\frac{G_1 G_3}{\Sigma} V_1 - \frac{G_2 G_3}{\Sigma} V_2 \,. \end{aligned}$$

In the limit $G_3 \to \infty$,

$$\begin{aligned} &I_1 \to G_1 V_1 \,, \quad I_2 \to G_2 V_2 \\ &I_3 \to -G_1 V_1 - G_2 V_2 \,, \end{aligned}$$

where it is clearly seen that the junction rule holds. Since the currents in each branch involve both V_1 and V_2, the Joule power cannot be computed via IV, but only through I^2/G. As such, the powers in the three branches are

$$P_1 = \left(1 - \frac{G_1}{\Sigma}\right)^2 G_1 V_1^2 + \left(\frac{G_2}{\Sigma}\right)^2 G_1 V_2^2 + 2\left(\frac{G_1 G_2}{\Sigma^2} - \frac{G_2}{\Sigma}\right) G_1 V_1 V_2 \,, \tag{5.5}$$

$$P_2 = \left(\frac{G_1}{\Sigma}\right)^2 G_2 V_1^2 + \left(1 - \frac{G_2}{\Sigma}\right)^2 G_2 V_2^2 + 2\left(\frac{G_1 G_2}{\Sigma^2} - \frac{G_1}{\Sigma}\right) G_2 V_1 V_2 \,, \tag{5.6}$$

$$P_3 = \left(\frac{G_1}{\Sigma}\right)^2 G_3 V_1^2 + \left(\frac{G_2}{\Sigma}\right)^2 G_3 V_2^2 + 2\frac{G_1 G_2}{\Sigma^2} G_3 V_1 V_2 \,. \tag{5.7}$$

Here it is seen that, due to the electrical connection, all three branches contain both V_1^2 and V_2^2 source terms, as well as an additional $V_1 V_2$ term, since the sound output is proportional to the power, rather than the voltage, *i.e.*, it is nonlinear with respect to the source signal. This additional, 'phantom' source is present throughout the circuit, and is not localised to a specific branch. It is important to also note that, if V_1 and V_2 differ in frequency or phase, the $V_1 V_2$ term will occur at frequencies/phases that are unique from both V_1^2 and V_2^2. This is a direct consequence of the second harmonic generation, as discussed in Section 2.1.

The impact of the phantom source can now be modelled when driving two elements of the array to produce a dipole-like sound output. The electric current and power dissipation in each branch as a function of time is shown in Fig. 5.23. For the case where the ground rail has high conductance, *i.e.*, it is a short circuit, the power dissipation in the two array elements shows the expected dipolar output. This is apparent from (5.5), (5.6) and (5.7) since, as $G_3 \to \infty$, $\Sigma \to \infty$, such that P_1 and P_2

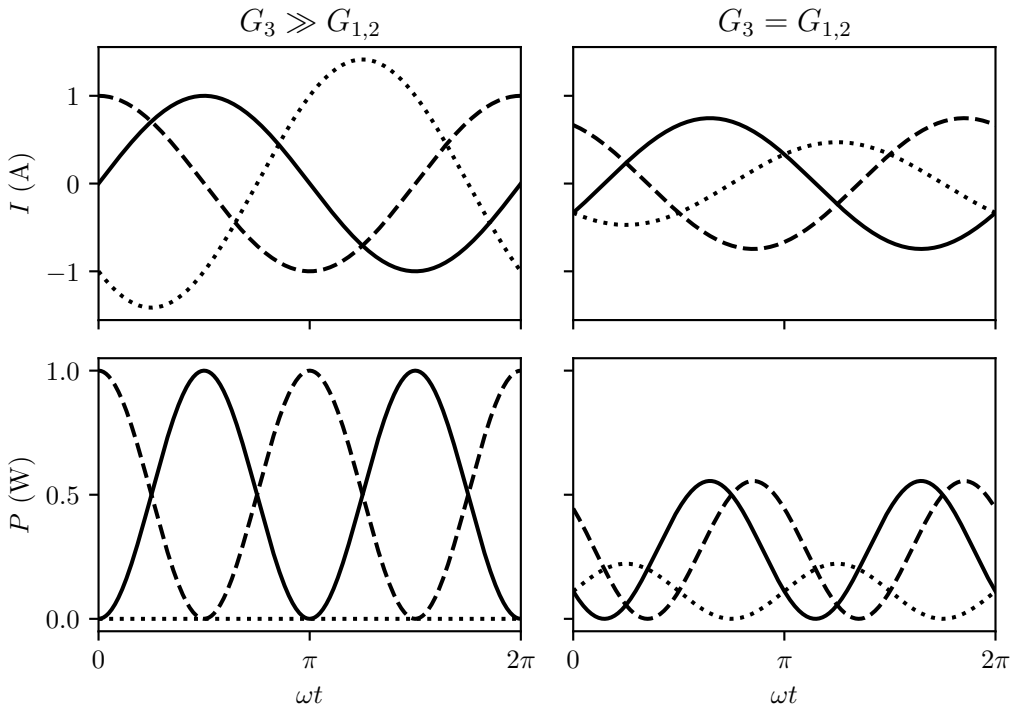

FIGURE 5.23: Electric current and power dissipated in each branch of a two-element array with a common ground rail. Here $|V_{1,2}| = 1\,\mathrm{V}$, with phase difference $\frac{\pi}{2}$ and $G_{1,2} = 1\,\Omega^{-1}$. Shown for $G_3 \gg G_{1,2}$ (left) and $G_3 = G_{1,2}$ (right). Data are plotted as solid lines for branch 1, dashed lines for branch 2, and dotted lines for branch 3.

will only contain V_1^2 and V_2^2 terms, respectively, with $P_3 \to 0$. As the conductance of the ground rail is decreased, the output becomes less dipolar as P_1 and P_2 now also contain terms relating to the other source and the phantom. There is also significant power dissipation in the ground rail itself, which occurs at a different phase to either array element. The unique phase can be seen in the electric current, where it is apparent that, at certain points in the cycle, there is also current flow between the two source branches (due to the opposing signs of I_1 and I_2, referencing the directions in Fig. 5.22), as well as the common ground. Experimentally, electrical measurements found that the device in Fig. 5.20 had a ground rail with $G_3 \approx 10G_{1,2}$. Since the rail was of a similar thin-film nature to the elements themselves, it could also contribute to the sound field. This resulted in significant heat dissipation in the ground rail at a unique phase, which is the cause of the vortex seen in Fig. 5.21, as well as the non-dipolar sound field. However, it is important to note that, even if the ground rail itself does not contribute to the sound field, the phantom source is also present in the array elements themselves, altering their phase. This will now be shown experimentally.

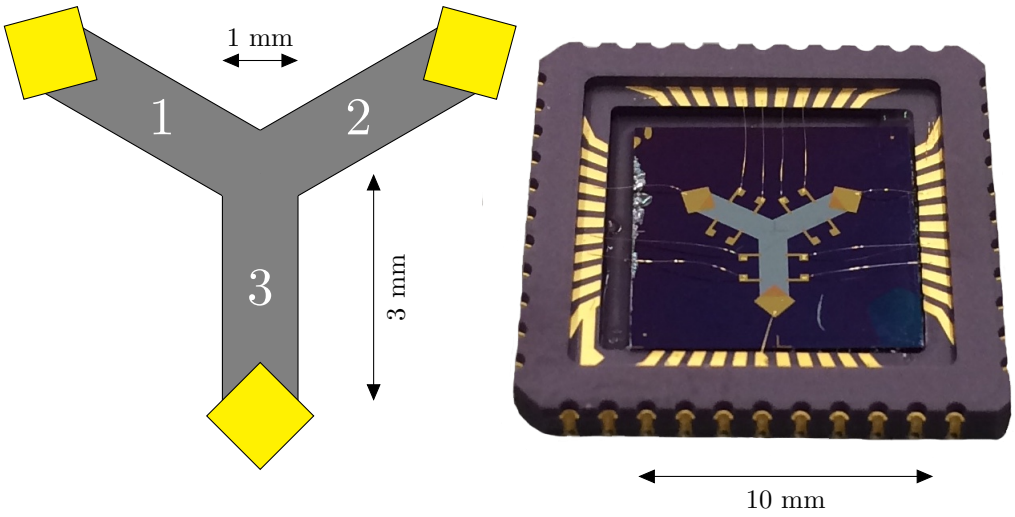

FIGURE 5.24: Three-branch device. A 30 nm zinc film (grey) with 5/100 nm Cr/Au contacts (yellow). **Left:** Device schematic. **Right:** Device photograph.

To demonstrate the universal nature of the phantom source, a new device design, shown in Fig. 5.24, was fabricated. This device consisted of a 30 nm zinc film, patterned into three radiating branches of dimensions $1 \times 3\,\text{mm}$, on an Si/SiO_2 substrate with 5/100 nm Cr/Au contacts. Since each branch was nominally identical ($G_1 = G_2 = G_3$), this produced measurable heat dissipation in each branch. As an initial test, branches 1 and 2 were individually sourced at 1 W, with $\varphi = \{0, \frac{\pi}{2}\}$, and branch 3 connected to ground. A thermal reconstruction ($f_2 = 2\,\text{Hz}$) was then performed, the results of which are shown in Fig. 5.25. The results clearly show that the heating in each branch occurs at a unique phase, in accordance with the circuit model. To further investigate the heat dissipation in this device, V_1 and V_2 were then driven at $f_1 = 1\,\text{Hz}$ and $f_2 = 4\,\text{Hz}$, respectively, with no phase difference. Here the subscript refers to the source number, rather than harmonics of the source frequency. From the circuit model, a difference in frequency of the sources results in the V_1^2, V_2^2 and V_1V_2 terms in the dissipated power occurring at unique frequencies ($V_1^2 \to 2f_1$, $V_2^2 \to 2f_2$, $V_1V_2 \to f_2+f_1, f_2-f_1$), allowing each term to be measured in isolation. Thermal reconstructions were then performed at each of these frequencies to determine the spatial distribution of the heating. The thermal reconstructions are shown in Fig. 5.26. While the V_1^2 and V_2^2 power terms are dominant in their respective branches, the phantom source is present throughout all branches. In addition to this, the phantom source has a dipolar nature, with the source and ground branches being out of phase. The phantom source therefore affects the performance of coupled array elements, regardless of whether the coupling pathway (ground rail) can produce sound or not.

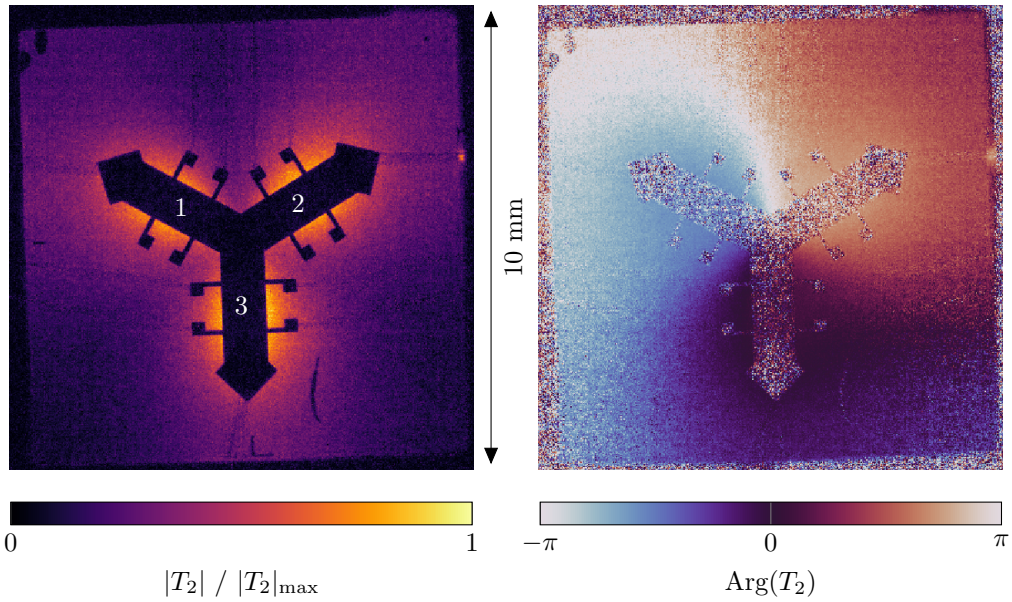

FIGURE 5.25: Thermal reconstruction ($f_2 = 2\,\text{Hz}$) of the three-branch device, with branches 1 and 2 driven with $\varphi = \{0, \frac{\pi}{2}\}$, and branch 3 connected to ground.

It was shown in Section 2.1 that the effects of second harmonic generation could be minimised by applying a DC bias to the source voltage, such that the heat dissipation occurs primarily at the fundamental of the source. This is also the case for the phantom source. To verify this, the dipole pair experiment in Fig. 5.21 was repeated with an additional DC bias. Elements 4 and 8 were again driven with $\varphi = \{0, \frac{\pi}{2}\}$ to dissipate 1 W, with the source DC offset set to double the magnitude of the oscillating source. A thermal reconstruction was then performed at $f_1 = 1\,\text{Hz}$. The results of this measurement are shown in Fig. 5.27, compared to the unbiased case. Without the DC bias, the thermal reconstruction shows a vortex in the phase, indicating the presence of more than two unique phases in the dissipated heat. Application of a DC bias successfully removes this vortex, recovering the intended dipolar heat dissipation.

The effect of the phantom source can also be negated with careful consideration of the applied signals. For example, consider the two-element array with common ground rail (Fig. 5.22). Here it is assumed that the ground rail itself does not contribute to the sound and that the two array elements are nominally identical, apart from their conductance. If a dipolar sound field is desired, then

$$P_1 + P_2 = 0\,,$$

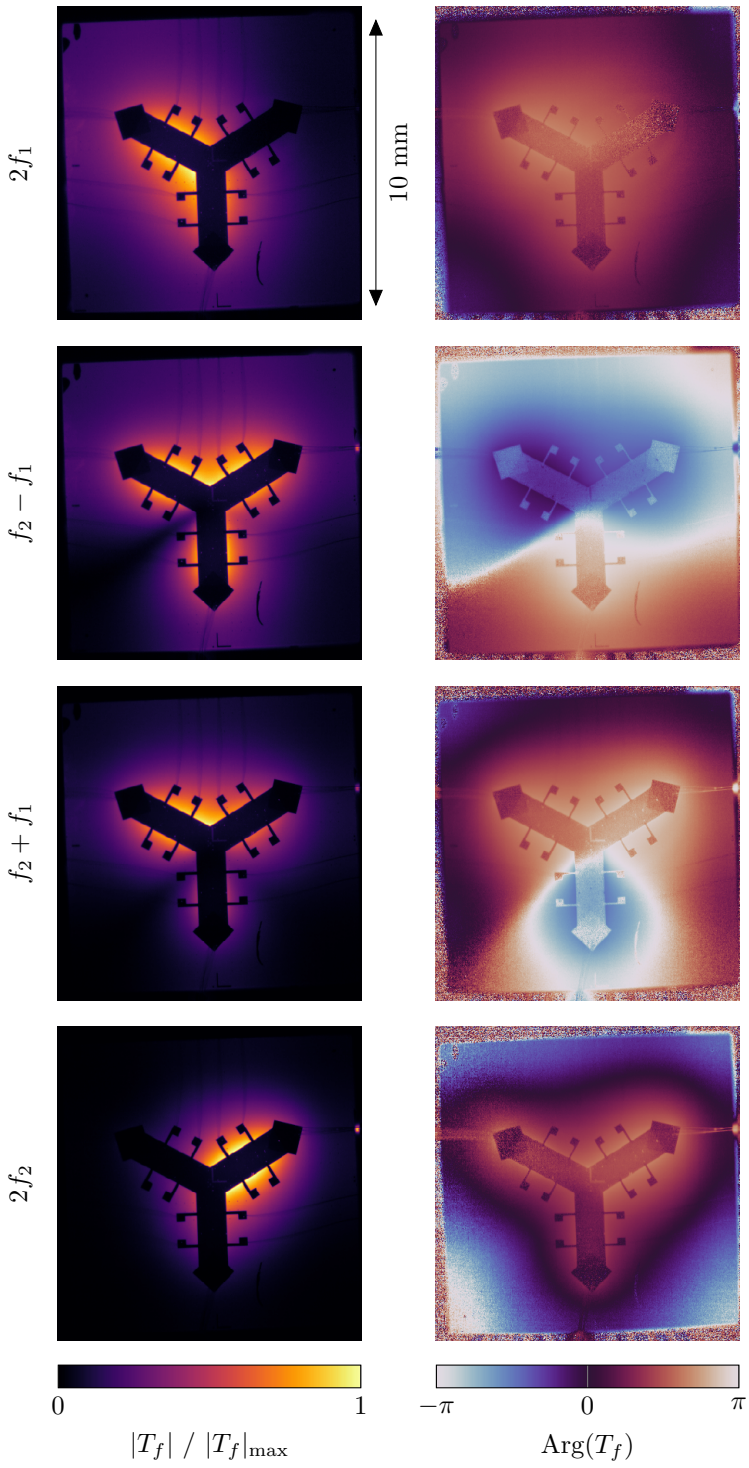

FIGURE 5.26: Frequency isolation of phantom source in the three-branch device. Branches 1 and 2 are driven at different frequencies ($f_1 = 1\,\mathrm{Hz}$ and $f_2 = 4\,\mathrm{Hz}$, where the subscript refers to the source at each branch), with branch 3 connected to ground. Thermal reconstructions are shown for each of the frequencies at which heat dissipation occurs.

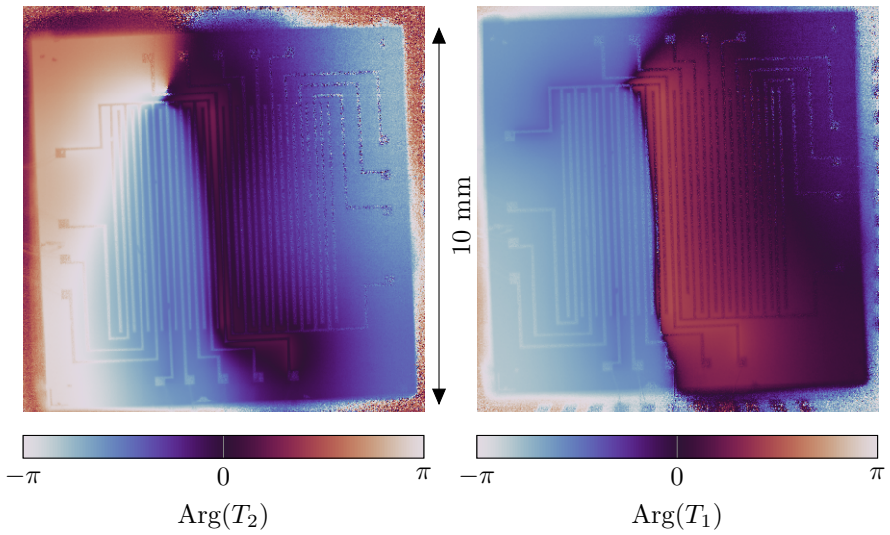

FIGURE 5.27: Elimination of the phantom source via a DC bias. Shown are thermal phase reconstructions of the coupled linear array, with elements 4 and 8 driven with a phase difference of $\frac{\pi}{2}$. **Left:** Unbiased case, $f_2 = 2\,\text{Hz}$. **Right:** Biased case, $f_1 = 1\,\text{Hz}$.

so, substituting (5.5) and (5.6),

$$\left[\left(1-\frac{G_1}{\Sigma}\right)^2 G_1 + \left(\frac{G_1}{\Sigma}\right)^2 G_2\right] V_1^2 + \left[\left(\frac{G_2}{\Sigma}\right)^2 G_1 + \left(1-\frac{G_2}{\Sigma}\right)^2 G_2\right] V_2^2 + \left[2\left(\frac{G_1 G_2}{\Sigma^2} - \frac{G_2}{\Sigma}\right) G_1 + 2\left(\frac{G_1 G_2}{\Sigma^2} - \frac{G_1}{\Sigma}\right) G_2\right] V_1 V_2 = 0\,.$$

If V_1 and V_2 are sinusoidal, with phase difference φ,

$$A|V_1|^2 + B|V_2|e^{2i\varphi} + C|V_1||V_2|e^{i\varphi} = 0\,,$$

where the square-bracketed terms above have been replaced with A, B and C for brevity. Defining

$$x \equiv \frac{|V_2|}{|V_1|} e^{i\varphi}\,,$$

the equation becomes a quadratic,

$$Bx^2 + Cx + A = 0\,,$$

which can be solved to determine the required voltage ratio and phase difference. It is important to note that, despite P_1 and P_2 having equal magnitude and opposite phase, P_3 is not necessarily zero, so a different approach is required in the case where the ground rail is able to contribute to the sound field. This approach also quickly becomes cumbersome for larger arrays.

The presence of the phantom source has important implications for thermoacoustic phased arrays. The ability to drive elements with a phase difference inherently requires a common reference point, *i.e.*, a ground. If the resistance of the path to this ground point is significant with respect to the array elements, the resulting sound field will contain an additional source. This can be avoided through use of a DC bias, or careful consideration of the applied voltages. Alternatively, the additional source could be exploited to further simplify array design by reducing the number of electrical sources and connections required. For example, the square device in Fig. 5.16 could be modified to generate OAM beams with only two sources.

5.6 Conclusions

In this chapter, thermophones were applied in the context of acoustic phased arrays. It was found that thermoacoustic phased arrays are capable of reproducing standard phased array behaviour, such as beam focusing and steering, but have some unique characteristics.

Thermoacoustic generation via Joule heating is an irreversible process. Because of this, thermoacoustic arrays transcend the issues encountered in traditional arrays involving mechanical cross-talk. This, combined with their ease of fabrication, makes miniaturisation of such arrays relatively trivial.

The sound generated from thermophone array elements is highly sensitive to the spatial distribution of the electric current. Regions of high current density result in localised heating within devices. These can be driven to behave as independent acoustic sources, allowing for array-like behaviour to be achieved from single film elements, enabling further simplification of array design.

Electrical coupling between thermophone array elements results in an additional, 'phantom' sound source due to the nonlinearity of the Joule heating mechanism. While this could be considered a detriment in some cases, it can also be used to further simplify array design by reducing the number of required electrical sources and connections. In the case where the phantom source is not desired, it was shown how this can be avoided through application of a DC bias or careful tuning of the source voltages. The mixing of phase components in the heat could also be exploited to achieve distributed heating across a single film with a phase gradient, effectively behaving as a continuous phased array.

The next chapter involves a deeper investigation of the electrical coupling between thermophone elements, where it will be shown that the resulting sound can be used

to infer properties of the elements themselves.

Chapter 6

A Thermoacoustic Bridge Circuit

6.1 Introduction

The previous chapter demonstrated the concept of thermoacoustic phased arrays. This chapter builds upon the work of the previous chapter by exploiting the unique electrical coupling present in thermoacoustic phased arrays to address the question of whether the sound generated by a thermophone can be used to infer properties of the device itself.

The chapter begins with the description of a new type of device: a thermoacoustic bridge. This is a device consisting of multiple thermophone branches, where electrical and thermal properties of the device can be measured by balancing the sound output from each of the branches. This is somewhat analogous to a Wheatstone bridge, where an unknown resistance can be measured by balancing the electric current flowing through two parallel branches. The remainder of the chapter is dedicated to experimentally demonstrating the operation of this device. The particular focus in this case is the measurement of the electrical resistance of the branches.

The work in this chapter contributed to the publication in [101].

6.1.1 The Wheatstone Bridge

The Wheatstone bridge is a circuit designed to measure an unknown resistance [102]. The circuit, shown in Fig. 6.1, consists of two parallel branches, each with two series resistors. One of the branches contains a known resistor, R_1, and a known, adjustable resistor, R_2. The other branch contains a known resistor, R_3, and an unknown resistor, R_x, which is to be measured. A voltmeter is then used to measure the potential difference between the two branches, V_AB.

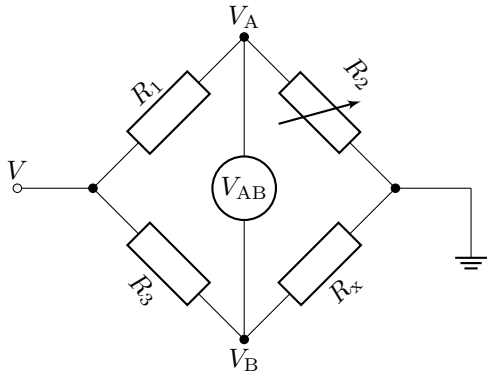

FIGURE 6.1: The Wheatstone bridge circuit. R_x can be measured by adjusting R_2 such that $V_{AB} = 0$, *i.e.*, the bridge is 'balanced'.

The Wheatstone bridge can be considered as two parallel potential dividers,

$$V_A = \frac{R_2}{R_1 + R_2} V \,,$$
$$V_B = \frac{R_x}{R_3 + R_x} V \,,$$

where the measured potential difference bridging the two branches is

$$V_{AB} = \frac{R_2}{R_1 + R_2} V - \frac{R_x}{R_3 + R_x} V \,.$$

The measurement of R_x involves adjusting R_2 such that $V_{AB} = 0$ (balancing the bridge), in which case,

$$R_x = \frac{R_1 R_3}{R_2} \,. \tag{6.1}$$

This method allows for R_x to be measured with high precision, assuming $R_{1,2,3}$ are known to high precision, since the balance of the bridge will be lost even for small differences between the branches. Bridge circuits have myriad applications in areas such as sensor design [103, 104].

6.2 The Thermoacoustic Bridge

The following section discusses the principles behind the thermoacoustic bridge, and how such a device can be used to measure electrical resistance.

Consider the device depicted in Fig. 6.2, consisting of three electrically conductive branches of conductance $G_{1,2,3}$. Two different voltage sources, V_1 and V_2, are applied to branches 1 and 2, respectively. Branch 3 is connected to ground. It was shown

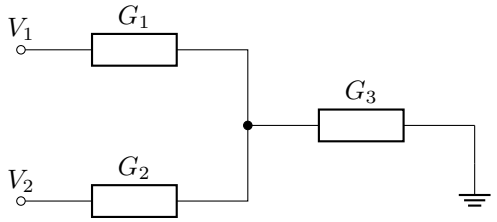

FIGURE 6.2: Thermoacoustic bridge circuit. The power dissipated, and therefore sound generated, by each conductance is dependent on all of the conductances in the circuit. By comparing measurements for different $V_{1,2}$ configurations, the conductance ratios can be determined.

in Section 5.5 that the Joule power dissipated in each branch is

$$P_1 = \left(1 - \frac{G_1}{\Sigma}\right)^2 G_1 V_1^2 + \left(\frac{G_2}{\Sigma}\right)^2 G_1 V_2^2 + 2\left(\frac{G_1 G_2}{\Sigma^2} - \frac{G_2}{\Sigma}\right) G_1 V_1 V_2 \,, \tag{6.2}$$

$$P_2 = \left(\frac{G_1}{\Sigma}\right)^2 G_2 V_1^2 + \left(1 - \frac{G_2}{\Sigma}\right)^2 G_2 V_2^2 + 2\left(\frac{G_1 G_2}{\Sigma^2} - \frac{G_1}{\Sigma}\right) G_2 V_1 V_2 \,, \tag{6.3}$$

$$P_3 = \left(\frac{G_1}{\Sigma}\right)^2 G_3 V_1^2 + \left(\frac{G_2}{\Sigma}\right)^2 G_3 V_2^2 + 2\frac{G_1 G_2}{\Sigma^2} G_3 V_1 V_2 \,. \tag{6.4}$$

Here it can be seen that, due to the electrical coupling, the power dissipated by each branch is dependent on the conductances of all other branches.

In Chapter 4 it was shown that the sound generated by a thermophone is linear with respect to the Joule power, where the proportionality is determined by the thermal parameters of the device. In the case of the thermoacoustic bridge, there are multiple thermophone sources, and it will be useful to consider the the sound field as the sum of these sources; in particular, the 'total' sound can be used,

$$p_{\text{total}} \equiv \oint_{\mathcal{S}} p \, \mathrm{d}\boldsymbol{\mathcal{S}} \,, \tag{6.5}$$

where $\boldsymbol{\mathcal{S}}$ is a surface enclosing the device. Since the sound pressure due to each source is linear with the power, it is therefore expected that this quantity depends on the sum of the Joule power from each branch, P_{total}. As with the acoustic power integrals in Section 2.4.2, the integral in (6.5) is difficult when the source dimensions are comparable to the acoustic wavelength. Instead, if the device dimensions are sufficiently small, then each branch can be assumed to act as a point source, for which p has no angular dependence. In this case, $p_{\text{total}} \propto P_{\text{total}}$. Therefore, by integrating the sound field produced by the thermoacoustic bridge, a measurement of the total Joule power can be obtained, bar some proportionality constant. By

combining multiple sound measurements, this proportionality constant can then be eliminated.

The remainder of this section involves outlining methods for using the generated sound field to determine the branch conductances. It is important to note that, similar to the Wheatstone bridge, these are all relative measurements. An exact conductance measurement therefore requires prior knowledge of some of the branch conductances.

6.2.1 Three-Branch Conductance Measurement

To begin with, consider the case where all branches act as thermoacoustic sources, depicted in Fig. 6.3. It is assumed that each of the branches are nominally identical, such that their transduction efficiencies are equal. The total Joule power contributing to sound generation in this case is

$$P_{\text{total}} \equiv P_1 + P_2 + P_3 \,,$$

which, from (6.2), (6.3) and (6.4), is

$$P_{\text{total}} = \left(1 - \frac{G_1}{\Sigma}\right) G_1 V_1^2 + \left(1 - \frac{G_2}{\Sigma}\right) G_2 V_2^2 - 2\frac{G_1 G_2}{\Sigma} V_1 V_2 \,.$$

If $V_{1,2}$ are alternating sources with phase difference $\varphi = \text{Arg}\,(V_2) - \text{Arg}\,(V_1)$, this can be recast in the form

$$P_{\text{total}} = \left(1 - \frac{G_1}{\Sigma}\right) G_1 |V_1|^2 + \left(1 - \frac{G_2}{\Sigma}\right) G_2 |V_2|^2 \mathrm{e}^{2\mathrm{i}\varphi} - 2\frac{G_1 G_2}{\Sigma} |V_1||V_2| \mathrm{e}^{\mathrm{i}\varphi} \,. \qquad (6.6)$$

Measurement of the total Joule power affords two methods for determining the conductances of the branches. The first, 'voltage-based', method involves simply comparing measurements of the total Joule power for different values of V_1 and V_2. The second, 'phase-based', method involves controlling both the voltages and the phase to balance the sound output from each branch, similar to a Wheatstone bridge. These two methods will now be described.

Voltage-Based Method

The source components in (6.6) can be isolated by performing measurements for different values of $|V_1|$ and $|V_2|$, with $\varphi = 0$. For instance, setting $|V_1| = |V|$, $|V_2| = 0$, where $|V|$ is an arbitrary voltage magnitude chosen to produce measurable

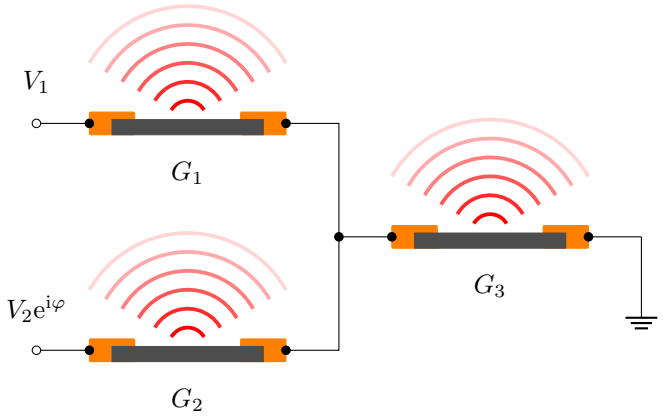

FIGURE 6.3: Three-branch conductance measurement. Here, all three branches produce sound. V_1 and V_2 can differ both in magnitude, $\frac{|V_2|}{|V_1|}$, and phase, φ. The total sound field generated gives a measure of the total Joule power dissipated in the circuit. This can be used to determine the relative conductances of the branches.

sound, the sound generated will be proportional to

$$P_{1,0} = \left(1 - \frac{G_1}{\Sigma}\right) G_1 |V|^2 \,, \tag{6.7}$$

where $P_{1,0}$ refers to source 1 being 'on' and source 2 being 'off'. Similarly, setting $|V_1| = 0$, $|V_2| = |V|$,

$$P_{0,1} = \left(1 - \frac{G_2}{\Sigma}\right) G_2 |V|^2 \,. \tag{6.8}$$

Setting $|V_1| = |V_2| = |V|$,

$$P_{1,1} = \left(1 - \frac{G_1}{\Sigma}\right) G_1 |V|^2 + \left(1 - \frac{G_2}{\Sigma}\right) G_2 |V|^2 - 2\frac{G_1 G_2}{\Sigma} |V|^2 \,,$$

which can be combined with (6.7) and (6.8) to determine the third component of (6.6),

$$\begin{aligned} P_{\mathrm{x}} &= P_{1,0} + P_{0,1} - P_{1,1} \\ &= 2\frac{G_1 G_2}{\Sigma} |V|^2 \,. \end{aligned}$$

$P_{1,0}$, $P_{0,1}$ and P_{x} can then be used to determine the conductance ratios,

$$\begin{aligned}\frac{P_{1,0}}{P_{\mathrm{x}}} &= \frac{\left(1-\frac{G_1}{\Sigma}\right)G_1|V|^2}{2\frac{G_1G_2}{\Sigma}|V|^2}\\ &= \frac{\Sigma-G_1}{2G_2}\\ &= \frac{G_2+G_3}{2G_2}\\ &= \frac{1}{2}\left(1+\frac{G_3}{G_2}\right),\\ \frac{G_3}{G_2} &= 2\frac{P_{1,0}}{P_{\mathrm{x}}}-1\,.\end{aligned}$$

Similarly,

$$\begin{aligned}\frac{P_{0,1}}{P_{\mathrm{x}}} &= \frac{\left(1-\frac{G_2}{\Sigma}\right)G_2|V|^2}{2\frac{G_1G_2}{\Sigma}|V|^2}\,,\\ \frac{G_3}{G_1} &= 2\frac{P_{0,1}}{P_{\mathrm{x}}}-1\,.\end{aligned}$$

The final conductance ratio can then be obtained by eliminating G_3,

$$\begin{aligned}\frac{G_1}{G_2} &= \frac{\left(\frac{G_3}{G_2}\right)}{\left(\frac{G_3}{G_1}\right)}\\ &= \frac{2\frac{P_{1,0}}{P_{\mathrm{x}}}-1}{2\frac{P_{0,1}}{P_{\mathrm{x}}}-1}\\ &= \frac{2P_{1,0}-P_{\mathrm{x}}}{2P_{0,1}-P_{\mathrm{x}}}\,.\end{aligned}$$

Therefore, using three measurements of $P_{1,0}$, $P_{0,1}$ and $P_{1,1}$, the electrical properties of the whole system can be characterised, where

$$\begin{aligned}\frac{G_1}{G_2} &= \frac{P_{1,0}-P_{0,1}+P_{1,1}}{P_{0,1}-P_{1,0}+P_{1,1}}\,,\\ \frac{G_3}{G_1} &= \frac{P_{0,1}-P_{1,0}+P_{1,1}}{P_{1,0}+P_{0,1}-P_{1,1}}\,,\\ \frac{G_3}{G_2} &= \frac{P_{1,0}-P_{0,1}+P_{1,1}}{P_{1,0}+P_{0,1}-P_{1,1}}\,.\end{aligned}$$

This can then be recast in the form

$$G_1P_{\mathrm{A}} = G_2P_{\mathrm{B}} = G_3P_{\mathrm{C}}\,, \tag{6.9}$$

where

$$P_{\mathrm{A}} \equiv -P_{1,0} + P_{0,1} + P_{1,1}\,, \tag{6.10}$$

$$P_{\mathrm{B}} \equiv P_{1,0} - P_{0,1} + P_{1,1}\,, \tag{6.11}$$

$$P_{\mathrm{C}} \equiv P_{1,0} + P_{0,1} - P_{1,1}\,. \tag{6.12}$$

Phase-Based Method

Now consider the behaviour of (6.6) when varying both $\frac{|V_2|}{|V_1|}$ and φ. This is modelled in Fig. 6.4 for $G_1 = G_2 = G_3$. As can be seen, ignoring the trivial case where $|V_1| = 0$, there are distinct points at which $P_{\mathrm{total}} = 0$. Here the magnitude and phase of the power dissipated by each branch is such that they perfectly interfere, resulting in zero total power. In this case, this occurs for $|V_1| = |V_2|$ and $\varphi = \pm\frac{\pi}{3}$. Changing either the voltage ratio or phase difference away from these values results in one of the sources dominating over the others, with non-zero total power. Since each source has its own distinct phase, this leads to a phase vortex in the total sound around the interference points. In general, it can be shown that the locations of the vortices depend on the conductances by defining $x \equiv \frac{|V_2|}{|V_1|}\mathrm{e}^{\mathrm{i}\varphi}$, such that (6.6) has non-trivial roots where

$$P_{\mathrm{total}} = \left(1 - \frac{G_2}{\Sigma}\right) G_2 x^2 - 2\frac{G_1 G_2}{\Sigma} x + \left(1 - \frac{G_1}{\Sigma}\right) G_1 = 0\,.$$

Solving for x then yields

$$x_{\pm} = \frac{G_1}{G_1 + G_3}\left(1 \pm \sqrt{-\frac{G_3}{G_1 G_2}\Sigma}\right)\,. \tag{6.13}$$

The dependence of $x_{\pm}$ on each of the conductances is shown in Fig. 6.5. In the limiting case $G_1 \to \infty$, this results in power dissipation purely from branches 2 and 3. For zero total Joule power, V_2 should then be adjusted such that $P_2 = -P_3$. In the case where $G_2 = G_3$, from (6.13) it is seen that $V_2 = \sqrt{2}V_1\mathrm{e}^{\mathrm{i}\pi/4}$. As $G_1 \to 0$, V_2 becomes the dominant source term for $P_{2,3}$, hence they are in phase. P_1, whose dominant source term is V_1, tends to zero. Zero total power can therefore be achieved by setting $\varphi = \frac{\pi}{2}$ and reducing V_2, such that P_1 is out of phase with $P_{2,3}$ and has equal magnitude. Similar behaviour is observed for G_2, where, for $G_2 \to \infty$ and $G_1 = G_3$, $V_2 = (\sqrt{2}/2)V_1\mathrm{e}^{\mathrm{i}\pi/4}$. For $G_2 \to 0$, zero total power is again achieved for $\varphi = \frac{\pi}{2}$, but instead V_1 is reduced. For $G_3 \to \infty$, $P_3 = 0$, whereas $P_{1,2}$ are dominated by their respective source voltages, hence, for $G_1 = G_2$, zero total power is achieved for $V_2 = V_1\mathrm{e}^{\mathrm{i}\pi/2}$. For $G_3 \to 0$, current only flows between V_1 and V_2, so zero total

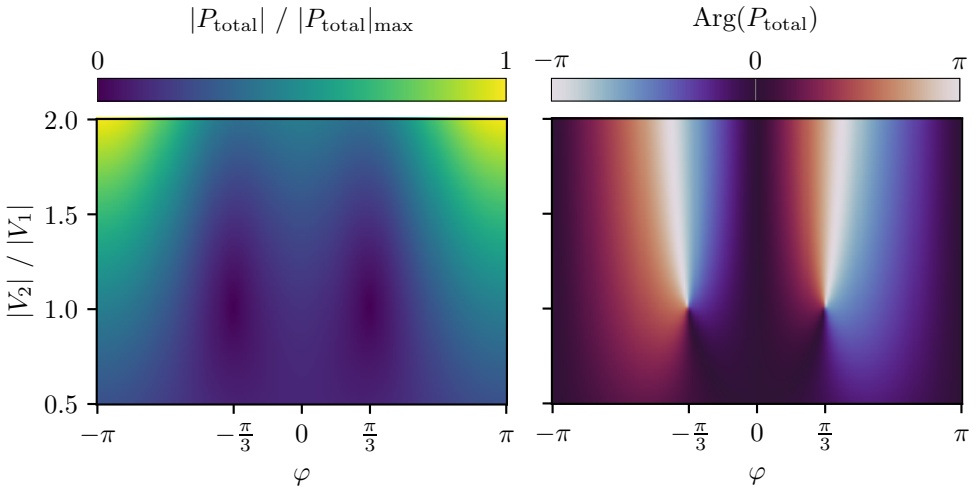

FIGURE 6.4: Modelled total Joule power for the three-branch device as a function of the magnitude and phase of the driving voltages, from (6.6). **Left:** Normalised magnitude. **Right:** Phase. The phase shows distinct vortices, at which the total Joule power is zero.

power occurs for $V_1 = V_2$.

It will now be shown how (6.13) can be used to obtain the conductance ratios. Combining the two roots,

$$x_+ + x_- = \frac{2G_1}{G_1 + G_3}\,,$$

which can be recast in terms of the conductance ratio,

$$\begin{aligned}\frac{G_3}{G_1} &= \frac{2}{x_+ + x_-} - 1 \\ &= \frac{2}{\left(\frac{|V_2|}{|V_1|}\right)_+ \mathrm{e}^{\mathrm{i}\varphi_+} + \left(\frac{|V_2|}{|V_1|}\right)_- \mathrm{e}^{\mathrm{i}\varphi_-}} - 1\,,\end{aligned}$$

where $\left(\frac{|V_2|}{|V_1|}\right)_\pm$ and $\varphi_\pm$ are the values of the respective quantities at the roots. A similar expression can be obtained for branch 2, by instead defining $x \equiv \frac{|V_1|}{|V_2|}\mathrm{e}^{\mathrm{i}\varphi}$, such that

$$\frac{G_3}{G_2} = \frac{2}{\left(\frac{|V_1|}{|V_2|}\right)_+ \mathrm{e}^{\mathrm{i}\varphi_+} + \left(\frac{|V_1|}{|V_2|}\right)_- \mathrm{e}^{\mathrm{i}\varphi_-}} - 1\,.$$

The final ratio is then obtained by combining the previous two,

$$\frac{G_1}{G_2} = \frac{G_1}{G_3}\frac{G_3}{G_2}\,.$$

The above applies also when the circuit components have both conductance and susceptance terms, in which case the conductance ratios are replaced with the ratio

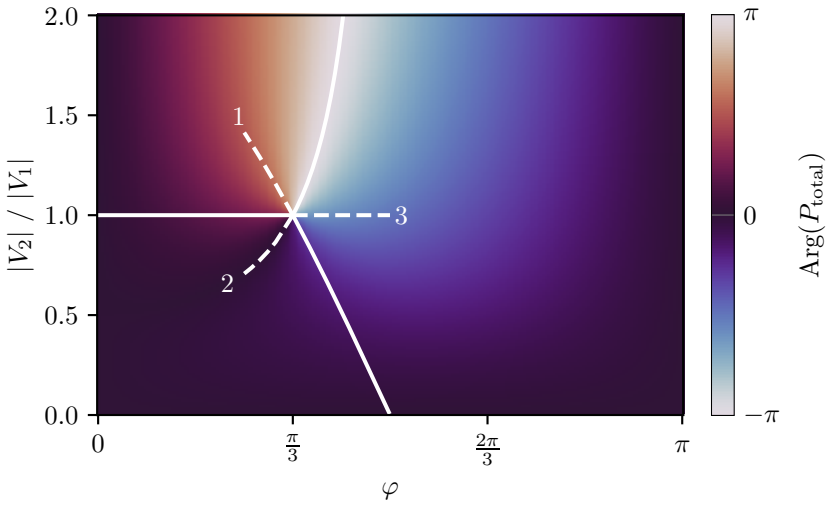

FIGURE 6.5: Modelling of the phase of the total Joule power for $G_1 = G_2 = G_3$ (colour plot) and the dependence of the vortex condition on each of the branch conductances G_x, whilst holding the other two fixed, with $G_y = G_z$ (white lines). The value of x is indicated by the numbers on each line. Solid white lines indicate $0 \leq G_x \leq G_{y,z}$, whereas dashed lines indicate $G_{y,z} \leq G_x \leq \infty$.

of the admittances. This work, however, focuses on the case where the branches only have conductance terms. In this case, the above ratios can be simplified by noting that

$$\left(\frac{|V_2|}{|V_1|}\right)_+ = \left(\frac{|V_2|}{|V_1|}\right)_- ,$$
$$\varphi_+ = -\varphi_- ,$$

such that

$$\frac{G_3}{G_1} = \left(\frac{|V_1|}{|V_2|}\right)_0 \sec\varphi_0 - 1 ,$$
$$\frac{G_3}{G_2} = \left(\frac{|V_2|}{|V_1|}\right)_0 \sec\varphi_0 - 1 ,$$

where $\left(\frac{|V_x|}{|V_y|}\right)_0$ and φ_0 are the respective values at either of the roots. As with the voltage-based method, this can then be recast into the form

$$G_1 P_{\mathrm{A}} = G_2 P_{\mathrm{B}} = G_3 P_{\mathrm{C}} , \tag{6.14}$$

where

$$P_{\mathrm{A}} \equiv \left(\frac{|V_1|}{|V_2|}\right)_0 - \cos\varphi_0\,, \tag{6.15}$$

$$P_{\mathrm{B}} \equiv \left(\frac{|V_2|}{|V_1|}\right)_0 - \cos\varphi_0\,, \tag{6.16}$$

$$P_{\mathrm{C}} \equiv \cos\varphi_0\,. \tag{6.17}$$

Therefore, all of the conductance ratios can be determined by measuring the voltages and phase difference required for the total sound generated to be zero.

With this method, only relative measurements can be obtained, unless one of the conductances has a prior known value. The use of known values to obtain an exact measurement, with the added complication of one of the branches not producing sound, will now be demonstrated.

6.2.2 Two-Branch Conductance Measurement

The case where one of the branches does not produce sound will now be considered. This is depicted in Fig. 6.6. Here branches 1 and 2 act as thermoacoustic sources and share the same known conductance, G. Branch 3 is an unknown conductance, G_{x}, to be measured. In this case, the total Joule power contributing to sound generation is

$$P_{\mathrm{total}} \equiv P_1 + P_2\,,$$

where

$$P_1 = \left(1 - \frac{G}{\Sigma}\right)^2 G V_1^2 + \frac{G^2}{\Sigma^2} G V_2^2 + 2\left(\frac{G^2}{\Sigma^2} - \frac{G}{\Sigma}\right) G V_1 V_2\,, \tag{6.18}$$

$$P_2 = \frac{G^2}{\Sigma^2} G V_1^2 + \left(1 - \frac{G}{\Sigma}\right)^2 G V_2^2 + 2\left(\frac{G^2}{\Sigma^2} - \frac{G}{\Sigma}\right) G V_1 V_2\,, \tag{6.19}$$

and $\Sigma = 2G + G_{\mathrm{x}}$.

As with the three-branch case, the conductance G_{x} can be measured by balancing the bridge to achieve zero total sound. An alternative approach for the two-branch case, shown in Fig. 6.7, is to consider the directivity of the far-field sound. When the bridge is balanced, the sound generated by the two acoustic branches must perfectly interfere, *i.e.*, they have equal magnitude and opposite phase. This will result in a dipolar sound field. Unbalancing the bridge causes the field to become more monopolar. It will now be shown how these two approaches can be used to measure G_{x}.

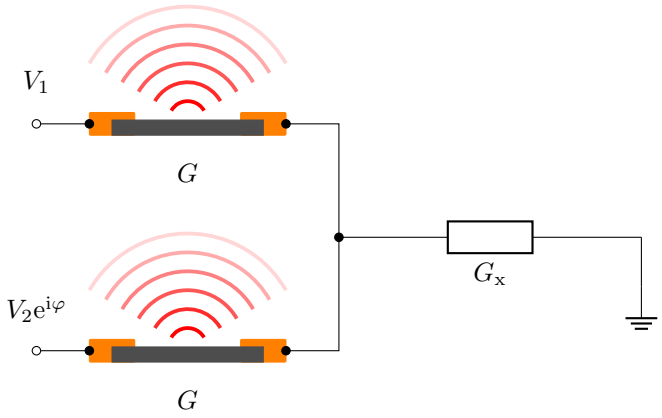

FIGURE 6.6: Two-branch conductance measurement. Two thermophones of equal, known conductance, G, are connected to an unknown conductance, G_x, which does not produce sound. As with the three-branch measurement, the conductance ratios can be determined from the total sound generated, allowing for G_x to be measured.

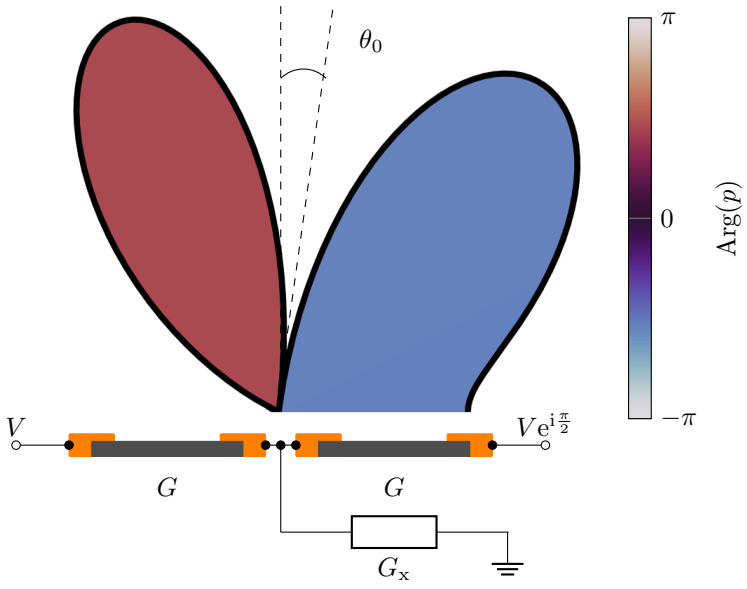

FIGURE 6.7: Simulation of two-branch far-field measurement. The driving voltages have equal magnitude and phase difference $\varphi = \frac{\pi}{2}$, such that, for $G_x \to \infty$, a dipolar sound field is observed. For finite G_x, the sound field becomes more monopolar, with a shift in the sound field null, θ_0. G_x can therefore be determined by measuring θ_0.

Phase-Based Method

Allowing V_1 and V_2 to differ in both magnitude and phase, $P_{\text{total}} = 0$ for

$$\left[\left(1-\frac{G}{\Sigma}\right)^2+\frac{G^2}{\Sigma^2}\right]\left(|V_1|^2+|V_2|^2\mathrm{e}^{2\mathrm{i}\varphi}\right)+4\left(\frac{G^2}{\Sigma^2}-\frac{G}{\Sigma}\right)|V_1||V_2|\mathrm{e}^{\mathrm{i}\varphi}=0\,.$$

Defining $x \equiv \frac{|V_2|}{|V_1|}\mathrm{e}^{\mathrm{i}\varphi}$,

$$x_+ + x_- = \frac{-4\left(\frac{G^2}{\Sigma^2}-\frac{G}{\Sigma}\right)}{\left(1-\frac{G}{\Sigma}\right)^2+\frac{G^2}{\Sigma^2}}\,.$$

Considering the symmetry of the system,

$$\left(\frac{|V_2|}{|V_1|}\right)_+ = \left(\frac{|V_2|}{|V_1|}\right)_- = 1\,,$$
$$\varphi_+ = -\varphi_-\,,$$

such that

$$\cos\varphi_0 = \frac{-2\left(\frac{G^2}{\Sigma^2}-\frac{G}{\Sigma}\right)}{\left(1-\frac{G}{\Sigma}\right)^2+\frac{G^2}{\Sigma^2}}\,.$$

Solving for G_{x} yields

$$\frac{G_{\mathrm{x}}}{G} = \frac{1+\sin\varphi_0}{\cos\varphi_0} - 1\,. \tag{6.20}$$

Since G is known in this case, this method permits an exact measurement of G_{x}. The fact that this method works with G_{x} not producing sound is also useful, since it would allow for a two-element thermoacoustic device to be connected to an external conductance to be measured. The procedure for the far-field method will now be described.

Far-Field Method

The acoustic pressure at a point $\boldsymbol{r}$ due to two sources of strength $Q_{1,2}$, located at $\boldsymbol{r}_{1,2}$ is

$$p(\boldsymbol{r}) = \frac{Q_1 D_1(\boldsymbol{r})}{|\boldsymbol{r}-\boldsymbol{r}_1|}\mathrm{e}^{\mathrm{i}k|\boldsymbol{r}-\boldsymbol{r}_1|} + \frac{Q_2 D_2(\boldsymbol{r})}{|\boldsymbol{r}-\boldsymbol{r}_2|}\mathrm{e}^{\mathrm{i}k|\boldsymbol{r}-\boldsymbol{r}_2|}\mathrm{e}^{\mathrm{i}\psi}\,,$$

where $D_{1,2}(\boldsymbol{r})$ are the source directivity functions, k is the acoustic wavenumber and ψ is the acoustic phase difference between the sources. In the far-field ($|\boldsymbol{r}| \gg \frac{2\pi}{k}$), this picture can be simplified with the approximation $|\boldsymbol{r}-\boldsymbol{r}_x| \approx r - \boldsymbol{r}_x\cdot\hat{r}$, where r is now the distance from the midpoint between the two sources. Modelling the device as two rectangular planar sources, lying on the x-axis and separated by distance

$|\boldsymbol{r}_1 - \boldsymbol{r}_2| = d$, the far-field pressure becomes, in spherical coordinates,

$$p(r,\theta,\phi) = \frac{Q_1 D_1(\theta,\phi)}{r} \mathrm{e}^{\mathrm{i}kr} \mathrm{e}^{\mathrm{i}kd\sin\theta\cos\phi/2} + \frac{Q_2 D_2(\theta,\phi)}{r} \mathrm{e}^{\mathrm{i}kr} \mathrm{e}^{-\mathrm{i}kd\sin\theta\cos\phi/2} \mathrm{e}^{\mathrm{i}\psi} ,$$

where it was seen in Section 2.4.1 that the directivity function for a rectangular planar source of dimensions $L_{x,y}$ is

$$D(\theta,\phi) = \mathrm{sinc}\left(\frac{kL_x}{2}\sin\theta\cos\phi\right) \mathrm{sinc}\left(\frac{kL_y}{2}\sin\theta\sin\phi\right) . \tag{6.21}$$

Considering the acoustic pressure in the upper xy-plane ($-\frac{\pi}{2} \leq \theta \leq \frac{\pi}{2}$, $\phi = 0$) the far-field sound will show a distinct pattern, dependent on the source dimensions, magnitudes and phase difference. If the sources are of equal magnitude ($Q_1 = Q_2 \equiv Q$) and dimensions ($L_{x,1} = L_{x,2} \equiv L$), the magnitude of the far-field sound ($|p|^2 = p^* p$) becomes

$$|p| = \frac{2Q}{r} \left| \mathrm{sinc}\left(\frac{kL}{2}\sin\theta\right) \cos\left(\frac{kd\sin\theta - \psi}{2}\right) \right| . \tag{6.22}$$

From inspection of (6.22), it is seen that the sinc function leads to nulls in the sound field ($|p| = 0$) at angles

$$\theta_0 = \arcsin\left(\frac{2n\pi}{kL}\right) ,$$

where n are non-zero integers. These diffraction-based nulls are not present for $kL < 2\pi$. More usefully, the cos function leads to a null at

$$\theta_0 = \arcsin\left(\frac{\pi + \psi}{kd}\right) . \tag{6.23}$$

When $\psi = -\pi$, this results in a dipolar sound field, consisting of two major lobes of equal magnitude and opposite phase with a null at $\theta_0 = 0$. Changing ψ causes θ_0 to shift, perceived as a rotation of the dipole. This can be used to measure G_x, as will now be shown.

To determine how the acoustic source strengths and phase differences depend on G_x, Equations (6.18) and (6.19) can be used. Setting $V_2 = V_1 \mathrm{e}^{\mathrm{i}\frac{\pi}{2}}$,

$$P_1 = \left(1 - \frac{G}{\Sigma}\right)^2 G|V_1|^2 - \frac{G^2}{\Sigma^2} G|V_1|^2 + 2\mathrm{i}\left(\frac{G^2}{\Sigma^2} - \frac{G}{\Sigma}\right) G|V_1|^2 ,$$
$$P_2 = \frac{G^2}{\Sigma^2} G|V_1|^2 - \left(1 - \frac{G}{\Sigma}\right)^2 G|V_1|^2 + 2\mathrm{i}\left(\frac{G^2}{\Sigma^2} - \frac{G}{\Sigma}\right) G|V_1|^2 ,$$

from which it is seen that

$$\begin{aligned}\mathrm{Re}\,(P_1) &= -\mathrm{Re}\,(P_2)\ ,\\ \mathrm{Im}\,(P_1) &= \mathrm{Im}\,(P_2)\ ,\end{aligned}$$

such that

$$\begin{aligned}|P_1| &= |P_2|\,,\\ \psi &= \mathrm{Arg}\,(P_2) - \mathrm{Arg}\,(P_1)\\ &= \frac{\pi}{2} - \arctan\left(\frac{\mathrm{Re}\,(P_2)}{\mathrm{Im}\,(P_2)}\right) - \frac{\pi}{2} + \arctan\left(\frac{\mathrm{Re}\,(P_1)}{\mathrm{Im}\,(P_1)}\right)\\ &= 2\arctan\left(\frac{\mathrm{Re}\,(P_1)}{\mathrm{Im}\,(P_1)}\right)\\ &= 2\arctan\left(-\frac{G_\mathrm{x}\,(G_\mathrm{x}+2G)}{2G\,(G_\mathrm{x}+G)}\right)\ ,\end{aligned} \tag{6.24}$$

where the factor of $\frac{\pi}{2}$ comes from the consideration or $\mathrm{Im}\,(P_{1,2}) > 0$ with the arctan function. Equation (6.24) can then be substituted into (6.23) to determine the dependence of θ_0 on G_x,

$$\theta_0 = \arcsin\left[\frac{\pi}{kd} + \frac{2}{kd}\arctan\left(-\frac{G_\mathrm{x}\,(G_\mathrm{x}+2G)}{2G\,(G_\mathrm{x}+G)}\right)\right]\ . \tag{6.25}$$

Solving for G_x,

$$\frac{G_\mathrm{x}}{G} = \frac{1-\sin\left(\frac{kd\sin\theta_0-\pi}{2}\right)}{\cos\left(\frac{kd\sin\theta_0-\pi}{2}\right)} - 1\,. \tag{6.26}$$

Therefore, by measuring the angle at which the far-field sound is zero, the value of G_x can be determined. The behaviour of (6.25) is shown in Fig. 6.8 for different values of kd. As can be seen, the choice of kd is important as it determines the sensitivity of θ_0 with respect to $\frac{G_\mathrm{x}}{G}$. From (6.25) it is seen that, as $G_\mathrm{x} \to \infty$, $\theta_0 = 0$, resulting in the expected dipolar sound field for any kd. For $G_\mathrm{x} \to 0$,

$$\theta_0 = \arcsin\left(\frac{\pi}{kd}\right)\ .$$

To make use of the maximum angular range, the bridge should be tuned with $kd = \pi$, such that, for $G_\mathrm{x} \to 0$, $\theta_0 = \frac{\pi}{2}$. However, this is not necessarily practical due to the difficulty in measuring θ_0 as the sound field becomes more monopolar. If instead $kd < \pi$, a minimum possible G_x for measurement can be defined, for which $\theta_0 = \frac{\pi}{2}$,

$$\left(\frac{G_\mathrm{x}}{G}\right)_{\min} = \frac{1-\sin\left(\frac{kd-\pi}{2}\right)}{\cos\left(\frac{kd-\pi}{2}\right)} - 1\,. \tag{6.27}$$

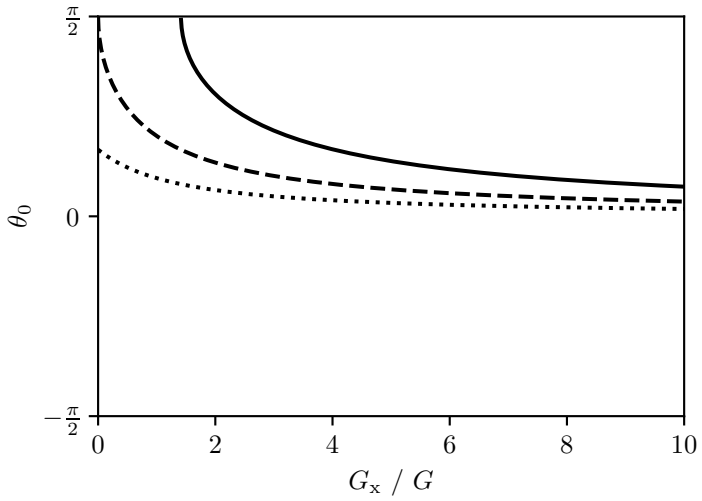

FIGURE 6.8: Null angle in the far-field sound as a function of the conductance ratio for the two-branch device, from (6.25). For $kd \geq \pi$ (dotted) there exists a null for every possible G_x; however, sensitivity is maximised when $kd = \pi$ (dashed). For $kd < \pi$ (solid) there is a threshold G_x, below which the sound field no longer contains a null and the measurement is not feasible.

Now that the physics behind the thermoacoustic bridge has been described, its operation will demonstrated experimentally. First, however, the measurement procedure will be described.

6.3 Experimental Methods

To demonstrate the conductance measurement methods, devices were made with two and three elements, shown in Fig. 6.9. The three-branch device consisted of a continuous ITO thin film patterned into three, nominally identical radiating branches on an Si/SiO_2 substrate. Each branch had planar dimensions 3×1 mm with thickness 50 nm, and gold contacts were placed with pitch 0.5 mm along its length. By choosing which contact to connect to source and drain, the length of each branch was varied, thus changing its conductance. The additional contacts also allowed for differential voltage measurements to be performed on each branch, such that the Joule power could be measured electrically for direct comparison with the sound. The two-branch device consisted of two 6×2 mm rectangular films on a fused quartz substrate with separation 5 mm. These two branches were individually sourced, and connected to ground via a variable conductance.

To electrically measure the conductance of the three-branch device, two-terminal

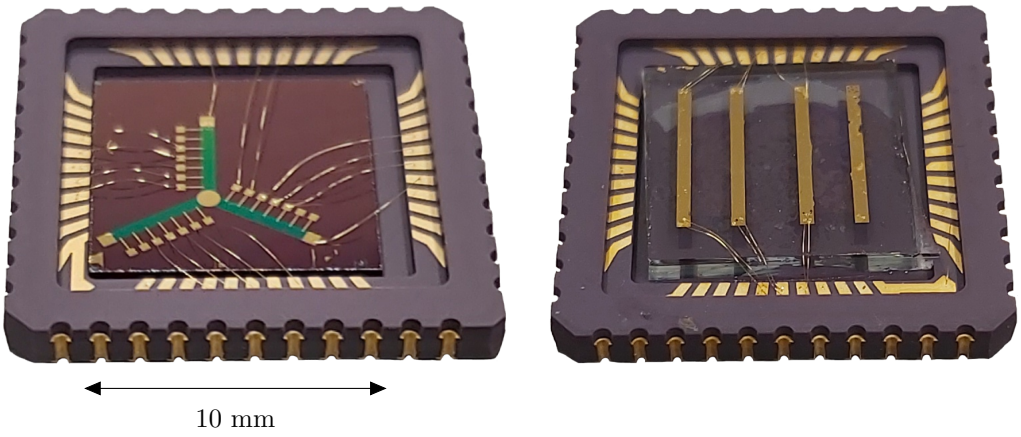

FIGURE 6.9: Photographs of devices used in this experiment. **Left:** Three-branch device. An ITO film patterned into three branches with gold contacts on an Si/SiO_2 substrate. The choice of contact along each branch allows its length, and, therefore, conductance, to be varied. **Right:** Two-branch device consisting of two ITO elements with gold contacts on a fused quartz substrate.

measurements were taken between the contact points of each of the branches, *i.e.*, $\frac{1}{G_{1,2}} = \frac{1}{G_1} + \frac{1}{G_2}$, $\frac{1}{G_{1,3}} = \frac{1}{G_1} + \frac{1}{G_3}$ and $\frac{1}{G_{2,3}} = \frac{1}{G_2} + \frac{1}{G_3}$. These were then combined to determine the individual conductances as follows,

$$G_1 = \frac{2}{\frac{1}{G_{1,2}} + \frac{1}{G_{1,3}} - \frac{1}{G_{2,3}}}, \tag{6.28}$$

$$G_2 = \frac{2}{\frac{1}{G_{1,2}} + \frac{1}{G_{2,3}} - \frac{1}{G_{1,3}}}, \tag{6.29}$$

$$G_3 = \frac{2}{\frac{1}{G_{1,3}} + \frac{1}{G_{2,3}} - \frac{1}{G_{1,2}}}. \tag{6.30}$$

Integration measurements of the sound field were performed using a pair of parabolic reflectors to focus the sound to a single point, as shown in Fig. 6.10. The device was placed at the focal point of one of the reflectors and the microphone at the other. The reflectors were then placed opposite each other, such that the sound emitted from the device was collected and focused onto the microphone. This is not a true measure of the total sound as the integration surface does not completely encompass the device; however, this method is more time-efficient as it only involves a single measurement, rather than a full mapping of the far-field sound. This inevitably leads to some discrepancy between the measured and actual total sound, which will be quantified in the following section.

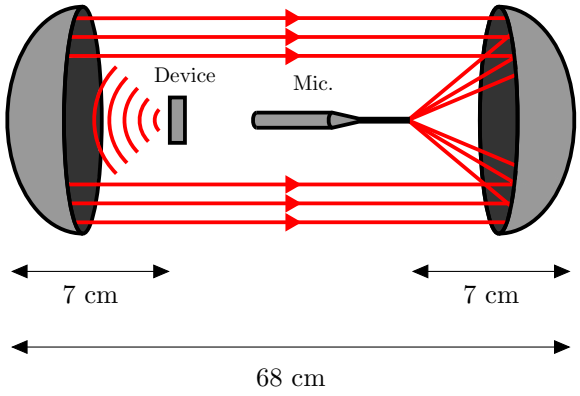

FIGURE 6.10: Experimental method for measuring the total sound. Two aluminium parabolic reflectors (Edmund Optics, radius 15 cm, depth 8 cm) collect the sound emitted from the device and focus it onto the microphone, allowing for the total sound produced to be determined with a single measurement.

6.4 Power-Sound Correspondence

In Section 6.2 it was mentioned that the thermoacoustic bridge relies on the integrated far-field sound pressure being proportional to the total Joule power dissipated by the device. This will now be verified with the parabolic reflector setup. The proportionality is based upon the point-source approximation for the device. Since, in practice, devices have finite dimensions, some discrepancy is expected due to diffractive effects that will depend on the frequency. Experimentally, the challenge is then to find a frequency that is low enough to minimise diffractive effects, whilst also providing a sufficiently high signal-to-noise ratio.

The effect of diffraction on the total sound pressure was modelled for the three-branch device shown in Fig. 6.9. Each branch was modelled as a planar rectangular source with dimensions 3.0 mm × 0.5 mm and equal conductance. For rectangular sources, (6.5) has no closed-form solution, hence the sound field integration was performed numerically. The total sound pressure was calculated for $-\pi \leq \varphi \leq \pi$, with $|V_1| = |V_2|$, for frequency values $1 \leq f_2 \leq 50\,\text{kHz}$. The simulated dependence of p_{total} on φ for each frequency is shown in Fig. 6.11, compared to P_{total}. The results show that, as the frequency is increased, the correspondence between p_{total} and P_{total} becomes worse. This is expected since, as the wavelength approaches the device dimensions, diffractive effects will be introduced and the point-source approximation will no longer hold. For frequencies below 20 kHz the error introduced by diffractive effects is less than 5%, hence this was the frequency range chosen for the experiment.

Following the modelling above, the correspondence between p_{total} and P_{total} was then

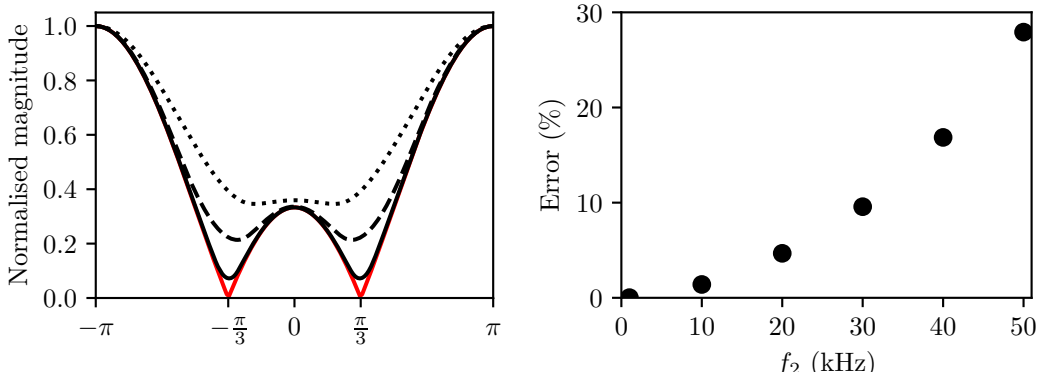

FIGURE 6.11: Simulation of the effects of diffraction on the total sound pressure for a device of finite size. The device in this case was the three-branch device seen in Fig. 6.9. The branches were modelled as rectangular sources using the directivity function in (6.21), where the far-field integral was calculated numerically. **Left:** Phase dependence of P_{total} (red line), compared to p_{total} for different acoustic frequencies, where $|V_1| = |V_2|$ and $G_1 = G_2 = G_3$. Frequencies shown are 10 (solid black), 30 (dashed) and 50 (dotted) kHz. **Right:** Relative error between p_{total} and P_{total} as a function of frequency.

measured experimentally. Using the setup shown in Fig. 6.10, the three-branch device was connected such that the lengths of the branches, hence their conductances, were equal at 3 mm. The phase was then swept across the range $-\pi \leq \varphi \leq \pi$, with $|V_1| = |V_2|$ and p_{total} measured at each point. A differential voltage measurement was also taken along each of the branches, from which P_{total} could be inferred. The measurements were performed for acoustic frequencies $2\,\text{kHz} \leq f_2 \leq 20\,\text{kHz}$. The results of the measurements are shown in Fig. 6.12. For $f_2 = 10\,\text{kHz}$, the Joule power shows excellent agreement with (6.6), including the zero points at $\varphi = \pm\pi/3$, as predicted from (6.13) when $G_1 = G_2 = G_3$. The total sound also successfully reproduces this behaviour. Looking at different frequencies, for $f_2 < 10\,\text{kHz}$ there is significant error, mainly caused by $1/f$ noise in the amplifiers seen in Fig. 3.4. The error also increases for $f_2 > 10\,\text{kHz}$. This is shown in both the model and experiment, as the point-source approximation breaks down due to diffractive effects. Experimentally, the error is further increased past this point due to scattering within the parabolic reflector setup. For $f_2 = 10\,\text{kHz}$ the error was smallest, hence this was chosen as the main working frequency as a compromise. The phase-based method also requires varying the source magnitudes, as well as the phase. The previous measurements were repeated for $0.5|V_1| \leq |V_2| \leq 2|V_1|$ at $f_2 = 10\,\text{kHz}$, the results of which are shown in Fig. 6.13. Again, there is good agreement between experiment and model. This includes the points of zero total sound, which are indicated by vortices in the phase.

The correspondence seen in all cases here confirms that the total sound can be

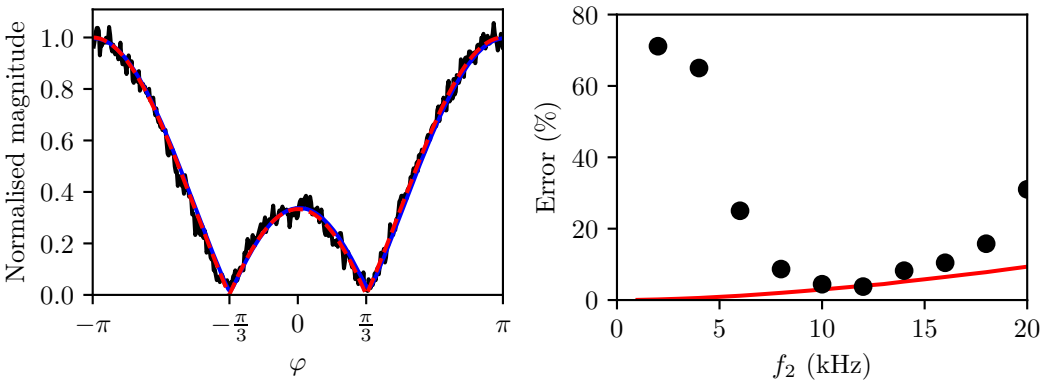

FIGURE 6.12: Measured correspondence between total sound pressure and total Joule power for the three-branch device. **Left:** Measured phase dependence of P_{total} and p_{total} for $f_2 = 10\,\text{kHz}$, compared to (6.6) for $|V_1| = |V_2|$ and $G_1 = G_2 = G_3$. **Right:** Relative error between p_{total} and P_{total} as a function of acoustic frequency. Black dots indicate experimental values, whereas the red line is the modelled diffraction-based error.

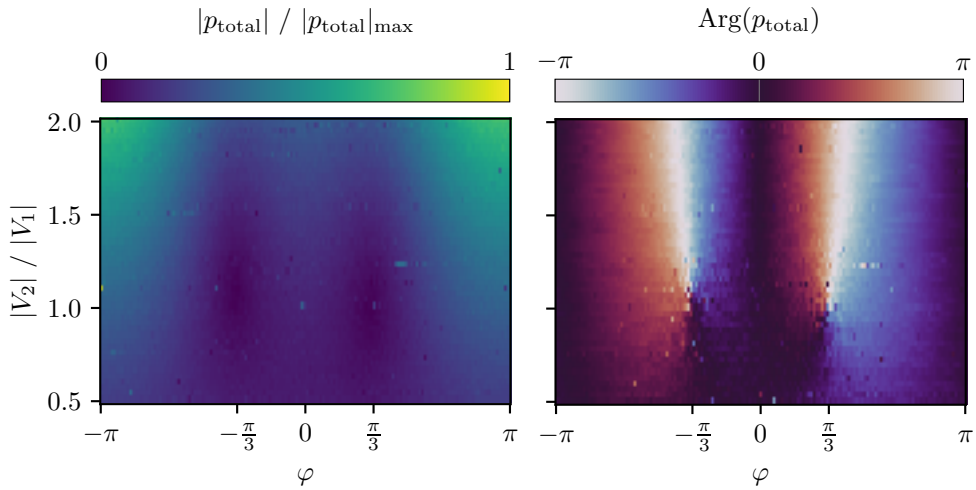

FIGURE 6.13: Measured total sound pressure for the three-branch device as a function of the magnitude and phase of the driving voltages at $f_2 = 10\,\text{kHz}$. **Left:** Normalised magnitude. **Right:** Phase

considered to be directly proportional to the total Joule power. The experimental operation of the thermoacoustic bridge will now be demonstrated.

6.5 Experimental Measurements

The total sound produced by the three-branch device was measured using both voltage-based and phase-based bridging methods for different values of the branch conductances, which was varied by the choice of contacts along each branch. These conductances were also measured electrically by a two-terminal method. For the voltage-based method, three measurements of the total sound were recorded, one for each of $P_{1,0}$, $P_{0,1}$ and $P_{1,1}$. The conductance ratios were then determined using (6.9). The phase-based method involved varying both $|V_2|$ and φ, with $|V_1|$ held fixed. The sound was measured for $0.5 \leq |V_2| \leq 2|V_1|$ and $-\pi \leq \varphi \leq \pi$. The conductance ratios were then determined from (6.14).

Three sets of measurements were taken. In each set, the length of one of the branches was varied while keeping the other two fixed at their maximum length. For each length, an electrical measurement was taken, and then both the voltage and phase-based measurements performed. The measured dependence of the point of zero total sound on the branch length, L, is compared to (6.13) in Fig. 6.14. A clear shift in the zero point is seen as a function of each of the branch lengths. While the experimental data shows the trends predicted by the model, there is an offset in the exact locations of the zero point. This is due to the device branches having slightly different conductances per unit length, such that G_1, G_2 and G_3 are not exactly equal when $L_1 = L_2 = L_3$. A comparison between the conductance ratios measured both electrically and acoustically is shown in Fig. 6.15. Both voltage-based and phase-based bridging methods quantitatively agree with the direct electrical measurements. The phase-based method, however, provides a more sensitive measurement. This is due to the much greater sensitivity of the point of zero total Joule power to the conductivity ratios – the bridge must be perfectly balanced to achieve zero total power.

For the two-branch device, the sources were set such that $|V_1| = |V_2|$ and $\varphi = \frac{\pi}{2}$ to create a dipolar sound field in the case where $G_\mathrm{x} \to \infty$. The directivity of the far-field sound was then measured for $0 < G_\mathrm{x} \leq 0.23G$. The measured directivity of the far-field sound for different values of G_x is shown in Fig. 6.16. When $G_\mathrm{x} \gg G$, a symmetric dipolar sound field is observed with a null $\theta_0 \approx 0$. A shift of this null is clearly seen as G_x is decreased. Since, experimentally, $kd < \pi$, the steering angle will saturate at a minimum G_x, as given by (6.27). In this case, this occurs for

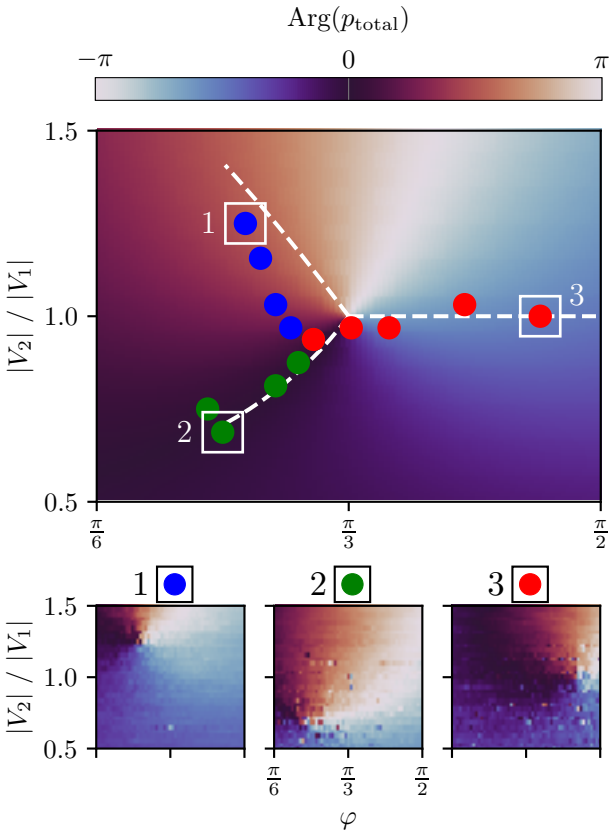

FIGURE 6.14: Experimental vortex tracking measurement. **Top:** Predicted phase of total Joule power (colourmap) as a function of relative source phase and magnitude for a three-branch device with equal branch conductances. The location of the point of zero power (phase vortex) and its dependence on individual branch conductances is shown: experimental total sound (circles) and modelled total Joule power (dashed line), where increasing conductance equates to increasing radial distance from the centre. The colours blue, red and green represent the branches 1, 2 and 3, respectively. **Bottom row:** Measured total sound phase maps for the boxed points in the top figure.

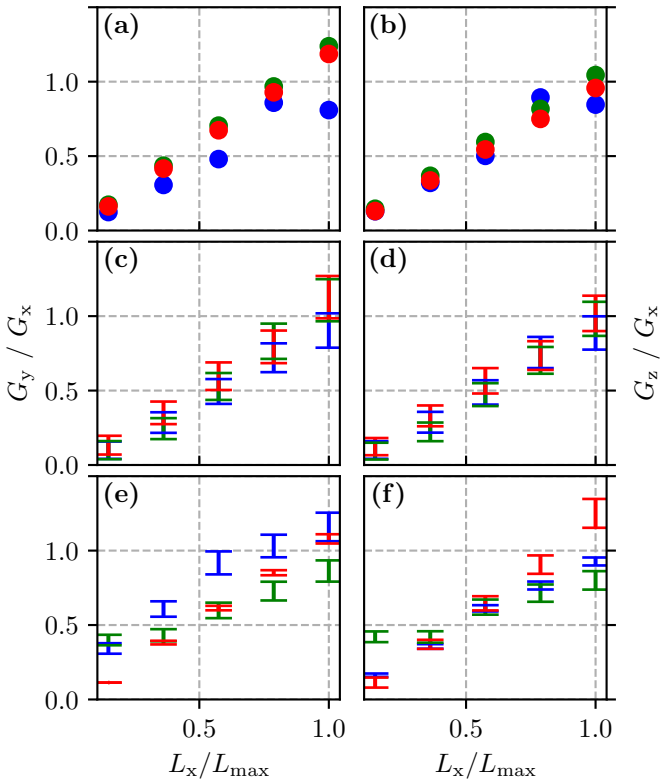

FIGURE 6.15: Measurements of three-branch device conductance ratios $G_{y,z}$ / G_x as a function of the branch lengths L_x, normalised to the maximum branch length L_{max}. Results shown for electrical measurements (**a,b**), as well as the voltage (**c,d**) and phase-based (**e,f**) acoustic methods. The colours blue, red and green represent x =1, 2 and 3, respectively, with y and z being the other two branches in each case. Error bars are calculated from time-averaged measurements and voltage sweep resolution for the voltage- and phase-based methods, respectively.

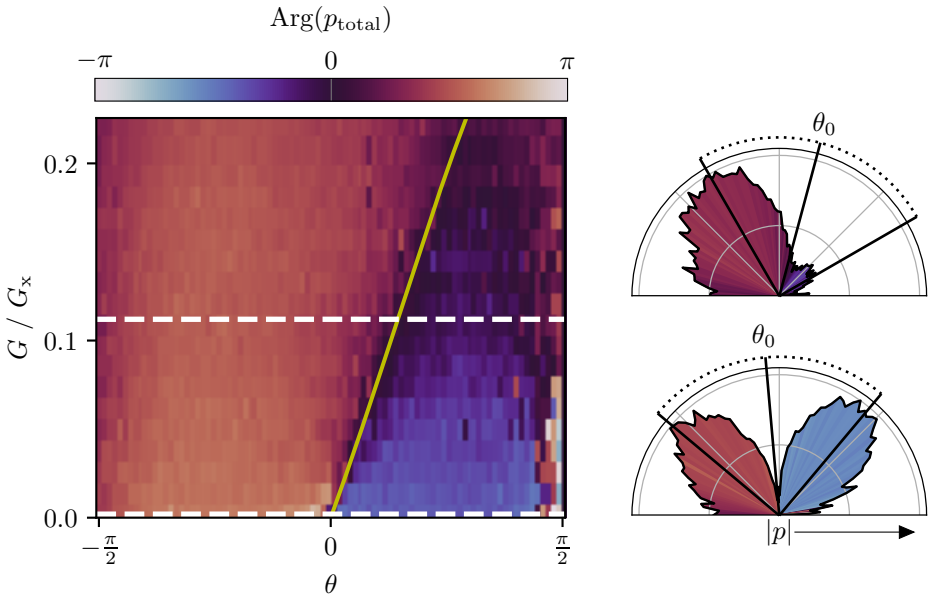

FIGURE 6.16: Far-field sound directivity as a function of conductance ratio for the two-branch device. **Left:** Stacked directivity plots showing experimental sound phase as a function of conductance ratio. The expected shift of the null from (6.25) is shown by the yellow line. **Right:** Experimental results for $G_x \gg G$ and $G_x = 0.11G$, respectively. The angle of the sound field null, θ_0, along with the positions of the lobes to either side are indicated.

$G_x = 3.3G$. It is therefore important to optimise G, k and d to achieve the greatest measurement sensitivity. The sensitivity can also be improved by increasing the measurement distance between the device and microphone. This is due to the radial nature of the measurement, where the arc length for a change in angle increases with the increased measurement distance

6.6 Conclusions

In this chapter, it was demonstrated how the sound generated by thermophone devices can be used to determine the electrical and thermal properties of the film directly from the sound they produce. This was achieved by using branched thin film devices configured as a thermoacoustic bridge. The observed behaviour is owed to the electrical coupling between thermophone elements, where the sound produced by each element is dependent on the properties of all other elements. By measuring the sound under different voltage driving conditions, the conductance of each branch and its temperature dependence can be determined. For the two- and three-branch devices demonstrated, the conductance measurement involves balancing the sound output from each branch. It was shown how this can be achieved using both the source magnitudes and relative phase. The behaviour of such devices is analogous

to the operation of a Wheatstone bridge, where, instead of balancing sound output from the branches, balance is achieved between the currents in the branches. The demonstration of the direct proportionality between sound and complex electric power shows its distinctive potential for thin film characterisation. In particular, this method of balancing the circuit, in contrast to the traditional method of balancing voltages, offers a way to determine the conductance without the need for additional contacts along the branches. Furthermore, when considering the spatial response of the generated sound, the sensitivity can be dictated by the choice of frequency and measurement distance.

The next chapter will explore a completely new direction for thermoacoustic generation, whereby the heat source is provided by the thermoelectric effect, rather than Joule heating.

Chapter 7

Thermo-Electro-Acoustics

7.1 Introduction

The work in this thesis thus far has focused primarily on the unique characteristics of Joule-based thermoacoustics, which arise from the fact that the sound generation occurs at the second harmonic of the driving signal. The aim of this chapter is to avoid these characteristics by generating sound instead at the first harmonic. This will be achieved by harnessing thermoelectric effects for sound generation, rather than Joule heating. This is currently an unexplored area for thermoacoustic generation, so this work aims to predict the characteristics of the sound generation in this case and validate them via experiment.

The chapter begins with a brief overview of the thermoelectric effects. The application of time-varying thermoelectric effects for thermoacoustic generation will then be considered, and a model for predicting the harmonic content of the sound and its dependence on the electric current will be derived. These predictions will then be compared to both FEM simulations and experimental measurements. It will be shown that first harmonic generation of sound is possible via the thermoelectric effect. This is a promising result, since it enables accurate audio reproduction, as well as offering unique opportunities for device optimisation and measurement.

7.2 Background Theory

This section will cover the background theory for describing the thermoelectric effect.

The thermoelectric effect is the coupling that occurs between the flows of electric current and heat in the presence of an electric field and/or temperature gradient [77]. Thermoelectricity is characterised by three distinct effects, which were discovered separately: the Seebeck, Peltier and Thomson effects. These will now be defined.

The Seebeck effect is the evolution of an electric field, $\boldsymbol{E}$, in a conductor due to a thermal gradient, ∇T. It is quantified by the phenomenological Seebeck coefficient, S, where

$$\boldsymbol{E} = S\nabla T\,.$$

Consider the circuit shown in Fig. 7.1, consisting of two branches, A and B, with a temperature difference, ΔT, applied across them. The potential difference between the ends of the branches is given by

$$\Delta V = (S_\mathrm{A} - S_\mathrm{B})\Delta T\,,$$

such that, for $S_\mathrm{A} \neq S_\mathrm{B}$, there will be a net flow of electric current. A simple way to achieve a difference in S is to use two different materials for A and B. In this particular case, the circuit is known as a thermocouple.

The Peltier effect describes the generation and absorption of heat at an interface due to an applied current. The effect is quantified by the Peltier coefficient, Π, which relates the flow of charge, $\boldsymbol{j}_e$, to the flow of heat, $\boldsymbol{j}_q$,

$$\boldsymbol{j}_q = \Pi\boldsymbol{j}_e\,.$$

Consider the junction in Fig. 7.1, with $\Pi_\mathrm{A} \neq \Pi_\mathrm{B}$, driven by an electric current, $\boldsymbol{j}_e$, in the absence of a temperature gradient. At the interface, $\boldsymbol{j}_e$ must be continuous, yet there is a change in the Peltier coefficient. To compensate this, there must be a discontinuity in the heat flow at the interface, *i.e.*, a heat source/sink, where

$$\frac{\mathrm{d}Q}{\mathrm{d}t} = (\Pi_\mathrm{A} - \Pi_\mathrm{B})\,\boldsymbol{j}_e\,.$$

The heat generated or absorbed at the interface will be simultaneously compensated for by an opposing source or sink elsewhere in the circuit. For instance, in a closed loop consisting of two materials, a driving current will cause heat generation at one interface and heat absorption at the other. Whether heat is generated or absorbed depends on the direction of the current and the sign of $\Delta\Pi = \Pi_\mathrm{A} - \Pi_\mathrm{B}$.

The Thomson effect is a more general form of the Peltier effect, whereby the Peltier coefficient is temperature dependent. In this case, a temperature gradient across a single conductor will lead to a gradient in the Peltier coefficient. This results in a continuous form of the Peltier effect when the conductor is driven with an electric current,

$$\frac{\mathrm{d}Q}{\mathrm{d}t} = -\mathcal{T}\boldsymbol{j}_e \cdot \nabla T\,,$$

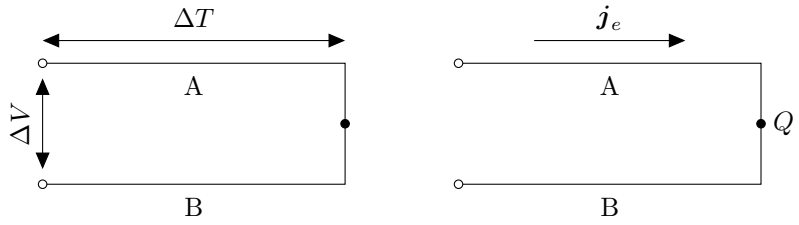

FIGURE 7.1: The Seebeck and Peltier effects in a junction between two conductors, A and B, with different material properties. **Left:** The Seebeck effect. In the absence of a driving current, a temperature gradient across the two branches results in a potential difference between the two ends. **Right:** The Peltier effect. In the absence of a thermal gradient, driving an electric current through the junction results in heat generation or absorption, depending on the direction of the current.

where $\mathcal{T}$ is the Thomson coefficient.

The thermoelectric effects are all manifestations of the same underlying principles [105]. The connection between the effects is described by the Thomson relations,

$$\begin{aligned}\mathcal{T} &\equiv \frac{\mathrm{d}\Pi}{\mathrm{d}T} - S\,,\\ \Pi &= TS\,,\\ \mathcal{T} &= T\frac{\mathrm{d}S}{\mathrm{d}T}\,.\end{aligned}$$

It can therefore be seen that all of the effects can be described in terms of one physical parameter. This is usually the Seebeck coefficient, due to the relative ease with which it can be measured. Combining the effects allows for a modified version of the thermal diffusion equation to be derived,

$$\underbrace{\kappa\nabla^2 T - \rho c_p \frac{\partial T}{\partial t}}_{\text{Fourier}} = \underbrace{-\frac{\boldsymbol{j}_e^2}{\sigma}}_{\text{Joule}} + \underbrace{T\nabla S\cdot\boldsymbol{j}_e}_{\text{Thermoelectric}}\,, \tag{7.1}$$

whereby the thermoelectric effect manifests itself as an additional source term in the thermal diffusion equation (a full derivation of this is included in Appendix B.)

It is important to note that the thermoelectric term depends on both the temperature and the driving current, hence the resulting source is nonlinear. In standard thermoelectric applications, which typically involve time-independent currents, this is not usually an issue. However, for thermoacoustic generation this is not the case, making any kind of solution difficult. The response to a time-varying current will be investigated in the following section.

7.3 Thermoelectric-Based Thermoacoustics

In this section, the thermoelectric heat equation will be applied in the context of thermoacoustic generation. In contrast to the previous chapters, here the Peltier effect will be the heat source used in sound generation, rather than the Joule heat.

Equation 7.1 shows that the heat generated by the Peltier effect is linear with respect to the electric current. This has important consequences for thermoacoustic generation, since it suggests that, for a thermoelectric device, thermoacoustic generation also occurs at the first harmonic, avoiding the issues with second harmonic generation encountered with Joule-based thermoacoustics. This is an attractive prospect – if a device could be constructed that minimises the Joule heat, while simultaneously maximising the Peltier heat, then sound generation with very low harmonic distortion could be realised. This picture is complicated, however, by the fact that the Peltier heat also depends on the temperature, resulting in a nonlinear source. For a time-varying current, it is therefore expected that there will be some additional harmonic distortion, which will need to be quantified. While a complete analysis of the thermoelectric response would require a numerical approach, some insight can be gained by studying some simplified cases.

Consider a thermoelectric system consisting of a single point, containing both Joule and Peltier sources. For a time-varying current, $I(t)$, (7.1) becomes

$$\kappa\frac{\partial^2 T}{\partial x^2} - \rho c_p \frac{\partial T}{\partial t} = -\frac{I(t)^2}{\sigma} + \Delta S T I(t)\,. \tag{7.2}$$

If the point is thermally isolated from its surroundings, *i.e.*, $\kappa = 0$, then this can be simplified to

$$\frac{\mathrm{d}T}{\mathrm{d}t} + \frac{\Delta S}{\rho c_p} I(t) T = \frac{I^2(t)}{\sigma \rho c_p}. \tag{7.3}$$

Using the integrating factor

$$\text{I.F.} = \exp\left(\frac{\Delta S}{\rho c_p}\int I(t)\,\mathrm{d}t\right)\,,$$

(7.3) can be solved, yielding

$$T(t) = \frac{\int \exp\left(\frac{\Delta S}{\rho c_p}\int I(t)\,\mathrm{d}t\right)\frac{I^2(t)}{\sigma\rho c_p}\,\mathrm{d}t}{\exp\left(\frac{\Delta S}{\rho c_p}\int I(t)\,\mathrm{d}t\right)}\,.$$

For a driving current consisting of a single frequency,

$$I(t) = I_0 \sin(\omega t)\,,$$

$$T(t) = \frac{\int \exp\left(-\frac{\Delta S I_0}{\omega \rho c_p}\cos(\omega t)\right) \frac{I_0^2 \sin^2(\omega t)}{\sigma \rho c_p}\,\mathrm{d}t}{\exp\left(-\frac{\Delta S I_0}{\omega \rho c_p}\cos(\omega t)\right)}\,,$$

which has no closed-form solution. To proceed, consider the case where the Joule heat is negligible ($\sigma \to \infty$), such that

$$T(t) = C \exp\left(-\frac{\Delta S I_0}{\omega \rho c_p}\cos(\omega t)\right),$$

where C is a constant defined by the initial condition. Performing a Taylor expansion,

$$\begin{aligned}\exp(a\cos(\omega t)) &= 1 + a\cos(\omega t) + \frac{a^2}{2!}\cos^2(\omega t) + \frac{a^3}{3!}\cos^3(\omega t) + \dots \\ &= C_0 + C_1\cos(\omega t) + C_2\cos(2\omega t) + C_3\cos(3\omega t) + \dots\,,\end{aligned}$$

where a and C_i are constants. It can therefore be seen that the nonlinearity of the Peltier source results in a first harmonic, as well as diminishing upper harmonics. These upper harmonics are the result of a feedback loop, where the heat generated in one instant is dependent on the heat that was generated in the previous instant.

Further insight can be gained by considering that, for a fixed heating rate, the magnitude of AC temperature oscillations decreases with frequency, since less heat is added to the system per cycle. For acoustic frequencies, the AC temperature oscillations are negligible compared to the background DC field. Because of this, it can be assumed that the Peltier source is primarily dependent on the DC temperature. This simplification allows for some basic current relationships to be derived. Consider an isolated Peltier junction, small enough that it approximates a point source. For convenience, the electrical parameters will be lumped, *i.e.*, $j_e \to I$, $\frac{1}{\sigma} \to R$. The junction is then driven by a time-varying current with a DC offset,

$$I(t) = I_0 + I_1 \sin(\omega t)\,.$$

The Joule heat dissipated in the junction is

$$\begin{aligned}Q_{\text{Joule}} &= I^2 R \\ &= I_0^2 R + \frac{I_1^2 R}{2} + I_0 I_1 R \sin(\omega t) - \frac{I_1^2 R}{2}\cos(2\omega t)\,.\end{aligned}$$

For a given heat source, Q, the temperature of the junction will be proportional to this source,

$$T = aQ\,,$$

where a is the coefficient of proportionality. The Joule heat source therefore results in two temperature harmonics, as well as a DC field,

$$\begin{aligned}
|T_0| &= T_\mathrm{a} + a_0 I_0^2 R + \frac{a_0}{2} I_1^2 R\,,\\
|T_1| &= a_1 I_0 I_1 R\,,\\
|T_2| &= \frac{a_2}{2} I_1^2 R\,,
\end{aligned}$$

where the subscript refers to the harmonic and T_a is the ambient temperature. The Peltier source will depend on the DC temperature field, such that

$$Q_\mathrm{Peltier} = -\Delta S \left(T_\mathrm{a} + a_0 I_0^2 R + \frac{a_0}{2} I_1^2 R\right) \left[I_0 + I_1 \sin(\omega t)\right]\,.$$

This results in DC and first harmonic contributions to the temperature field. Combining this with the contributions from the Joule heat yields

$$|T_0| = (1 - a_0 \Delta S I_0) \left(T_\mathrm{a} + a_0 I_0^2 R + \frac{a_0}{2} I_1^2 R\right)\,, \tag{7.4}$$

$$|T_1| = a_1 I_1 \left[I_0 R - \Delta S \left(T_\mathrm{a} + a_0 I_0^2 R\right)\right] - \frac{a_0 a_1}{2} \Delta S R I_1^3\,, \tag{7.5}$$

$$|T_2| = \frac{a_2}{2} I_1^2 R\,. \tag{7.6}$$

The first harmonic temperature component contains both linear and cubic terms with respect to the driving current, I_1. These terms are due to the Peltier effect acting on the DC temperature of the junction, as well as the first harmonic response from a DC-biased Joule source. The dependence of $|T_1|$ on I_0 is quadratic. This response is not necessarily symmetric with respect to the sign of I_0, with a minimum in the first harmonic temperature occurring at

$$I_{0,\mathrm{min}} = \frac{1}{2\alpha_0 \Delta S}\,. \tag{7.7}$$

This asymmetry is expected, since the DC Peltier effect serves to either increase or decrease the junction temperature, depending on the current direction. This difference in the interface temperature then feeds into the magnitude of the AC Peltier effect.

The rest of the chapter will now focus on validating these claims, both through FEM modelling and experimental measurements.

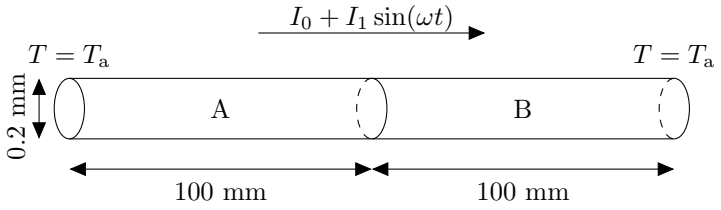

FIGURE 7.2: Schematic of FEM thermocouple model. The model consists of two cylindrical conducting branches in electrical and thermal contact. The outer ends of each branch are held at T_a and an out-of-plane heat flux, corresponding to convection into air, is present along the entire length of the model. Electric current is then passed through the branches and the interface.

7.4 FEM Modelling

To test the predictions in the previous section, an FEM model of a thermocouple junction was used. This model is outlined in Fig. 7.2. Two thermocouple material pairs were tested: chromel/alumel (K-type), and copper/constantan (T-type). Material parameters used are given in Appendix E.

To begin with, the frequency components and spatial extent of the temperature field were analysed. Here, the junction was driven at a single frequency, without DC bias. The results of these simulations are shown in Fig. 7.3. Looking at the spectral response of the temperature at the interface, it can be seen that the response is primarily first harmonic, with much smaller second harmonic and third harmonics. The reason for the large difference in amplitude can be seen from the spatial distribution of each of the harmonics – the heat generated by the Peltier effect manifests as a point heat source located purely at the interface, whereas the Joule source is distributed throughout the branches. The first harmonic temperature field around the interface is governed by the thermal diffusion lengths of the two branches and is therefore frequency-dependent, becoming more focused around the interface as the frequency is increased. Note that there appears to be a point-like source in the second harmonic response as well. This is not physical, and is instead due to the small second harmonic distortion present in the input current as a result of the finite time stepping in the model.

The dependence of the temperature field on the driving current was then investigated. The dependence of the first and second harmonics on $|I_1|$, for $I_0 = 0$, is shown in Fig. 7.4 for both K and T-type material pairs. As can be seen, the first harmonic demonstrates the expected cubic dependence on $|I_1|$, in accordance with (7.5). The magnitude of the temperature is dependent on more than just ΔS at the interface, for which there is a 7% difference between the two material pairs. The dependence on the DC bias current, I_0, was also simulated, shown in Fig. 7.5, from which a

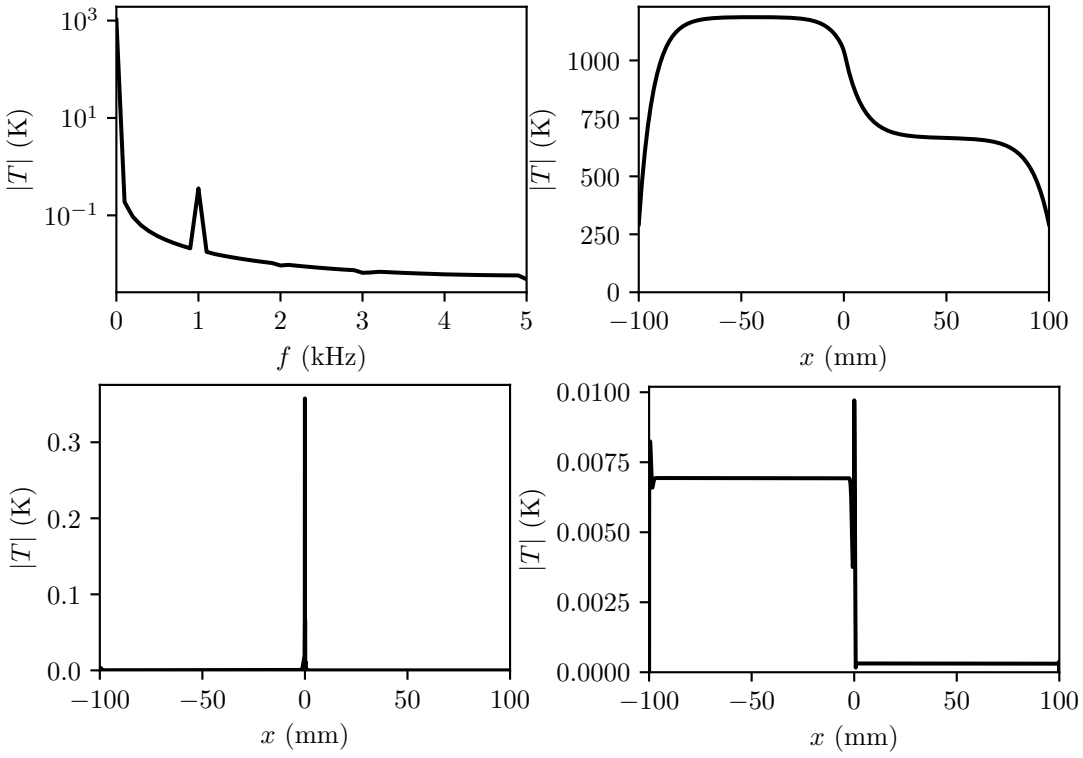

FIGURE 7.3: Spatial dependence of thermal harmonics for a K-type junction when driven at 1 kHz without dc bias. $|I_1| = 1\,\mathrm{A}$. **Top left:** Spectral response of the temperature at the interface between A and B. **Top right:** Spatial dependence of the DC temperature field. **Bottom left:** First harmonic. **Bottom right:** Second harmonic.

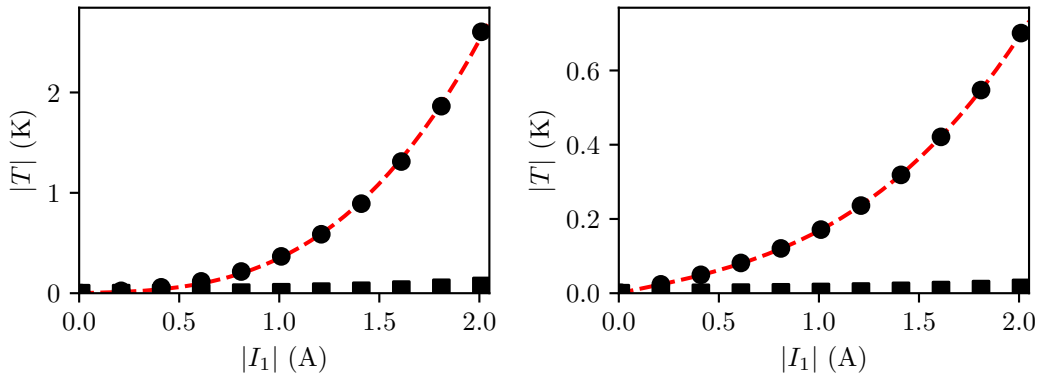

FIGURE 7.4: First (circles) and second (squares) temperature harmonics at the interface as a function of $|I_1|$, where $I_0 = 0$. **Left:** K-type. **Right:** T-type. The red dashed lines are cubic functions, fitted to the model data.

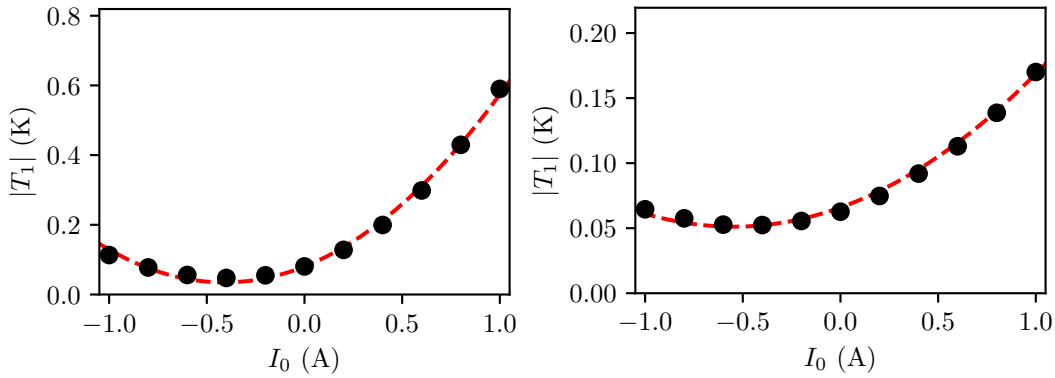

FIGURE 7.5: First harmonic temperature as a function of I_0, where $|I_1| = 0.5\,\mathrm{A}$. **Left:** K-type. **Right:** T-type. The red dashed lines are quadratic functions, fitted to the model data.

quadratic dependence is evident, with the location of the minimum depending on the system thermal parameters, as with (7.7).

The agreement seen here suggests that the current relationships in the previous section may be sufficient for describing thermoelectric effects in thermophones. This will now be tested experimentally.

7.5 Experiment

To demonstrate thermoacoustic generation via the Peltier effect, thermal and acoustic measurements were performed on commercially available thermocouples, an example of which is shown in Fig. 7.6. Two thermocouple types were measured for this work: K-type and T-type. The K-type thermocouple had a branch length of 1 m and diameter of 0.5 mm, resulting in a total resistance of 6 Ω. The length of the T-type thermocouple was 27 cm, with diameter 60 mm and $R = 0.6\,\Omega$.

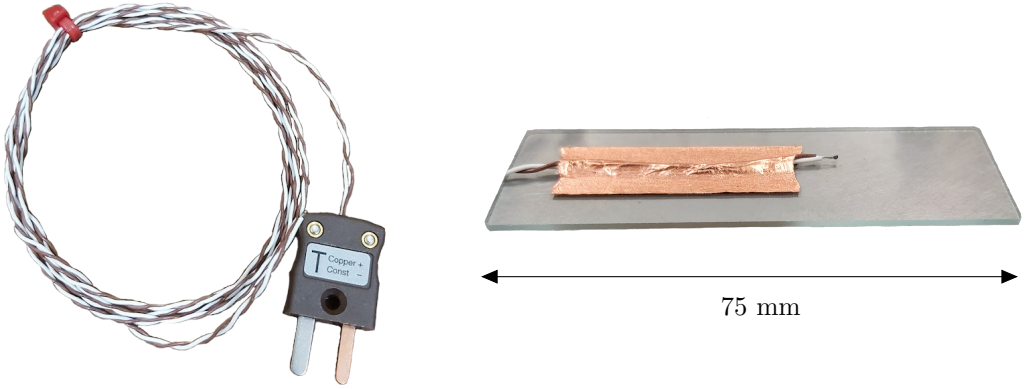

FIGURE 7.6: Example thermocouple used in this study. **Left:** T-type (copper/constantan) thermocouple. **Right:** Thermocouple mounted on microscope slide for measurement.

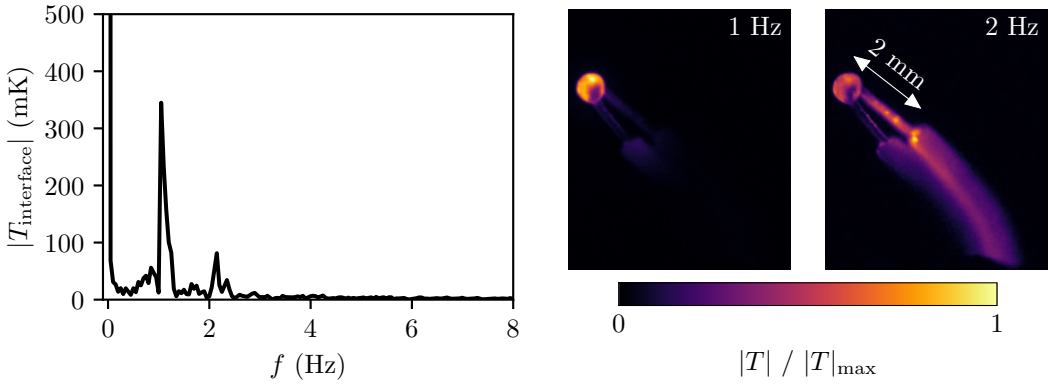

FIGURE 7.7: Thermal measurements of a K-type thermocouple driven with $I_1 = 0.1\,\text{A}$ and $f_1 = 1\,\text{Hz}$. **Left:** Average temperature of the thermocouple interface as a function of frequency. **Right:** Thermal reconstructions at the frequency peaks in the frequency spectrum.

To begin with, the thermal response of a thermocouple was measured. The K-type thermocouple was driven at 1 Hz and the temperature at the interface was measured. The results of these measurements are shown in Fig. 7.7. From the spectral measurements, the presence of both first and second harmonics is evident, with a significantly greater first harmonic. Looking at the spatial distribution of the temperature field at each harmonic reveals that the heat dissipation at the first harmonic occurs primarily at the interface, whereas the second harmonic response is more global. This is in direct correspondence with the predictions from the FEM model, suggesting that the Peltier and Joule effects are responsible for the observed thermal response.

The acoustic properties of the thermocouples were then measured. The devices were placed on a bench top and acoustic measurements were performed normal to the device at a distance of 30 cm. The spectral response of the K-type thermocouple was

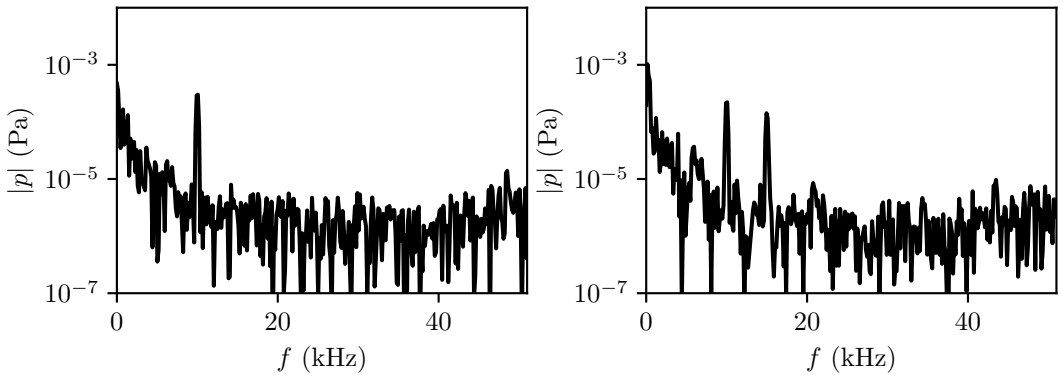

FIGURE 7.8: First harmonic sound generation from a K-type thermocouple. **Left:** Acoustic frequency spectrum for a single driving frequency, $f_1 = 10\,\text{kHz}$. **Right:** Acoustic spectrum for two driving frequencies, 10 and 15 kHz.

first measured for both a single drive frequency (10 kHz), as well as a combination of frequencies 10 and 15 kHz). The resulting sound spectra are shown in Fig. 7.8. First harmonic sound generation is clearly seen, with no discernible second harmonic. In the multi-frequency case, this results in an accurate reproduction of the input signal, without additional heterodyne distortion. The lack of Joule-related harmonics is attributed to the low driving power for these measurements (around 0.4 W for the entire device, where only the small region of wire around the interface was exposed to air).

The dependence of the sound on the driving current was also measured for the two thermocouple types, for both unbiased and DC-biased cases. These measurements were performed for a driving frequency of $f_1 = 10\,\text{kHz}$. The measured dependence on $|I_1|$ is shown in Fig. 7.9. The expected cubic and quadratic dependence is seen for the first and second harmonics, respectively. Interestingly, the first harmonic sound generated by the K-type thermocouple is much greater than that of the T-type thermocouple. This was also seen in the FEM modelling; however, in the experimental case the difference is much greater. The reason for this is currently unclear, since considerations such as the geometric differences between the devices cannot account for such a difference in output. One potential line of investigation is the electromagnetic response of the devices, since the materials in the K-type thermocouple are magnetic, whereas those in the T-type are not. This constitutes part of the future work for this chapter.

Finally, the dependence on the DC bias was measured for both thermocouple types. Again, $f_1 = 10\,\text{kHz}$. The results of these measurements are shown in Fig. 7.10. The K-type thermocouple shows the expected quadratic dependence, with an asymmetric dependence on the sign of the offset current. This is less the case with the T-type

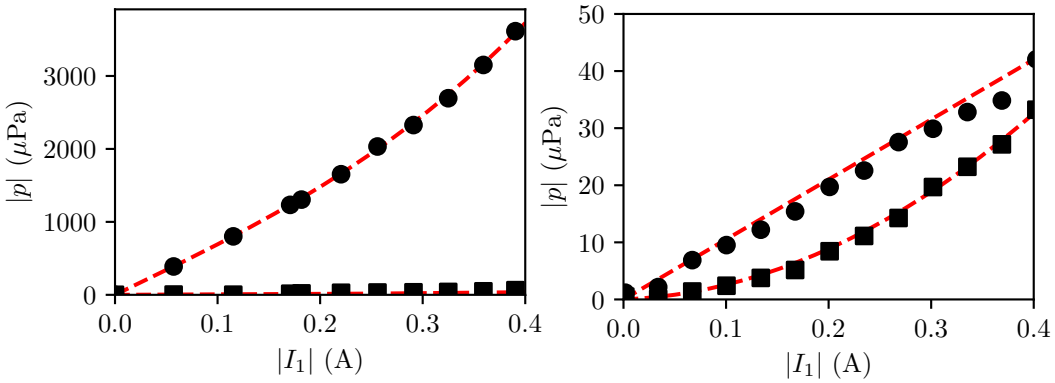

FIGURE 7.9: Measured dependence of both first (circles) and second (squares) harmonics on $|I_1|$, for $I_0 = 0$ and $f_1 = 10\,\text{kHz}$. Red dashed lines are cubic and quadratic fits to the data for the first and second harmonics, respectively. **Left:** K-type thermocouple. **Right:** T-type.

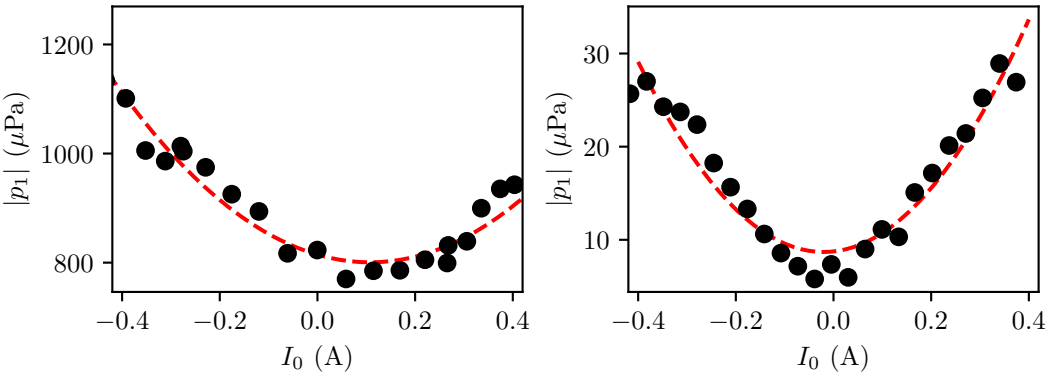

FIGURE 7.10: Measured dependence on the first harmonic sound on the DC bias current for the two thermocouple types. Black circles indicate measurements, and red dashed lines are quadratic fits. $|I_1| = 0.1\,\text{A}$, $f_1 = 10\,\text{kHz}$. **Left:** K-type thermocouple. **Right:** T-type.

thermocouple, for which the dependence is more linear and symmetric. The first harmonic sound in this case is therefore more likely due to the Joule heat from a DC-biased source, rather than the Peltier effect. Despite this, the quadratic dependence seen, with the differing locations for the minima, is potentially very useful. Equation (7.7) suggests that the minimum could be used to measure the thermal properties of devices. To achieve this, the unknown proportionality constant would first need to be accounted for, either via a direct measurement and/or a better model, or by performing relative measurements, as with Chapter 6. This remains a line for future investigation.

7.6 Conclusions

This chapter explored a novel direction for thermoacoustic generation, whereby the heat source was provided by the Peltier effect, rather than Joule heating. This method of sound generation leads to further possibilities that cannot be achieved by Joule-based thermoacoustics.

The thermal response of a simplified thermocouple junction to a time-varying current was modelled analytically. It was found that the Peltier effect leads to heat dissipation at the first harmonic, rather than the second harmonic generation encountered with Joule heating. The reason for this is the ability of the Peltier effect to dissipate or absorb heat, depending on the direction of the electric current. This was then compared to an FEM model of a thermocouple, which produced similar results.

Thermal and acoustic measurements were then performed on standard thermocouples. For this, K-type and T-type thermocouples were measured. Both thermocouple types exhibited clear first harmonic generation of sound, with a cubic dependence on the driving current, in agreement with the analytical model. The sound generated by the K-type thermocouple was much greater than that of the T-type. The reason for this is unclear, and a more detailed characterisation of the electromagnetic properties of the two thermocouple types is required to understand this behaviour.

Sound generation at the first harmonic is an attractive prospect for thermoacoustic generation. This is particularly the case in applications such as audio reproduction, where the harmonic distortion associated with Joule heating could be avoided without the use of a DC bias. In the absence of a DC bias, the device equilibrium temperature would also be lower, increasing device efficiency. This could be further improved by utilising the DC Peltier effect to provide cooling at the thermocouple junction.

This chapter concludes the experimental work undertaken in this thesis. The following chapter suggests some future directions for continuing the work presented here.

Chapter 8

Future Work

In this chapter, some suggestions will be made for expanding on the work presented in this thesis.

8.1 Chapter 4: Acoustic Sources

An immediate continuation of the work from this chapter would be to investigate the suppression of the sound at increased frequencies, seen in Fig. 4.9. This effect was only seen with this particular device, so it would be instructive to identify whether this is due to a device defect, or some physical effect that was unaccounted for. Outside of this, a natural extension of the work would be to explore the effect of the average device temperature on the sound generation; in particular, how the efficiency scales with the applied power. The thermoacoustic model could also be extended to include the effects of thermal expansion of the substrate and film, as well as thermal convection and radiation.

8.2 Chapter 5: Thermoacoustic Phased Arrays

To gain a deeper understanding of thermoacoustic arrays, future works could aim to investigate the effects of other coupling mechanisms between array elements, such as mutual inductance or thermal coupling. Here, thermal coupling will be discussed.

Joule heating as a transduction method is irreversible, hence thermoacoustic array elements are not expected to be able to couple directly through temperature or pressure. Array elements do, however, have the potential to affect each other via temperature-dependent material properties (such as the thermal properties of the device and surrounding air, or the conductivity of the films), as seen with hot-wire anemometry [60].

There are two contributing factors from Joule heating to the local temperature field: the AC heat associated with the sound waves, and the DC heat. It was shown in Section 2.2 that the local temperature changes due to the AC component have a characteristic decay length of

$$\delta = \sqrt{\frac{2\kappa}{\rho c_p \omega}},$$

where κ is the thermal conductivity, ρ is the density, c_p is the isobaric specific heat capacity, and ω is the angular frequency. At equilibrium values, with a heating frequency of $f_2 = 1\,\text{kHz}$, this results in decay lengths of the order of $10^{-5}\,\text{m}$ in the air and substrate. Considering this, as well as the small amplitude of the AC oscillations, it is unlikely that the AC component had any effect in this chapter, especially as the frequency was increased. This is confirmed in the thermal reconstructions, such as Fig. 5.5, where, even for $f_1 = 1\,\text{Hz}$, it is clear that the decay length is short enough for the elements to act independently. Despite this, the thermal decay length may pose an upper limit on the density of array elements as arrays are miniaturised.

The DC heat is much more likely to lead to an effect on device performance. Some preliminary experiments were performed to quantify this. The influence of the DC heat was studied by measuring the sound pressure from a pair of elements as a function of driving power. The two central elements on the 16-element linear array (separation 0.4 mm) were driven by independent voltage sources, with $f_2 = 10\,\text{kHz}$, and the sound pressure was measured normal to the device ($r = 30\,\text{cm}$) as the driving power was varied. For each power step, the device was allowed 30 s to reach equilibrium, before averaging the sound pressure over a period of 10 s. These measurements were performed for three cases: driving element 8 only, driving element 9 only, and driving both elements in-phase. The sound pressure when driving the elements simultaneously was then compared to the sum of the sound pressures when driving the elements independently. It is expected that any thermal coupling would cause a discrepancy between these two results, with the difference increasing as a function of driving power. The results of the measurements are shown in Fig. 8.1. As can be seen, the difference between the simultaneous and sum of isolated cases is negligible up until a power of 1 W, where the two cases begin to diverge. This may be some evidence of thermal coupling, although further experiments would be needed to identify whether they continue to diverge, or if this is simply an artefact. Experimentation would also need to determine the coupling mechanism itself, whether this be a temperature dependence resistance of one of the elements, or coupling within the air itself.

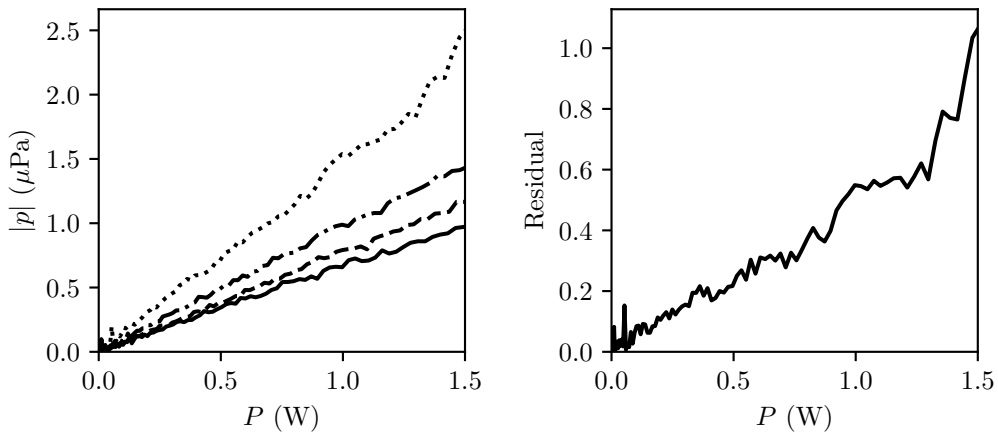

FIGURE 8.1: Thermal coupling between adjacent thermophones, using elements 8 and 9 from the 16-element linear array in Fig. 5.20. **Left:** Sound pressure normal to the device ($f_2 = 10\,\text{kHz}$, $r = 30\,\text{cm}$) as a function of driving power. Shown are measurements for each element driven in isolation (8: solid line. 9: dashed line), as well as both elements driven simultaneously (dotted line), compared to the sum of the isolated cases (dashdotted line). **Right:** Difference between the simultaneous driving case and sum of the isolated cases as a function of power.

8.3 Chapter 6: A Thermoacoustic Bridge Circuit

The thermoacoustic bridge technique can be extended to determine additional properties of the thin film. For example, if the conductance is temperature dependent then, for small changes around a reference temperature, T_0, the resistance can be modelled using a first-order Taylor expansion [106], such that the conductance is

$$G(T) = \frac{G_0}{1 + a(T - T_0)},$$

where a is a material constant and G_0 is the conductance at T_0. The temperature of the film is linearly dependent on the Joule power. This was verified experimentally in Chapter 4. As a result, the material constant a can be determined from measurements of the conductance at different power values. In the case where only G_3 is temperature dependent, the minimum in the total Joule power shifts in phase as a function of the temperature. This is simulated in Fig. 8.2. Looking at the directivity of the far-field sound, a shift also occurs in the sound field null. By measuring the location of this null as a function of temperature, a can be determined directly from the sound field. Moreover, as the sound also depends on the thermal conductivity and heat capacity (from the full thermophone model presented in Chapter 4) it could be used to measure these properties simultaneously with the electrical ones. As such, there is significant scope in the future to develop the thermoacoustic bridge

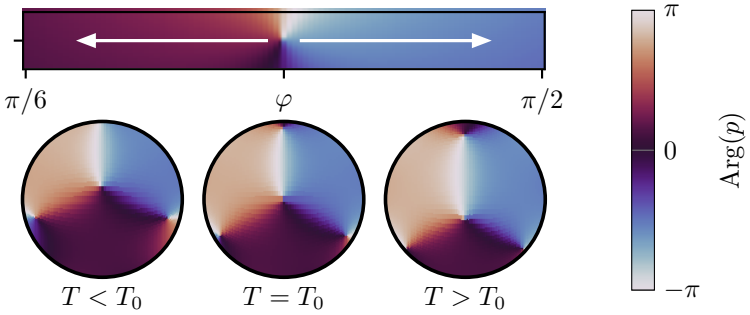

FIGURE 8.2: Simulated temperature dependence of the point of zero total Joule power. **Top:** Shift in the zero point as a function of temperature. White arrows indicate direction of shift. **Bottom:** Orthographic projections of the far-field sound directivity at three different temperatures relative to T_0, showing a shift in the central null for $T \neq T_0$.

into a powerful technique for precision measurements of thin-film parameters.

8.4 Chapter 7: Thermo-Electro-Acoustics

The work in this chapter was only a proof-of-concept for this transduction mechanism. There are, therefore, many future directions this work could take. To begin with, however, it is necessary to gain a more complete understanding of the effects of the various material parameters at play. A more comprehensive study of different junction materials would be very beneficial to this end. Quantification of the acoustic efficiency of such devices would also play an important role in defining the future of this transduction method. Of particular interest is be how the effect would scale with multiple junctions in series. Outside of these more standard experiments, the reversibility of the thermoelectric effect could allow for some more unique behaviours, such as devices acting as receivers.

One curiosity presented by the modelling in Section 7.3 is that a DC bias would allow for control over the average operating temperature of the device. This seems reasonable since, for one current direction, there would be a net cooling effect at the junction, lowering its temperature. From (7.4) it can be seen that the dependence of the average temperature on the bias is a cubic,

$$T_0 - T_\mathrm{a} = -a_0^2 \Delta S R I_0^3 + a_0 R I_0^2 - \left(a_0 \Delta S T_\mathrm{a} - \frac{a_0^2}{2} \Delta S R I_1^2 \right) I_0 + \frac{a_0}{2} I_1^2 R \,.$$

Careful adjustment of the device parameters may cause this equation to have a real root. In this case, the DC heat from the device could be eliminated (at least at the junction), improving device performance.

8.5 Conclusions

In this chapter, some directions for future investigation were suggested, based upon the work presented in this thesis.

Firstly, for the work on single thermoacoustic sources, the suggested work involved clarifying discrepancies in the experimental results. Further validation of the presented thermoacoustic model was then suggested.

Secondly, for thermoacoustic arrays, it was suggested that other coupling mechanisms should be investigated. Some preliminary results for measurements of thermal coupling were shown, which suggested there may be some coupling at higher powers due to the DC background field generated by the elements.

Suggestions for the thermoacoustic bridge circuit involved extending the method to measure other material parameters. It was shown how the temperature dependence of the conductance could be measured, as well as suggesting methods for determining thermal properties.

Finally, for thermoelectric-based thermoacoustics, suggestions mainly involved further characterisation of the effect itself, since it is still not well understood. On top of this, it was shown how the electrical DC bias may be able to be exploited to reduce the DC heat produced by the device, improving its efficiency.

The next chapter is the final chapter of the thesis, and summarises all of the findings of this work.

Chapter 9

Conclusions

In this chapter, the findings from all of the work undertaken in this thesis will be summarised. The chapter, and therefore this thesis, concludes with a final statement from the author.

9.1 Chapter 4: Acoustic Sources

In this chapter, a simple point source solution for the thermoacoustic equations was derived, which was then developed into an analytical model for real thermoacoustic devices. This model was then compared to and validated with finite element modelling and experimental measurements, where good agreement was seen. The acoustic and thermal reconstruction methods outlined in Chapter 3 were also tested, and shown to be effective characterisation techniques for thermophone design. Finally, finite element modelling was used to quantify some of the erroneous features seen in the experimental data, the origin of which was shown to be diffraction and scattering from the measurement apparatus, rather than any notable result. These effects were shown to be minimised by reducing the acoustic frequency.

9.2 Chapter 5: Thermoacoustic Phased Arrays

This chapter investigated the feasibility of thermoacoustic sources for use in ultrasonic phased arrays. Thermoacoustic arrays were tested and were able to reproduce the beam forming and steering effects that make phased arrays desirable. On top of the ease of fabrication and lack of mechanical cross-talk compared to traditional phased arrays, thermoacoustic arrays were found to exhibit some unique characteristics that can be used to further improve their effectiveness. In particular, thermoacoustic sources were found to be incredibly sensitive to the local electrical current density, where increased current density results in 'hot-spots' on the device.

It was demonstrated how, by careful choice of device geometry, these regions could be tailored to behave as individual acoustic sources, producing a phased array using a single conductive film. It was also found that electrical coupling of thermoacoustic array elements leads to additional, 'phantom' sources of sound, due to the inherent nonlinearity of Joule heating. While these sources can be negated via DC biasing or careful tuning of the driving signal, they also enable the potential for simplification of array design by reducing the total number of electrical contacts, or even array elements, required.

9.3 Chapter 6: A Thermoacoustic Bridge Circuit

The work in this chapter expanded upon the findings on thermoacoustic arrays, exploiting the electrical coupling between array elements to produce an acoustic analogue of an electrical bridge circuit. It was shown how the sound field produced by this type of device can be used to measure the electrical and thermal properties of the elements themselves, as well as additional, non-thermoacoustic elements.

9.4 Chapter 7: Thermo-Electro-Acoustics

The final experimental chapter in this thesis pushed thermoacoustics in an entirely new direction. It was found that utilising the thermoelectric effect as the primary heat source offers the potential for the sound generation to be 1:1 with the source signal, as opposed to the second harmonic generation seen with Joule-based thermoacoustics. The reason for this is the reversible nature of the thermoelectric effect, allowing for both heat generation and absorption at an interface. A set of relationships describing the behaviour of each of the harmonics was then derived and verified experimentally, using thermocouples as thermophones. Clear first harmonic generation was seen, which was found to occur almost entirely at the material interface. Thermoelectric generation of sound therefore shows great promise for more faithful audio reproduction, as well as device miniaturisation.

9.5 Concluding Remarks

The aim of this work was to expand upon the existing literature to help realise the full potential of thermoacoustic generation. This method of sound generation has a number of unique characteristics compared to more traditional transduction methods. Previous works have mostly considered these as detrimental aspects and sought to mitigate them. In contrast, the salient message this work aims to convey is that

such phenomena should not be readily dismissed, as they often lead to interesting – and useful – applications. While thermoacoustics may not necessarily be able to compete with its mechanical counterparts in traditional applications, its unique nature may make it much more desirable in others. In any case, thermoacoustics certainly isn't *just* hot air.

Appendix A

The Navier-Stokes Equation

The Navier-Stokes equation is the key equation for describing the motion of fluids. Here it will be derived for a Newtonian fluid in the absence of external forces (such as gravity) by constructing a continuity equation for fluid momentum. This derivation is based upon the work of Morse and Ingard [75].

The continuity of fluid momentum is described by

$$\frac{\partial}{\partial t}\left(\rho' \boldsymbol{u}\right) + \nabla \cdot \mathfrak{J} = 0\,,$$

where $\mathfrak{J}$ is the momentum flux. The momentum flux is a tensor quantity, since it is the product of the momentum density and the fluid velocity, both of which are vectors. Therefore,

$$\mathfrak{J} = \rho' \begin{bmatrix} u_x u_x & u_x u_y & u_x u_z \\ u_y u_x & u_y u_y & u_y u_z \\ u_z u_x & u_z u_y & u_z u_z \end{bmatrix}\,. \tag{A.1}$$

The continuity of fluid momentum can be converted to an equation of motion by considering that a net force will act as a source of momentum. Defining the stress tensor, $\mathfrak{P}$, the net force on a volume element is given by the divergence of this quantity. The continuity equation then becomes

$$\frac{\partial}{\partial t}\left(\rho' \boldsymbol{u}\right) + \nabla \cdot \left(\mathfrak{J} + \mathfrak{P}\right) = 0\,. \tag{A.2}$$

In the absence of viscous effects, the stress tensor is simply described by the fluid pressure,

$$\mathfrak{P} = \begin{bmatrix} p' & 0 & 0 \\ 0 & p' & 0 \\ 0 & 0 & p' \end{bmatrix}\,.$$

Viscosity is a result of momentum diffusion in a fluid. In a simple 2D case, the shear stress produced by two adjacent fluid regions moving in y at different velocities is given by

$$D_{xy} = -\mu \frac{\partial u_y}{\partial x}\,, \tag{A.3}$$

where μ is the coefficient of viscosity. Viscous dissipation manifests as a sink term in the momentum continuity equation, which is described by the viscous-stress tensor,

$$\mathfrak{D} = \begin{bmatrix} D_{xx} & D_{xy} & D_{xz} \\ D_{yx} & D_{yy} & D_{yz} \\ D_{zx} & D_{zy} & D_{zz} \end{bmatrix}\,.$$

To construct this tensor in the 3D case, a few additional considerations must be made. For this purpose, the shear-strain tensor,

$$\mathfrak{U} = \begin{bmatrix} U_{xx} & U_{xy} & U_{xz} \\ U_{yx} & U_{yy} & U_{yz} \\ U_{zx} & U_{zy} & U_{zz} \end{bmatrix}\,,$$
$$U_{ij} = \frac{\partial u_i}{\partial x_j}\,,$$

will be used, where $i, j = \{1, 2, 3\}$, such that $u_1 = u_x$, $x_1 = x$, etc.

The first consideration is that pure rotation of the volume element about its origin should produce no strain. The vector representing the angular velocity of pure rotation is

$$\frac{1}{2}\nabla \times \boldsymbol{u} = \frac{1}{2}\begin{bmatrix} \frac{\partial u_z}{\partial y} - \frac{\partial u_y}{\partial z} \\ \frac{\partial u_x}{\partial z} - \frac{\partial u_z}{\partial x} \\ \frac{\partial u_y}{\partial x} - \frac{\partial u_x}{\partial y} \end{bmatrix}\,.$$

This rotational part should be subtracted from the shear-strain tensor, such that the non-diagonal elements become

$$U_{ij} = \frac{1}{2}\frac{\partial u_i}{\partial x_j} + \frac{1}{2}\frac{\partial u_j}{\partial x_i}\,, \qquad i \neq j\,.$$

The second consideration is that the shear-strain tensor should not contain terms relating to the efflux of fluid. Comparison to

$$\nabla \cdot \boldsymbol{u} = \frac{\partial u_x}{\partial x} + \frac{\partial u_y}{\partial y} + \frac{\partial y_z}{\partial z}\,,$$

reveals that this can be achieved by setting

$$U_{ii} = \frac{\partial u_i}{\partial x_i} - \frac{1}{3}\nabla \cdot \boldsymbol{u}\,.$$

The viscous-stress tensor can now be constructed. For a Newtonian fluid, the viscous stress is linearly proportional to the strain rate. By comparing $\mathfrak{U}$ to (A.3), it is apparent that $\mathfrak{D} = -2\mu\mathfrak{U}$. One final term must be added to complete $\mathfrak{D}$, representing the resistance of the fluid to compressional stress. This is achieved via the term $-\mu_\mathrm{b}\nabla \cdot \boldsymbol{u}$, where μ_b is the coefficient of bulk viscosity. The complete viscous-stress tensor is therefore

$$\begin{aligned} D_{ii} &= -\left(\mu_\mathrm{b} - \frac{2}{3}\mu\right)\nabla \cdot \boldsymbol{u} - 2\mu\frac{\partial u_i}{\partial x_i}\,, \\ D_{ij} &= -\mu\frac{\partial u_i}{\partial x_j} - \mu\frac{\partial u_j}{\partial x_i}\,, \qquad i \neq j\,. \end{aligned}$$

The total stress tensor can then be obtained by combining the normal pressure and viscous-stress tensor,

$$\begin{aligned} P_{ii} &= p' - \left(\mu_\mathrm{b} - \frac{2}{3}\mu\right)\nabla \cdot \boldsymbol{u} - 2\mu\frac{\partial u_i}{\partial x_i}\,, \\ P_{ij} &= -\mu\frac{\partial u_i}{\partial x_j} - \mu\frac{\partial u_j}{\partial x_i}\,, \qquad i \neq j\,, \end{aligned}$$

which can be recast as

$$\mathfrak{P} = \left[p' - \left(\mu_\mathrm{b} - \frac{2}{3}\mu\right)\nabla \cdot \boldsymbol{u}\right]\mathfrak{I} - \mu\left(\nabla\boldsymbol{u} + \boldsymbol{u}\nabla\right)\,,$$

where $\mathfrak{I}_{ij} = \delta_{ij}$ is the identity tensor.

Returning to the continuity equation, (A.2), application of the product rule and the mass continuity equation, (2.16), to the time derivative results in

$$\rho'\frac{\partial \boldsymbol{u}}{\partial t} - \boldsymbol{u}\nabla \cdot (\rho'\boldsymbol{u}) + \nabla \cdot (\mathfrak{J} + \mathfrak{P}) = 0\,.$$

The divergences of the momentum flux and stress tensors are

$$\begin{aligned} \nabla \cdot \mathfrak{J} &= \boldsymbol{u}\nabla \cdot (\rho'\boldsymbol{u}) + \rho'\left(\boldsymbol{u} \cdot \nabla\right)\boldsymbol{u}\,, \\ \nabla \cdot \mathfrak{P} &= \nabla p' - \left(\mu_\mathrm{b} + \frac{4}{3}\mu\right)\nabla\left(\nabla \cdot \boldsymbol{u}\right) + \mu\nabla \times \nabla \times \boldsymbol{u}\,. \end{aligned}$$

Substitution then yields

$$\rho' \left[\frac{\partial \boldsymbol{u}}{\partial t} + (\boldsymbol{u} \cdot \nabla) \boldsymbol{u} \right] = -\nabla p + \left(\mu_{\mathrm{b}} + \frac{4}{3}\mu \right) \nabla (\nabla \cdot \boldsymbol{u}) - \mu \nabla \times \nabla \times \boldsymbol{u} \,, \tag{A.4}$$

which is the Navier-Stokes equation for a viscous, compressible fluid.

Appendix B

The Thermoelectric Diffusion Equation

Here, the modified thermal diffusion equation will be derived, taking into account thermoelectric effects. This derivation follows the works of Ashcroft and Mermin [107], Blundell and Blundell [77] and Narducci [108].

Consider a thermodynamic system capable of exchanging both heat and particles with its surroundings. This exchange can be described by fluxes (or current densities) for both heat, $\boldsymbol{j}_q$, and particles, $\boldsymbol{j}_p$, at the system boundaries. For small differences between the system and the environment, a linear response can be assumed, such that

$$\begin{bmatrix} \boldsymbol{j}_q \\ \boldsymbol{j}_p \end{bmatrix} = \mathfrak{L} \begin{bmatrix} \boldsymbol{F}_q \\ \boldsymbol{F}_p \end{bmatrix} = \begin{bmatrix} L_{qq} & L_{qp} \\ L_{pq} & L_{pp} \end{bmatrix} \begin{bmatrix} \boldsymbol{F}_q \\ \boldsymbol{F}_p \end{bmatrix} , \tag{B.1}$$

where $\boldsymbol{F}_{qp}$ are the driving thermodynamic forces, $\mathfrak{L}$ is the Onsager matrix, and L_{ij} are the associated kinetic coefficients. These thermodynamic forces and kinetic coefficients can now be determined to obtain a complete set of transport equations for the system.

First, the thermodynamic forces will be considered. Assuming that the particle current consists only of electrons/holes, the overall energy current can be expressed as

$$\boldsymbol{j}_u = \boldsymbol{j}_q + \bar{\mu}_e \boldsymbol{j}_p, \tag{B.2}$$

where $\bar{\mu}_e$ is the electron electrochemical potential. An entropy current density can also be defined,

$$\boldsymbol{j}_s \equiv \frac{1}{T} \boldsymbol{j}_q \,,$$

which, substituted into (B.2), yields

$$\boldsymbol{j}_s = \frac{1}{T}\boldsymbol{j}_u - \frac{\bar{\mu}_e}{T}\boldsymbol{j}_p \,. \tag{B.3}$$

Each of these currents will obey a continuity equation of the form

$$\frac{\partial \rho_i}{\partial t} + \nabla \cdot \boldsymbol{j}_i = 0 \,,$$

where ρ_i is the associated density. With this in mind, taking the divergence of (B.3),

$$\begin{aligned}\nabla \cdot \boldsymbol{j}_s &= \nabla \cdot \left(\frac{1}{T}\boldsymbol{j}_u\right) - \nabla \cdot \left(\frac{\bar{\mu}_e}{T}\boldsymbol{j}_p\right) \\ &= \frac{1}{T}\nabla \cdot \boldsymbol{j}_u + \nabla\frac{1}{T} \cdot \boldsymbol{j}_u - \frac{1}{T}\nabla\bar{\mu}_e \cdot \boldsymbol{j}_p - \nabla\frac{1}{T} \cdot \bar{\mu}_e\boldsymbol{j}_p - \frac{\bar{\mu}_e}{T}\nabla \cdot \boldsymbol{j}_p \,.\end{aligned}$$

Since there are no current sources or sinks, $\nabla \cdot \boldsymbol{j}_u = \nabla \cdot \boldsymbol{j}_p = 0$. Using this, as well as the continuity equation for entropy,

$$\frac{\mathrm{d}s}{\mathrm{d}t} = \nabla\frac{1}{T} \cdot \boldsymbol{j}_u - \nabla\frac{1}{T} \cdot \bar{\mu}_e\boldsymbol{j}_p - \frac{1}{T}\nabla\bar{\mu}_e \cdot \boldsymbol{j}_p \,.$$

Substituting (B.2),

$$\frac{\mathrm{d}s}{\mathrm{d}t} = \nabla\frac{1}{T} \cdot \boldsymbol{j}_q - \frac{1}{T}\nabla\bar{\mu}_e \cdot \boldsymbol{j}_p \,. \tag{B.4}$$

The entropy production rate is related to the forces and currents by

$$\frac{\mathrm{d}s}{\mathrm{d}t} = \sum_i \boldsymbol{F}_i \cdot \boldsymbol{j}_i \,,$$

so, by comparison with (B.4),

$$\begin{aligned}\boldsymbol{F}_q &= \nabla\left(\frac{1}{T}\right) = -\frac{1}{T^2}\nabla T \,, \\ \boldsymbol{F}_p &= -\frac{1}{T}\nabla\bar{\mu}_e \,.\end{aligned}$$

A flux of charged particles results in an electric current, $\boldsymbol{j}_e = e\boldsymbol{j}_p$, where e is the electron charge. Considering that the electrochemical potential is

$$\bar{\mu}_e = \mu_e + eV \,,$$

where μ_e is the chemical potential and V the electric potential,

$$\begin{aligned}\boldsymbol{F}_e &= e\boldsymbol{F}_p \\ &= -\frac{e}{T}\nabla\bar{\mu}_e \\ &= -\frac{e^2}{T}\nabla V\,.\end{aligned}$$

Therefore, (B.1) can be recast in a more convenient form,

$$\begin{bmatrix}\boldsymbol{j}_e \\ \boldsymbol{j}_q\end{bmatrix} = \begin{bmatrix}L_{ee} & L_{eq} \\ L_{qe} & L_{qq}\end{bmatrix}\begin{bmatrix}-\frac{e^2}{T}\nabla V \\ -\frac{1}{T^2}\nabla T\end{bmatrix}\,. \tag{B.5}$$

The kinetic coefficients can be determined by comparison with known experimental results. First, consider $\Delta T = 0$, such that

$$\begin{aligned}\boldsymbol{j}_e &= -L_{ee}\frac{e^2}{T}\nabla V\,, \\ \boldsymbol{j}_q &= -L_{qe}\frac{e^2}{T}\nabla V\,.\end{aligned}$$

The electric current can be compared directly to Ohm's law, yielding

$$\begin{aligned}\boldsymbol{j}_e = -\sigma\nabla V &= -L_{ee}\frac{e^2}{T}\nabla V \\ L_{ee} &= \frac{T}{e^2}\sigma\,.\end{aligned}$$

The electric and heat currents can also be combined to obtain

$$\begin{aligned}-\frac{e^2}{T}\nabla V = \frac{\boldsymbol{j}_e}{L_{ee}} &= \frac{\boldsymbol{j}_q}{L_{qe}}\,, \\ \boldsymbol{j}_q &= \frac{L_{qe}}{L_{ee}}\boldsymbol{j}_e\,,\end{aligned}$$

which can then be compared to the Peltier effect,

$$\begin{aligned}\boldsymbol{j}_q = \Pi\boldsymbol{j}_e &= \frac{L_{qe}}{L_{ee}}\boldsymbol{j}_e\,, \\ \Pi &= \frac{L_{qe}}{L_{ee}}\,, \\ L_{qe} &= \frac{T}{e^2}\sigma\Pi\,.\end{aligned}$$

Next, consider $\boldsymbol{j}_e = 0$,

$$\begin{aligned}\boldsymbol{j}_e = 0 &= -L_{ee}\frac{e^2}{T}\nabla V - L_{eq}\frac{1}{T^2}\nabla T \\ \boldsymbol{j}_q &= -L_{qe}\frac{e^2}{T}\nabla V - L_{qq}\frac{1}{T^2}\nabla T\,.\end{aligned}$$

Using the Seebeck coefficient,

$$S = -\frac{\Delta V}{\Delta T}\,,$$

with the equation for electric current,

$$\begin{aligned}0 &= L_{ee}\frac{e^2}{T}S\nabla T - L_{eq}\frac{1}{T^2}\nabla T\,, \\ S &= \frac{1}{e^2 T}\frac{L_{eq}}{L_{ee}}\,, \\ L_{eq} &= T^2\sigma S\,.\end{aligned}$$

Combining both electric and heat currents

$$\begin{aligned}\boldsymbol{j}_q &= L_{qe}\frac{L_{eq}}{L_{ee}}\frac{1}{T^2}\nabla T - L_{qq}\frac{1}{T^2}\nabla T \\ &= \frac{1}{T^2}\left(\frac{L_{eq}L_{qe} - L_{ee}L_{qq}}{L_{ee}}\right)\nabla T\,,\end{aligned}$$

which can be compared to Fourier's law,

$$\begin{aligned}\boldsymbol{j}_q = -\kappa\nabla T &= \frac{1}{T^2}\left(\frac{L_{eq}L_{qe} - L_{ee}L_{qq}}{L_{ee}}\right)\nabla T\,, \\ \kappa &= \frac{1}{T^2}\left(\frac{L_{ee}L_{qq} - L_{eq}L_{qe}}{L_{ee}}\right)\,, \\ L_{qq} &= T^2\left(\kappa + \sigma\Pi S\right)\,.\end{aligned}$$

Now that the thermodynamic forces and kinetic coefficients have been determined, they can be substituted into (B.5) to obtain the coupled transport equations,

$$\begin{bmatrix}\boldsymbol{j}_e \\ \boldsymbol{j}_q\end{bmatrix} = \begin{bmatrix}\sigma & \sigma S \\ \sigma\Pi & \kappa + \sigma\Pi S\end{bmatrix}\begin{bmatrix}-\nabla V \\ -\nabla T\end{bmatrix}\,. \tag{B.6}$$

To make further progress, some constraints on the kinetic coefficients are required. These come in the form of the Onsager reciprocal relations, which state that

$$L_{ij} = L_{ji}\,. \tag{B.7}$$

This relationship is proved in Appendix C. This yields the relation

$$\Pi = TS\,, \tag{B.8}$$

such that

$$\begin{aligned}\boldsymbol{j}_q &= -\sigma TS\nabla V - \left(\kappa + \sigma TS^2\right)\nabla T \\ &= TS\boldsymbol{j}_e - \kappa\nabla T\,.\end{aligned}$$

From the continuity equation, the rate of heat generation is

$$\frac{\mathrm{d}Q}{\mathrm{d}t} = -\nabla\cdot\boldsymbol{j}_u\,,$$

where the total energy current is

$$\begin{aligned}\boldsymbol{j}_u &= \boldsymbol{j}_q + \bar{\mu}_e\boldsymbol{j}_p \\ &= \boldsymbol{j}_q + \frac{\bar{\mu}_e}{e}\boldsymbol{j}_e \\ &= \boldsymbol{j}_q + V\boldsymbol{j}_e\,.\end{aligned}$$

Therefore,

$$\begin{aligned}\frac{\mathrm{d}Q}{\mathrm{d}t} &= -\nabla\cdot(\boldsymbol{j}_q + V\boldsymbol{j}_e) \\ &= -\nabla\cdot(TS\boldsymbol{j}_e - \kappa\nabla T + V\boldsymbol{j}_e) \\ &= -\nabla(TS)\cdot\boldsymbol{j}_e - TS\nabla\cdot\boldsymbol{j}_e + \kappa\nabla^2 T - \nabla V\cdot\boldsymbol{j}_e - V\nabla\cdot\boldsymbol{j}_e\,.\end{aligned}$$

Noting that $\nabla\cdot\boldsymbol{j}_e = 0$,

$$\begin{aligned}\frac{\mathrm{d}Q}{\mathrm{d}t} &= \kappa\nabla^2 T - \nabla(TS)\cdot\boldsymbol{j}_e - \nabla V\cdot\boldsymbol{j}_e \\ &= \kappa\nabla^2 T - T\nabla S\cdot\boldsymbol{j}_e - \nabla V\cdot\boldsymbol{j}_e - S\nabla T\cdot\boldsymbol{j}_e \\ &= \kappa\nabla^2 T - T\nabla S\cdot\boldsymbol{j}_e + \frac{\boldsymbol{j}_e^2}{\sigma}\,.\end{aligned}$$

The rate of change of heat is related to the temperature by the heat capacity, such that

$$\kappa\nabla^2 T - \rho c_p\frac{\partial T}{\partial t} = -\frac{\boldsymbol{j}_e^2}{\sigma} + T\nabla S\cdot\boldsymbol{j}_e\,. \tag{B.9}$$

Appendix C

The Onsager Reciprocal Relations

Here the Onsager reciprocal relations will be proved, following the work by Blundell and Blundell [77].

Consider a microscopic thermodynamic system parameterised by n variables, with generalised densities ρ_i, that are allowed to fluctuate. The continuity equation permits the definition of generalised current densities for these variables, $\boldsymbol{j}_i$. Assuming the microscopic fluctuations behave similarly to macroscopic flows, these current densities are the result of thermodynamic forces, $\boldsymbol{F}_i$, acting upon the system to displace it from equilibrium. Therefore, to first order,

$$\begin{bmatrix} \boldsymbol{j}_1 \\ \vdots \\ \boldsymbol{j}_n \end{bmatrix} = \mathfrak{L} \begin{bmatrix} \boldsymbol{F}_1 \\ \vdots \\ \boldsymbol{F}_n \end{bmatrix} , \tag{C.1}$$

where $\mathfrak{L}$ is the Onsager matrix and L_{ij} are the kinetic coefficients. For such a system, the Onsager reciprocal relations state that

$$L_{ij} = L_{ji} \, . \tag{C.2}$$

The reason for this will now be shown.

Small temporal fluctuations (or displacements) from the equilibrium values, $\rho_i(0)$, can be defined as

$$x_i(t) = \rho_i(t) - \rho_i(0) \, .$$

Assuming that the fluctuations and their reverse processes take place with the same frequency,

$$\langle x_i(0) x_j(t) \rangle = \langle x_i(0) x_j(-t) \rangle = \langle (x_i(t) x_j(0) \rangle \, .$$

Subtracting $\langle x_i(0)x_j(0)\rangle$ and dividing by t on both sides,

$$\left\langle x_i(0)\left[\frac{x_j(t)-x_j(0)}{t}\right]\right\rangle = \left\langle\left[\frac{x_i(t)-x_i(0)}{t}\right]x_j(0)\right\rangle ,$$

such that, for $t \to 0$,

$$\langle x_i \dot{x_j}\rangle = \langle \dot{x}_i x_j\rangle . \tag{C.3}$$

Assuming the fluctuations behave the same as macroscopic flows,

$$\dot{x}_i = \sum_k L_{ik}\frac{\partial s}{\partial x_k} ,$$

which, substituted into (C.3), yields

$$\begin{aligned}\left\langle x_i \sum_k L_{jk}\frac{\partial s}{\partial x_k}\right\rangle &= \left\langle \sum_k L_{ik}\frac{\partial s}{\partial x_k}x_j\right\rangle ,\\ \sum_k L_{jk}\left\langle x_i\frac{\partial s}{\partial x_k}\right\rangle &= \sum_k L_{ik}\left\langle \frac{\partial s}{\partial x_k}x_j\right\rangle .\end{aligned} \tag{C.4}$$

To determine the average quantities, consider Boltzmann's entropy equation, which states that the probability of the system being in the state
$\boldsymbol{x} = (x_1, x_2, \ldots, x_n)$ is

$$P(\boldsymbol{x}) \propto \exp\left(\frac{\Delta s}{k_\mathrm{B}}\right) , \tag{C.5}$$

where k_B is the Boltzmann constant. Here the probability is normalised such that

$$\int P \,\mathrm{d}\boldsymbol{x} = 1 .$$

The term Δs can be expressed as a Taylor expansion with respect to $\boldsymbol{x}$. The linear term here vanishes since only differences are considered, and the first derivative is zero since Δs is maximised. Therefore, to leading order,

$$\Delta s = -\frac{1}{2}\sum_{ij}\frac{\partial^2 \Delta s}{\partial x_i \partial x_j}x_i x_j ,$$

such that

$$\begin{aligned}\ln P &= \frac{\Delta s}{k_\mathrm{B}} + \text{constant} ,\\ \frac{\partial s}{\partial x_i} &= k_\mathrm{B}\frac{\partial \ln P}{\partial x_i} ,\end{aligned}$$

$$\begin{aligned}\left\langle \frac{\partial s}{\partial x_i} x_j \right\rangle &= k_\mathrm{B} \left\langle \frac{\partial \ln P}{\partial x_i} x_j \right\rangle \\ &= k_\mathrm{B} \int \frac{\partial \ln P}{\partial x_i} x_j P \,\mathrm{d}\boldsymbol{x} \\ &= k_\mathrm{B} \int \frac{\partial P}{\partial x_i} x_j \,\mathrm{d}\boldsymbol{x} \\ &= k_\mathrm{B} \left(\int [x_j P]_{-\infty}^{\infty} \frac{\mathrm{d}\boldsymbol{x}}{\mathrm{d}x_i} - \int \frac{\partial x_j}{\partial x_i} P \,\mathrm{d}\boldsymbol{x} \right) ,\end{aligned}$$

where the final step involves integration by parts with respect to x_i. From (C.5) it is apparent that $P \to 0$ as $x_i \to \pm\infty$, hence

$$\left\langle \frac{\partial s}{\partial x_i} x_j \right\rangle = -k_\mathrm{B} \delta_{ij} \,.$$

The averages can then be substituted into (C.4) to obtain the final result,

$$\begin{aligned}\sum_k L_{jk} \left(-k_\mathrm{B} \delta_{ik}\right) &= \sum_k L_{ik} \left(-k_\mathrm{B} \delta_{jk}\right) \\ L_{ji} &= L_{ij} \,.\end{aligned}$$

Appendix D

Lock-in technique

The majority of electrical and acoustic measurements taken during this work relied heavily on the use of lock-in amplifiers. A lock-in amplifier [109] takes an arbitrary electrical signal and isolates a single frequency component. It achieves this by multiplying the input signal by an internal reference signal at the frequency of interest, which allows for the magnitude and phase of the isolated frequency component to be measured relative to the reference. Lock-in amplifiers are particularly useful for sensitive acoustic measurements as they are able to measure a signal that is orders of magnitude smaller than the background noise. The remainder of this section is dedicated to explaining the basic principles behind the lock-in technique.

The lock-in amplifier has an internal reference signal that is set to the frequency of interest ω_{x}

$$V_A(t) = V_{\mathrm{ref}} \sin(\omega_{\mathrm{x}} t),$$

where V_{ref} is the rms amplitude. The measured input signal typically consists of many frequency components

$$V_{\mathrm{in}}(t) = \sum_{i=0}^{\infty} V_i \sin(\omega_i t + \varphi_i),$$

,where φ is the phase of a specific frequency relative to the reference signal. The lock-in amplifier multiplies the input and reference signals

$$\begin{aligned} V_A(t)\, V_{\mathrm{in}}(t) &= V_{\mathrm{ref}} \sin(\omega_{\mathrm{x}} t) \sum_{i=0}^{\infty} V_i \sin(\omega_i t + \varphi_i) \\ &= \frac{1}{2} V_{\mathrm{ref}} \sum_{i=0}^{\infty} V_i \left\{ \cos\left[(\omega_{\mathrm{x}} - \omega_i) t - \varphi_i\right] - \cos\left[(\omega_{\mathrm{x}} + \omega_i) t + \varphi_i\right] \right\}, \end{aligned}$$

from which it can be seen there is a special case for $\omega_i = \omega_x$. The contribution of this frequency component to the total signal will be

$$A(t) = \frac{1}{2} V_{\mathrm{ref}} V_{\mathrm{x}} \left[\cos(\varphi) - \cos(2\omega_{\mathrm{x}} t + \varphi)\right].$$

The resulting signal therefore has a DC component that is proportional to the amplitude of the signal at ω_{x}. This component is extracted via low-pass filter, leaving

$$A_{\mathrm{dc}} = \frac{1}{2} V_{\mathrm{ref}} V_{\mathrm{x}} \cos(\varphi).$$

The lock-in amplifier also multiplies the input signal by the reference phase-shifted by $\frac{\pi}{2}$. Following the same process as before, this returns a second DC component,

$$B_{\mathrm{dc}} = \frac{1}{2} V_{\mathrm{ref}} V_{\mathrm{x}} \sin(\varphi).$$

The amplitude and relative phase of the input signal at ω_x can then be determined by combining both of these dc components,

$$\begin{aligned}\sqrt{A_{\mathrm{dc}}^2 + B_{\mathrm{dc}}^2} &= \sqrt{\frac{1}{4} V_{\mathrm{ref}}^2 V_{\mathrm{x}}^2 \left[\cos^2(\varphi) + \sin^2(\varphi)\right]} \\ &= \frac{1}{2} V_{\mathrm{ref}} V_{\mathrm{x}},\end{aligned}$$

$$\begin{aligned}\arctan\left(\frac{B_{\mathrm{dc}}}{A_{\mathrm{dc}}}\right) &= \frac{\frac{1}{2} V_{\mathrm{ref}} V_{\mathrm{x}} \sin(\varphi)}{\frac{1}{2} V_{\mathrm{ref}} V_{\mathrm{x}} \cos(\varphi)} \\ &= \varphi.\end{aligned}$$

Appendix E

Material Parameters

Property	Value	Units
κ	0.0258	W m^{-1} K^{-1}
ρ	1.20	kg m^{-3}
c_p	1010	J kg^{-1} K^{-1}
μ	1.18×10^{-5}	kg m^{-1} s
μ_b	1.09×10^{-5}	kg m^{-1} s
v_s	343	m s^{-1}
β	3.41×10^{-3}	K^{-1}
γ	1.4	

Table E.1: Air [110]

Property	Value	Units
κ	29.7	W m^{-1} K^{-1}
ρ	8610	kg m^{-3}
c_p	523	J kg^{-1} K^{-1}
σ	3.40×10^{6}	S m^{-1}
S	-17.3×10^{-6}	V K^{-1}

Table E.2: Alumel [111]

Property	Value	Units
κ	19.2	W m^{-1} K^{-1}
ρ	8730	kg m^{-3}
c_p	448	J kg^{-1} K^{-1}
σ	1.42×10^{6}	S m^{-1}
S	21.7×10^{-6}	V K^{-1}

Table E.3: Chromel [111]

Property	Value	Units
κ	398	W m^{-1} K^{-1}
ρ	8950	kg m^{-3}
c_p	384	J kg^{-1} K^{-1}
σ	60×10^6	S m^{-1}
S	6.0×10^{-6}	V K^{-1}

TABLE E.4: Copper [112]

Property	Value	Units
κ	21.2	W m^{-1} K^{-1}
ρ	8920	kg m^{-3}
c_p	393	J kg^{-1} K^{-1}
σ	2.05×10^6	S m^{-1}
S	-35.0×10^{-6}	V K^{-1}

TABLE E.5: Constantan [111]

Property	Value	Units
κ	318	W m^{-1} K^{-1}
ρ	19300	kg m^{-3}
c_p	129	J kg^{-1} K^{-1}
σ	45.6×10^6	S m^{-1}

TABLE E.6: Gold [112]

Property	Value	Units
κ	1.38	W m^{-1} K^{-1}
ρ	2200	kg m^{-3}
c_p	745	J kg^{-1} K^{-1}

TABLE E.7: Fused quartz [112]

Bibliography

[1] J. A. P. Bodhika, "A brief study on thunder claps", Applied Acoustics **145**, 98–103 (2019).

[2] A. M. Arndt, W. Moore, W. K. Lee, and C. Ortiz, "Mechanistic origins of bombardier beetle (brachinini) explosion-induced defensive spray pulsation", Science **348**, 563–567 (2015).

[3] D. Noda and Y. Ueda, "A thermoacoustic oscillator powered by vaporized water and ethanol", American Journal of Physics **81**, 124–126 (2013).

[4] H. D. Arnold and I. B. Crandall, "The thermophone as a precision source of sound", Physical Review **10**, 22–38 (1917).

[5] W. H. Preece, "On some thermal effects of electric currents", Proc. R. Soc. Lond. **30**, 408–411 (1880).

[6] P. de Lange, "On thermophones", Proceedings of the Royal Society of London. Series A **91**, 239–241 (1915).

[7] H. Shinoda, T. Nakajima, K. Ueno, and N. Koshida, "Thermally induced ultrasonic emission from porous silicon", Nature **400**, 853–855 (1999).

[8] T. Nishioka, Y. Teshima, T. Mano, K. Sakai, T. Asada, M. Matsukawa, T. Ohta, and S. Hiryu, "Ultrasound radiation from a three-layer thermoacoustic transformation device", Ultrasonics **57**, 84–89 (2015).

[9] T. A. Brungard, J. J. Chatterley, B. S. Beck, B. L. Kline, and Z. W. Yoas, "Thermal saturation and its suppression in high-power, compact carbon nanotube thin-film thermophones", Proc. Mtgs. Acoust. **29**, 1–9 (2016).

[10] A. E. Aliev, M. D. Lima, S. Fang, and R. H. Baughman, "Underwater sound generation using carbon nanotube projectors", Nano Lett. **1010**, 2374–2380 (2010).

[11] M. Daschewski, R. Boehm, J. Prager, M. Kreutzbruck, and A. Harrer, "Physics of thermo-acoustic sound generation", Journal of Applied Physics **114**, 1–12 (2013).

[12] P. L. Torraca, M. Bobinger, M. Servadio, P. Pavan, M. Becherer, P. Lugli, and L. Larcher, "On the frequency response of nanostructured thermoacoustic loudspeakers", Nanomaterials **2018**, 833 (2018).

[13] M. Daschewski, *Thermophony in real gases. theory and applications.* (Universität Potsdam, 2016).

[14] G. Chitnis, A. Kim, S. H. Song, A. M. Jessop, J. S. Bolton, and B. Ziaie, "A thermophone on porous polymeric substrate", Appl. Phys. Lett. **101**, 1–4 (2012).

[15] C. S. Kim, S. K. Hong, J. M. Lee, D. S. Kang, B. J. Cho, and J. W. Choi, "Free-standing graphene thermophone on a polymer-mesh substrate", Small **12**, 185–198 (2016).

[16] H. Tian, T. L. Ren, D. Xie, Y. F. Wang, C. J. Zhou, T. T. Feng, D. Fu, Y. Yang, P. G. Peng, L. G. Wang, and L. T. Liu, "Graphene-on-paper sound source devices", ACS Nano **5**, 4878–4885 (2011).

[17] A. O. Niskanen, J. Hassel, M. Tikander, P. Maijala, L. Grönberg, and P. Helistö, "Suspended metal wire array as a thermoacoustic sound source", Appl. Phys. Lett. **95**, 1–3 (2009).

[18] Y. Yang and J. Liu, "Computational characterization on the thermoacoustic thermophone effects induced by micro/nano-heating elements", Microfluid Nanofluid **14**, 873–884 (2013).

[19] R. Dutta, B. Albee, W. E. van der Veer, T. Harville, K. C. Donovan, D. Papamoschou, and R. M. Penner, "Gold nanowire thermophones", The Journal of Physical Chemistry C **118**, 29101–29107 (2014).

[20] L. H. Tong, C. W. Lim, S. K. Lai, and Y. C. Li, "Gap separation effect on thermoacoustic wave generation by heated suspended cnt nano-thinfilm", Applied Thermal Engineering **86**, 135–142 (2015).

[21] Q. Y. Xie, Z. Y. Ju, H. Tian, Q. T. Xue, Y. Q. Chen, L. Q. Tao, M. A. Mohammad, X. Y. Zhang, Y. Yang, and T. L. Ren, "A point acoustic device based on aluminum nanowires", Nanoscale **8**, 5516–5525 (2016).

[22] M. Daschewski, A. Harrer, J. Prager, M. Kreutzbruck, U. Beck, T. Lange, and M. Weise, "A resonance-free nano-film airborne ultrasound emitter", AIP Conference Proceedings **1511**, 1541–1546 (2013).

[23] R. R. Boullosa and A. O. Santillán, "Sound radiation from thermal nonresonant sources: planar and nonplanar geometries", Japanese Journal of Applied Physics **45**, 2794–2800 (2006).

[24] H. Tian, D. Xie, Y. Yang, T. L. Ren, Y. X. Lin, Y. Chen, Y. F. Wang, C. J. Zhou, P. G. Peng, L. G. Wang, and L. T. Liu, "Flexible, ultrathin, and transparent sound-emitting devices using silver nanowires film", Appl. Phys. Lett. **99**, 1–4 (2011).

[25] H. Tian, D. Xie, Y. Yang, T. Ren, Y. Wang, C. Zhou, P. Peng, L. Wang, and L. Liu, "Transparent, flexible, ultrathin sound source devices using indium tin oxide films", Appl. Phys. Lett. **99**, 1–3 (2011).

[26] H. Tian, D. Xie, Y. Yang, T. Ren, Y. Wang, C. Zhou, P. Peng, L. Wang, and L. Liu, "Poly(3,4-ethylenedioxythiophene):poly(styrenesulfonate)-based organic, ultrathin, and transparent sound-emitting device", Appl. Phys. Lett. **99**, 1–3 (2011).

[27] A. Odagawa, A. Matsushita, and M. Hashimoto, "Thermally induced ultrasound emission from printable semiconductor nanoparticles", Journal of Applied Physics **108**, 1–3 (2010).

[28] J. W. Suk, K. Kirk, Y. Hau, N. A. Hall, and R. S. Ruoff, "Thermoacoustic sound generation from monolayer graphene for transparent and flexible sound sources", Advanced Materials **24**, 6342–6347 (2012).

[29] W. Fei, J. Zhou, and W. Guo, "Low-voltage driven graphene foam thermoacoustic speaker", Small **11**, 2252–2256 (2015).

[30] M. Rabbani, A. W. Syed, S. Khalid, and M. A. Mohammad, "Fabrication and characterization of a thermophone based on laser-scribed graphene intercalated with multiwalled carbon nanotubes", Nanomaterials **11**, 1–10 (2021).

[31] B. J. Mason, S. W. Chang, J. Chen, S. B. Cronin, and A. W. Bushmaker, "Thermoacoustic transduction in individual suspended carbon nanotubes", ACS Nano **9**, 5372–5376 (2015).

[32] M. Kozlov and J. Oh, "Thermo-electromagnetic sound transducer based on carbon nanotube sheet", Journal of Applied Physics **116**, 1–5 (2014).

[33] P. Kumar, R. Sriramda, A. E. Aliev, J. B. Blottman, N. K. Mayo, R. H. Baughman, and S. Priya, "Understanding the low frequency response of carbon nanotube thermoacoustic projectors", Journal of Sound and Vibration **498**, 1–16 (2021).

[34] Y. Wei, X. Lin, K. Jiang, P. Liu, Q. Li, and S. Fan, "Thermoacoustic chips with carbon nanotube thin yarn arrays", Nano Letters **13**, 4795–4801 (2013).

[35] J. Wang, H. Li, Y. Feng, Z. Tong, Z. Zhou, X. Xu, and C. W. Lim, "New high fidelity (hi-fi) three-dimensional thermophone cnt sponge", Extreme Mechanics Letters **49**, 1–8 (2021).

[36] A. E. Aliev, N. K. Mayo, R. H. Baughman, D. Avirovik, S. Priya, M. R. Zarnetske, and J. B. Blottman, "Thermal management of thermoacoustic sound projectors using a free-standing carbon nanotube aerogel sheet as a heat source", Nanotechnology **25**, 1–11 (2014).

[37] L. Xiao, Z. Chen, C. Feng, L. Liu, Z. Bai, Y. Wang, L. Qian, Y. Zhang, Q. Li, K. Jiang, and S. Fan, "Flexible, stretchable, transparent carbon nanotube thin film loudspeakers", Nano Letters **8**, 4539–4545 (2008).

[38] D. Passeri, U. Sassi, A. Bettucci, E. Tamburri, F. Toschi, S. Orlanducci, M. L. Terranova, and M. Rossi, "Thermoacoustic emission from carbon nanotubes imaged by atomic force microscopy", Advanced Functional Materials **22**, 2956–2963 (2012).

[39] A. Harrer, M. Daschewski, J. Prager, M. Kreutzbruck, M. Guderian, and A. Meyer-Plath, "Thermoacoustic generation of airborne ultrasound using carbon materials at the micro- and nanoscale", International Journal of Applied Electromagnetics and Mechanics **39**, 35–41 (2015).

[40] T. Luqi, W. Danyang, J. Song, L. Ying, X. Qianyi, T. He, D. Ninqin, W. Xuefeng, Y. Yi, and R. Tian-Ling, "Fabrication techniques and applications of flexible graphene-based electronic devices", Journal of Semiconductors **37**, 1–11 (2016).

[41] K. R. Lee, S. H. Jang, and I. Jung, "Analysis of acoustical performance of bi-layer graphene and graphene-foam-based thermoacoustic sound generating devices", Carbon **127**, 13–20 (2018).

[42] A. E. Aliev, N. K. Mayo, M. J. de Andrade, R. O. Robles, S. Fang, R. H. Baugman, M. Zhang, Y. Chen, J. A. Lee, and S. J. Kim, "Alternative nanostructures for thermophones", ACS Nano **9**, 4743–4756 (2015).

[43] L. Q. Tao, Y. Liu, H. Tian, Z. Y. Ju, Q. Y. Xie, Y. Yang, and T. L. Ren, "A novel thermal acoustic device based on porous graphene", AIP Advances **6**, 1–5 (2016).

[44] T. M. Bouman, A. R. Barnard, and M. Asgarisabet, "Experimental quantification of the true efficiency of carbon nanotube thin-film thermophones", The Journal of the Acoustical Society of America **139**, 1353–1363 (2016).

[45] A. E. Aliev, D. Codoluto, R. H. Baughman, R. Ovalle-Robles, K. Inoue, S. A. Romanov, A. G. Nasibulin, P. Kumar, S. Priya, N. K. Mayo, and J. B. Blottman, "Thermoacoustic sound projector: exceeding the fundamental efficiency of carbon nanotubes", Nanotechnology **29**, 1–17 (2018).

[46] S. A. Romanov, A. E. Aliev, B. V. Fine, A. S. Anisimov, and A. G. Nasibulin, "Highly efficient thermophones based on freestanding single-walled carbon nanotube films", Nanoscale Horizons **4**, 1158–1163 (2019).

[47] V. Vesterinen, A. O. Niskanen, J. Hassel, and P. Helistö, "Fundamental efficiency of nanothermophones: modeling and experiments", Nano Letters **10**, 5020–5024 (2010).

[48] J. R. Clynch, L. A. Thompson, and T. G. Muir, "Thermoelectric sound generation in water", The Journal of the Acoustical Society of America **56**, 824–826 (1974).

[49] H. A. Fairbank, W. M. Fairbank, and C. T. Lane, "The thermophone as a source of sound in liquid helium and liquid hydrogen", The Journal of the Acoustical Society of America **19**, 475–477 (1947).

[50] T. H. Tong, C. W. Lim, and Y. C. Li, "Gas-filled encapsulated thermal-acoustic transducer", Journal of Vibration and Acoustics **135** (2013).

[51] D. Wawng, H. Hu, and Z. Wang, "Modeling of the acoustic field of thermally induced ultrasonic emission from a spherical cavity surface", Ultrasonics **56**, 497–504 (2015).

[52] B. R. Dzikowicz, J. F. Tressler, and J. W. Baldwin, "Cylindrical heat conduction and structural acoustic models for enclosed fiber array thermophones", The Journal of the Acoustical Society of America **142**, 3187–3197 (2017).

[53] A. E. Aliev, D. H. Mueller, J. N. Tacker, N. K. Mayo, J. B. Blottman, S. Priya, and R. H. Baughman, "Improved thermoacoustic sound projectors by vibration mode modification", Journal of Sound and Vibration **524**, 1–16 (2022).

[54] A. Hall, J. Gaston, W. Wolde, E. Baker, M. Okada, Y. Wang, and S. Karna, "Signal conditioning of carbon nanotube thin film loudspeakers", Proceedings of the 14th IEEE International Conference on Nanotechnology, 668–671 (2014).

[55] T. M. Bouman, *Development of the carbon nanotube thermoacoustic loudspeaker* (Michigan Technological University, 2021).

[56] L. Deng, X. He, S. He, Q. Ren, J. Zhao, and D. Wang, "Research on frequency doubling effect of thermoacoustic speaker based on graphene film", Sensors **21**, 1–11 (2021).

[57] T. Sugimoto and Y. Nakajima, "Second harmonic distortion suppression of thermoacoustic transducer using square root circuit", Acoust. Sci. & Tech. **37**, 99–105 (2016).

[58] P. L. Torraca, Y. Ricci, M. Bobinger, P. Pavan, and L. Larcher, "Linearization of thermoacoustic loudspeakers by adaptive predistortion", Sensors and Actuators A: Physica **297**, 1–7 (2019).

[59] M. S. Heath and D. W. Horsell, "Multi-frequency sound production and mixing in graphene", Scientific Reports **7**, 1–9 (2017).

[60] M. M. Thiery, *Advanced uses for carbon nanotubes: a spherical sound source and hot-films as microphones* (Michigan Technological University, 2017).

[61] M. Gaal, J. Bartusch, F. Schadow, U. Beck, M. Daschewski, and M. Kreutzbruck, "Airborne ultrasonic systems for one-sided inspection using thermoacoustic transmitters", 2016 IEEE International Ultrasonics Symposium Proceedings, 1–4 (2016).

[62] T. Asada, S. Sasaki, and Y. Watabe, "Airborne µm-level vibration measurement with thermophone and phase tracking method", 2021 IEEE International Ultrasonics Symposium (IUS), 1–4 (2021).

[63] B. R. Gopal, R. Chahine, M. Földeàki, and T. K. Bose, "Noncontact thermoacoustic method to measure the magnetocaloric effect", Review of Scientific Instruments **66**, 232–238 (1995).

[64] F. Schütt, F. Rasch, N. Deka, A. Reimers, L. M. Saure, S. Kaps, J. Rank, J. Carstensen, Y. K. Mishra, D. Misseroni, A. R. Vázquez, M. R. Lohe, A. S. Nia, N. M. Pugno, X. Feng, and R. Adelung, "Electrically powered repeatable air explosions using microtubular graphene assemblies", Materials Today **48**, 7–17 (2021).

[65] R. Hopper, D. Popa, F. Udrea, S. Z. Ali, and P. Stanley-Marbell, "Miniaturized thermal acoustic gas sensor based on a cmos microhotplate and mems microphone", Scientific Reports **12**, 1–6 (2022).

[66] S. M. Vaglica, *Application of carbon nanotube thermophones as duct noise cancelling speakers: using new technology with old theories* (Michigan Technological University, 2021).

[67] S. Julius, R. Gold, A. Kleiman, B. Leizeronok, and B. Cukurel, "Modeling and experimental demonstration of heat flux driven noise cancellation on source boundary", Journal of Sound and Vibration **434**, 442–455 (2018).

[68] S. Prabhu, *Development of a method to model an enclosed, coaxial carbon nanotube speaker with experimental validation* (Michigan Technological University, 2021).

[69] Z. Zhang, H. Tian, P. Lv, Y. Yang, Q. Yang, S. Yang, G. Wang, and T. Ren, "High-performance sound source devices based on graphene woven fabrics", Appl. Phys. Lett **110**, 1–5 (2017).

[70] S. Kang, S. Cho, R. Shanker, H. Lee, J. Park, D. S. Um, Y. Lee, and H. Ko, "Transparent and conductive nanomembranes with orthogonal silver nanowire arrays for skin-attachable loudspeakers and microphones", Science Advances **4** (2018).

[71] H. Hu, T. Zhu, and J. Xu, "Model for thermoacoustic emission from solids", Appl. Phys. Lett. **96**, 1–3 (2010).

[72] C. W. Lim, L. H. Tong, and Y. C. Li, "Theory of suspended carbon nanotube thinfilm as a thermal-acoustic source", Journal of Sound and Vibration **332**, 5451–5461 (2013).

[73] J. Bin, W. S. Oates, and K. Taira, "Thermoacoustic modeling and uncertainty analysis of two-dimensional conductive membranes", Journal of Applied Physics **117**, 1–10 (2015).

[74] P. Guiraud, S. Giordano, O. Bou-Mater, P. Pernod, and R. Lardat, "Multilayer modeling of thermoacoustic sound generation for thermophone analysis and design", Journal of Sound and Vibration **455**, 275–298 (2019).

[75] P. M. Morse and K. U. Ingard, *Theoretical acoustics* (Princeton University Press, 1968).

[76] D. J. Griffiths, *Introduction to electrodynamics* (Cambridge University Press, 2017).

[77] S. J. Blundell and K. M. Blundell, *Concepts in thermal physics* (Oxford University Press, 2010).

[78] L. E. Kinsler, A. R. Frey, A. B. Coppens, and J. V. Sanders, *Fundamentals of acoustics* (John Wiley & Sons Inc., 2000).

[79] W. Pijls, "Some properties related to mercator projection", The American Mathematical Monthly **108**, 537–543 (2001).

[80] E. G. Williams, *Fourier acoustics: sound radiation and nearfield acoustical holography* (Academic Press, 1999).

[81] O. C. Zienkiewicz and R. L. Taylor, *The finite element method: fluid dynamics*, Vol. 3 (John Wiley & Sons Inc., 2000).

[82] S. Kirkup, "The boundary element method in acoustics: a survey", Appl. Sci. **9**, 1–50 (2019).

[83] *Air - thermophysical properties*, `https://www.engineeringtoolbox.com/air-properties-d_156.html`, Accessed: 2022-04-05.

[84] D. M. Tatnell, M. S. Heath, S. P. Hepplestone, A. P. Hibbins, S. M. Hornett, S. A. R. Horsley, and D. W. Horsell, "Coupling and confinement of current in thermoacoustic phased arrays", Science Advances **6**, 1–5 (2020).

[85] B. W. Drinkwater and P. D. Wilcox, "Ultrasonic arrays for non-destructive evaluation: a review", NDT&E International **39**, 525–541 (2006).

[86] J. F. Pazos-Ospina, F. Quiceno, J. L. Ealo, R. B. Muelas, and J. Camacho, "Focalization of acoustic vortices using phased array systems", Physics Procedia **70**, 183–186 (2015).

[87] P. D. Wilcox, J. Zhang, and B. W. Drinkwater, "Defect characterization using ultrasonic arrays", Proc. of SPIE **6935**, 1–12 (2008).

[88] A. Marzo, S. A. Seah, B. W. Drinkwater, D. R. Sahoo, B. Long, and S. Subramanian, "Holographic acoustic elements for manipulation of levitated objects", Nature Communications **6**, 1–7 (2015).

[89] S. Inoue, Y. Makino, and H. Shinoda, "Active touch perception produced by airborne ultrasonic haptic hologram", 2015 IEEE World Haptics Conference (WHC), 362–367 (2015).

[90] V. F. G. Tseng, S. S. Bedair, and N. Lazarus, "Phased array focusing for acoustic wireless power transfer", IEEE Transactions on Ultrasonics, Ferroelectrics, and Frequency Control **65**, 39–49 (2018).

[91] C. Shi, M. Dubois, Y. Wang, and X. Zhang, "High-speed acoustic communication by multiplexing orbital angular momentum", PNAS **114**, 7250–7253 (2017).

[92] Y. Ohara, T. Oshiumi, H. Nakajima, K. Yamanaka, X. Wu, T. Uchimoto, T. Takagi, T. Tsuji, and T. Mihara, "Ultrasonic phased array with surface acoustic wave for imaging cracks", AIP Advances **7**, 1–7 (2017).

[93] A. Marzo, T. Corkett, and B. W. Drinkwater, "Ultraino: an open phased-array system for narrowband airborne ultrasound transmission", IEEE Transactions on Ultrasonics, Ferroelectrics, and Frequency Control **65**, 102–111 (2018).

[94] B. Long, S. A. Seah, T. Carter, and S. Subramanian, "Rendering volumetric haptic shapes in mid-air using ultrasound", ACM Transactions on Graphics **33**, 1–9 (2014).

[95] M. Celmer and K. J. Opieliński, "Research and modeling of mechanical crosstalk in linear arrays of ultrasonic transducers", Archives of Acoustics **41**, 599–612 (2016).

[96] S. T. Lau, H. Li, K. S. Wong, Q. F. Zhou, Y. C. Li, H. S. Luo, K. K. Shung, and J. Y. Dai, "Multiple matching scheme for broadband 0.72pb(mg1/3nb2/3)o3-0.28pbtio3 single crystal phased-array transducer", Journal of Applied Physics **105**, 1–5 (2009).

[97] P. Muralt, N. Ledermann, J. Baborowski, A. Barzegar, S. Gentil, B. Belgacem, S. Petitgrand, A. Bosseboeuf, and N. Setter, "Piezoelectric micromachined ultrasonic transducers based on pzt thin films", IEEE Transactions on Ultrasonics, Ferroelectrics, and Frequency Control **52**, 2276–2288 (2005).

[98] O. Oralkan, A. S. Ergun, J. A. Johnson, M. Karaman, U. Demirci, K. Kaviani, T. H. Lee, and B. T. Khuri-Yakub, "Capacitive micromachined ultrasonic transducers: next-generation arrays for acoustic imaging?", IEEE Transactions on Ultrasonics, Ferroelectrics, and Frequency Control **49**, 1596–1609 (2002).

[99] K. N. Tu, Y. Liu, and M. Li, "Effect of joule heating and current crowding on electromigration in mobile technology", Applied Physics Reviews **4**, 1–24 (2017).

[100] F. B. Hagedorn and P. M. Hall, "Right-angle bends in thin strip conductors", Journal of Applied Physics **34**, 128–133 (1963).

[101] D. M. Tatnell, M. S. Heath, A. P. Hibbins, and D. W. Horsell, "A thermophone-based bridge circuit for the measurement of electrical and thermal properties of thin films", Journal of Physics D: Applied Physics **55**, 1–7 (2022).

[102] K. Hoffmann, *Applying the wheatstone bridge circuit* (HBM, Darmstadt, 1974).

[103] A. Nemecek, K. Oberhauser, and H. Zimmermann, "Distance measurement sensor with pin-photodiode and bridge circuit", IEEE Sensors Journal **6**, 391–397 (2006).

[104] X. Tan, Y. Lv, X. Zhoue, X. Song, Y. Wang, G. Gu, H. Guo, S. Liang, Z. Feng, and S. Cai, "High performance algan/gan pressure sensor with a wheatstone bridge circuit", Microelectronic Engineering **219**, 111143 (2020).

[105] W. Thomson, "On the dynamical theory of heat. part v. thermo-electric currents.", Transactions of the Royal Society of Edinburgh **21**, 123–171 (1857).

[106] M. R. Ward, *Electrical engineering science* (McGraw-Hill, New York, 1971).

[107] N. W. Ashcroft and N. D. Mermin, *Solid state physics* (Brooks/Cole, 1976).

[108] D. Narducci, P. Bermel, B. Lorenzi, N. Wang, and K. Yazawa, *Hybrid and fully thermoelectric solar harvesting* (Springer International Publishing, 2018).

[109] J. H. Scofield, "Frequency-domain description of a lock-in amplifier", American Journal of Physics **62**, 129–133 (1994).

[110] *Comsol multiphysics®* (COMSOL AB, Stockholm, Sweden).

[111] *Thermocouple sensors physical properties of thermoelement materials* (Omega Engineering).

[112] J. H. Lienhard and J. H. Lienhard, *A heat transfer textbook* (Phlogiston Press, 2020).